Radar rainfall forecasting for sewer flood modelling to support decision-making in sewer network operations

Submitted by Arshan Iqbal to the University of Exeter
as a thesis for the degree of
Doctor of Engineering in Water Engineering
In November 2017

I certify that all material in this thesis which is not my own work has been identified and that no material has previously been submitted and approved for the award of a degree by this or any other University.

Signature: ……..

Abstract

Radar quantitative precipitation estimates (QPEs) and forecasts (QPFs) are useful in urban hydrology because they can provide real time or forecasted rainfall information for flood forecasting/warning systems. Sewer flooding is a disruptive problem in England and Wales. Wastewater companies have reported that more than 4,700 customers are at risk of internal sewer flooding. Currently in the UK, mitigating sewer flooding before it occurs is difficult to achieve operationally because of the lack of accurate and specific data. As radar rainfall data is available from the UK Met Office, particularly radar QPFs with a maximum lead time of 6 hours, these datasets could be used to predict sewer flooding up to this maximum lead time.

This research investigates the uses of radar Quantitative Precipitation Forecasts and Quantitative Precipitation Estimates to support short term decisions of sewer network operation in reducing the risk of sewer flooding. It is achieved by increasing the accuracy of deterministic radar quantitative precipitation forecasts, developing on probabilistic radar quantitative precipitation forecasts, and using spatial variability of radar quantitative precipitation estimates to estimate flood extents in sewer catchments from the North East of England. Radar rainfall data used in the case study is also sourced from this region of size 184 km x 140 km.

The temporal and spatial resolutions of rainfall forecasts are important to producing accurate hydrological output. Hence, increasing these resolutions is identified to improving deterministic radar quantitative precipitation forecasts for hydrological applications. An interpolation method involving temporal interpolation by optical flow and spatial interpolation by Universal Kriging is proposed to increase the resolution of radar QPF from a native resolution of 15 mins and 2-km to 5 mins and 1-km. Key results are that the interpolation method proposed outperforms traditional interpolation approaches including simple linear temporal interpolation and spatial interpolation by inverse distance weighting.

Probabilistic radar quantitative precipitation forecasts provide information of the uncertainty of the radar deterministic forecasts. However, probabilistic approaches have limitations in that they may not accurately depict the uncertainty

range for different rainfall types. Hence, postprocessing probabilistic quantitative precipitation forecasts are required. A Bayesian postprocessing approach is introduced to postprocess probability distributions produced from an existing stochastic method using the latest radar QPE. Furthermore, non-normal distributions in the stochastic model are developed using gamma based generalised linear models. Key successes of this approach are that the postprocessed probabilistic QPFs are more accurate than the pre-processed QPFs in both cool and warm seasons of a year. Furthermore, the postprocessed QPFs of all the verification events better correlate with their QPE, thus improving the temporal structure.

Spatial variability of radar QPE/QPF data influences flood dynamics in a sewer catchment. Moreover, combination of different percentiles of probabilistic QPFs, per radar grid, over a sewer catchment would produce different spatial distributions of rainfall over the area. Furthermore, simulating many probabilistic QPFs concurrently is computationally demanding. Therefore, generalised linear models have been used to estimate model flood variables using a spatial analysis of radar QPE. Spatial analysis involves using indexes representing specific information of the spatial distribution of rainfall. The novelty of this estimation method includes faster estimations of flood extents. The main points of success of this approach are that more detailed spatial analysis of large sewer catchments produce more accurate flood estimations that could be used without running hydraulic simulations. This makes the approach suitable for probabilistic sewer flood forecasting in real-time applications.

A business case is proposed to use the outputs of this research for commercial applications. Probabilistic sewer flood forecasting is evaluated and recommended for industry application using a financial appraisal approach for Northumbrian Water Limited. The business case shows that the methods could be adopted by the wastewater company to mitigate sewer flooding before it occurs. This would support decision making and save costs with better intervention management.

Table of Contents

Acknowledgments

“Coming together is a beginning. Keeping together is progress. Working together is success.” - Henry Ford

I would like to sincerely thank my supervisors, Professor Guangtao Fu and Professor David Butler for their supervision that had helped me complete my EngD. Their support and inspiring ways of challenging and pushing my academic potential had enabled me to express it in dynamic ways in the four years of my research. I would also like to thank members of Centre for Water Systems and Exeter Climate Systems who had wilfully, or unexpectedly, joined my academic journey and had witnessed me taking major steps to furthering my research area. The inspiration, training and personal support I had received from them throughout my programme has been outstanding. I am lucky to have been around such great, positive, genuine, diverse and selfless people, and have even made friendships that are life-long.

My academic journey had been influenced by life outside of academia, particularly in the industry. I would like to express sincere gratitude to staff in Northumbrian Water who had had continuously supported me in providing data, material and guidance to using my research to solve a commercial problem. Particularly, I would like to thank Andrew Moore who provided brilliant mentorship, humour and support to helping me understand the water industry, which brought a refreshing perspective to my research. Thanks also go to Northumbrian Water staff members Daniel Jenkin, Hervé Vicente, Martin Kennedy and Martin Huttly for their active support.

Furthermore, much thanks to Alistair Dalton from AMEC Foster Wheeler for providing data, hydraulic models and dedicated guidance to helping me throughout the project.

Also, I would like to pass deep thanks to the STREAM management team for hosting this research project, particularly Professor Paul Jeffrey and Tania Rice. It’s been a pleasure to work with all STREAM colleagues and to have made great

friends throughout the four years. Furthermore, I would like to acknowledge Joanne Strachan who had warmly accommodated me in Durham and became very supportive of my academic goals. I would also like to acknowledge great-hearted friends I had made internationally during my adventurous research trips to National Taiwan University (NTU), Indian Institute of Science (IISc) and New Mexico State University (NMSU). Especially, great thanks to Chandra Rupa from IISc and Usman Khan from York University in Toronto, Canada for their sincere efforts in helping me understand Bayesian statistics. This was crucial when developing my second methodology.

Last, but not least, I would like to express deep gratitude and happiness to the support and encouragement from my family members Mum, Dad, Yasir, Shazeen and Zeba, and our cats Naomi, Enjaye, Tumble, Flake and Tango. Dad (Zahid Iqbal), I have taken so much from your reassuring behaviour, confidence and honest hard work. A most special thanks to Mum (Khurshida Begum). You are the pillar of my journey to the success I have achieved due to the limitless love, joy, positivity and mercy you show.

It goes without saying that one may meet challenging people in any difficult endeavour. They provide challenging experiences from which we may learn more about ourselves and, more particularly, to identify those who can bring out the best in us and to move on from those who cannot. Therefore, I am incredibly lucky to have made acquaintance, or to have kept together with the above people. We have all worked together each taking a different role, and that is why I have successfully completed my EngD, which is both an academic and personal endeavour. I could not have done it without you all.

List of Figures

List of Tables

List of Abbreviations

ANC	Auto-Nowcaster
ANN	Artificial Neural Network
BFS	Bayesian Forecasting System
BJM	Bayesian Joint Model
BPPM	Bayesian Post Processing Model
BR	Bias Ratio
CDF	Cumulative Distributions Function
CFS	Climate Forecast System
CO-TREC	Continuous-TREC
CRA	Contiguous Rain Areas
CSO	Combined Sewer Overflow
DQ	Direct Quartile
DSD	Drop Size Distribution
EPS	Ensemble Prediction System
ESP	Ensemble Streamflow Prediction
FFGS	Flash Forecast Guidance System
FOG	Fats, Oil and Grease
GAM	Generalised Additive Model
GLM	Generalised Linear Model
GLUE	Generalised Likelihood Uncertainty Estimation
HEFS	Hydrologic Ensemble Forecast Service
HEPS	Hydrological Ensemble Prediction Systems
IDW	Inverse Distance Weighting

IRR	Internal Rate of Return
LHS	Latin Hypercube Sampling
MCMC	Monto Carlo Markov Chain
MH	Metropolis Hastings
NCAR	National Center for Atmospheric Research
NPV	Net Present Value
NWP	Numerical Weather Prediction
NWS	National Weather Service
NWSRFS	National Weather Service River Forecast System
OKR	Ordinary Kriging
OSM	Original Stochastic Model
PDF	Probability Distribution Function
QPE	Quantitative Precipitation Estimates
QPF	Quantitative Precipitation Forecasts
RMSE	Root Mean Square Error
SREF	Short-Range Ensemble Forecast
STEPS	Short-Term Ensemble Prediction System
SUDs	Sustainable Urban Drainage systems
TITAN	Thunderstorm Identification, Tracking, Analysis, and Nowcasting
TREC	Tracking Radar Echoes by Correlation
UKR	Universal Kriging
VET	Variational Echo Tracking
VPR	Vertical Profile of Reflectivity

List of Notations

Chapter 3

$\boldsymbol{x}$	x-coordinate
$\boldsymbol{y}$	y-coordinate
$\boldsymbol{X}$	coordinate in a radar image
$\boldsymbol{w}$	movement vector
$\boldsymbol{u}$	movement vector in the x-direction
$\boldsymbol{v}$	movement vector in the y-direction
$\boldsymbol{i}$	index of timestep
$\boldsymbol{j}$	index of spatial grid location of radar image
$\boldsymbol{T^i}$	timestep of radar QPF with index $\boldsymbol{i}$ of radar image
$R(\boldsymbol{X}, \boldsymbol{T^i})$	intensity of radar image at coordinate $\boldsymbol{X}$ at timestep $\boldsymbol{T^i}$
e	stabilising constant
$E(\boldsymbol{w})$	energy function at movement vector $\boldsymbol{w}$
$E_{DATA}(\boldsymbol{w})$	energy function (data component) at movement vector $\boldsymbol{w}$
$E_{SMOOTH}(\boldsymbol{w})$	energy function (smooth component) at movement vector $\boldsymbol{w}$
REG	regularisation parameter
Ψ	increasing concave function
ω	domain of radar QPE
γ	weight constant
N	number of interpolations per timestep
$\boldsymbol{T}$	timestep of radar QPF
$\boldsymbol{t}$	timestep of radar QPE
α	temporal interpolation weight constant

k	kth interpolation between two radar QPF images
A	threshold value in temporal interpolation algorithm
$\boldsymbol{f}$	forward movement coordinates
$\boldsymbol{b}$	backward movement coordinates
$I(\boldsymbol{X})$, $I^*(\boldsymbol{X})$	rainfall intensity at $\boldsymbol{X}$ coordinate
λ	weight function used in Universal Kriging
n	variable used in summation notation
Y	noise function
m	deterministic function
q	arbitrary functions in local trend analysis of Universal Kriging
v	coefficients in local trend analysis of Universal Kriging
h	distance vector
$\gamma(h)$	empirical variogram
$\gamma^*(h)$	covariance variogram
$\gamma_S^*(h)$	spherical model variogram
$\bar{N}(h)$	number of pairs with distance vector h
Cov	covariance
β_{nugget}	nugget of variogram
β_{struct}	structural heterogeneity of variogram
β_{corr}	range of variogram
$y_{i,j}^{qpf}$	historical QPF at ith timestep and radar grid j
$y_{i,j}^{qpe}$	historical QPE at ith timestep and radar grid j
$QPF_{i,j}$	live QPF at ith timestep and radar grid j

$QPE_{i,j}$	live QPE at ith timestep and radar grid j
$\bar{n}$	number of timesteps
K	number of radar grids used in case study
$RMSE$	root mean square error
BR	bias ratio

Chapter 4

α	gamma shape parameter
β	gamma rate parameter
$\emptyset^{INITIAL}$	initial parameter of distribution
$\alpha^{INITIAL}$	initial shape parameter of gamma distribution
$\beta^{INITIAL}$	initial rate parameter of gamma distribution
H	set representing historical data
D	set representing recent QPE
$\emptyset_i$	parameter set of posterior distribution of first MCMC stage
α_i	gamma shape parameter set of posterior distribution of first MCMC stage
β_i	gamma rate parameter set of posterior distribution of first MCMC stage
$\emptyset_j$	parameter set of posterior distribution of second MCMC stage
α_j	gamma shape parameter set of posterior distribution of second MCMC stage
β_j	gamma rate parameter set of posterior distribution of second MCMC stage
$\emptyset^{FINAL}$	final parameter of distribution

α^{FINAL}	final shape parameter of gamma distribution
β^{FINAL}	final rate parameter of gamma distribution
S	radar QPE rainfall intensity value (observed data)
$\dot{S}$	radar QPF rainfall intensity value (forecast data)
x, y	random realisations
P	probability
Γ	gamma function
E	expectation
Var	variance
b_0, b_1	glm coefficients
N	size of $\{S, \dot{S}\}$
K	target distribution
$\emptyset^i$, $\emptyset^j$	sampled parameters
q	proposal distribution
$\bar{r}$	arbitrary distribution
$\delta_{\emptyset^i}$	variable used MCMC
v	acceptance probability
A	subset of H
α_A	gamma shape parameter of set A
β_A	gamma rate parameter of set A
$\bar{A}$	rainfall accumulation
p	exceedance probability (or percentile)
r	Pearson's r

Chapter 5

ev	event number
EV	total number of events
j	index of radar grid
A_j	rainfall accumulation over radar grid j
A_{total}	total rainfall accumulation over sewer catchment
AC	set of rainfall accumulation A_j
N	total radar grids over sewer catchment
E	expectation
$\boldsymbol{I_1}$	spatial index 1
$\boldsymbol{I_2}$	spatial index 2
F_j	flow distance from radar grid j to outlet node
B	total area of sewer catchment
$\boldsymbol{V^a}$	total flood volume in the model sewer catchment
$\boldsymbol{V^b}$	total floods in the model sewer catchment
x	random realisation
μ_a	gaussian mean parameter
σ_a	gaussian standard deviation parameter
β_b	Poisson rate parameter
$\boldsymbol{VAR}$	variance
SD	standard deviation
$\boldsymbol{MR}$	mean rainfall
$GLM1, GLM2$	generalised linear models
$GLM1_a$, $GLM2_a$	gaussian generalised linear models

$GLM1_b$, $GLM2_b$	Poisson generalised linear models
b^{GLM1}, b^{GLM2}	coefficients of gaussian generalised linear models
g^{GLM1}, g^{GLM2}	coefficients of Poisson generalised linear models

Chapter 6

NPV	net present value
$periods$	total number of periods
$month$	period
$CASH_{month}$	cash inflow per period
$CASH_{out}$	total cash outflow
dis	discount rate

1 Introduction

1.1 Background and motivation

Prolonged or heavy rainfall is the primary cause of sewer flooding in the UK. Due to urbanisation, imperviousness in many urban areas has increased. Therefore, urban runoff is accumulated quickly and the time for the runoff to reach the outlet of the catchment decreases (i.e. reduction of time of concentration). This overwhelms the sewer network as it reaches full hydraulic capacity quickly, which causes surcharge or flooding problems. When the combined stormwater and sewage escapes back onto the surface (i.e. pluvial flooding) flooding streets, pathways, road and houses causing costly damage. Moreover, sewage may escape back through toilets within households causing internal sewer flooding.

Most sewer systems in the UK are combined systems with a small proportion of separate systems handling rainfall only. Combined systems carry both sewage and stormwater to the wastewater treatment plant. When the system becomes overloaded with stormwater entering the network, Combined Sewer Overflows (CSOs) release sewage to the river and results in water pollution problems. Sewer flooding is a disruptive problem in England and Wales, with more than 4,700 customers at risk of internal sewer flooding (Ofwat, 2011). Research shows that the intensity of rainfall is projected to increase and would occur at shorter durations (Ref). Therefore, the risk of sewer flooding is likely to increase.

Flood management strategies include developing new structural measures such as upgrading separate systems, constructing Sustainable Urban Drainage Systems (SUDs) and investing into new technological hardware (Esteves, 2013; Brown *et al.*, 2010). However, these strategies can be expensive and take a long time before they are operational and for their benefits to be evaluated. They would also cause disruption to sewerage services which should be minimised. Hence, non-structural approaches have been used to reduce the risk of sewer flooding. Particularly, the use of radar rainfall forecasts has been studied for flood risk management in urbanised areas.

1.1.1 Radar rainfall data

There are three approaches of quantifying rainfall measurements. They include the use of rain gauges, weather radar and satellite data. Radar rainfall data has become popular in urban hydrology. The advantage of radar rainfall is the extents of representing spatial rainfall values, which is a limitation of point rainfall sources such as rain gauges (Einfalt *et al.*, 2004). Although, rain gauges are considered the most accurate source for measuring rainfall. Satellite sources uses electromagnetic waves to detect rainfall. An example is METEOSAT – the European geostationary satellite – which uses visible and infrared (Golding, 2000; Golding *et al.*, 1998; Koriche and Rientjes, 2016). However, satellite sources are not reliable for measuring fine rates of rainfall rates. This is exacerbated in night time conditions due to infrared only being available and thus satellites are unreliable for producing rainfall data.

Therefore, radar rainfall has increasingly been used in hydrology, particularly for studying storm characteristics (i.e. evolution, distribution etc.) due to the wide spatial availability of rainfall values. This allows studying impacts of different storms on catchments. Generally, radar rainfall shows more uncertainty for predicting higher intensity rainfall. However, these storms are more easily detected in comparison to light intensity rainfall or drizzles. Figure 1.1 shows probability of detection of rainfall as a function of the range of the measured rainfall from the radar. This figure explains two attributes of radar rainfall: the first attribute is that the probability of detecting rainfall is reduced for increasing distances, and the second is that higher intensity rainfall is more likely to be detected.

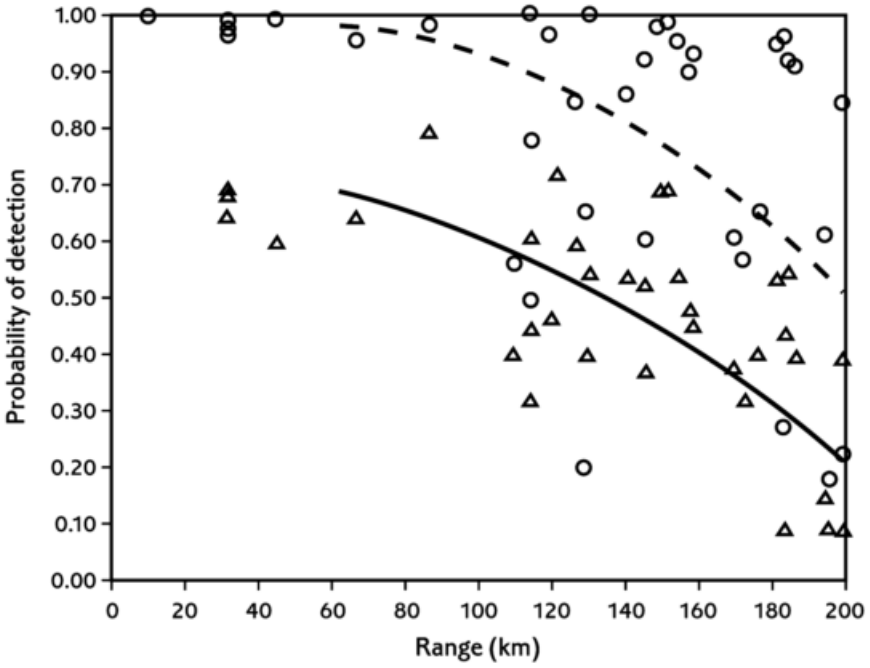

Figure 1.1. Probability of detection against the range for two rainfall events: light rain (solid line and triangle) and heavy rain (dashed line and circles) (Golding, 2000).

Various radar uncertainties have been extensively explored. However, in urban hydrology the catchments are usually smaller decreasing the time of runoff accumulating. This has specific requirements of radar rainfall in urban hydrology. For example, temporal and spatial resolutions of radar rainfall data in urban hydrology were recommended by Schilling (1991) to be between 1-5 min and 1 km, respectively. The uncertainty range of the rainfall intensity should be less than 10% and in the range of 10 – 150 mm/h. The applications of radar rainfall have been distinguished as offline or online applications (Einfalt *et al.*, 2004). offline applications include the development of network models, analysing the impact of different storms over a catchment, or the study of extreme rainfall events. Online applications include qualitative control, quantitative control of sewer systems, operational application such as flood warning and management, and the use of forecasts for flood forecasting.

Another advantage of radar technology is that the data could be extrapolated to the near future to product rainfall forecasts, particularly at real-time settings. Quantitative Precipitation Forecasts (QPFs) could be generated from radar Quantitative Precipitation Estimates (QPEs) this way and have been used for online hydrological applications (Bowler *et al.*, 2004). One of the fundamental

properties of rainfall forecasts is that the longer the forecast horizon, the higher the uncertainty. This is also true for increasing intensity (i.e. higher uncertainty associated to higher rainfall intensities). Figure 1.2 demonstrates this for rainfall intensity as the Root Mean Square Error (RMSE) of the rainfall forecast field against the observed rainfall is increasing for higher rainfall values. high intensity Rainfalls have been of greater focus because these are normally dynamic and of short duration (i.e. convective storms), which are often difficult to predict in hydrology, especially over small catchments.

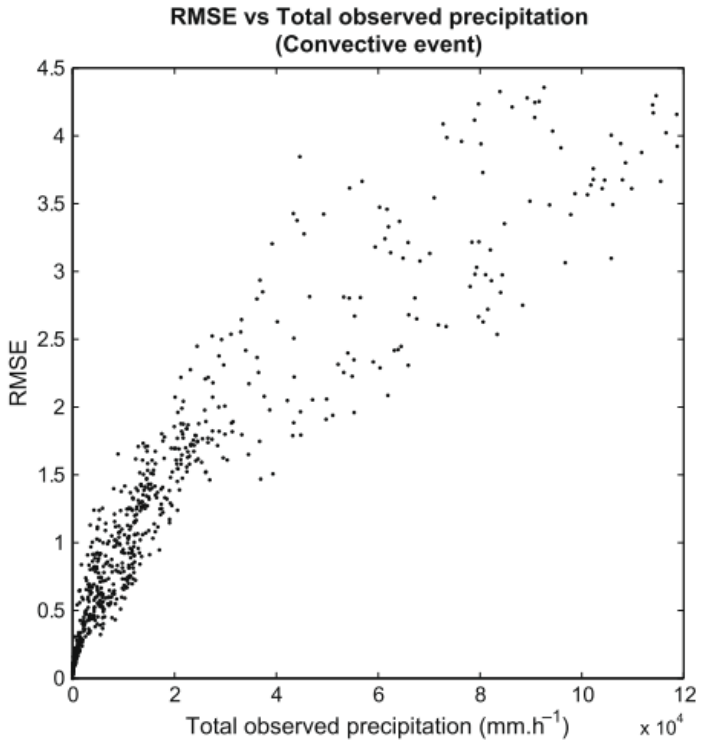

Figure 1.2. The RMSE against precipitation (rainfall) intensity (Barillec and Cornford, 2009).

QPFs are categorised in three ways depending on their forecast horizons: nowcasts, short-range forecasts and medium-range forecasts (Golding, 2000). Nowcasts estimate rainfall between 0 – 6 hours into the future and commonly produced using radar QPE in extrapolation techniques. Most short-range forecasts estimate rainfall between 12 – 72 hours into the future. These forecasts are primarily generated from Numerical Weather Prediction (NWP) models that depend on mathematical methods and assumptions to construct rainfall values. Medium-range estimate rainfall typically beyond 2 days (i.e. 48 hours) into the future. The uncertainty at this range is large and meteorological services make

use of probabilistic forecasting by predicting the probability distribution of rainfall. These approaches outperform deterministic methods at this forecast range and make use of storm characteristics such as evolution, growth and decay.

Two types of forecasts are recognisable in meteorological and hydrological studies: they are deterministic and probabilistic forecasts (Golding, 2000). Deterministic forecasts are single valued forecasts that are commonly used to indicate an estimate of the rainfall. Probabilistic forecasts provide a range of forecasts with a probability of occurrence assigned to each one. The fundamental difference between deterministic and probabilistic forecasts is that the latter provides information of the uncertainty of the deterministic forecast. Probabilistic forecasts are integral part of decision making systems are thus useful for online hydrological applications. Typically, they make use of probability distribution functions, which show the probability of occurrence for different rainfall intensities. Figure 1.3 shows a probability distribution function for a varying rainfall values of a QPF. Higher intensity QPF values are more unlikely to occur (i.e. lower probability of occurrence) but they have higher potential of damage. Thus, more preparedness is required. The figure demonstrates how thresholds are defined directly from a probability distribution function to mitigate flooding.

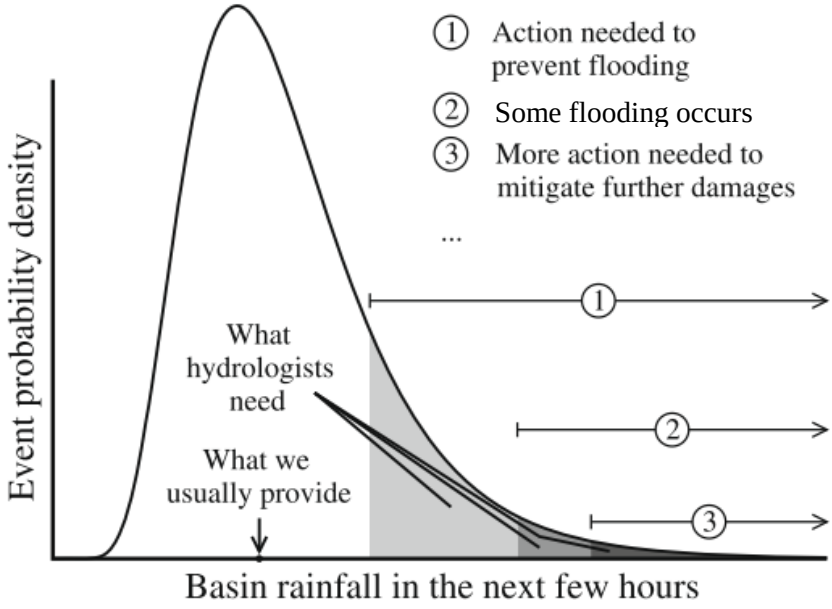

Figure 1.3. Example of decision making process using the probability distribution function (Event probability density) for rainfall forecast (Basin rainfall in the next few hours) (Fabry and Seed, 2009).

Repeatedly stated in radar rainfall and urban hydrology is the inherent uncertainties of radar technology. These uncertainties begin from the hardware and the physical processes involved measuring rainfall reflectivity from raindrops, and mathematical methods used to quantify rainfall estimates also introduce uncertainty. There are issues associated to radar rainfall adjustment techniques to uncertainties in extrapolation and numerical schemes generating radar rainfall forecasts. Furthermore, radar rainfall forecasts include several uncertainties that require further analysis to make flood forecasting more reliable. This is explored in detail in this project.

1.1.2 Flood forecasting in urban hydrology

Flood management would normally include policy control, design, planning and operational management. Infrastructural approaches ensure development of flood protection and SUDs. However, real-time monitoring and management of flooding is recognised to be useful and cost-effective way of reducing the impact of flooding operationally. This would help reduce investment to expensive infrastructure based interventions and increase preparedness. This is achieved by increasing the lead time to take measures to control the flood before it occurs.

Approaches of operational flood warning systems have been developed extensively in the past. Generally, the stages for an operational flood warning system consists of: detection, forecasting, warning and response (Werner *et al.*, 2005)(see Figure 1.4). Detection involves collecting the data from sources such as rain gauge, radar, satellites etc in real-time. Forecasting is the stage where the real-time data is input to hydrological models to produce estimates of model variables used to generate flood warnings. The warning stage involves translating the predictions of the forecasting stage to warnings for specific mitigating bodies. This is considered a crucial stage in the operational flood warning system as the level of mitigation depends on how the warning is communicated. The last stage is response, which determines the level of mitigation required based on the flood warning.

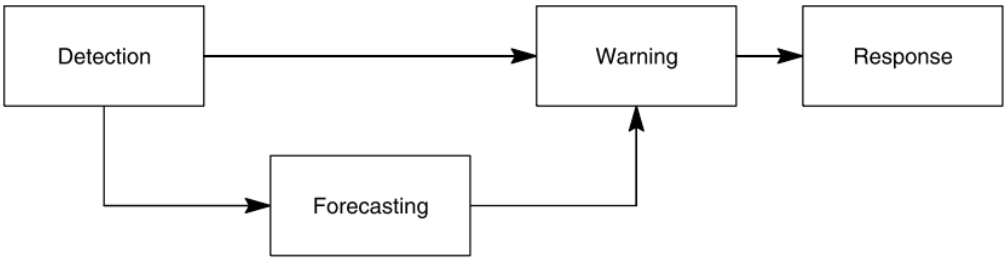

Figure 1.4. Stages in a flood warning system (Werner et al.*, 2005).*

As explained in section 1.1.1, QPFs could be used hydrological models for forecasting. This is an example of an online application of radar QPFs. Real-time flood forecasting systems could be classified in terms of the way the QPF is used in the model or for determining the response in the case that a model is not used. Four systems describing different ways QPFs could be part of real-time flood forecasting are described as follows (Hénonin *et al.*, 2013):

Empirical scenarios – scenarios of flooding have been collected based historical data or from experience. An intervention may be directly related to this such as the use of resources, access of knowledge or people. The rainfall is used as input to select the scenario, hence there is no use of models or direct need of technology. Therefore, it is simple and may not be robust.

Pre-simulated scenarios – offline simulations of floods are conducted and these become the historical data by which real-time QPFs are used to select from. Hydrological models are used to produce pre-simulated scenarios. The main disadvantage of this approach is that of the difficulty of updating the scenarios in the case that hydrological model needs to be modified.

Real-time data assimilation – this uses real-time QPFs as input to hydrological models in online settings. Real-time data is used to produce simulations and the output is used to determine the warning and response. This system is considered reliable and may be supported with pre-simulated scenarios (i.e. offline simulations) to reduce computational time. The main disadvantages of this approach is forecast accuracy and updating model parameters.

Real-time data assimilation with feedback – like the real-time data assimilation approach but with active feedback to the drainage system. Remote control and automated features enable changing physical components of the drainage system using the forecasting system in real-time. The limitations of this approach

the risk of equipment or systems failure in the automation and remote control of the drainage system.

The focus of this project is on developing forecasting methodologies (forecasting stage in Fig. 4) and not on conceptualising operational flood warning systems. Furthermore, concepts of pre-simulated scenarios together with data-assimilation are key components to some methodologies developed in this study. They are to support flood forecasting in real-time settings.

1.1.3 Motivations for sewer flood forecasting in the water sector

Damage caused by flooding could be categorised in three ways: direct, indirect and social (König *et al.*, 2002). Direct damages are immediate physical consequences of flooding in the affected area. For example, inundated roads, pathways and houses. Indirect damages include disruption of services or systems that have been affected by the direct consequences. Examples include traffic disruption, spread of disease, labour costs and mitigating expenses. Social damage includes economic and psychological impacts. This could be loss of money for businesses, unsatisfied customers, increased/decreased house prices and perceptions of flood risk when buying a house. In the case of sewer flooding, the damages mitigated by governmental bodies and the wastewater companies include all three of these categories. For wastewater companies, reducing social damages of sewer flooding is crucial for maintaining profitability and economic sustainability.

Damage caused by flooding needs to be mitigated. Presently in the water sector, damage associated with sewer flooding is mitigated predominantly after the flood occurs. Post-analysis of the hydrological characteristics is done and damage is evaluated for deciding on the interventions to mitigate the flooding. Several wastewater companies attempt to plan mitigation based on predicting sewer flooding. However, these systems are simple and rely on coarse datasets and knowledge that are not consistent and lack robustness (e.g. such as use of radar QPE to approximate flood locations). These systems are like the empirical scenario operational flood warning system described in section 1.1.2. However,

objective systems that are reliable or holistic are not actively operational presently in the UK water sector. Therefore, there is no active means to predict sewer flooding in the UK so that actions could be taken before the flood occurs.

As the UK water sector is driven to satisfy customers, which is a key objective for maintaining competitiveness the motivation to develop a sewer flood forecasting system is explored using impersonal customer data. The following section describes customer response to various sewer flooding and their causes. This was conducted by Ofwat (2004) with three UK wastewater companies participating providing impersonal customer data.

Table 1.1. Percentage of various sewer flooding due to different causes (Ofwat, 2004).

Causes	**Internal hydraulic flooding**	**Internal flooding due to other causes**	**Flooding in unoccupied cellars**	**External flooding**
Overload	66%	32%	19%	40%
Blockage	17%	48%	52%	38%
Equipment failure	7%	9%	4%	6%
Collapse	4%	19%	16%	6%
Other	1%	2%	2%	1%
Don’t know	18%	17%	17%	21%
Number of cases	190	178	134	146

Table 1.2. Percentage of various sewer flooding due to different types of rainfall (Ofwat, 2004).

Type of rainfall	**Internal hydraulic flooding**	**Internal flooding due to other causes**	**Flooding in unoccupied cellars**	**External flooding**
Dry	3%	20%	25%	12%
Light rain/drizzle	1%	8%	8%	5%
Heavy rain	81%	53%	43%	63%
Prolonged rain	24%	28%	20%	23%
Other	1%	2%	2%	1%
Don’t know	1%	6%	13%	4%
Number of cases	190	178	134	146

Table 1.1 shows the percentage of customer who have experienced sewer flooding for different types and causes. Table 1.2 shows the percentages of these sewer flooding cases but based on different types of rainfall. Most of the customer base have been affected by internal hydraulic flooding in comparison to other internal sewer flooding types and external flooding. The primary cause of internal hydraulic flooding is overload (i.e. the lack of hydraulic capacity) due to rainfall. Overload of sewer systems is also the primary cause of external sewer flooding followed by blockages. Blockages may occur due to non-rainfall sources, such as Fats, Oils and Grease (FOG) or tree root intrusion. Data in Table 1.2 shows that across all the various sewer flooding most of the sewer floods had occurred due to heavy rainfall. This is followed by prolonged rainfall (except for flooding in unoccupied cellars, which has the second largest majority of customers flooded due to no rainfall. This might be due to cellars being lower than ground level and closer to damaged or disconnected piping increasing the susceptibility to flooding). Note that the percentages across each cause of sewer flooding due to type of rainfall or type of sewer flood do not total 100%. This is because the percentages include more than one customer in the customer base (i.e. a customer may have experienced more than one type of sewer flood or experienced sewer flooding from different types of rainfall).

Based on this customer research, rainfall is a primary contributor to sewer flooding and particularly heavy or prolonged rainfall causes the most damage. This motivates the study to use rainfall data to predict sewer flooding to support decision making in sewer operations. This would help the water sector develop an operational flood warning system for sewer flooding so that actions could be taken before the floods occurs. Thus, as part of this thesis a business case (see section 6) is presented for the water sector to use the research to tackle sewer flooding.

1.2 Aims and objectives

The aim of this research project is to:

Investigate the applications of radar Quantitative Precipitation Forecasts and Quantitative Precipitation Estimates to support short term decisions of sewer network operation in reducing the risk of sewer flooding.

The focus is to use radar rainfall forecasts to predict sewer flooding. As explained in section 1.1.1, there are various uncertainties in radar rainfall data and this has impacts on forecasting applications. To fulfil the aim the following objectives have been identified:

1. Gather case studies of radar quantitative precipitation forecasts/estimates and sewer models.
2. Assess effectiveness of rainfall estimation and quantifying uncertainty in radar data for flood modelling applications.
3. Improve radar deterministic quantitative precipitation forecasts.
4. Increase the accuracy of radar probabilistic quantitative precipitation forecasts.
5. Conduct analysis of the spatial variation characteristics of radar quantitative precipitation data associated to the sewer network model.
6. Develop business case for methodologies developed in the project.

1.3 Scope and thesis structure

The uses of weather radar in hydrology are wide and include different research areas in both meteorology and hydrology. Recent contributions have been classified in various categories highlighting the focus of research (Moore *et al.*, 2012). The areas are weather radar theory and technology, rainfall estimation, rainfall forecasting (nowcasting and numerical weather prediction), uncertainty estimation, hydrological impact and design, hydrological applications and flood forecasting and water management in urban hydrology. This classification is useful for showing the broad areas of how radar rainfall could be used in hydrology. This thesis focuses on the following areas:

Rainfall estimation – this involves assessing the methods that produce estimates of radar QPE. Radar QPE is initially estimated using radar processes and then improved via adjustment techniques.

Uncertainty estimation – after radar rainfall is estimated inherent uncertainties are then explored. Inherent uncertainties of radar technology are propagated to radar rainfall forecasts. These uncertainties could be quantified using statistical techniques and could further be postprocessed. Various methods are discussed for uncertainties in radar QPFs.

Hydrological applications and flood forecasting – rainfall forecasts could be used in hydrological modelling to form part of a flood forecasting system. After ensuring the rainfall estimate is sufficiently accurate and the uncertainty is quantified, hydrological output of rainfall forecasts could be used for real-time applications. Further uncertainty sources and practicality issues in flood forecasting are explored.

A schematic of the thesis components is shown in Figure 1.5 along with the objectives that are associated to them. The following components are related to the areas stated above:

- Improving deterministic radar Quantitative Precipitation Forecasts (*Rainfall estimation*)
- Probabilistic radar Quantitative Precipitation Forecasts (*Uncertainty estimation*)
- Estimating flood extent using spatial analysis of radar Quantitative Precipitation Estimates (*Hydrological applications and flood forecasting*)

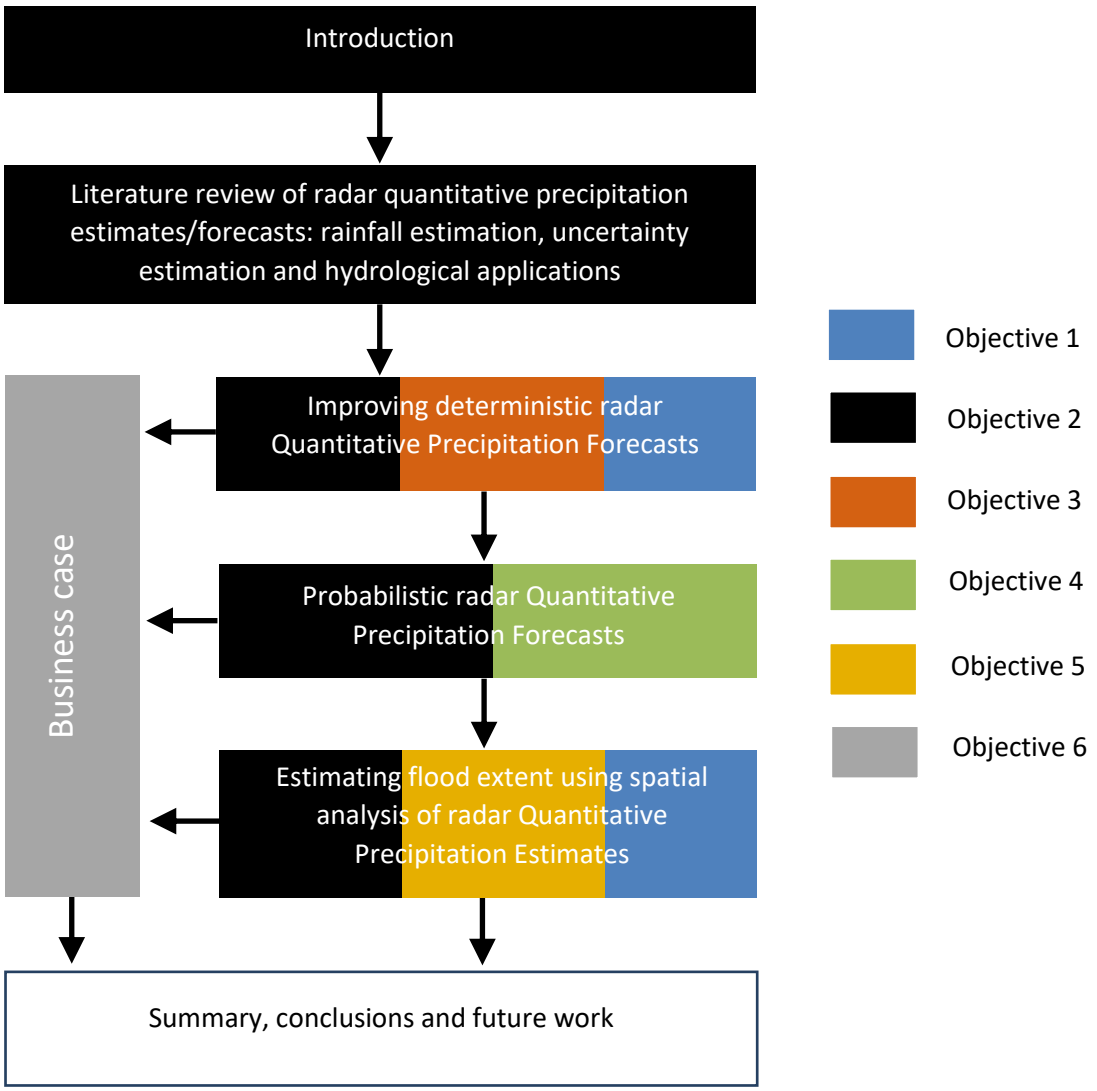

Figure 1.5. Thesis structure showing the connections between the components and objectives they fulfil.

Thesis structure

This thesis has seven chapters that correspond to the components shown in Figure 1.5. They are explained as follows:

Chapter 1: Introduction

Background and motivation of the research project is provided along with the commercial motivations. Aims and objectives, scope and originality and contribution to knowledge.

Chapter 2: Literature review of radar quantitative precipitation estimates/forecasts: rainfall estimation, uncertainty estimation and hydrological applications

A literature review is conducted for the three research areas identified: rainfall estimation, uncertainty estimation and hydrological applications. The review identifies the key approaches, their strengths and limitations and gaps for these research areas.

Chapter 3: Improving deterministic radar Quantitative Precipitation Forecasts

Deterministic radar QPFs are improved using temporal and spatial interpolation. This chapter demonstrates that higher resolution QPFs could be obtained without acquiring additional datasets and the increased resolution is useful for hydrological modelling. Furthermore, the case study used in Chapters 3, 4 and 5 is also introduced.

This chapter is based on the publication (in review) (Iqbal *et al.*, 2017):

Iqbal, A., Xuan, Y., Butler, D., and Fu, G. (2017) Improving the accuracy of temporally and spatially interpolated radar Quantitative Precipitation Forecasts. *Journal of Hydrology*.

Chapter 4: Probabilistic radar Quantitative Precipitation Forecasts

Probabilistic radar QPFs are generated and postprocessed using a Bayesian approach. A two-step application of a Markov Chain Monto Carlo algorithm is used to update the forecasts to make them more accurate in varying rainfall storms.

Chapter 5: Estimating flood extent using spatial analysis of Quantitative Precipitation Estimates

Flood extents are estimated using spatial analysis of radar QPE over a sewer catchment without running online hydrological simulations. This chapter shows that spatial variability of radar QPE could be used for real-time probabilistic sewer flood forecasting.

Chapter 6: Business case

A business case is developed using the methods and analysis conducted in this research project. This is aimed for the water sector to develop an operational sewer flood warning system.

Chapter 7: Summary, conclusions and future work

A summary of the research project is provided along with the main conclusions associated to each objective in section 1.2. Further work is recommended to extend the research based on the methods developed.

1.4 Originality and contribution to knowledge

The following explain the originality and contribution to knowledge of this research project:

1. Improving deterministic radar Quantitative Precipitation Forecasts

- Applied optical flow theory to temporally interpolate radar QPF to increase the temporal resolution, which is more accurate than linear-based interpolation.
- Applied a Kriging method to increase the spatial resolution of radar QPF.
- Showed that temporal interpolation by optical flow and spatial interpolation by Universal Kriging outperforms combinations of simple linear temporal interpolation and spatial interpolation by Inverse Distance Weighting and Universal Kriging.

2. Probabilistic radar Quantitative Precipitation Forecasts

- Applied a probabilistic forecasting model previously used for NWP/rain-gauge to radar QPE/QPF data.
- Modified a probabilistic forecasting model to apply a generalised linear model to representing non-normal distributions of radar QPE/QPF data.
- Developed a Bayesian based postprocessing method that provides new Probability Distribution Functions (PDFs) using latest radar QPE data updating pre-processed PDFs generated from historical radar QPE/QPF data. This postprocessing method produces probabilistic QPFs that are more accurate than the pre-processed probabilistic QPFs.

3: Estimating flood extent using spatial analysis of Quantitative Precipitation Estimates

- Applied spatial indexes from literature to extract spatial information of radar QPE over a sewer catchment.
- Conducted a spatial analysis of radar QPE related to flood extents over four sewer catchments in the North-East of England using historical data.
- Developed a flood forecasting approach using spatial analysis of radar QPE over specific sewer catchments and generalised linear models to estimate flood extents. The approach could be used for probabilistic QPFs as many forecasts would require simulating but simple statistical models reduce computational time. Thus, this approach is ideal for real-time flood forecasting.
- Shown that spatial information of spatial indexes of large sewer catchments is more useful to predicting flood extents than small sewer catchments.

2 Literature Review

This project focuses on radar quantitative precipitation estimates and forecasts. Specifically, the uncertainties of these rainfall data are explored and a hydrological analysis involving these data sets is conducted for sewer flooding.

Radar technology exhibits uncertainty that is inherent in the processes producing rainfall estimates. In the following review of literature, radar rainfall estimation is discussed, the methods by which uncertainties in radar rainfall data are evaluated followed by a review of statistical techniques used to quantify these uncertainties. Finally, the uncertainties in hydrological applications involving radar rainfall forecasts are discussed.

2.1 Rainfall estimation

2.1.1 Inherent uncertainties in radar rainfall

The main physical components of radar consists primarily of the transmitter, antenna and receiver (Dai, 2014). The transmitter produces a signal which is a form of electromagnetic radiation where the frequency and power are controlled. The antenna concentrates the transmitted signal into a beam that is typically between 1 – 2 degrees wide. Usually, the signal transmitted and received is measured in decibels. Radar produces rainfall estimates by sending out a signal towards the rainfall storm. The signal is then reflected from the droplets of the rainfall and is received by the radar transmitter, which calculates the rainfall intensity based on the information received (Bringi and Chandrasekar, 2001; Collier, 1989). Immediately, there are potential issues that may hinder the quality of the receiving signal. For example, attenuation is commonly observed in signal transmission and this reduces the quality of the rainfall estimate (Met Office, 2013). Secondly, ground clutter at the location of the radar obstructs the signal received (Met Office, 2013). There are other issues also. For example, the radar signal may not reach the heavier rainfall because of light rainfall masking heavier rainfall (Met Office, 2013). Hence the radar would record underrepresented rainfall values. These physical obstructions contribute to the inherent uncertainties of radar technology, which propagate through to the calculation of rainfall estimate. However, the way rainfall estimates are calculated is another

source of uncertainty. The reflectivity of the signal is typically represented as Z and the rainfall intensity is represented as R (in mm/h). The relationship between these two variables shows how R is calculated. This is referred to as the $Z - R$ relationship and is given as $Z = xR^y$ where x and y are values dependant on the droplet size of the rainfall (Einfalt *et al.*, 2004; Fournier, 1999; Hasan *et al.*, 2014; Smith, *et al.*, 2007). This is deduced empirically from the droplets detected by the signal. Particularly, the reflectivity Z is a three-dimensional field that is determined from the distribution of the droplet size. This size distribution is referred to as drop size distribution (DSD) and is calculated by fitting a theoretical distribution to the empirical droplet size (Einfalt *et al.*, 2004). The DSD varies for different types of rainfall storms due to varying droplet sizes. Hence, for a known category of rainfall, the coefficients x and y differ and Table 2.1 present examples of $Z - R$ relationships for the some identifiable rainfall storms (Einfalt *et al.*, 2004).

Table 2.1. Example Z-R relationships for various rainfall storms (Einfalt *et al.*, 2004).

$\boldsymbol{Z - R}$ **relationship**	**Type of rainfall storm or climate**
$Z = 200R^{1.6}$	Stratiform (or frontal)
$Z = 250R^{1.2}$	Tropical climates
$Z = 300R^{1.4}$	Convective

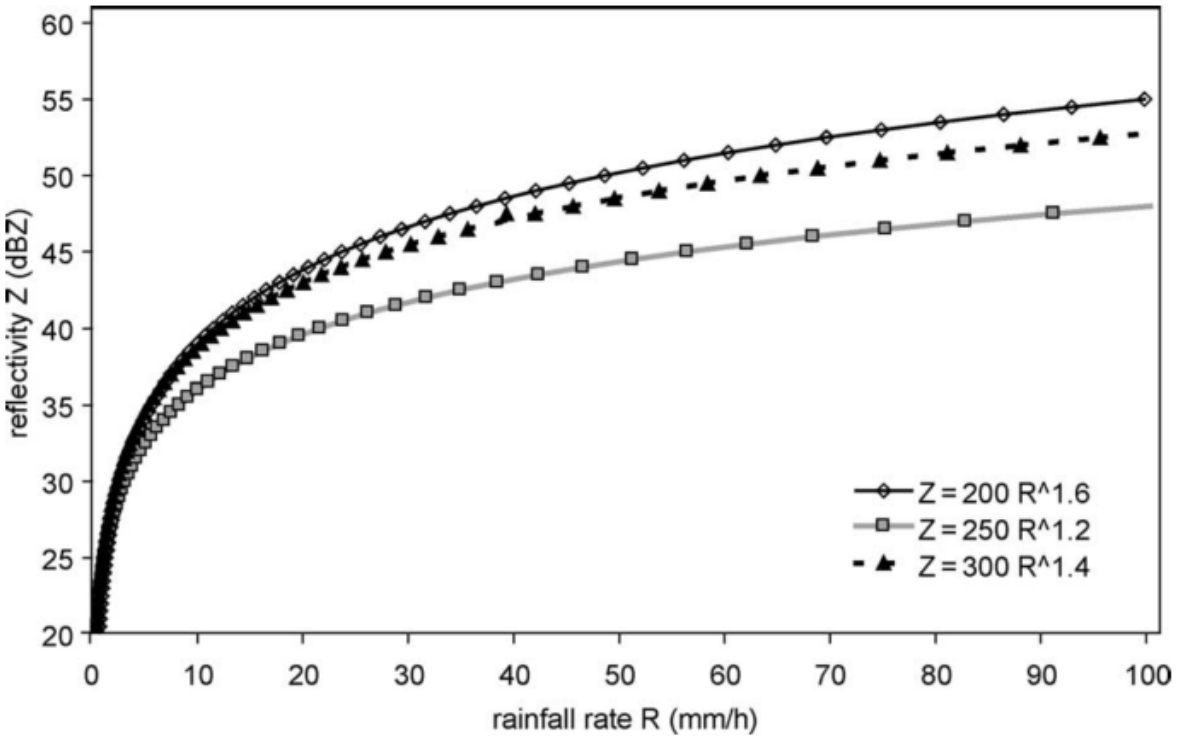

Figure 2.1. Comparisons of example Z-R relationships for different rainfall storms (Einfalt *et al.*, 2004).

Furthermore, Figure 2.1 shows the $Z - R$ relationships in Table 2.1 plotted for different values of rainfall intensities R. This demonstrates that the biggest differences between the $Z - R$ relationships of different rainfall are especially observed for higher rainfall intensities.

The selection of the appropriate $Z - R$ relationship is of high importance. A common way to choose the appropriate $Z - R$ relationship is to formulate a DSD which would help deduce values for x and y (Einfalt *et al.*, 2004). However, a second way to choose a $Z - R$ relationship is to relate the reflectivity measured in the atmosphere to ground observations (i.e. rainfall intensities produced from rain gauge networks) (Krajewski and Smith, 2002). This integral process assumes that the biggest uncertainties of radar rainfall are associated with the differences between the radar reflectivity at the surface and the reflectivity captured in the atmosphere where factors such as bright band, incomplete beam filling, hail contamination etc would affect this measurement parameter (Krajewski and Smith, 2002). This provides means to reduce the errors between reflectivity measurements at the atmosphere and ground. The algorithm for this approach treats the $Z - R$ relationship as an empirical formula and finds the 'best'

values for the coefficients x and y based on a known criterion. This optimisation exercise is not limited to factors such as the statistical approach, sample size or an instrument, all that are factors considered when calculating the $Z - R$ relationship using the DSD approach. The advantage of this is that the calculation of the $Z - R$ relationship performs better in nonlinear relationships between Z and R (Krajewski and Smith, 2002). Nonlinearity may occur due to the random errors found in the radar reflectivity measurements, which particularly occurs for high intensity rainfall.

Latest radar technology incorporates these selection techniques, particularly with the introduction of dynamic selection of $Z - R$ relationships which has vastly improved estimates during periods exhibiting different types of rainfall (Einfalt *et al.*, 2004). Such radar is referred to as dual-polarisation where sources of uncertainty such as effects of ground clutter and attenuation are minimised (Bringi and Chandrasekar, 2001; Collier, 1989). These improvements have helped produce better rainfall estimates in recent years. Particularly, the dynamic adjustment of the $Z - R$ relationship had allowed meteorologists and hydrologists to closely study extreme or heavy rainfall.

However, whilst the inherent uncertainties in radar rainfall have been reduced with the use of better technological hardware and algorithms, the process by which the rainfall is produced is still an estimate. This means that a substantial portion of the inherent uncertainties are still propagated through to the rainfall data.

2.1.2 Rain gauge adjustment

The use of rain gauges has been the traditional method to measure rainfall data. This measures the rainfall accumulation at high temporal resolutions (typically 1-min) at specific points at ground level. For tipping-bucket rain gauges, the 1-min resolutions are achieved by use of interpolation algorithms, such as cubic spline (CS) algorithm (Wang et al. 2006). Hence, rainfall data from rain gauges is the most accurately measured rainfall estimate. The reflectivity produced by the radar measures a specific point in three-dimensional space in the atmosphere, which

may not represent the true state of rainfall characteristics in comparison to the ground. This was discussed earlier as the differences in measuring reflectivity at ground level and the atmosphere could be large. The uncertainty of the estimated rainfall in the interval between these two regions could be more than 20% when producing radar rainfall data at 5-min temporal resolutions (Einfalt *et al.*, 2004). Therefore, rain gauges produce more accurate rainfall estimates than radar rainfall.

The main advantage of radar rainfall over rain gauge rainfall is the estimation of rainfall at different spatial locations (i.e. gridded rainfall). Rain gauge can only provide data where the gauge is installed and so they do not provide extensive information on the spatial variability of rainfall storms, unless a dense rain gauge network is installed at any region. However, this is an onerous and expensive task, which is remedied by radar due to its capability of providing wide information of spatial variability at every time step. This makes radar rainfall suitable for studying different types of storms (Einfalt *et al.*, 2004). Though, the accuracy of the radar rainfall estimate is limited based on the distance of the spatial point from the radar hardware. It is noted that the spatial accuracy of points near the radar are generally higher than points further from the radar. Hence, it is beneficial for hydrologists to use radar data that has been produced from multiple radar which minimises this uncertainty on the resulting rainfall data sets.

Temporal, spatial and intensity resolutions are crucial parameters of radar rainfall (Einfalt *et al.*, 2004). The accuracy of the rainfall intensity is particularly important when studying heavy rainfall as the higher the intensity the more uncertainty is associated to the estimate. This is because at high reflectivity values the relationship with the rainfall intensity in $Z - R$ relationship is nonlinear. Hence, this is another source of uncertainty with radar rainfall. Based on the uncertainties associated with the temporal, spatial and intensity resolutions, radar rainfall should be adjusted with other types of measurement data. Correcting radar rainfall with rain gauge data reduces the uncertainties between the measurements taken from the atmosphere and the ground, and this is the most common way to improve the accuracy of radar rainfall.

2.1.3 Methods to adjust radar rainfall

In literature, there are a several methods for correcting radar rainfall with rain gauge data (Borga *et al.*, 2002; Gjertsen *et al.*, 2003; Goudenhoofdt and Delobbe, 2009a; Rafieeinasab *et al.*, 2015; Segond *et al.*, 2007; Wang *et al.*, 2015; Wang *et al.*, 2013). These vary from simple approaches such as using scaling factors being applied at every radar grid (i.e. using mean field bias) or more sophisticated methods employing geostatistical techniques. Meteorological services produce radar rainfall products that incorporate these adjustment methods using rain gauge data. The National Weather Service (NWS) in the United States uses mean field bias correction applied to its radar rainfall (called BMOSAIC), which applies a spatially uniform multiplicative adjustment factor to the gridded rainfall data points (Seo *et al.*, 2010). They also use local bias correction which applies a spatially non-uniform adjustment factor, which performs especially well for storms exhibiting highly varied rainfall spatially. The use of mean (or local) field bias correction provides sufficiently good results for minimum resource requirements. This means that adjustment procedure would take less time to process. In fact, in their work the mean field bias correction method had outperformed the other adjustment methods, including methods incorporating geostatistical techniques (Habib *et al.*, 2012). However, the authors had scrutinised the accuracy of the rain gauges used in the study and highlight that the limited performance of other merging techniques was due to this reason. The rain gauge rainfall generally underestimated estimates with an overall hit bias of -10.2% (Einfalt *et al.*, 2004). For context, when rain gauges are averaged to reach temporal resolutions of 1 mins, the MAE is 22% for intensities above 3 mm/h, which reduced to 5% for temporal resolution of 7 mins. Particularly for geostatistical techniques, the accuracy of rain gauge data is important which determines the accuracy of the corrected radar estimates. Furthermore, the density of rain gauge networks also determines the accuracy of the correct radar rainfall data (Einfalt *et al.*, 2004).

Recently, geostatistical techniques have been employed to determine the spatial variability of rain gauge data in a specified region. Various techniques show to improve the accuracy of radar rainfall. For example, Yeung *et al.*, (2017) had explored a co-kriging interpolation scheme whereby radar rainfall estimates were

combined with interpolated rain gauges in the field. The results show that the co-kriging method was useful to detecting the spatial structure of the rain gauge field at a high level. However, it struggled to represent rainfall values at locations of gauges during extreme events. Lin and Lee (2011) had also used co-kriging to merge radar rainfall and rain gauge data and concluded that co-kriging generally underestimates rainfall in regions lacking rain gauges. Another method, called modified co-kriging had shown in the same study to outperform co-kriging. However, modified co-kriging requires the computation of semi-variograms, which is a more resource-heavy task hence requiring more time to process. However, generating semi-variograms introduces further uncertainty. Furthermore, modified co-kriging requires more radar rainfall data points and this may not be available in scenarios where the availability of radar rainfall is sparse. Wang et al., (2015c, 2015b) use block kriging to interpolate rain gauge data at radar rainfall points. The covariance of this interpolated rainfall field is then derived which represents the uncertainty of the rain gauge estimates. Similarly, the covariance of the radar rainfall field is obtained. Based on these covariances, the two rainfall fields are optimally merged using a Kalman filter. This is an example of Bayesian based merging method that is dynamically applied thus making it suitable for real time applications. The advantages of this is that the error realisations of the rainfall field would differ at every time step thus correcting the radar rainfall field with more precision. Results show large improvement over mean field bias correction. However, the preservation of peaks in the rainfall field was weak and a 'smoothing effect' had been noted. Similarly, Berndt et al., (2014) compare different geostatistical techniques with addition of smoothing the rainfall fields to make them more accurate. It had been shown that the smoothing process improved the merging of radar and rain gauge rainfall data. However, there was noticeable loss of spatial field structure of rainfall. This highlights the requirement to preserve the spatial structure of the rainfall field.

Goudenhoofdt and Delobbe (2009) had developed a method to improve radar rainfall estimation by directly correcting the errors in radar measurements in the atmosphere and the ground, a consequence of this is so called VPN. They perform VPN correction followed by rain gauge merging using mean field and local bias correction methods. Particularly, they use Ordinary Kriging (OKR) and another variant of OKR called External Drift Kriging. The latter method had shown

the biggest improvements on the accuracy of corrected radar rainfall estimates, even more than methods using mean field or local bias correction. External Drift Kriging treats the radar field as the secondary data (i.e. interpolations are performed for the radar rainfall field at rain gauge locations). As such, defining the instantaneous, anisotropic and non-stationary spatial variability model using the radar field was shown to be more accurate than using other estimators such as interpolating rain gauge (Sempere-Torres *et al.*, 2012).

The merging techniques discussed highlight that the radar rainfall estimates/forecasts could be made more accurate using other sources of rainfall. They would typically ensure that radar data are of high quality suitable for hydrological applications. However, radar rainfall forecasts present additional challenges when applied to hydrological analysis. The next section discuss how radar rainfall forecasts are produced and what challenges are associated to their accuracy and applications in short range flood forecasting.

2.1.4 Radar rainfall forecasts

NWP models provide quantitative information of future precipitation. However, these models lack the resolution capacities to represent the rainfall structure at a spatial scale with reasonable accuracy sufficient for hydrological applications. Especially, they are not useful to produce rainfall forecasts at very near periods in the future. Hence, based on the wide availability of radar rainfall, extrapolation schemes have been developed to use the motion and intensity parameters of the gridded data to produce forecast rainfall up to several hours into the future (Mueller *et al.*, 2003). This is referred to as Nowcasting, which uses radar rainfall to produce QPFs up to 6 hours (Pierce *et al.*, 2004; Ruzanski *et al.*, 2011). Ruzanski et al. (2011) describes that radar Nowcasts could be classified in four ways: area-based, object-based, statistical and probabilistic. In hydrology, Nowcasting is most commonly referred to using principles of area-based Nowcasting. This involves using the radar field to estimate the motion of the storm and predict the future precipitation. Object-based Nowcasting focuses on identifying regions in the radar field that shows high reflectivity. Coherent features of the storm such as size and shape are used to predict future precipitation.

Statistical and probabilistic Nowcasting takes a step further to study the atmospheric properties of storms to produce more accurate forecasts. Probabilistic Nowcasting represent percentiles of rainfall intensity values and this provides a holistic way of assessing future precipitation. Probabilistic methodologies are discussed in section 2.2. Examples of object-based Nowcasting systems include the Thunderstorm Identification, Tracking, Analysis, and Nowcasting (TITAN) algorithm (Dixon *et al.*, 1993). An example of a statistical Nowcasting system is the Terminal Weather Convective Forecast System (Boldi *et al.*, 2002; Sharif *et al.*, 2005)and Auto-Nowcaster (ANC) developed at the National Center for Atmospheric Research (NCAR) (Mueller *et al.*, 2003; Sharif *et al.*, 2005).

The UK Met Office have rainfall products, referred to as Nimrod, that generate Nowcasts in the same way. The forecasting horizon is very short (i.e. around 1 – 2 hours) for single radar but this can be extended by combining data from multiple radar to produce short range forecasts with longer lead times (Golding, 2000). However, the lead time could be further extended by merging radar rainfall forecasts with NWP models that have longer forecasting capabilities. An example of a system that incorporates this technique is the STEPS system by the UK Met Office (Bowler *et al.*, 2006). Convective storms are dynamic and have highly fluctuating rainfall intensities over short durations. The forecast horizon is thus shorter for such storms and this presents the challenge of increasing the alertness in hydrological applications for such storms (Einfalt *et al.*, 2004). Olsson et al. (2013) found that extreme events of short duration were concentrated over small spatial regions (and even over singular radar grids) whereas extreme events of long duration were more spatially uniform and involved large regions in the catchment. Einfalt et al., (2004) highlights that this a difficulty in urban rainfall forecasting and further states that highly accurate radar rainfall forecasts are required especially for catchments of small size.

Nowcasting has been applied to urban flood forecasting in several studies (discussed separately in section 2.3), which have demonstrated key attributes of Nowcasts. Schellart et al., (2012) demonstrate the uses of Nowcasting in sewer flow prediction. The outputs of their study show that the forecasting skill reduces with longer forecast horizons and for small spatial scales. Furthermore, distinctions between frontal and convective storms were made where frontal

events showed to better predict sewer flow. Furthermore, Achleitner et al., (2009) showed that forecasting of sewer variables had been constrained by the forecast horizon, with large bias observed for forecasts above 90 minutes. Like the study outputs of Schellart et al., (2012), they found that the forecast skill increases with increasing spatial scales. The benefits of using radar Nowcasting demonstrates that flood forecasting is feasible in sewer catchments with reasonable accuracy (Sharif *et al.*, 2005). However, radar Nowcasts may exhibit large uncertainty. Most of these uncertainties originate from the radar estimate - as discussed earlier - and this is propagated through to extrapolation schemes (or other methods) by which the forecasts are produced. Extrapolation techniques (i.e. Nowcasting algorithms) are not the focus of this project as this is predominantly meteorological. However, in recent hydrological literature, a characteristic of radar rainfall studied closely, and to a lesser extent of radar forecasts, is the temporal and spatial resolutions of the data.

2.1.5 Resolution requirements in urban flood forecasting using radar rainfall

The temporal and spatial resolution of radar rainfall data are important attributes considered in hydrology. Wang et al. (2015a) state that resolutions of radar estimates (typically 1-km, 10-min) may be insufficient for urban scale applications. Sharif et al. (2005) also demonstrated the improved accuracy of flood forecasting was attributed to the high resolution of radar estimates. Given this, it is important to select precipitation data with appropriate temporal and spatial resolutions for hydrological purposes (Wang *et al.*, 2015). The size of catchment, for example, is a factor determining what resolution would be appropriate to obtaining relatively accurate model outputs (Emmanuel *et al.*, 2012). Small spatial regions present larger deviations between in the forecasted model variables (Vieux and Vieux, 2005). Hence, for these sized catchments they require precipitation data of suitable temporal and spatial resolutions to produce sufficiently accurate forecast output (Wang *et al.*, 2015). Berne et al. (2004) recommended that for a 1000 ha (10 km^2) catchment a respective spatial and temporal resolution of 3-km and 5-min would be sufficient to conduct accurate analysis. Loewe et al., (2014) suggested that a 1-km spatial resolution would be

appropriate for real-time hydrological predictions, which would involve the most up-to-date data being used by the model in real time, and mean a higher demand on data and time to update the model to the required performance standards in comparison with offline models. Schellart et al., (2012) compared the impacts of 15-min and 5-min time steps of rain gauges on sewer flow predictions and demonstrated how the increased temporal resolution highlighted peaks that would have been missed or not fully represented from lower resolution data sources. Higher resolution data will show more spatial and temporal information in comparison to lower resolution sets in each location or time, therefore they are more useful for real-time flood hydrological predictions.

High resolution data may be limited in availability. This is especially the case where both the temporal and spatial resolutions are required to be high. Looking at a finer scale, a temporal resolution of 2-min to model at street level and individual properties in urban areas is recommended but this would depend on the availability of data with very high temporal resolutions (Rico-Ramirez *et al.*, 2015; WaPug, 2004). Furthermore, it has been demonstrated that for radar estimates with a particular temporal resolution there is an optimal spatial resolution which would minimise the uncertainties in the data (Schellart *et al.*, 2012). Hence, this presents a challenge in sourcing the highest available temporal and spatial resolutions.

When the required radar QPFs are not available at sufficiently high resolutions, various techniques exist to improve their resolutions. Previous research investigated temporal interpolation of radar QPEs to match corresponding rain gauge data (Wang *et al.*, 2015). Seo and Krajewski (2015) explored improving temporal errors in radar precipitation by considering advection parameters in a linear interpolation method. Whilst their method struggled to demonstrate any improvement in events with little precipitation, there was a clear improvement in the accuracy of precipitation estimates for events with heavier precipitation. Increasing the resolution of radar data preserves the small-scale precipitation structures which would be of direct relevance and interest in hydrological applications.

Temporal interpolation

Previous work has identified the uncertainties present in temporal gaps of radar rainfall. Piccolo and Chirico (2005) and Shucksmith et al., (2011) applied analysis of movement and evolution of rainfall storms to radar data with high resolutions. They demonstrated that temporal gaps significantly impact the accuracy of the rainfall data. They recommended that temporal interpolation is necessary to reduce these uncertainties. Fabry et al., (1994) had developed an advection based extrapolation scheme that computed rainfall accumulations. This inspired later work producing higher temporal resolution radar rainfall using a temporal interpolation method (Nielsen *et al.*, 2014). The concept taken from Fabry et al., (1994) includes the consideration of advection parameters as vector fields distributed over the radar field. These vector fields represent the movement of rainfall storms and have shown to estimate interpolated points to a reasonable level of accuracy. However, due to the complexity of parameterising changes of rainfall at very short periods, two assumptions are made in this interpolation method: the vector field between two radar maps are constant, and evolution of rainfall changes linearly over one radar map to another. The interpolation method consists of three main stages: (1) advection-based extrapolation forward in time, (2) advection-based extrapolation backward in time, and then (3) merge the two extrapolations to form one combined interpolated radar rainfall dataset. This method had been adopted by Wang et al., (2015a) with a modification that includes occlusion reasoning. This ensures that the interpolated radar maps change smoothly without anomalous magnitudes of rainfall values emerging in the data sets (Herbst *et al.*, 2009; Sadek *et al.*, 2012)

Furthermore, Wang et al., (2015a) derive vector fields in the radar maps using optical flow estimation instead of Continuous-TREC (or CO-TREC) (Li and Schmid, 1994; Mecklenburg *et al.*, 2000). This is a modified version of Tracking Radar Echoes by Correlation (TREC) which was developed by Rinehart and Garvey (1978). These two approaches essentially divide the rainfall field into contiguous rain areas (CRAs), or blocks, and then calculate the optimal advection vector at each block using a correlation method. CO-TREC improves the TREC method by minimising the divergence of the velocities in neighbouring blocks, which would cause gaps in various regions in the radar image. Furthermore, a smoothing constraint is introduced as part solving the advection equations.

Another method to obtain advection vectors is the Variational Echo Tracking (VET) method which similarly relies on correlation methods using a block based approach but additionally considers radial velocities (Laroche and Zawadzki, 1994, 1995). However, this additional data is not always available. Optical flow approaches use a Lagrangian approach directly instead of using correlation methods and the optical flow constraint equation is solved before the smoothness constraint. This reduces computational processing of the algorithm for obtaining the advection vectors that are more accurate (Bowler *et al.*, 2004).

Optical flow is commonly used for temporal interpolation of image sequences outside of meteorological and hydrological studies. For example, Ehrhardt et al., (2006) had showed that optical flow based interpolation proved to be more accurate than linear or shape based interpolation for interpolated medical image sequences. In the same study, linear based interpolation is stated to be the most commonly used interpolate method and shape-based is usually the most accurate against the other methods (not including optical flow based interpolation). Furthermore, optical flow techniques have been used in nowcasting extrapolation schemes to produce radar rainfall forecasts (Bowler *et al.*, 2004). Hence, its versatility and accuracy is proven to be useful in short term rainfall forecasting (Cheung and Yeung, 2012; Krajewski and Smith, 2002)

Artificial Neural Networks (ANNs) have been commonly used in hydrological studies (Coppola *et al.*, 2005; Darsono and Labadie, 2007; Kasiviswanathan and Sudheer, 2016; Koizumi, 1999; Lallahem *et al.*, 2005; Maier *et al.*, 2010; Samani *et al.*, 2007; Siswantoro *et al.*, 2016; Trichakis *et al.*, 2009). This is an example of a data-driven approach that does not depend on specific parameters of the data to develop nonlinear relationships between the independent and dependant variables. As they are data-driven, it treats the processing as ‘black box’ and the nonlinearity of ANNs is advantageous over linear statistical approaches. ANNs are thus considered as alternative methods to statistical approaches and have been previously used to predict hydrological variables on a temporal scale (Tapoglou *et al.*, 2014). Hence, ANNs could be applied in temporal interpolation problems in hydrology. These models are discussed in detail in section 2.3.2.

Spatial interpolation

There are many methods of spatial interpolation, and these are comprehensively articulated and evaluated by Li and Heap (2008). In this publication, a range of techniques are classified broadly in two categories: non-geostatistical and geostatistical. Also, Tapoglou et al., (2014) describes these categories as mechanical and statistical/probability-based, respectively. The non-geostatistical techniques use empirical parameters that include methods Inverse Distance Weighting (IDW), regression models, splines and local trend surfaces, Fourier series and trend surface analysis. Geostatistical techniques allow for the analysis of the uncertainty of the spatial structure of the data. They feature more strict assumptions on the spatial variability of rainfall and rely on fundamental concepts in probability theory (Tapoglou *et al.*, 2014). This is the main benefit of using geostatistical techniques. This is because approximation of the uncertainty helps explore more specific ways to improve the accuracy. The techniques in this category include Kriging methods (i.e. simple, ordinary, block Kriging etc) and multivariate variations of Kriging including co-Kriging and External Drift Kriging.

In recent literature, geostatistical techniques, particularly Kriging methods, have been explored extensively chiefly due to providing information of the uncertainty of the spatial field (Cressie, 2015; Gotway *et al.*, 1996; Schloeder *et al.*, 2001). In comparison to IDW, Yasrebi et al., (2009) and Zare-mehrjardi et al., (2010) found that Kriging methods performed better than IDW. Several multivariate Kriging methods have been evaluated in section 2.1.3 (co-Kriging and External Drift Kriging). These methods are popular for merging radar and rain gauge rainfall fields and have proven to be effective in producing accurate estimates. However, in the field of radar rainfall forecasting this is limited because the spatial interpolation problem in this area must be conducted historically to correct it against observed rainfall sources (e.g. radar estimates or rain gauge data) and not in real-time. Hence, the choices of geostatistical techniques are smaller and their application are more constraining when improving rainfall forecasts. However, univariate techniques could be used as these require only one spatial field data set for interpolation, which is appropriate for rainfall forecasts. OKR is the most common type used in the field (Zhang and Wu, 2015). Its applications are seen across different studies in hydrology, computer vision and earth sciences. However, UKR has been often compared with OKR and in many cases

it has produced better results (Eom *et al.*, 2006; Selby and Kockelman, 2013). This is due to the trend analysis that is integral to UKR. The benefits of this is that a trend function is defined for the spatial structure of the interpolated points, which is useful for determining predicting points in the rainfall field whose trend resembles a rainfall storm, as an example. Outside of geostatistical techniques, a Bayesian approach had been developed by Hussain et al., (2012). The benefit highlighted using this technique is that the spatio-temporal variability of the uncertainty and covariance models could also be used to interpolate spatial data, which is evidently lacking in Kriging methods. However, this study was limited to a single case study and more evidence of such techniques are required to prove its usefulness. Particularly, their work had focussed on spatio-temporal estimations of rainfall, which considers temporal uncertainties together with spatial uncertainties. Considering spatio-temporal aspects of rainfall has also been studied using Kriging. The benefit of this includes studying different rainfall in locations with different topographies and also in different seasons.

2.2 Uncertainty estimation

In section 2.1 the inherent uncertainties of radar due to the processes involving rainfall estimation had been explored. These uncertainties are propagated to radar rainfall forecasts and, particularly, uncertainty characteristics of this type of data have been identified (Boucher *et al.*, 2012; Dale *et al.*, 2014; Krzysztofowicz, 2001; McCollor and Stull, 2008; Ramos *et al.*, 2013; Verkade and Werner, 2011). Uncertainty characteristics include that the forecast uncertainty increases with lead time. Furthermore, the spatial area of rainfall is a factor determining the uncertainty extent as the accuracy generally increases with increasing area where the forecasts are sourced (Rezacova *et al.*, 2007). This is because there is a larger area of validation of the forecasts. Furthermore, Rezacova et al., (2007) concluded that forecast uncertainties are high for local convective storms, particularly at short lead times. Whilst these studies have established that uncertainty is present and at varying extents in hydrological applications, the rainfall forecast itself is not indicative of the uncertainty. This is because deterministic (or singular) forecasts do not present information of the uncertainty (Berrocal *et al.*, 2008) . This section explores literature that have focussed on quantifying uncertainty of rainfall forecasts in hydrology.

2.2.1 Exploring uncertainty of rainfall forecasts

In hydrology, the total uncertainty is typically categorised in two ways: the input uncertainty and hydrological uncertainty (Regonda *et al.*, 2013). The input uncertainty refers to uncertainties in rainfall and temperature data that are used in hydrological models. Moreover, the rainfall is considered the most important input uncertainty source (Gjertsen *et al.*, 2003). Often, the uncertainties in rainfall are quantified separately to the hydrological uncertainties. Such systems that incorporate this way of quantifying the total uncertainty in the hydrological forecast are the Bayesian Forecasting System (BFS) by Krzysztofowicz (2001) and the Hydrologic Ensemble Forecast Service (HEFS) of the NWS (Demargne *et al.*, 2013). Regonda et al., (2013) describe a source-specific approach to how the total predictive uncertainty could be explored. This states that input and hydrological uncertainties are modelled separately so that the residual uncertainty can be modelled stochastically (Demargne *et al.*, 2013; Krzy, 1999; Seo *et al.*, 2006; Seo *et al.*, 2010). The purpose of this is that the uncertainty becomes random (i.e. lacking structure) which is advantageous because it would have less data requirements, hence making the stochastic modelling less complex. This provides a practical way of understanding uncertainty sources of hydrological forecasts.

Krzysztofowicz (2001) had presented the BFS which constitutes several components that separately quantify the uncertainty in flood forecasting. This concept has been used extensively in later studies (Kelly and Krzysztofowicz, 2000; Krzysztofowicz and Herr, 2001; Krzysztofowicz and Kelly, 2000). The purpose of the BFS is that it separates processing of different uncertainties. The three components representing different uncertainties are input uncertainty processor, hydrological uncertainty and the integrator uncertainty. An advantageous aspect of the BFS is that it is designed to update its components whilst maintaining statistical consistency (i.e. not deviating from the uncertainty relationships identified in the forecast data), which is conducive for operational use. However, Reggiani and Weerts (2007) modify the BFS by enhancing the input uncertainty processor. They had identified that rainfall is the most influential

forcing to hydrological models in short term flood forecasting (and assuming that at this scale temperature and evaporation are negligible). Hence, a large degree of uncertainty is attributed to this source. Furthermore, a Bayesian method is incorporated to this processor, where the prior knowledge of the historical forecasts is used to obtain the posterior forecasts (i.e. updated forecasts). This study highlights the significance of segregating the input and hydrological uncertainties. Seo et al., (2000) used the BFS to generate probabilistic forecasts that consider temporal and spatial factors of the data. However, the work was limited by operational issues. Nonetheless, it further highlighted benefits of segregating the input and hydrological uncertainties, as more scientific methods could be applied to the input data to determine total predictive uncertainty.

Coccia and Todini (2011) and Montanari and Brath (2004) explain that there are three ways the uncertainty in forecasts are quantified, albeit in the context of streamflow forecasts. The first method generates probabilistic forecasts based on the initial conditions that generate the streamflow forecast (Cloke and Pappenberger, 2009). The second method quantifies uncertainty based on comparisons of forecast errors in historical data (Rene, 2014; Schaake *et al.*, 2007; Wood and Schaake, 2007). The third method uses Monte Carlo and resampling methods to explore the uncertainty (Montanari and Brath, 2004). In recent literature, probabilistic methods have been directly applied to the hydrological forecasts. Examples of these studies are (Bogner and Pappenberger, 2011; Coccia and Todini, 2011; Montanari and Grossi, 2008; Reggiani and Weerts, 2007; Smith, P. J. *et al.*, 2012; Weerts *et al.*, 2011). However, more focus has been invested in hydrological uncertainty whereby the hydrological variables in simulations are used to generate probabilistic forecasts (Bogner and Pappenberger, 2011; Brown and Seo, 2013; Chen and Yu, 2007; Hantush and Kalin, 2008; Montanari and Brath, 2004; Montanari and Grossi, 2008; Seo *et al.*, 2006; Zhao *et al.*, 2011). Therefore, more work is required to explore probabilistic rainfall (or hydrological) forecasting based on uncertainties in the rainfall forecast.

2.2.2 Probabilistic rainfall forecasting

Recent studies have attempted to assess the usefulness of probabilistic (or ensemble) forecasts in hydrology. For example, Hardy et al., (2016) produces probabilistic hydrological forecasts based on the input of high resolution forecasts obtained from the NWS Ensemble Prediction System (EPS). The STEPS model by the UK Met Office had been applied to predict flow in urban catchments (Liguori and Rico-Ramirez, 2012). Results show that these probabilistic forecasts are better at estimating flow prediction particularly for low intensity rainfall. However, several studies have focussed on the methods generating probabilistic rainfall forecasts (i.e. further exploring the input uncertainty before propagating them to hydrological models). Such studies have used Kalman Filter as part of a probabilistic forecasting framework (Georgakakos and Smith, 1990; Kitanidis and Bras, 1980; Young, 2002). The Kalman Filter is used to quantify the uncertainty for every discharge forecast produced. Each of these are accompanied with a probability of precipitation and, collectively, their discharge values indicate of the uncertainty range. However, many statistical models are simultaneously run to indicate the probability of the forecasts. This introduces uncertainty in selecting the appropriate model to calculate the probability of precipitation which is disadvantageous to the end user. Another method, called Generalised Likelihood Uncertainty Estimation (GLUE), had been introduced with the rationale that different parameter sets are equally possible and thus are all acceptable (Beven and Binley, 1992). This approach is based on Monto Carlo methods (the third method of quantifying the uncertainty of forecasts by Montanari and Brath (2004) and Coccia and Todini (2011) and has been used in several studies (Beven and Freer, 2001; Franks *et al.*, 1998; Hossain and Anagnostou, 2005; Hunter *et al.*, 2005; Kuczera and E Parent, 1998; Montanari, 2005; Pappenberger *et al.*, 2005). Many parameter sets are selected within a certain range and are used to run the rainfall forecasting model. However, several studies had shown that the predictive uncertainty is not always accurately estimated using this method (Mantovan and Todini, 2006; Montanari, 2005; Thiemann *et al.*, 2001).

Chen and Yu (2007) uses a ‘possibilistic’ approach whereby probability distributions are produced from the forecasts errors using fuzzy inference methods. Ben Bouallègue (2011) uses a similar approach to widen the samples

of probabilistic values produced with a probabilistic approach. Fu et al., (2011) present a method of imprecise evaluation of probabilistic sewer flooding forecasting with use of random set theory. They had concluded that an imprecise probabilistic approach is more suitable for stochastic uncertainty modelling when more than one probability distribution fits the sample data. The use of fuzzy approaches is useful as an alternative approach to probability-based methods. However, these studies have demonstrated that they can supplement probability-based frameworks.

Based on the first method to quantify uncertainty described by Montanari and Brath (2004) and Coccia and Todini (2011), several forecast products develop probabilistic forecasts using initial boundary conditions. For example, NWS has several forecast products that include short, medium and long-range ensemble rainfall forecasts purely from numerical models at a regional and global scale. These include the Short-Range Ensemble Forecast (SREF) and the Climate Forecast System (CFS). The UK Met Office have developed the STEPS probabilistic rainfall forecasting system which produces rainfall ensembles by merging radar Nowcasts with NWP forecasts (Bowler, N. E. *et al.*, 2006). However, as these probabilistic forecasts are constructed predominantly using numerical models and altering the initial boundary conditions there are issued associated to the forecasts. There is a lack of dependence on the spatio-temporal variabilities influencing the uncertainty estimate. Hence, there is a bias or generalisation of the mean and bias that is not representative of the local spatial and temporal characteristics of the forecast source. The second method of quantifying uncertainty explained by Montanari and Brath (2004) and Coccia and Todini (2011) is thus used as a way of statistically calibrating rainfall forecasts which considers spatio-temporal aspects to reduce the bias of forecast errors using local observed data (Eckel and Walters, 1998; Montanari and Brath, 2004; Tapoglou *et al.*, 2014). Producing probability distributions from the forecast errors of the forecast and observed data sets allows quantifying the uncertainty of deterministic forecasts (Buizza *et al.*, 2005).

An example of statistically calibrating rainfall forecasts based on the second method of quantifying the uncertainties is described as follows. Schaake et al., (2007) developed a methodology to construct probabilistic forecasts for deterministic rainfall and temperature forecasts for the Ensemble Streamflow

Prediction (ESP) for the National Weather Service River Forecast System (NWSRFS). Deterministic QPFs are used to produce marginal distributions based on forecast errors between historical forecast and observed rainfall data (or joint distributions for nonzero forecast and observed rainfall values). Then, random rainfall values are sampled from the marginal distributions using the 'Schaake Shuffle' (McCollor and Stull, 2008). These random values are used to produce probabilistic forecasts in time series format. The method produces the probabilistic forecasts independently for a specific location. Hence, spatial dependence is not considered. Also, various assumptions are made in the statistics employed in the methodology. For example, variable transformations are used to model new variables using rainfall forecasts and observations with bivariate standard normal distribution. Wu et al., (2011) improves this method by modifying various statistical parameters. This includes introducing a mixed-type bivariate meta-Gaussian distribution for modelling part of the forecast and observed rainfall data. Results showed that producing probabilistic QPFs is more reliable and skilful using the modified stochastic models. Rene (2014) had adopted the approach of Schaake et al., (2007) and Wu et al., (2011) to generate probabilistic QPFs using historical NWP forecasts and rain gauge data. The key contribution of this study is that the concept of ensemble generation had been applied to urban pluvial flood forecasting, which presents different challenges in comparison to coastal or river flooding. The NWP forecast had a maximum lead time of 12 hours and so probabilistic forecasts were generated over this period with 1 hourly time steps. Furthermore, . Rene (2014) compared two sampling techniques which are Latin Hypercube Sampling (LHS) and Direct Quartile (DQ), instead of using the 'Schaake Shuffle'. Their study showed that quantifying the uncertainty of NWP QPFs can be done with a good level of skill. However, the forecasts had the tendency to underestimate the observed rainfall during heavy rainfall events and overestimate the observed rainfall during light rainfall events.

2.2.3 Postprocessing probabilistic rainfall forecasts

NWP-based probabilistic rainfall forecasts are generated based on altering the parameters of the initial boundary conditions representative of the atmospheric

conditions influencing the forecast, and the mathematical assumptions made in producing the forecasts (Bowler *et al.*, 2006). These are the two main sources of uncertainty of NWP-based probabilistic rainfall forecasts (Ebert, 2001). However, as they generate different variations of the forecast with the same temporal and spatial parameters, they do not provide information of the probability of precipitation and are thus strictly referred to as ensembles (Robertson *et al.*, 2013). The problems associated to the ensembles generated from NWP models is that the error range lacks depth and does not provide probability of precipitation. Furthermore, the ensembles produced are spatially and temporally independent, and so could not perform in local, operational settings (i.e. where spatial variability of rainfall would typically be considered in distributed hydrological modelling). Even when probability of precipitation is included in an ensemble forecasting system, the other issues stated could still hinder the skill of predicting rainfall. When probabilistic rainfall forecasts are produced this way (i.e. even from a radar-based probabilistic rainfall forecasting system), it is necessary to consider postprocessing them to increase their accuracy in better estimating the uncertainty, especially at specific spatial locations (Hamill *et al.*, 2008; Kleiber *et al.*, 2010; Schaake *et al.*, 2007; Sloughter *et al.*, 2007; Wilks, 2011; Wu *et al.*, 2011).

It is evident in recent literature of the techniques used to postprocess probabilistic rainfall forecasts, particularly in the field of streamflow forecasts. For example, a probability model introduced by Sloughter et al., (2007) is used to model two components of probabilistic forecasting systems: the probability of precipitation and the rainfall values. The probability of precipitation is postprocessed using logistic regression and the rainfall values are postprocessed by using a gamma distribution model conditioned on the deterministic rainfall forecast. Furthermore, their approach introduced using a Bayesian technique to calculate the PDFs of the probabilistic rainfall forecasts across any rainfall value. This contribution would prevent probability models being produced for specific forecast thresholds that would be selected by the end-user. The main issue of this approach as highlighted by Robertson et al., (2013) is that when generalising this technique to other scenarios of rainfall forecasting there are many parameters to consider and this risks over fitting the models involved in the technique. Furthermore, Scheuerer (2014) states that the methods described in studies like Sloughter et

al., (2007) may alter the original scale of ensemble spread of the probabilistic rainfall forecasts. This may cause differing performances of estimating uncertainty in the postprocessed probabilistic rainfall forecasts at varying rainfall intensities (i.e. low intensity rainfall may have an exaggerated uncertainty range). Therefore, whilst methods developed in recent literature allow for better approximations of the probability distributions of forecast rainfall, it is crucial to consider updating the distributions to maintain or increase the skill of predicting the uncertainty based on varying rainfall types.

The aforementioned methods by Schaake et al., (2007) and Wu et al., (2011) are considered postprocessing methods for NWP rainfall forecast as the probabilistic forecasts are produced from joint distributions between the forecast and observed data. However, these methods allow for various transformations and choices of distribution for the marginal distributions, which affects the skill of predicting the uncertainty. This could also be location dependant and the parameterisations involved in the methods are multifaceted. Furthermore, these methods are applied to singular spatial and temporal locations making the task of extracting the spatial and temporal structures a difficult one that needs to be done in addition to the probabilistic rainfall forecasting, which is computationally expensive (Khajehei and Moradkhani, 2017). Methods like the 'Schaake Shuffle' solve computational issues such as this by selecting probabilistic values based on the spatial and temporal structure of historical rainfall (Clark *et al.*, 2004). However, considering the spatial and temporal structure of probabilistic rainfall forecasts has more recently been identified as an area of further work accompanying postprocessing probabilistic rainfall forecasts (Reggiani and Weerts, 2007).

Bayesian methods have particularly been studied in recent literature to postprocess probabilistic rainfall forecasts. The Bayesian Joint Model (BJM) had been introduced by Wang et al., (2009) and Wang and Robertson (2011) to generate probabilistic rainfall forecasts for a sub-daily weather forecast in Australia. This method had been adopted by Robertson et al., (2013) which they drew comparisons with the methods of Schaake et al., (2007) and Wu et al., (2011) as joint distributions are similarly produced between the forecast and observed data. However, the purpose of using this Bayesian technique is that of simplifying the parametric transformation for data normalisation making it very

flexible as a probability model. Thus few parameters are required as part of the model development using the data in comparison with the methods of Schaake et al., (2007) and Wu et al., (2011). With fewer parameters involved the computational processing time is reduced and the uncertainty in the number of parameters involved is also reduced. The study shows the success of the BJM by accurately determining the uncertainty range for both small and large rainfall events. It also highlighted the effectiveness of using Bayesian inference methods to postprocess probabilistic rainfall forecasts. As the study by Robertson et al., (2013) had used sub-daily rainfall forecasts, they emphasised that these forecasts differ to rainfall forecasts of shorter range (i.e. such as radar Nowcasts). This is could be potentially explored due to the challenges associated to the accuracy of short range rainfall forecasts. It also highlights potentially exploring Bayesian inference methods to postprocess probabilistic rainfall forecasts at short forecast horizons. This is particularly conducive for real-time sewer flood applications.

Another study had also explored the challenges of the methods by Schaake et al., (2007) and Wu et al., (2011). Khajehei and Moradkhani (2017) argues that these types of probability models use joint distributions to produce parametric transformations of data with non-Gaussian properties to a normal space (i.e. to model the joint distribution as a multivariate normal distribution, as also modelled by Rene (2014), is an assumption that could lead to inaccurate representation of the uncertainty of the ensembles (Brown and Seo, 2013; Madadgar *et al.*, 2014). Furthermore, heavy or extreme rainfall may not follow a normal distribution (Katz *et al.*, 2002). Due to this, Khajehei and Moradkhani (2017) suggested using copula functions to bypass parametric transformation of the forecast and observed rainfall variables. The advantage of this technique is that the marginal distributions are not required to be produced for the joint distribution of nonzero forecast and observed rainfall variables (Favre, 2004). The success of this approach was particularly noted in predicting the uncertainty estimates for extreme rainfall events. Hence, normal distributions may not be suitable for modelling rainfall.

Other techniques that have been explored for postprocessing probabilistic rainfall forecasts preceding the more recent statistical techniques are linear regression, quantile regression (i.e. methods by Schaake et al., (2007), Wu et al., (2011) and

Robertson et al., (2013)), logistic regression (i.e. Sloughter et al., (2007)), neural networks (i.e. Koizumi (1999)) and binning techniques (i.e. Yussouf and Stensrud (2007)).

2.3 Hydrological applications of radar rainfall forecasts

Rainfall forecasts have been widely used for hydrological purposes, particularly for developing forecasting techniques for pluvial flooding, sewer flooding, river flooding, coastal flooding, surface flooding, landslides, flash floods and debris flow (Schellart *et al.,* 2011; Hénonin *et al.,* 2013; Faure *et al.,* 2002; Parker *et al.,* 2011; Krzysztofowicz and Herr, 2001; Onyutha and Willems, 2017; Thompson and Frazier, 2014; Priest *et al.,* 2011; Schellart *et al.,* 2009; Liguori *et al.,* 2012; Lee *et al.,* 2013; Even *et al.,* 2007; Wu and Lin, 2017; Olsson *et al.,* 2013). The requirements of a forecasting system differ based on the source of the forecast data and the type of flood predicted. Thus, they present different challenges in determining the thresholds of uncertainty in operational forecasting settings. Particularly, the temporal and spatial resolution requirements of the forecast data is a requirement alongside other factors such as lead time for mitigating disasters (Golding, 2000). This section focuses on the potential of applying radar forecasts to sewer flood forecasting based on studies that have explored radar rainfall forecasts in different types of flood forecasting systems.

2.3.1 Radar rainfall flood forecasting

QPE/QPF data have been extensively used for hydrological flood modelling in operational settings. For example, NWP QPFs had been mainly used as part of Hydrological Ensemble Prediction Systems (HEPS) to analyse predictions based on propagating these forecasts into hydrological models (Cloke and Pappenberger, 2009). The propagation of the uncertainty of QPE and QPF data had also been evaluated by Rossa et al., (2011) to ascertain the feasibility of an operational flood forecasting system. However, recently radar QPE and QPF data had been explored for this application. Versini (2012) had used radar QPE and

QPF data to develop a road inundation warning system as a way of preventing flash flooding. Coustau et al., (2012) conducted a study to analyse the usefulness of radar QPE in a rainfall-runoff model. The purpose was to see the practicability of radar QPE capturing the variability of rainfall and accurately representing the initial wet conditions of the catchment. However, hydrological modelling was challenging when there are convective storms with more spatial variability. Their study demonstrates that radar data is useful for hydrological modelling for credibly representing flood scenarios, and it highlights potential for real-time applications. The popularity of radar data for flood modelling and forecasting is due to the wide spatial availability of rainfall data and the ability to generate radar forecasts at a short range (Moore *et al.*, 2004). These are attributes that rain gauges lack despite generally being a more accurate rainfall source. Further benefits of radar QPE and QPF data are articulated by Germann et al., (2009).

Much effort has been invested in assessing the uncertainty propagation to river flood forecasting systems (Borga *et al.*, 2002; Vivoni *et al.*, 2007). However, there is a need to understand these uncertainties in pluvial (or sewer) flood forecasting. Schellart et al., (2012), Rico-Ramirez et al., (2015) and Liguori et al., (2012) had conducted studies involving exploring the propagation of radar QPE in sewer drainage systems. Schellart et al., (2012) had evaluated the uncertainties associated to radar QPE and rain gauge, and had found distinguishable differences in the hydrological output. They concluded the temporal resolution of the rainfall source plays an important role on the uncertainty of hydrological output in a sewer model. Rico-Ramirez et al., (2015) had conducted similar analysis using a sewer model with the goal of determining the proportion of uncertainty related to the radar QPE and the sewer model. They showed that there are other uncertainty sources related to model calibration and measured sewer variable data, which should be considered as part of a flood forecasting system.

Whilst several studies have explored forecasting (or Nowcasting) techniques, which is a constituent of the total flood uncertainty, the rainfall-runoff model is an integral component of the flood forecasting process. This may include combined use of rain gauge, QPE and QPF data. For example, Brezkova et al., (2012) study the operational feasibility of nowcasting methods for flash flood forecasting based on a continuous analysis of the state of hydrological conditions in the catchment.

This involves correcting the radar QPE data with rain gauge every 5 minutes and simultaneously producing hydrological simulations using the correct radar QPE and QPF at these time steps. (Šálek *et al.*, 2004). Silvestro and Rebora (2014) similarly combine QPE estimation via rain gauge adjustment, implement a nowcasting procedure to produce probabilistic radar QPFs and then produce probabilistic hydrological forecasts, all in a single system.

The concept of probabilistic QPFs were previously introduced to show estimates of the uncertainty accompanying deterministic QPFs. In flood forecasting, radar probabilistic QPFs have been highlighted as a promising solution to produce accurate flood forecasts in an operational system (Germann *et al.*, 2009; Zappa *et al.*, 2008). An ensemble generator developed at MeteoSwiss was used to produce the first operational system utilising hydrological forecasts based on radar probabilistic forecasts and a hydro-meteorological model in a mountainous region (Zappa *et al.*, 2008). In their work, Liechti et al., (2013) had evaluated that the probabilistic QPFs used to produce hydrological forecasts outperformed deterministic values on all thresholds. Silvestro and Rebora (2014) highlighted that the output of different hydrological forecasts is particularly useful in that the user may assess the severity of the flooding incident. This is especially conducive for decision making. Furthermore, their study had concluded that a probabilistic approach requires additional processes, such as data assimilation or considering more data, to increase the accuracy of probabilistic hydrological output and tackle uncertainties in spatial structure and atmospheric dynamics. Villarini et al., (2010) proposes a probabilistic framework for flood forecasting system that uses deterministic radar QPFs, called the Flash Forecast Guidance System (FFGS) (Mogil *et al.*, 1978). Their approach study different scenarios that exploit the uncertainties in two components of the FFGS: the first component focussing on the uncertainties in ascertaining the conditions issuing a flood warning, and the second component relates to representation of the forecast, hence the uncertainties in a deterministic QPF. The outputs of their study demonstrate that the probabilistic approach provides deeper information of flooding extents based on varying forecast scenarios. Particularly it pressed further research to focus on the error structure of the flood forecasting system components and to study extreme rainfall events. Several studies have highlighted considering the spatial structure of QPFs over a catchment, particularly in probabilistic frameworks

(Ahmadisharaf *et al.*, 2016; Mei *et al.*, 2014; Yang *et al.*, 2012). It had been recommended by Yang et al., (2012) that uncertainties in spatial variation of QPFs should be modelled explicitly.

2.3.2 Flood forecasting models

Kimura et al. (2012) had described the potential of using high resolution X-band polametric radars to produce high resolution QPFs for real-time flood forecasting. However, they articulate uses of different flood forecasting models for assessing the efficiency of the flood forecasting process. Particularly, they explain that detailed models would increase computational processing and so take longer to produce operational forecasts. Whereas simplified models are flexible and require less computer resources but suffer from producing accurate hydrological estimates. Their analysis evaluates different physically based flood forecasting models. The main models described are as follows:

Detailed models

These models provide extensive tools for deep analysis of flooding and physically based processes associated to the hydrological system. Examples of these are commercial software models Infoworks ICM, ISIS 2D, MIKE FLOOD, TUFLOW and XPSTORM (Néelz and Pender, 2013). Other models include Soil Conservation Service rainfall-runoff model (Coustau *et al.*, 2012; Xianzhao and Jiazhu, 2008) and HYDROG model (Brezkova *et al.*, 2012). All characteristics of the drainage area model are modelled including pipes, manholes, weirs and pumps). Due to the many complex physical processes involved in detailed models, these require high computational resources and would generally require more time to simulate flooding.

Simplified models

These represent less computationally demanding versions of the detailed models. Various model parameters are modified to meet these requirements such as considering pipes with a diameter above a threshold and ignoring those smaller. Kimura et al., (2011) had shown that the prediction accuracy remained the same by taking this approach in comparison to using the detailed model. A

detailed model could thus be simplified strategically to maintain prediction accuracy, which is conducive for a real-time flood forecasting system to the improvements of processing times.

Rainfall-runoff models that could be considered as simplified models are the Probability-Distributed Model by Moore (2007) which considers error prediction and state correction methods. It is also designed for real-time forecasting applications. It had been used by Jongh et al., (2012) in their operational flood forecasting system.

More simplified models

The aforementioned models could be simplified further by developing a simplified overland surface model. Hartnack et al., (2009) showed that such a model could greatly reduce the computational requirements whilst maintaining sufficient accuracy. Examples include CADDIES 2D (Ghimire *et al.*, 2013).

Statistical models

Purely mathematical based models could be used to deduce the hydrological variables instead of using hydrological models. Kimura et al., (2010) had adopted a statistically-based model for predicting hydrological output using radar QPFs in real-time. This is especially useful for reducing the computational resources because there would be no requirement to run hydrological simulations. Though not often directly used for predicting hydrological output, the benefits of specific statistical methods could be useful for this application. Methods based on Generalised Linear Models (GLMs) had been applied to probabilistic rainfall forecasting applications (Yang *et al.*, 2012). They included the use of Generalised Additive Models (GAMs), which are extensions of GLMs in that they allow parametric regression. The advantages of GLMs include that they are suitable for applications that are sensitive in time and space, thus being ideal for rainfall and flood modelling (Chandler and Wheater, 2002).

Artificial Neural Network based models

ANNs have commonly been used in hydrological studies. One of the core advantages of using a neural network over commonly used statistical methods is the nonlinearity of the model. Complex nonlinear relationships and imprecise data sets are manipulated with relative ease using ANNs, which would otherwise be

constraining using statistical approaches (Haykin, 1994). The makeup of ANNs are described as layers and network nodes (Tapoglou *et al.*, 2014). Networks nodes are presented in three categories: input, output and hidden nodes. The output and hidden nodes are directly involved in the derivation of parameters based on the input parameters. Various topics of ANN including the uncertainty characteristics of the different ANN models and a thorough review is given by Kasiviswanathan and Sudheer (2016) and Maier et al., (2010), respectively. ANNs have been applied to various hydrological applications including the prediction of groundwater flow, well levels and identifying parameters in aquifers (Coppola *et al.,* 2005; Lallahem *et al.,* 2005; Nayak *et al.,* 2006; Samani *et al.*, 2007; Tapoglou *et al.,* 2014). Other studies using ANNs incorporated the prediction of floods and rainfall distribution (Duncan *et al.*, 2012; Luk *et al.*, 2000).

The basic mechanisms of an ANN include a training method, which include back propagation, Genetic Algorithms and Differential Evolution (Coppola *et al.*, 2007; Trichakis *et al.*, 2009). Back propagation methods are the most commonly used and typically display good result in a range of applications. Also the activation method is an integral part of the ANN calculation and the sigmoid function is most commonly adopted (Trichakis *et al.*, 2011). This is chiefly because the ANN is operating optimally in terms of extracting nonlinear relationships in the data sets using this function.

The choice between using ANN or statistical approaches is debatable depending on the hydrological application and could be explored as a research topic of its own. However, this is outside the scope of this project and thus a rigorous evaluation is not required. Nonetheless, the benefits and drawbacks of this approach are articulated by Tu (1996). The main benefits are that the model is relatively less complex to setup, the ability to detect complex nonlinear relationships between the independent and dependant variables, the ability to detect relationships between the predictor variables and that multiple training methods could be applied improving the versatility of the model. The main drawbacks originate from the ‘black box’ aspects of the model process, which makes identifying causal relationships difficult. Also, higher computational resources may be required and the model may overfit data sets.

Kimura et al., (2012) applies ANN to each mesh point in an overland model. The purpose of this is to express relationships between the temporal and spatial rainfall information to flood depth. However, for this to be achievable at a good level of accuracy ample flooding data is required from the hydrological model. Furthermore, the data required to be setup for the ANN depends on the quality (i.e. accuracy) of the input (rainfall) and output (flood depth) data.

Kimura et al., (2012) conclude that the models with lower computational requirements showed to be most effective in predicting hydrological flood variables using the radar data in operational settings.

2.3.3 Influence of spatial variability on flood forecasting

Spatial variability of rainfall over a catchment could be readily characterised using radar rainfall. This is has led to a several studies exploring the spatial variability of rainfall storms and their influence on hydrological models (Cole and Moore, 2008, 2009; He *et al.*, 2013; Looper and Vieux, 2012; Smith *et al.*, 2007; Vieux *et al.*, 2009). Particularly, several studies have focussed on the impacts of spatial variability of radar rainfall on flash flooding (Anquetin *et al.*, 2010; de Lima and Singh, 2003; Douinot *et al.*, 2016; Lay and Saulnier, 2007; Lobligeois *et al.*, 2014; Morin and Yakir, 2014; Tramblay *et al.*, 2010; Wood *et al.*, 1988). However, there is the need to further study the hydrological variable responses based on varying spatial characteristics of rainfall. Much of previous work concentrate on radar-rain gauge adjustment and then characterising the spatial patterns over a catchment. Where hydrological models are used the number of rainfall events as case studies were limited (Emmanuel *et al.*, 2015). Furthermore, it had been highlighted by Michaud and Sorooshian (1994) that distributed modelling is improved if spatial information of rainfall is considered in the hydrological process. Schellart et al., (2012) had shown that due to the spatial variation of rainfall presented by the radar rainfall in several events the estimates of sewer flow varied in comparison to estimates simulated using rain gauge data. Clearly, spatial variability of rainfall needs to be considered in hydrological modelling.

Emmanuel et al., (2012) outlines that the influence of rainfall variability has on runoff modelling is based on three factors: spatial and temporal patterns of the rainfall, catchment behaviour and the physical processes generating runoff. Depending on the spatial heterogeneity and duration of the rainfall storm, the flood dynamics could vary. Viglione et al., (2010) had found in their study that a storm with high spatial heterogeneity over a short duration would cause highly fluctuating flood responses in a catchment. Whereas, a storm that is largely uniform and longer in duration would have minimal impact on the hydrological flood response (Mei *et al.*, 2014). However, their results are contested by a similar study conducted by Seo et al., (2012) who had demonstrated that a long duration uniformly structured storm may have large influence on the flood dynamics based on the storm movement. This shows that there are uncertainties in the spatial and temporal structure of rainfall in relation to the flood dynamics.

Catchment behaviour had been particularly highlighted as a contributing factor to varied flood extents combined with spatially varying rainfall. Anquetin et al., (2010) and Delrieu et al., (2005) conclude that the spatial variability of rainfall particularly influences the flood extents based on the spatial distribution of the soil properties. This becomes significant for catchments that receive highly varied rainfall when the soil infiltration is high (Sangati *et al.*, 2009). Different catchments have been identified by Segond et al., (2007) and are as follows: urban catchments, semiarid catchments located in locations commonly featuring convective storms and catchments located in mild climates. Urban catchments were the distinguishably sensitive to spatial and temporal variations of the rainfall storm. This was similarly the case with semiarid catchments receiving rainfall from convective storms that are highly varied as the flood extents widely fluctuated with different rainfall patterns. Catchments located in mild climates, however, showed the least flood dynamics against spatial varying rainfall patterns due to a smoothing effect noticed in the catchment runoff with rainfall of a temperate climate (Emmanuel *et al.*, 2012; Rozalis *et al.*, 2010). Furthermore, Zoccatelli et al., (2010) shown that the modelling efficiency is reduced to 30% for a catchment of size in a range of 36-167 km^2 if spatial variability of rainfall is not considered. Thus, when conducting spatial analysis of radar rainfall over a catchment or sewer drainage area, it is crucial to combine analysis with sewer catchment characteristics. Moreover, this is particularly important for building a

flood forecasting framework (Ahmadisharaf *et al.*, 2016; Foudi *et al.*, 2015; Mei *et al.*, 2014).

The spatial patterns of rainfall over a catchment could be quantified with the development of spatial indexes. Smith et al., (2004) had characterised the spatial variability of rainfall by introducing indexes. Zoccatelli et al., (2011) had similarly introduced indexes representing the spatial moments of catchment rainfall. The two indexes provide specific information on the concentration of rainfall over the catchment relative to the outfall of the catchment, and the type of rainfall being concentrated or multimodal, respectively. These indexes had been adopted by later studies investigating the spatial variability of rainfall for several hydrological applications. For example, Douinot et al., (2016) use the spatial indexes by Zoccatelli et al., (2011) to combine a spatial analysis of rainfall with the FFG method. Emmanuel et al., (2015) use these spatial indexes in their method and propose additional two indexes as improvement over the original indexes. The study had shown that based on an evaluation of the original and additional indexes proposed, they perform similarly in explaining the hydrological output related to spatial variability of rainfall. Thus, the indexes are useful in describing various dynamics of hydrological variables based on spatial varying rainfall. These could be used as an alternative to simple statistical methods such as variance or mean.

It is useful to consider analysing events in a historical or post-event analysis to obtain an understanding of the flood dynamics of spatially varying rainfall related to the catchment. Various studies have highlighted or conducted such analysis, which provides opportunities to study catchment response from extreme events (Borga *et al.*, 2007; Morin and Yakir, 2014; Smith *et al.*, 2007). Morin and Yakir (2014) describe that in literature two types of analysis had been conducted to understand impact of spatial distribution of rainfall on catchment response. One type of analysis considers using actual rainfall events and the subsequent hydrological output based on their simulations (performed by Younger et al., (2009)), and the second type considers synthetic rainfall with controlled spatial parameters to assess the hydrological response based on these varying characteristics (Sapriza-Azuri *et al.*, 2015; van Werkohoven *et al.*, 2008). Actual events are constraining in that they specify very specific conditions whereas synthetic events may not propagate realistic characteristics of rainfall. Hence,

Morin and Yakir (2014) propose combining the approaches by using actual rainfall storms in the hydrological model and then altering various characteristics such as changing the spatial structure of the rainfall grids. This sensitivity analysis is conducted to produce several hydrological outputs for which the flood dynamics could be better understood. This approach had been previously introduced by Moore et al., (2006) and Morin et al., (2006). Their study showed the flood extents of the catchment were strongly dependant on the spatio-temporal aspects of the convective rainfall, particularly the spatial structure of rainfall influenced by wind, direction and speed. However, their study was conducted for one type of catchment: a semiarid catchment and specifically for convective rainfall.

In conclusion, considering the spatial variability of radar rainfall in flood modelling produces more accurate model outputs. The flood dynamics could be studied more closely in relation to the spatial variability especially by conducting historical analysis based on many rainfall events with varying spatial characteristics. This would become an essential component of flood forecast management.

3 Improving deterministic radar Quantitative Precipitation Forecasts

3.1 Introduction

Chapter 2 has discussed that the accuracy requirements of hydrological applications depend on the resolutions of the rainfall datasets. One of the key approaches identified is to increase the resolution of rainfall data to meet the requirements of hydrological applications with sufficient accuracy. Higher resolution rainfall shows more spatial and temporal information in comparison to lower resolution datasets at any spatial or temporal period. However, higher resolution rainfall data may be limited in availability. This is especially the case where both the temporal and spatial resolutions are required to be high. When the required radar QPFs are not available at sufficiently high resolutions, various techniques exist to improve their resolutions.

The aim of the work presented in this chapter is to improve radar QPFs by increasing the resolution that is suitable for hydrological applications. This will be achieved by: 1) temporal interpolation by the optical flow technique, and 2) spatial interpolation by UKR. The temporal and spatial interpolation approaches are demonstrated using radar based Nowcasts provided by the UK Met office, in which QPFs have a resolution of 15 min and 2 km and QPEs have a resolution of 5 min and 1 km. Results are compared with traditional interpolation techniques to validate the interpolation methodology. The interpolation process proposed in this chapter is of great practical use when higher resolution, more frequent, higher accuracy QPFs are needed, for example, in the case of urban flood forecasting or flash flood forecasting. Moreover, this approach is suitable for interpolating QPFs so that coincidental timesteps of the QPF/QPE datasets could be compared. This is particularly useful for hydrological applications where historical comparisons of coincidental timesteps could be used in interpolation techniques to improve the accuracy of QPFs.

3.2 Interpolation process for improving the resolution of QPFs

The method involves two processes where two interpolated datasets are produced. Table 3.1 shows the different rainfall data use or produced in this

study. QPF-5-1 and QPF-15-2 are the observed and forecast rainfall datasets at their native resolutions, respectively. L-QPF-5-2, OI-QPF-5-1, LK-QPF-5-1, LI-QPF-5-1 and LS-QPF-5-1 are interpolated datasets produced using simple interpolated techniques. They are used in this study for validation purposes only, and are thus not part of the methodology. See section 1.2.4 for further details on validation experiments.

Table 3.1. Different rainfall data used or produced in this study, including the observed QPE and QPFs with different resolution characteristics.

QPF/E data reference	Derivation of the QPF product	Temporal resolution	Spatial resolution
QPE-5-1	QPE data at native resolutions	5-min	1-km
QPF-15-2	QPF data at native resolutions	15-min	2-km
O-QPF-5-2	Optical-flow temporal interpolation of QPF-15-2 from 15-min to 5-min	5-min	2-km
L-QPF-5-2	Linear temporal interpolation of QPF-15-2 from 15-min to 5-min	5-min	2-km
OK-QPF-5-1	Kriging spatial interpolation of O-QPF-5-2 from 2-km to 1-km	5-min	1-km
OI-QPF-5-1	IDW spatial interpolation of O-QPF-5-2 from 2-km to 1-km	5-min	1-km
LK-QPF-5-1	Kriging spatial interpolation of L-QPF-5-2 from 2-km to 1-km		
LI-QPF-5-1	IDW spatial interpolation of L-QPF-5-2 from 2-km to 1-km	5-min	1-km
LS-QPF-5-1	Simple parting spatial interpolation of L-QPF-5-2 from 2-km to 1-km	5-min	1-km

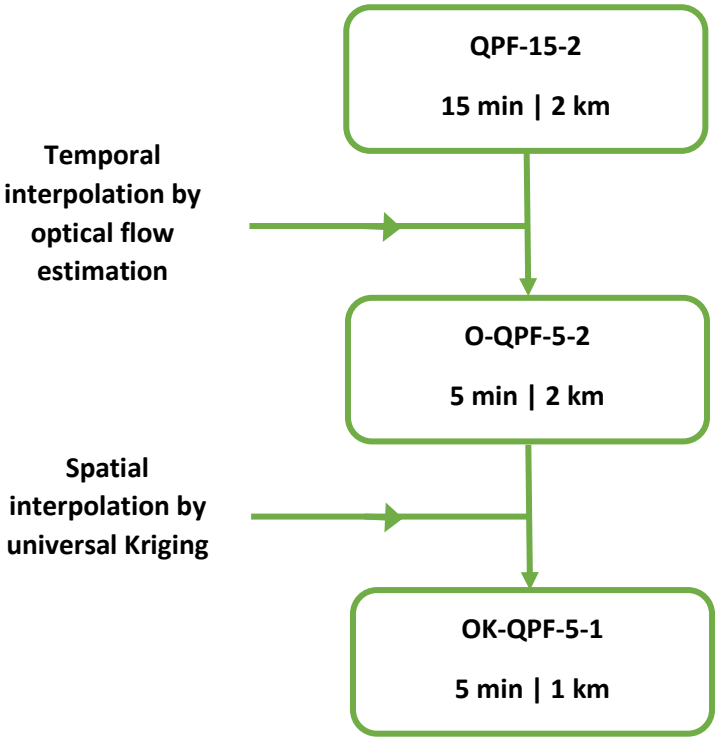

Figure 3.1. The different stages of the interpolation process to temporally and spatially interpolate QPF data.

As shown in Figure 3.1, temporal and spatial interpolation is carried out on QPF-15-2 from a resolution of 15-min and 2-km to 5-min and 1 km which would make it match corresponding QPE-5-1 data. Temporal interpolation is carried out using movement vectors derived from optical flow estimation to derive O-QPF-5-2 with resolution of 5-min and 2-km. Spatial interpolation is carried out on O-QPF-5-2 using universal Kriging to produce OK-QPF-5-1 with resolution of 5-min and 1-km.

3.2.1 Temporal interpolation of radar QPFs

1.1.1.1 The optical flow approach

The optical flow technique is used to obtain movement vectors, which can accurately represent detailed movement information in images. It is related to the motion of images that would be viewed by the observer, similar to how a stream of light can be characterised (Hongwei *et al.*, 2015).It is typically superior to other similar methods in terms of accuracy and also computational speed (Ehrhardt *et*

al., 2006; Wang *et al.,* 2015). This method has previously been used in computer vision, laser technology and in studying fluid motion and the imaging processes in biological and medical applications (Lan *et al.,* 2013; Andalibi *et al.,* 2015; Hongwei *et al.,* 2015; Wen *et al.,* 2015; Barba-J *et al.,* 2016). It has also been used to compute various distributions of the optical flow which highlights a key area in understanding the uncertainty of it in a number of applications (Simoncelli and Adelson, 1991). The dominant attribute of this method is that of picking up small-scale image structures at fine temporal scales, making it ideal for processing computer images. In rainfall studies and forecasting, this method has been applied to capture the rainfall structures at short time steps and to produce radar QPFs as part of an extrapolation scheme (Bowler *et al.,* 2004).

For a specific coordinate $\boldsymbol{X}$ in an image**,** the movement vector $\boldsymbol{w}$ is computed using the optical flow equation (Ehrhardt et al. 2006):

$$\boldsymbol{w} = -\frac{\nabla R\, \partial R}{\|\nabla R\|^2} \tag{3.1}$$

$$\boldsymbol{w} = -\frac{\mathbf{2}\left(\nabla R(\boldsymbol{X},\boldsymbol{T^i}) + \nabla R(\boldsymbol{X},\boldsymbol{T^{i+1}})\right)\partial R}{\left\|\nabla R(\boldsymbol{X},\boldsymbol{T^i}) + \nabla R(\boldsymbol{X},\boldsymbol{T^{i+1}})\right\|^2 + e} \tag{3.2}$$

Where $R(\boldsymbol{X},\boldsymbol{T^i})$ and $R(\boldsymbol{X},\boldsymbol{T^{i+1}})$ are the intensities of the image at timestep $\boldsymbol{T^i}$ and $\boldsymbol{T^{i+1}}$, respectively, $\nabla R = (\nabla R(\boldsymbol{X},\boldsymbol{T^i}) + \nabla R(\boldsymbol{X},\boldsymbol{T^{i+1}}))/2$ is the spatial image gradient, and is approximated by averaging the neighbouring rainfall intensities, and e is a stabilising constant estimated from local image properties (Ehrhardt et al. 2006).

Previous research has used movement vectors to interpolate on a temporal scale (Schmid et al., 2002; Ehrhardt et al., 2006; Nielsen et al., 2014). The method described by Nielsen et al. (2014) uses forward and backward advection as part of a temporal interpolation algorithm between the radar rainfall image sequences, using movement vectors from Equation (3.2), and then combined them both in an interpolated radar data set.

Equation (3.2) was used by Ehrhardt et al., (2006) to interpolate image sequences and it was demonstrated that it outperformed linear or shape-based interpolation. However, Brox et al., (2004) produced a variation model of the optical flow equation that incorporated four modifications: the conservation of the grey level (or rainfall intensity), the gradient constancy in relation to the grey level,

the smoothness of the flow field to consider areas where the gradient is inconsistent, and finally the consideration of a multiscale approach. The grey level is an issue in computer vision where the constancy can be violated between image sequences and this variation model takes this into account when deriving the movement fields (Charbal *et al.*, 2016). This means interpolating radar image sequences using the variation model will ensure a smooth change of rainfall intensity in the interpolated time steps.

Wang et al., (2015) adopted a similar temporal interpolation method and used a variation optical flow model described by Brox et al., (2004) to interpolate radar QPE with a temporal scale of 5-min to 1-min to match rain gauge values. However, their technique also takes into account the interpolation of those values situated near the boundaries of the rainfall field, which produces more accurate interpolations in these regions.

The variation model was proposed as follows where $\boldsymbol{X_T}$ is the coordinate of the rainfall intensity and $\boldsymbol{w_T} = (\boldsymbol{u_T}, \boldsymbol{v_T})$ is the movement vector to be derived in the x-direction (u) and y-direction (v), at timestep $\boldsymbol{T}$:

$$E(\boldsymbol{w_T}) = E_{DATA}(\boldsymbol{w_T}) + REG * E_{SMOOTH}(\boldsymbol{w_T}), \tag{3.3}$$

Where REG is a regularisation parameter and $E(\boldsymbol{w_T})$ is called an energy function that is the summation of two specific energy functions, $E_{DATA}(\boldsymbol{w_T})$ and $E_{SMOOTH}(\boldsymbol{w_T})$, represented as follows:

$$E_{DATA}(\boldsymbol{w_T}) = \int_{\omega} \Psi * (|I(\boldsymbol{X_T} + \boldsymbol{w_T}) - I(\boldsymbol{X_T})|^2 + \gamma * |\nabla I(\boldsymbol{X_T} + \boldsymbol{w_T}) - \nabla I(\boldsymbol{X_T})|^2) * dx, \tag{3.4}$$

and

$$E_{SMOOTH}(\boldsymbol{w_T}) = \int_{\omega} \Psi * (\nabla^2 \boldsymbol{u_T} + \nabla^2 \boldsymbol{v_T}) * dx \tag{3.5}$$

$I(\boldsymbol{X_T} + \boldsymbol{w_T})$ and $I(\boldsymbol{X_T})$ represent the intensities of the image at coordinates $\boldsymbol{X_T} + \boldsymbol{w_T}$ and $\boldsymbol{X_T}$, respectively. Ψ is an increasing concave function which ensures anomalous values do not have a significant impact on the resulting values. ω is the domain of the radar QPF. Based on an extensive literature review by (Roth *et al.*, 2010) and experimentation, the weight values $REG = 0.012$ and $\gamma = 50.0$ are used (Wang *et al.*, 2015). Due to being outside the scope of application, it is not necessary to conduct a sensitivity analysis on these figures. The reference to

literature and initial experimentation is sufficient to prove the robustness of choosing these values. Though, the effects on the movement vectors of varying these values over different temporal and spatial locations could be explored as further study.

The movement vectors between two consecutive radar QPF images, at 15-minute time steps, are obtained using the variation model described by Brox et al., (2004). The interpolation algorithm described by Wang et al., (2015) is adopted in this study to use these vectors to deduce values between $\boldsymbol{T}$ and $\boldsymbol{T} + \mathbf{15}\,\boldsymbol{min}$ radar images.

1.1.1.2 Implementation of temporal interpolation

The radar QPF has a 15-min temporal resolution (consecutive values at $\boldsymbol{T}$ and $\boldsymbol{T} + \mathbf{15}\,\boldsymbol{min}$ time steps) and the new interpolated data will produce two further values at the $\boldsymbol{T} + \mathbf{5}\,\boldsymbol{min}$ and $\boldsymbol{T} + \mathbf{10}\,\boldsymbol{min}$ time steps, between any two radar images at specific grid coordinates.

In the following implementation, the number of interpolations per timestep is N, $\boldsymbol{\Delta T}$ is the timestep change of the radar QPF and $\boldsymbol{\Delta t}$ is the timestep change of the radar QPE. In this study, we have $N = 3$, $\boldsymbol{\Delta T} = 15$ mins and $\boldsymbol{\Delta t} = 5$ mins. The timestep of the radar QPE is represented by $\boldsymbol{t}$.

The variation optical flow equation is applied to obtain the movement vector $\boldsymbol{w_T}$ between two consecutive images in the forward direction, denoted by $\boldsymbol{w_T^f}$. The rainfall intensities of the image are then represented using the coordinates of the grid location specified by $\boldsymbol{X_T}$:

$$\boldsymbol{f_T} = \boldsymbol{X_T} - \alpha * \boldsymbol{w_T^f} \tag{3.6}$$

$$\boldsymbol{f_{T+\Delta T}} = \boldsymbol{X_T} + (1 - \alpha) * \boldsymbol{w_T^f} \tag{3.7}$$

where $\alpha = \frac{k}{N}$ and k is the kth interpolation between the two images. Here, only the 1st and 2nd interpolations are considered i.e. $k = 1$ and $k = 2$.

Next, the intensities at these coordinates, $I(\boldsymbol{f_T})$ and $I(\boldsymbol{f_{T+\Delta T}})$ can be used to obtain the interpolated intensities between the two images, denoted as $I(\boldsymbol{X_{T+\Delta t}})$. However, as Wang *et al.,* (2015) considered occlusion reasoning, there is a

condition that the difference between $I(\boldsymbol{f_T})$ and $I(\boldsymbol{f_{T+\Delta T}})$ must be below a certain threshold. In other words,

$$|I(\boldsymbol{f_T}) - I(\boldsymbol{f_{T+\Delta T}})| < A \tag{3.8}$$

where A needs to be chosen for the threshold value. This ensures that the pixel change doesn't indicate a significant decay or growth, which would produce inaccurate interpolated values.

The interpolation process can then be done:

$$I(\boldsymbol{X_{T+k\Delta t}}) = (1 - \alpha) * I(\boldsymbol{f_T}) + \alpha * I(\boldsymbol{f_{T+\Delta T}}) \tag{3.9}$$

Now, if $|I(\boldsymbol{f_T}) - I(\boldsymbol{f_{T+\Delta T}})| > A$ then this process will not be conducted. Instead, the algorithm will be performed again but for the movement vector $\boldsymbol{w_T^b}$ in equations (3.6) and (3.7), between each consecutive image in the backward direction to get backward movement coordinates:

$$\boldsymbol{b_T} = \boldsymbol{X_T} - \alpha * \boldsymbol{w_T^b} \tag{3.10}$$

$$\boldsymbol{b_{T+\Delta T}} = \boldsymbol{X_T} + (1 - \alpha) * \boldsymbol{w_T^b} \tag{3.11}$$

If the inequality in Equation (3.8) is still not met, then use a combination of the forward and backward interpolation processes i.e.:

$$I(\boldsymbol{X_{T+k\Delta t}}) = (1 - \alpha) * I(\boldsymbol{f_T}) + \alpha * I(\boldsymbol{b_{T+\Delta T}}) \tag{3.12}$$

Equation (3.9) using backward movement coordinates (i.e. backward interpolation) is used if the forward interpolation does not interpolate any value between two pixels. Equation (3.12) ensures that any values not interpolated are interpolated. The primary reason why interpolation in either forward or backward direction may not produce interpolated values is that the condition in equation (3.8) is not met. Any value of $I(\boldsymbol{f_T})$ within the radar image would meet this condition providing a suitable value for A H is selected. Hence, an appropriate value for A is selected to ensure that the interpolation occurs using the pixels within the range of the radar image. For specific data, selecting the appropriate value for A may be achieved by experimentation.

3.2.2 Spatial interpolation of radar QPF

Kriging methods are versatile and are commonly used in hydrology, particularly for problems in groundwater analysis (Kumar and Remadevi, 2006). The concept was first introduced by Krige (1951), however, the derivation of the formulates equating the interpolated points were performed by Matheron (1971). The applications of Kriging methods have mainly been applied for spatial interpolation, although, its usefulness has been demonstrated in spatio-temporal interpolation problems (Ta'any *et al.*, 2009).

Kriging methods provide information on the uncertainty by estimating the error variance along with the exact estimations of the interpolated values(Cheng, 2013; Li, Lewis *et al.*, 2015; Sepúlveda *et al.*, 2012). It can be defined as a random value interpolation using nearby observations that are weighted according to the spatial covariance values (Guntaka *et al.*, 2014). The commonly used Kriging methods are OKR and UKR (Aboufirassi and Mariño, 1983; Yan *et al.*, 2008)However, OKR is the most often used based in literature (Zhang and Wu, 2015). Despite this, it had been shown that UKR produces better results based on several studies (Selby and Kockelman, 2013). Other Kriging methods are popular, such as co-Kriging and External Drift Kriging, and have shown to produce more accurate results in comparison to the non-geostatistical methods. However, these are multivariate methods that require secondary data and this study interpolates a single data set.

UKR is used to spatially interpolate the QPF from 2-km grids to 1-km after it has been adjusted to the 5-min temporal resolution. The estimation of an unknown point $\boldsymbol{X_u}$ using sample points $\boldsymbol{X_T}$ at timestep $\boldsymbol{T}$ in OK can be represented by (Emery, 2006; Tapoglou *et al.*, 2014; Zhang and Wu, 2015):

$$I^*(\boldsymbol{X_u}) = \sum_{\bar{\imath}=1}^{n} \lambda_T(\boldsymbol{X_u}) I\left(\boldsymbol{X_{T_{\bar{\imath}}}}\right) \tag{3.13}$$

where I and I^* represent rainfall intensities of known and unknown points, respectively. λ_T is the weight function that is selected so that it is unbiased and results in minimal variance (Sepúlveda *et al.*, 2012). This is calculated when solving the Lagrangian function, which is implicitly performed in the Kriging interpolation.

In the case of UKR, a trend analysis for the rainfall intensity I in the study area is defined, which means that the expectation value (or the mean) is unknown and is calculated implicitly based on the function used for the trend with the different data points. This is what distinguishes OKR and UKR (Freier and von Lieres, 2015). A trend analysis is conducted as the study assumes that trends in rainfall intensities surrounding unknown points would have a significant influence on their values.

I is represented in the following form with m being the deterministic function and Y the stochastic component representing the noise (Cressie 1993; Matheron 1971; Freier & von Lieres 2015; Li *et al.*, 2015; Selby & Kockelman 2013; Brus & Heuvelink 2007):

$$I(\boldsymbol{X_T}) = m(\boldsymbol{X_T}) + Y(\boldsymbol{X_T}) \tag{3.14}$$

A basic trend can be assumed with the deterministic component defined as,

$$m(\boldsymbol{X_T}) = \sum_{\bar{k}=1}^{h} v_{\bar{k}} q_{\bar{k}}(\boldsymbol{X_T}) \tag{3.15}$$

which is simply a linear combination of functions $q_{\bar{k}}$ with coefficients $v_{\bar{k}}$.

For spatial points $\boldsymbol{X_T}$ with rainfall intensity values defined as $I(\boldsymbol{X_T})$ separated by a distance vector h, an empirical variogram $\gamma(h)$ can be constructed using the expectation of $[I(\boldsymbol{X_T} + h) - I(\boldsymbol{X_T})]^2$, represented as (Moustafa and Yomota, 1998; Schlather and Gneiting, 2006; Vieira *et al.*, 1983):

$$2\gamma(h) = E\{[I(\boldsymbol{X_T} + h) - I(\boldsymbol{X_T})]^2\} \tag{3.16}$$

Hence, for a given number of observation pairs $N(h)$ the variogram $\gamma(h)$ can be estimated using (Bowman and Crujeiras, 2013; Moustafa and Yomota, 1998; Vieira *et al.*, 1983):

$$2\gamma(h) = \frac{1}{\bar{N}(h)} \sum_{\bar{j}=1}^{N(h)} [I(\boldsymbol{X_T} + h) - I(\boldsymbol{X_T})]^2 \tag{3.17}$$

For the number of pairs of $\bar{N}(h)$, the methodology takes recommendation from Journel and Huijbregts (1978) of considering values of h for which there are at least 30 pairs. Hence, $\bar{N}(h)$ is chosen to be 30 for consistency. The maximum and minimum distances are calculated implicitly in the empirical variogram. However, the number of lag bins is selected to be 10. These parameters would ensure of a good variogram to be calculated (Tapoglou *et al.*, 2014). Furthermore,

as the variogram is calculated at every time step, the values for the sill, nugget and range will vary (and would be used when fitting a theoretical variogram).

To reduce the sampling error of the data when using the variograms in further stages, it is common to fit the empirical variogram to theoretical models. There are several models to select from but the one used in this study is the spherical model, which is commonly used (Lebel and Bastin, 1985; Moustafa and Yomota, 1998). Consider the covariance variogram $\gamma^*(h)$ defined as:

$$\gamma^*(h) = Cov(0) - Cov(h) \tag{3.18}$$

Then the spherical model to be used is denoted as:

$$\gamma_S^*(h) = \beta_{nugget} + \beta_{struc}\left[\frac{3}{2}\left(\frac{h}{\beta_{corr}}\right) - \frac{1}{2}\left(\frac{h}{\beta_{corr}}\right)^3\right] \quad for\ 0 \le h \le \beta_{corr} \tag{3.19}$$

$$\gamma_S^*(h) = \beta_{nugget} + \beta_{struc} \quad for\ h > \beta_{corr} \tag{3.20}$$

where β_{nugget} is the nugget effect of the variogram, β_{struct} is the component representing the structural heterogeneity and β_{corr} is the correlation range of the variogram. Note that $\beta_{nugget} + \beta_{struc}$ is the sill of the variogram.

Furthermore, the spherical model is chosen as it best chooses values for and that closely resemble the empirical variogram.

3.2.3 Measuring performance

For quantitative measurements of performance, RMSE and BR are used in this study to compare the performance of final QPF data against the observed data.

RMSE is the standard deviation of the difference between QPE and QPF data, which provides an indication of how close the QPF is to the observed rainfall. The values can be from 0 to infinity and values closer to zero are more accurate. The RMSE of the live QPF and QPE data, denoted $QPF_{i,j}$ and $QPE_{i,j}$, respectively, at grid j is calculated as follows:

$$RMSE^j = \sqrt{\frac{\sum_{i=1}^{n}\left(QPE_{i,j} - QPF_{i,j}\right)^2}{\bar{n}}} \tag{3.21}$$

where $\bar{n}$ is the number of time steps, $QPE_{i,j}$ and $QPF_{i,j}$are QPE and QPF values at the ith time step, respectively. As there are QPF data in multiple grids

(representing the study area), the average RMSE, denoted $RMSE$, over K grids is calculated in the following way:

$$RMSE = \frac{\sum_{j=1}^{K} RMSE^{j}}{K} \tag{3.22}$$

BR provides an indication of the overestimation or underestimation of the QPF in comparison with the QPE, and is calculated at the jth grid using:

$$BR^{j} = \frac{\sum_{i}^{\bar{n}} QPE_{i,j}}{\sum_{i}^{\bar{n}} QPF_{i,j}} \tag{3.23}$$

Similarly as calculating the average RMSE over K grids, the average BR, denoted BR, is calculated as follows:

$$BR = \frac{\sum_{j=1}^{K} BR^{j}}{K} \tag{3.24}$$

A BR value of 1 show that the total QPF rainfall values over the forecast period at all of the grids matches the total QPE rainfall values over the same temporal and spatial locations. It can also indicate overestimation with value larger than 1 or underestimation when BR value is less than 1.

Comparison with different QPF data

To demonstrate the benefits of the interpolation approaches suggested in this study, comparisons of the interpolated datasets are made with datasets that have been interpolated with simple approaches. Simple approaches are often used for relative ease of application. The following describes the simple interpolation approaches used to validate the methodology presented in this study:

Simple linear temporal interpolation*.* Interpolated points of QPF-15-2 are calculated by averaging techniques between two timesteps on a temporal scale

Simple parting spatial interpolation. QPF data at 2-km resolutions are interpolated to 1-km resolutions by dividing 2-km QPF grids to 1-km grids and using the value at the 2-km as the values of the 1-km grids. This approach is very simple to implement.

Inverse Distance Weighting spatial interpolation. As explained in section 2, spatial interpolation techniques are classified in two categories: geostatistical and simple techniques. IDW is an example of a simple spatial interpolation technique.

Therefore, it is relatively simpler to implement. IDW calculates interpolated points based on the distance between interpolated and measured data points. The closer the measured point the more influence it has on the interpolated value. IDW does not use spatial uncertainty (i.e. covariance) to calculate interpolated values.

Validation studies are organised in the following way:

O-QPF-5-2 verses L-QPF-5-2

Compares temporal interpolation by optical flow estimation and temporal interpolation using simple linear temporal interpolation.

OK-QPF-5-1 verses OI-QPF-5-1

Compares spatial interpolation by UKR and IDW after both QPF data have been temporally interpolated by optical flow estimation.

OK-QPF-5-1 verses LK-QPF-5-1

Compares temporal interpolation by optical flow estimation and temporal interpolation using simple linear temporal interpolation when both QPF data have been spatially interpolated by UKR.

OK-QPF-5-1 verses LI-QPF-5-1

Compares temporal and spatial interpolation by optical flow and UKR, respectively, with temporal and spatial interpolation by simple linear temporal interpolation and IDW, respectively.

OK-QPF-5-1 verses LS-QPF-5-1

Compares temporal and spatial interpolation by optical flow and UKR, respectively, with temporal and spatial interpolation by simple linear temporal interpolation and parting, respectively.

3.3 Case study

3.3.1 Introduction to study area

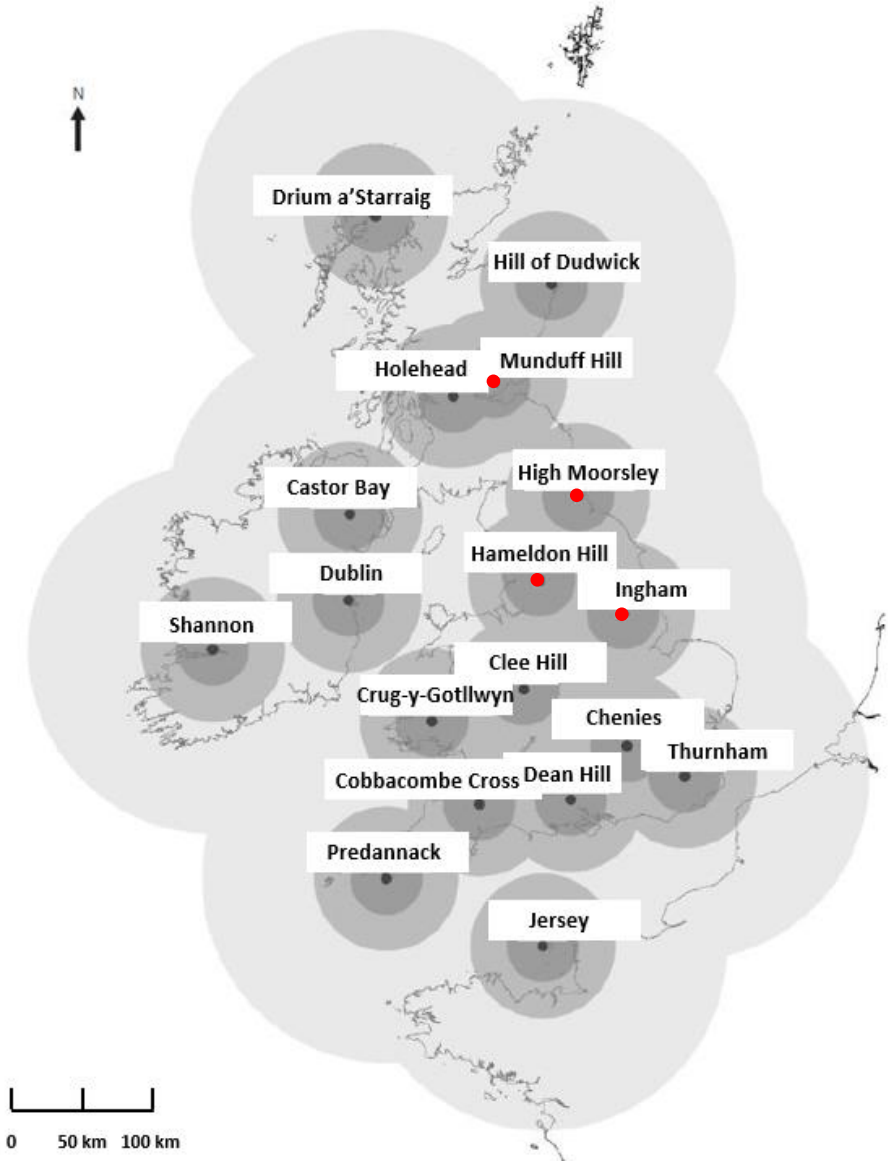

Figure 3.2. The UK radar network showing the four radars in the North East of England (highlighted in red) producing rainfall data for Northumbrian Water.

Rainfall data

The region sourced for the QPE/F data in this study and in Chapters 4 and 5 is in the North East of England and the data is provided for Northumbrian Water. This region is highlighted in Figure 3.2 which shows the weather radar network across the UK operated by the UK Met Office. Four radars are used to produce the precipitation data for the region of interest. They are Munduff Hill, High Moorsley, Hameldon Hill and Ingham, highlighted with a red point on the left image in Figure 3.2. The source used for QPE data is referred to as Radar rain-rate and the

source for QPF data is referred to as Nowcasts. The four radars cover a region that has dimensions of 184 x 140 km. The QPE data has temporal and spatial resolutions of 5-mins and 1-km, respectively. The QPF data has temporal and spatial resolutions of 15-mins and 2-km, respectively.

Source information of rainfall data

The UK Met Office describe the processes generating Radar rain-rate and Nowcasts. The main processes are outlined as follows:

Scanning – the radars scan the atmosphere measuring the rainfall reflectivity which is sent back to the UK Met Office (based in Exeter).

Data processing – correction procedures and quality checks are conducted to produce accurate estimate of Radar rain-rate. Outputs of this stage is composite radar image.

Nowcasting – using the Radar rain-rates extrapolation schemes are applied to produce Nowcasts up to 6 hours in the future. These are blended with NWP models.

Post-processing – this processes Nowcasts to meet specific format requirements of customer use.

Quality control of the data is crucial to producing accurate datasets. During the data processing stage, the QPE data is quality checked by removing noise, spurious echo and attenuation and reducing the impact of beam blockage. Furthermore, anomalies in reflectivity measurements are tackled by reducing differences between measurements taken in the atmosphere to the surface (i.e. Vertical Profile of Reflectivity (VPR)) and reducing effects from ‘bright banding’. Bright banding refers to inaccurate reflectivity measurements at a layer of liquid rainfall formed between rainfall zones with different temperatures.

Rain gauge adjustment is conducted to reduce errors in the rainfall estimates at the surface. Conditions ensuring quality of correction includes using rain gauges within 100 km of the radar location, using measurements only where radar rainfall is estimated and have recorded rainfall within a certain time window.

Nowcasting process uses a series of algorithms that rely on movement vectors to calculate future rainfall. These schemes use ‘optical flow theory’ to derive movement and it is recognised as an industry-standard technique for obtaining movement vectors.

3.3.2 Grid selection

To interpolate a single 2-km QPF grid, the grids surrounding this specific grid need to be processed in the Kriging interpolation process. There are in total 6440 QPF grids (corresponding to the 2-km QPF grids) and 25,760 QPE grids (corresponding to the 1-km QPE grids) in the Northumbrian Water radar domain. It would be advantageous to consider many QPF grid points in order to get more accurate interpolated QPE values, but to do so would be computationally demanding (Cheng, 2013). For this reason, for each event, the minimum number of QPE grids has been defined as the size of the study areas, which is chosen to be a 36-square region of 6 x 6 QPE grids. This has led to performing the whole procedure on a 100-km square region of 5 x 5 QPF grids. This would enable the interpolation of the 36 QPE grid values enclosed within the 100-km square region. However, the demerits of this approach are that it would be difficult to distinguish the spatial characteristics of rainfall, for example, storm development, or whether the rainfall is convective or frontal. However, although outside the scope of this study, different number of QPF grids could be explored in order to study the influence on the accuracy of the QPE values to be interpolated.

3.3.3 Rainfall events for verification

16 verification events are obtained from the four meteorological seasons between June 2016 and May 2017 to validate the methodology presented in this chapter. Specifically, four events are extracted from each meteorological season.

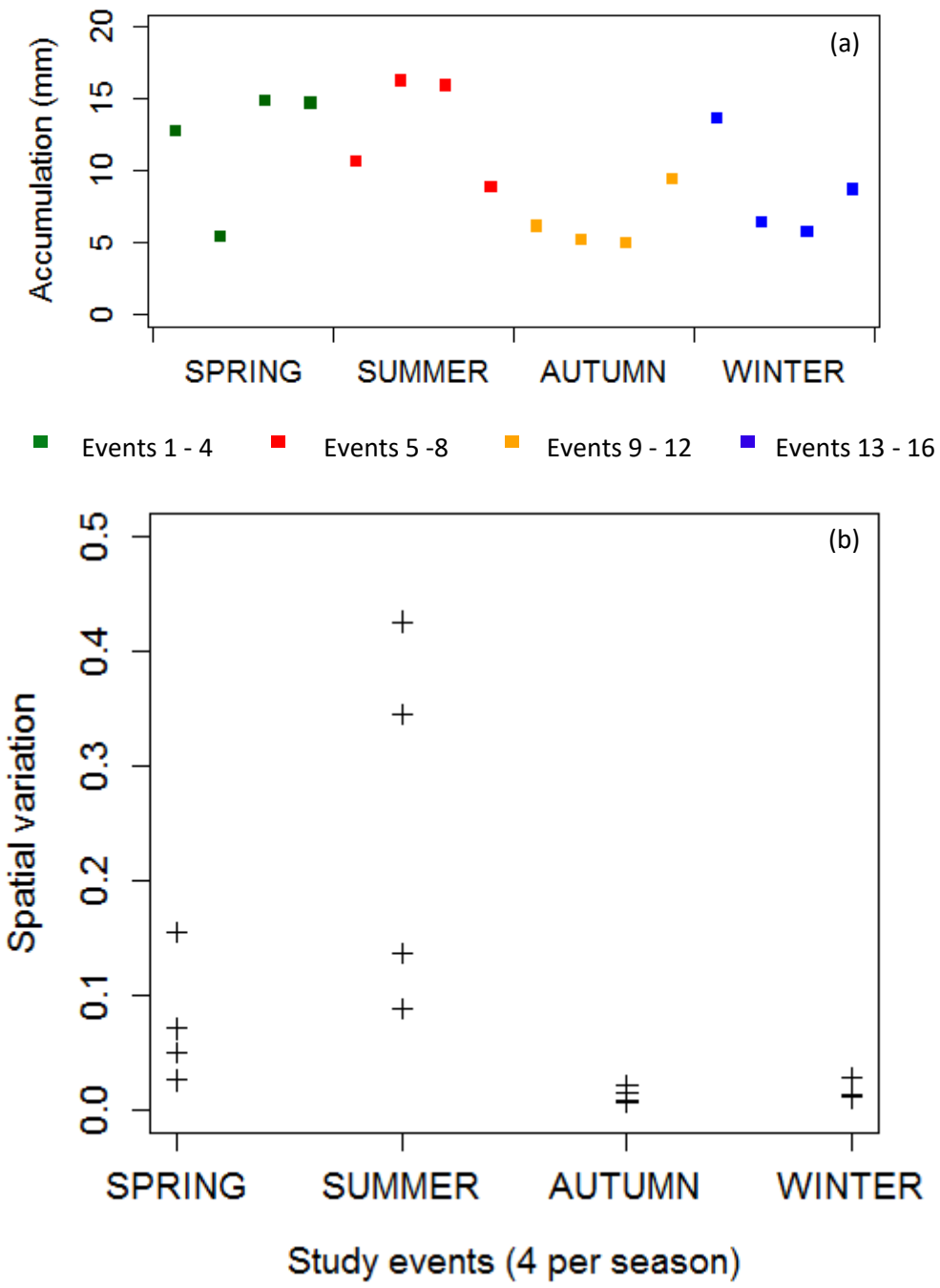

Figure 3.3. (a) The average QPE rainfall accumulation of each event across the four seasons over the six-hour forecast period over a 36 km2 (6 x 6 km2) region. (b) The spatial variation of the 16 verification events are presented in the four seasons.

The average QPE rainfall accumulation over the study area for all 16 verification events are shown in Figure 3.3(a). This highlights that the interpolation processes would be tested on light and heavy rainfall events throughout four seasons. Spring and summer seasons are warm periods of the year and autumn and winter

are cool periods of the year. Hence, events in their respective seasons are also referred to the warm/cool period of the year.

Figure 3.3(b) shows the different spatial characteristics of the 16 verification events based on the four seasons. The spatial metric used is the variation of the total QPE rainfall value over the forecast period of each grid in the study area. The four events in the summer period show the largest values for the variation followed by the events in the spring period. These two seasons are the warmer periods of the year and hence convective storms are typically observed in these periods, which often show large spatial variation. The cooler seasons are autumn and winter and the verification events in these periods have the lowest spatial variation, which is commonly observed in frontal storms typically seen in these periods. The interpolation process is thus tested for different types of rainfall with varying spatial characteristics.

3.4 Results and discussion

The accuracy of the temporally and spatially interpolated QPFs of the verification events are presented in section 3.4.1 and 3.4.2 using rainfall maps, hyetographs, RMSE and BR values. Furthermore, due to the large uncertainties between the QPF/QPE sources of this study, specific events that show the QPF relatively close to the QPE are used to show to rainfall maps demonstrating the benefits of the interpolated QPF.

3.4.1 Temporally interpolated QPF

O-QPF-5-2 verses L-QPF-5-2

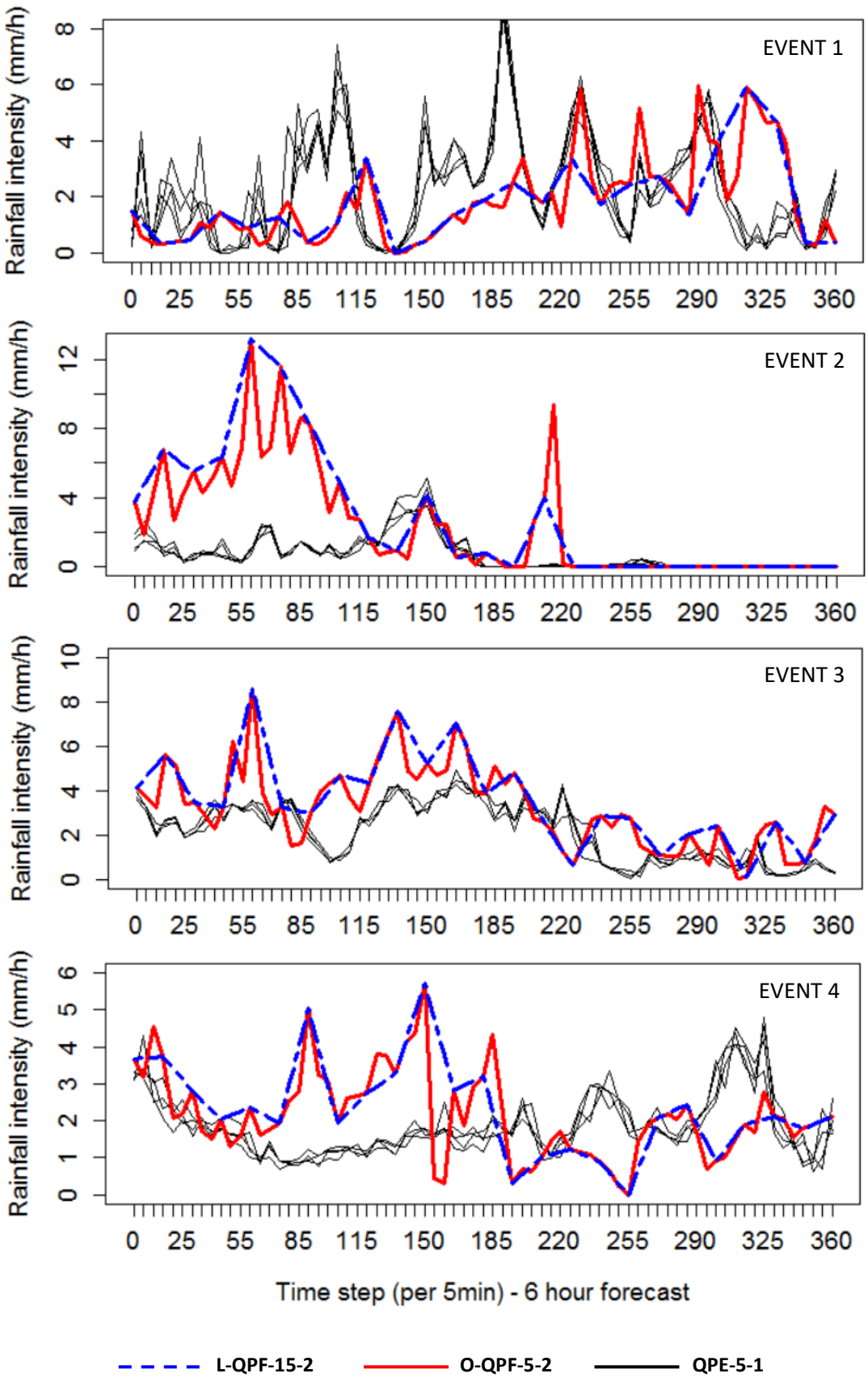

Figure 3.4. Hyetographs showing O-QPF-15-2, L-QPF-5-1 and QPE-5-1 data at a selected single QPF grid for spring events 1 - 4.

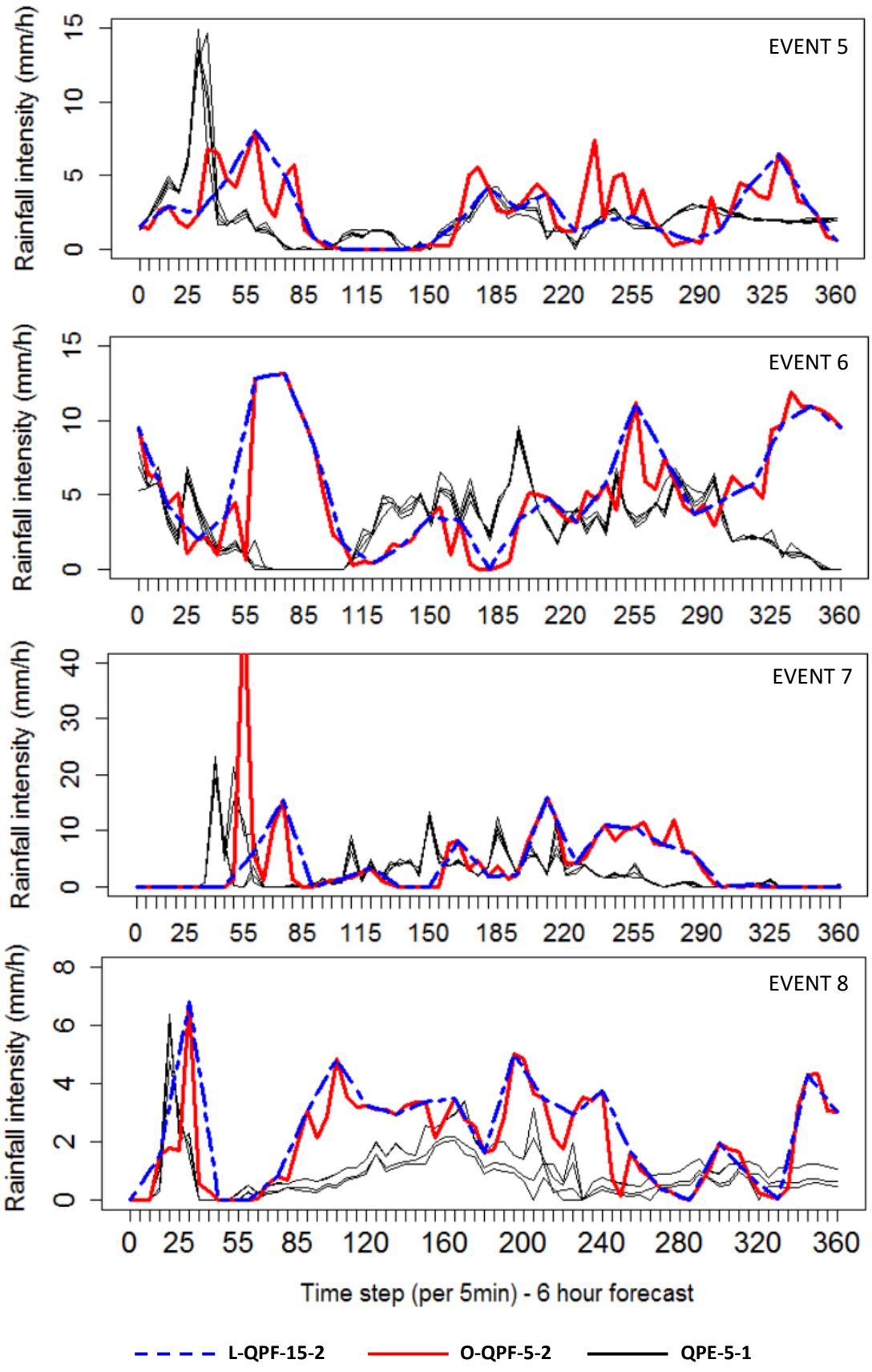

Figure 3.5. Hyetographs showing O-QPF-15-2, L-QPF-5-1 and QPE-5-1 data at a selected single QPF grid for summer events 5 - 8.

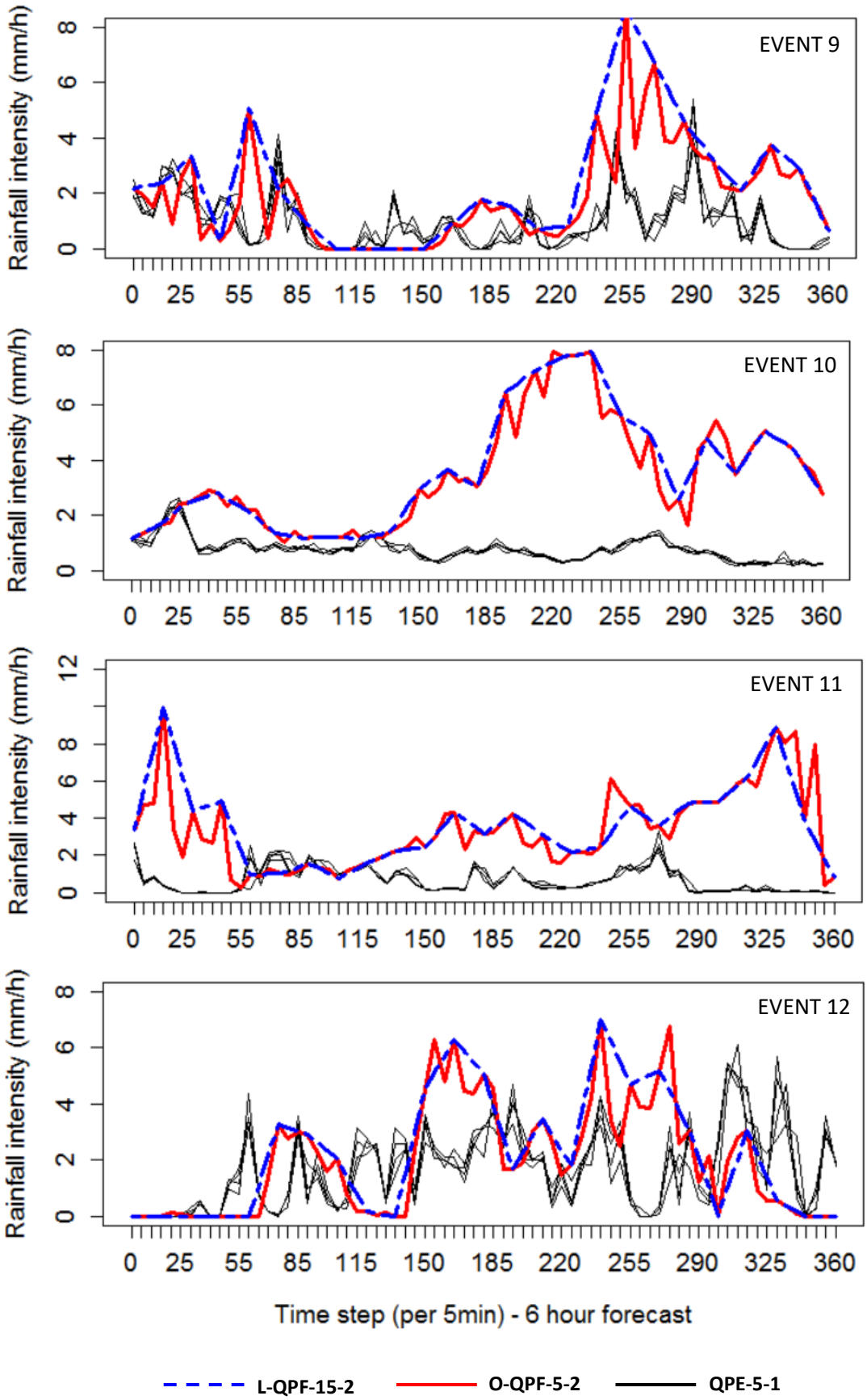

Figure 3.6. Hyetographs showing O-QPF-15-2, L-QPF-5-1 and QPE-5-1 data at a selected single QPF grid for autumn events 9 – 12.

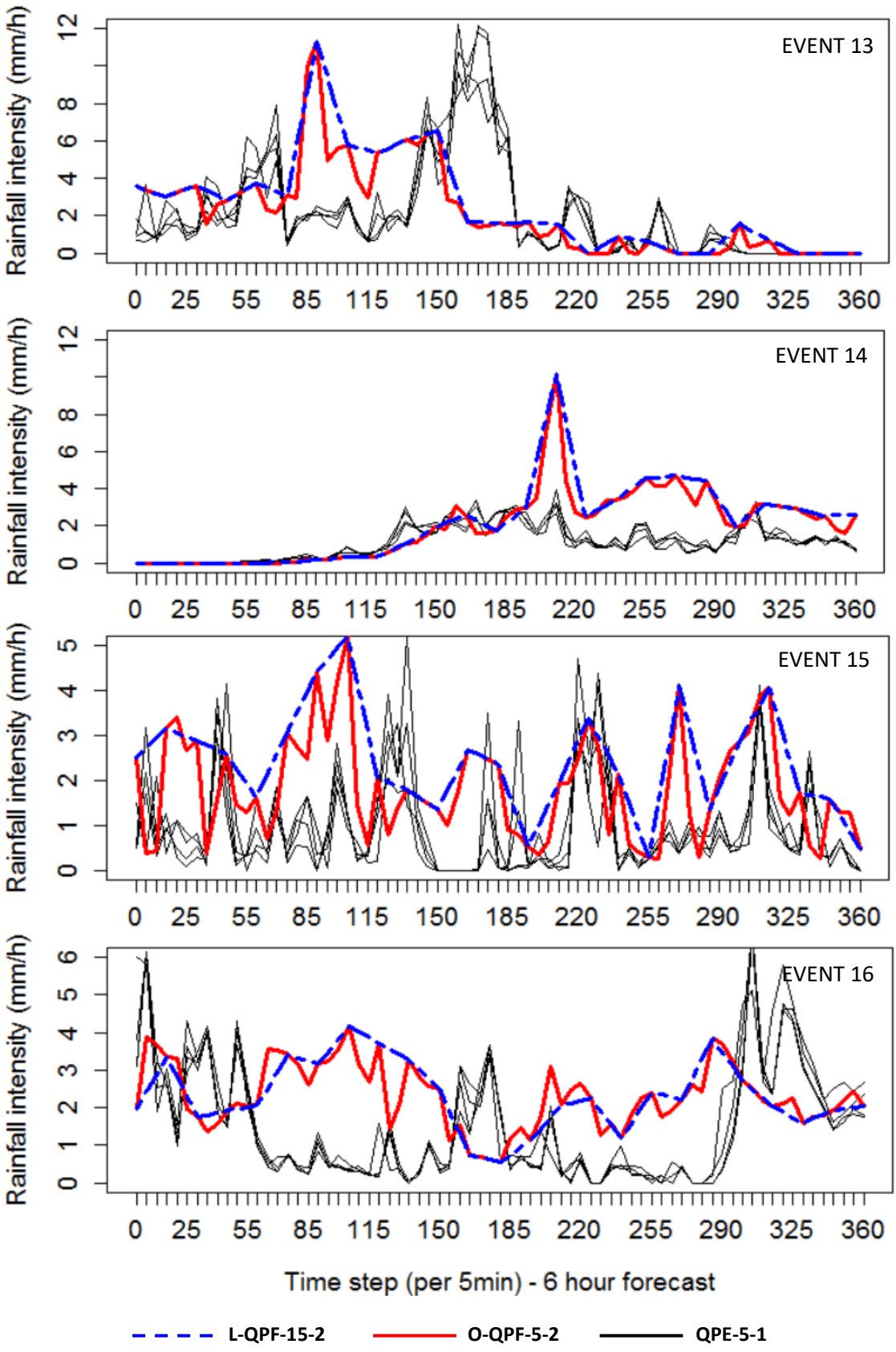

Figure 3.7. Hyetographs showing O-QPF-15-2, L-QPF-5-1 and QPE-5-1 data at a selected single QPF grid for winter events 13 – 16.

The benefits of temporal interpolation are observed in Figure 3.7. Although, there are not any noticeable differences in performance between seasons, the figures show the performance for low/high QPF values, especially where peaks are observed or where the QPF over/underestimates the QPE. For example, events 9 – 12 (autumn events) show several periods within the QPF where L-QPF-5-2 overestimates the QPE. The O-QPF-5-2 data in the same periods are shown to decrease the overestimation of L-QPF-5-2 (i.e. time steps 240 – 360 in event 12). Events 5 – 8 (spring events) present some extreme characteristics of L-QPF-5-2 such as in event 2 between time steps 0 – 115. This period shows forecast rainfall between 2 – 12 mm/h whereas the QPE-5-1 data shows little rainfall. However, the O-QPF-5-2 data shows several 'downward peaks' in this period, which is due to the movement vectors (in the temporal interpolation process) for the interpolated time steps indicating lower rainfall intensities. This proves the usefulness of optical flow in the temporal interpolation process as O-QPF-5-2 is more accurate in this period and overall. Conversely, in this season, a large peak is seen in the QPE of event 7 i.e. between time steps 30 – 90. Here, L-QPF-5-2 under predicts the observed peak. Though, the movement vectors derived between time steps 30 – 90 of L-QPF-5-2 reflect the magnitude of rainfall intensity realised in the temporal interpolation process. Due to this, the observed peak is highlighted in O-QPF-5-1, which shows the success of the temporal interpolation process.

Another observation from Figures 3.3 – 3.7 is the fluctuations of the O-QPF-5-2 against the L-QPF-5-2. Although this is attributed to the interpolations matching the fluctuations of QPE-5-1 the fluctuations of O-QPF-5-2 could be made 'smoother' by interpolating to higher resolutions (i.e. increase the interpolation from 5-min time steps to, say, 1-min time steps). In practice, this could be achieved using the interpolation methods proposed in this study.

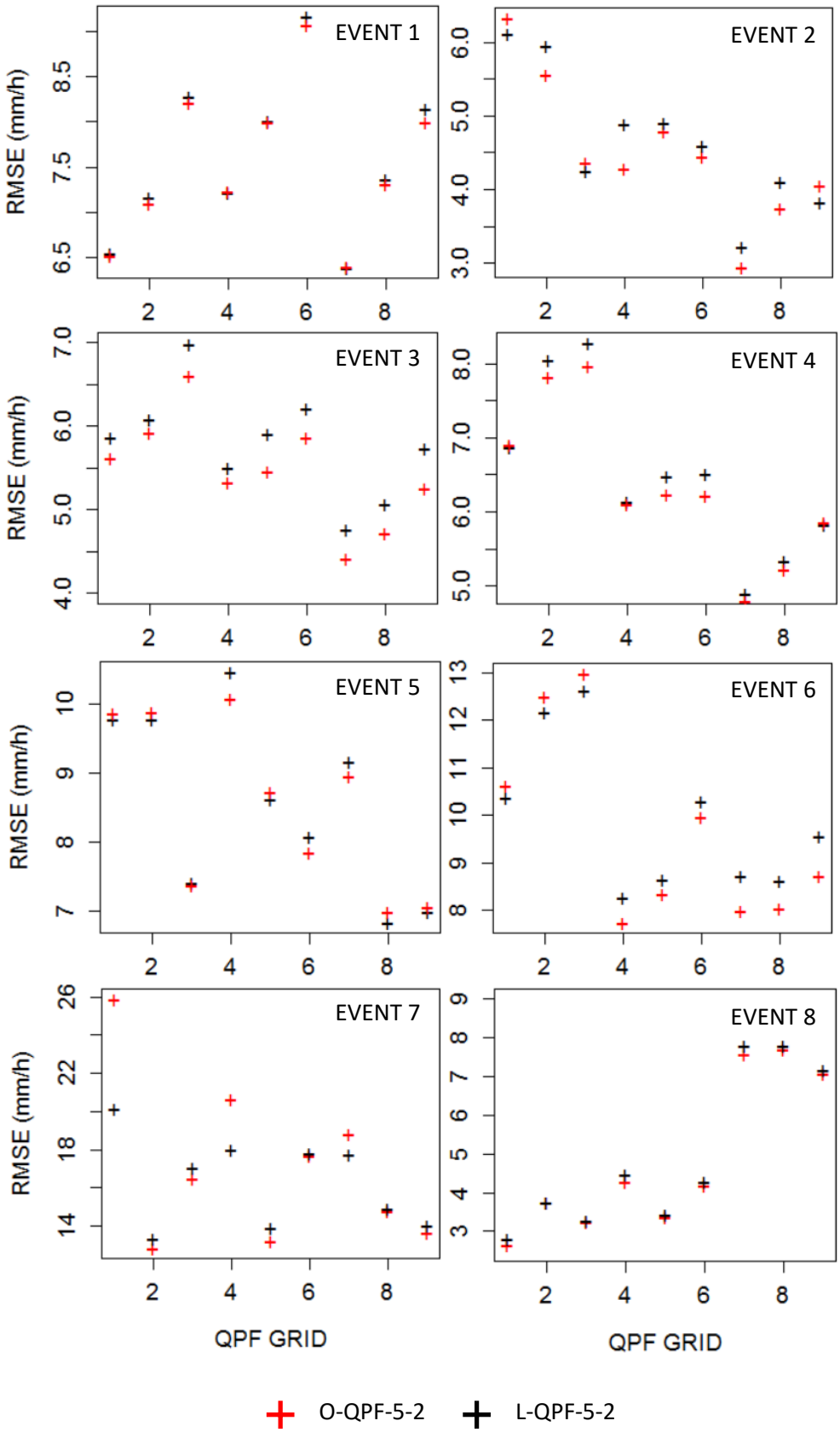

Figure 3.8. Scatter graphs showing the RMSE values of O-QPF-5-2 and L-QPF-15-2 over the six-hour forecast period across all nine QPF grids in the study area for events 1-4 (spring) and events 5 – 8 (summer).

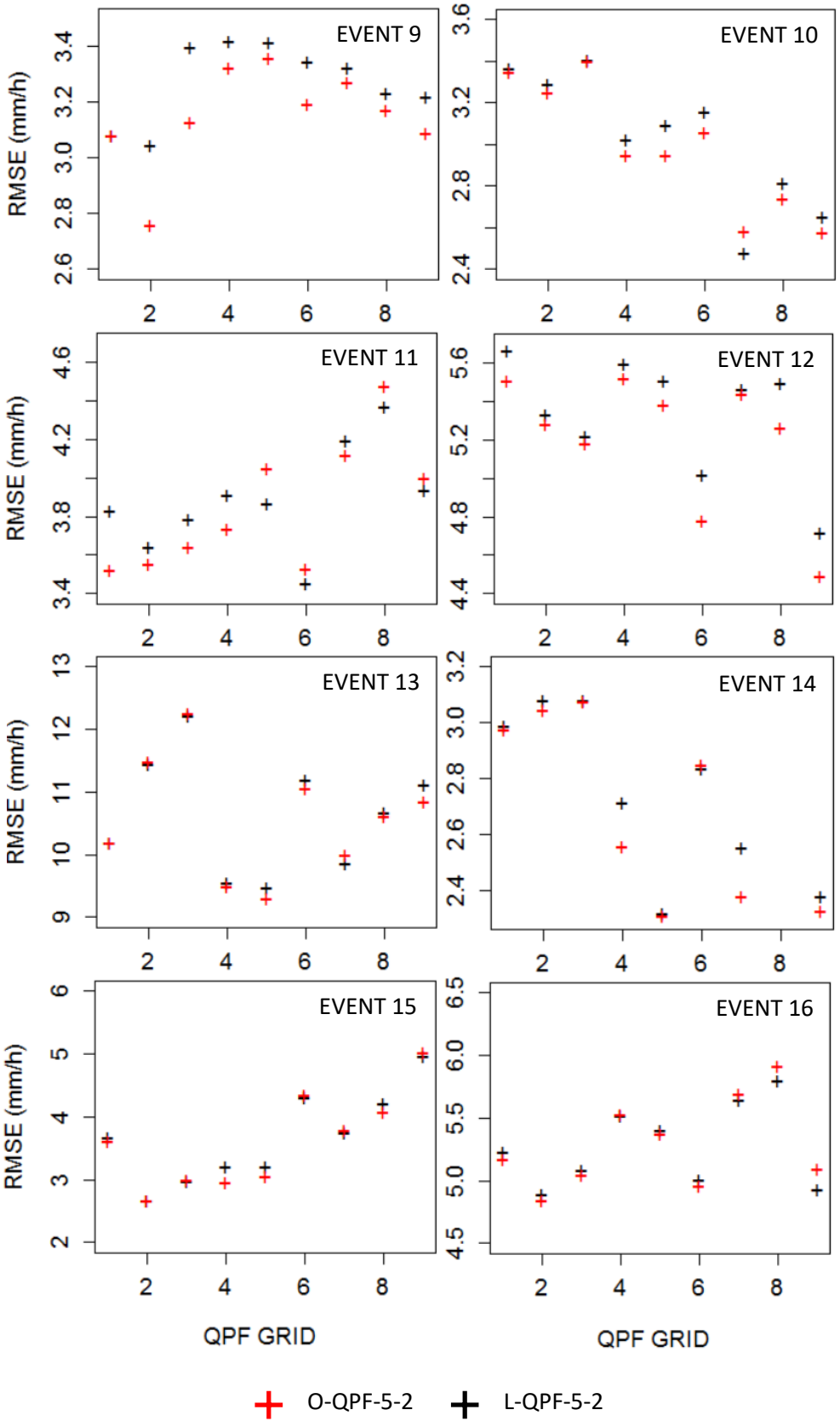

Figure 3.9. Scatter graphs showing the RMSE values of O-QPF-5-2 and L-QPF-15-2 over the six-hour forecast period across all nine QPF grids in the study area for 9 – 12 (autumn) and 13 – 16 (summer).

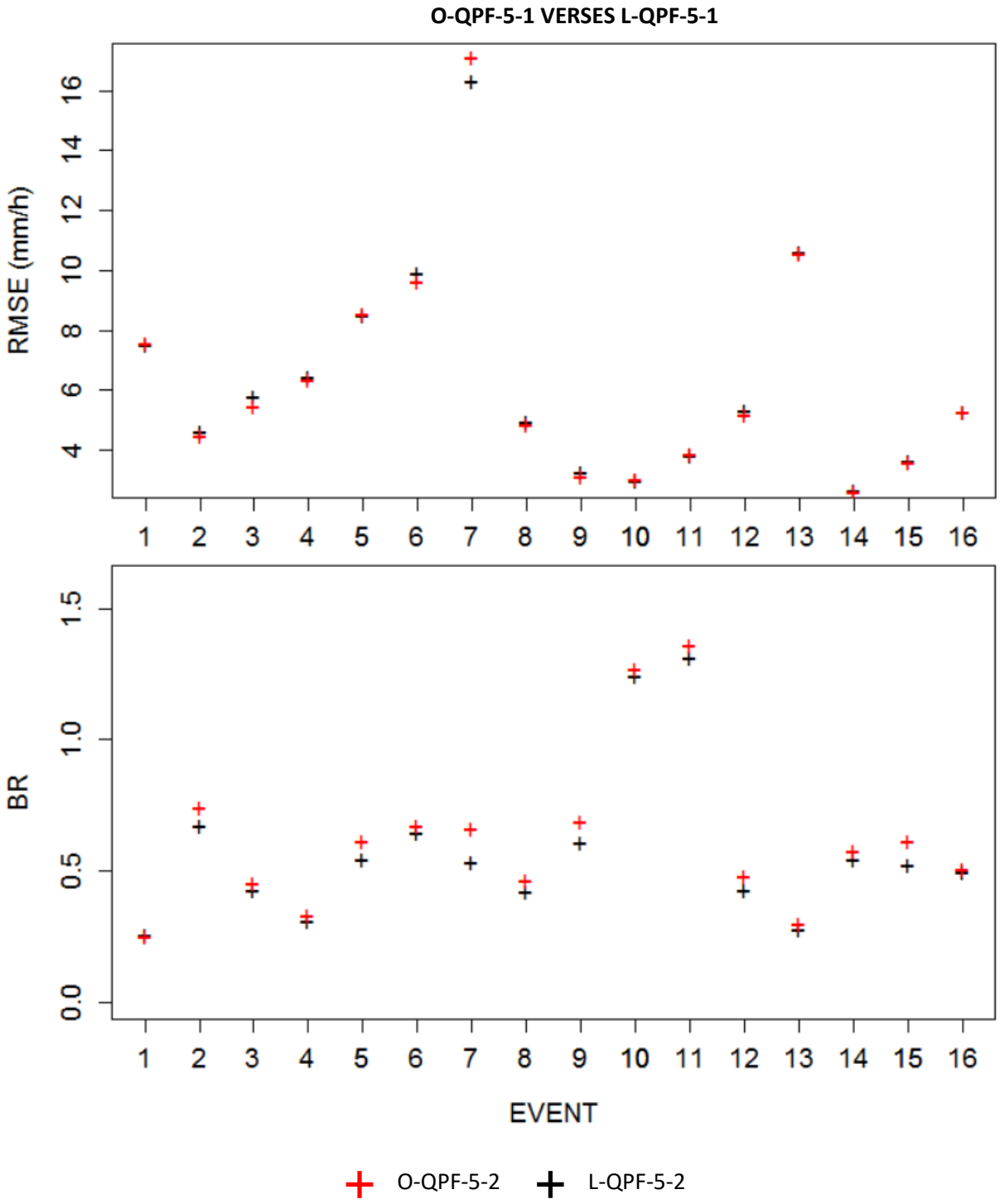

Figure 3.10. Scatter graphs showing the overall RMSE (top) and Bias Ratio (BR) (bottom) values of O-QPF-5-1 and L-QPF-5-1 against coincidental QPE-5-1 data for all verification events 1- 16.

Figure 3.8 and Figure 3.9 show the RMSE values of O-QPF-5-2 and L-QPF-5-1 against coincidental QPE-5-1 data over individual QPF grids in the study area. It

clear that temporal interpolation by optical flow estimation produces more accurate interpolated points in comparison to simple linear temporal interpolation. This is better observed in Figure 3.10 where the nearly all verification show lower RMSE values for O-QPF-5-2. The BR values of OK-QPf-5-2 have increased closer to 1 for all verification except for Events 1, 10 and 11, which show worsening of the overall overestimation/underestimation of the QPF. These events also show marginally worse performance for O-QPF-5-2 in the RMSE values. Worse performance of OK-QPF-5-2 is justified due to the additional interpolated points introduced that may fluctuate more readily than linear approaches. This may introduce higher variance of the data which may produce worse estimates in any temporal period. Linear interpolation introduces smoothing effect between measured points, which reduces variance of the data.

Nonetheless, O-QPF-5-2 is shown to be more accurate than L-QPF-5-2 in this study.

3.4.2 Temporal and spatial interpolated QPF

Visualising OK-QPF-5-1

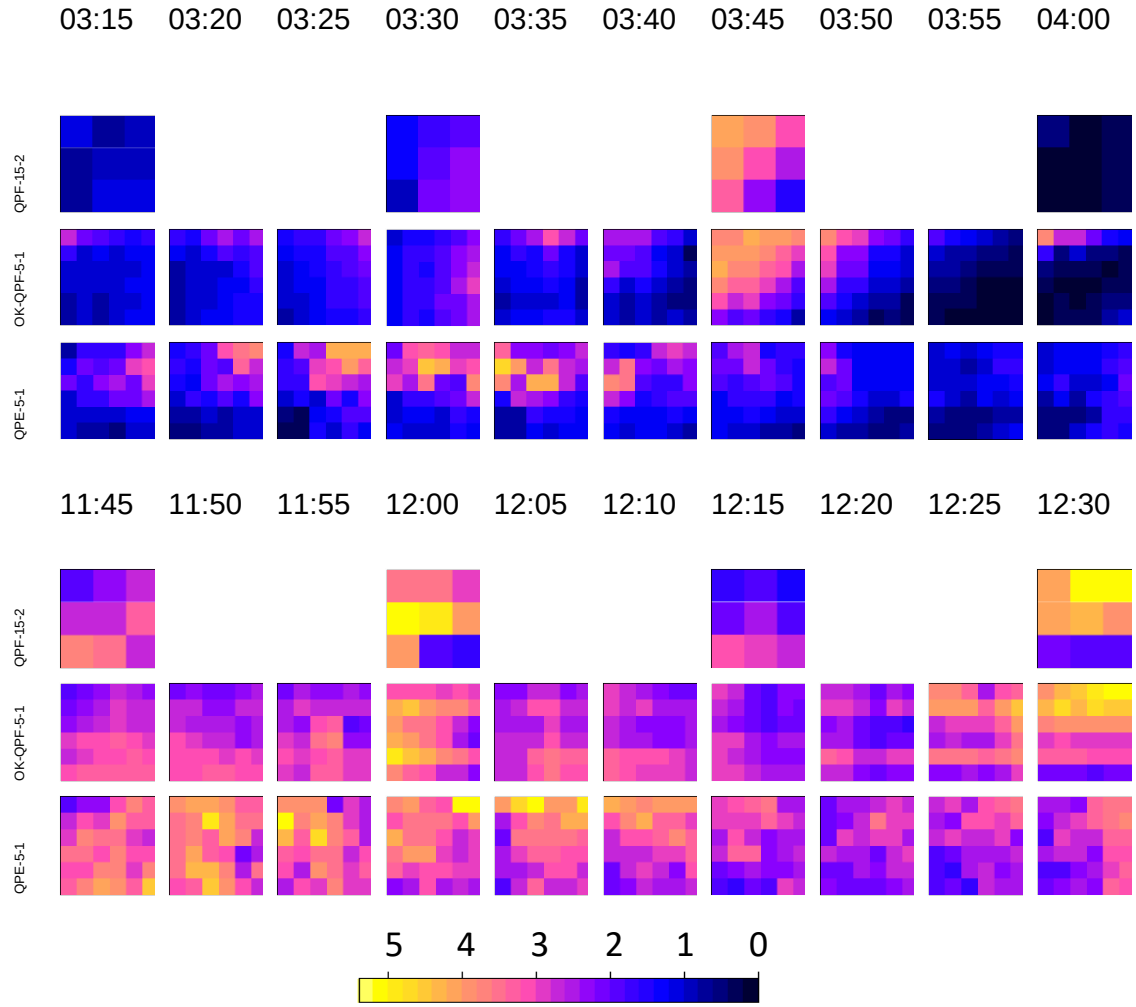

Figure 3.11. Rainfall maps of Event 3 (above) between 03:15 and 04:00 and Event 4 (below) between 11:45 and 12:30 of QPF-15-2, OK-QPF-5-1 and QPE-5-1 (scale is rainfall intensity (mm/h)). These demonstrate the effectiveness of the temporal and spatial interpolation methods.

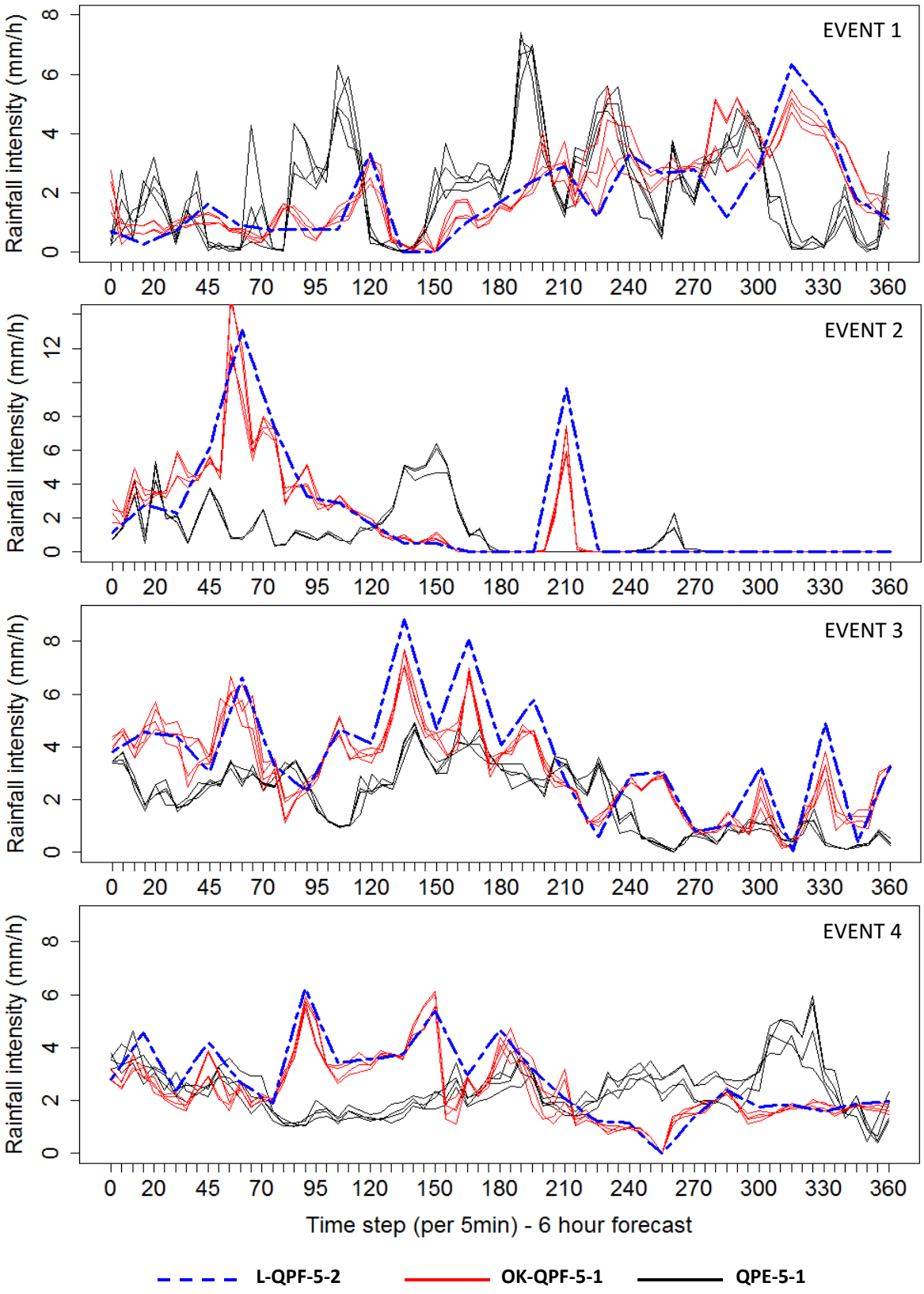

Figure 3.12. Hyetographs showing L-QPF-5-2, four OK-QPF-5-1 and QPE-5-1 data at a selected single QPF grid for spring events 1 - 4.

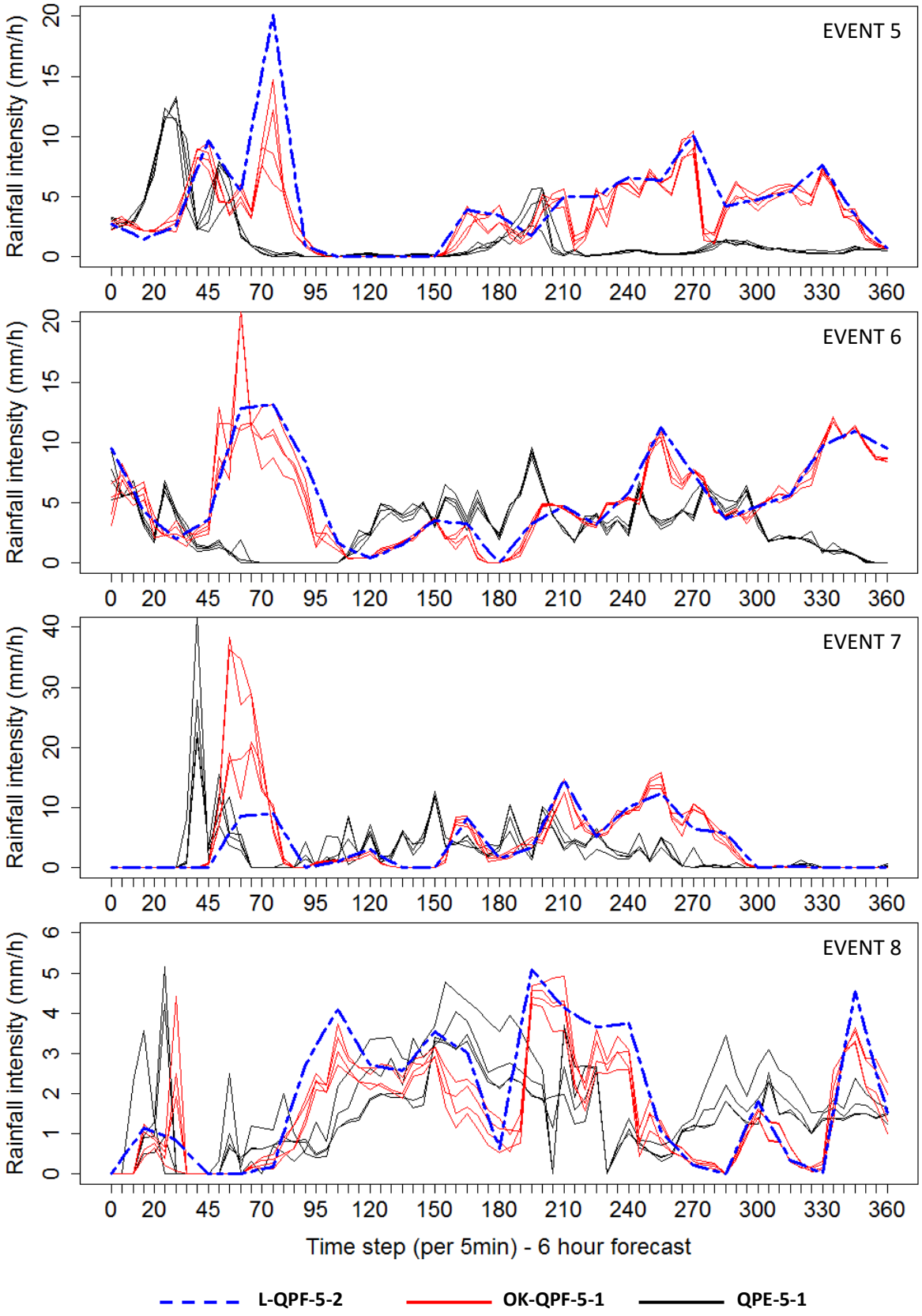

Figure 3.13. Hyetographs showing L-QPF-5-2, four OK-QPF-5-1 and QPE-5-1 data at a selected single QPF grid for summer events 5 - 8.

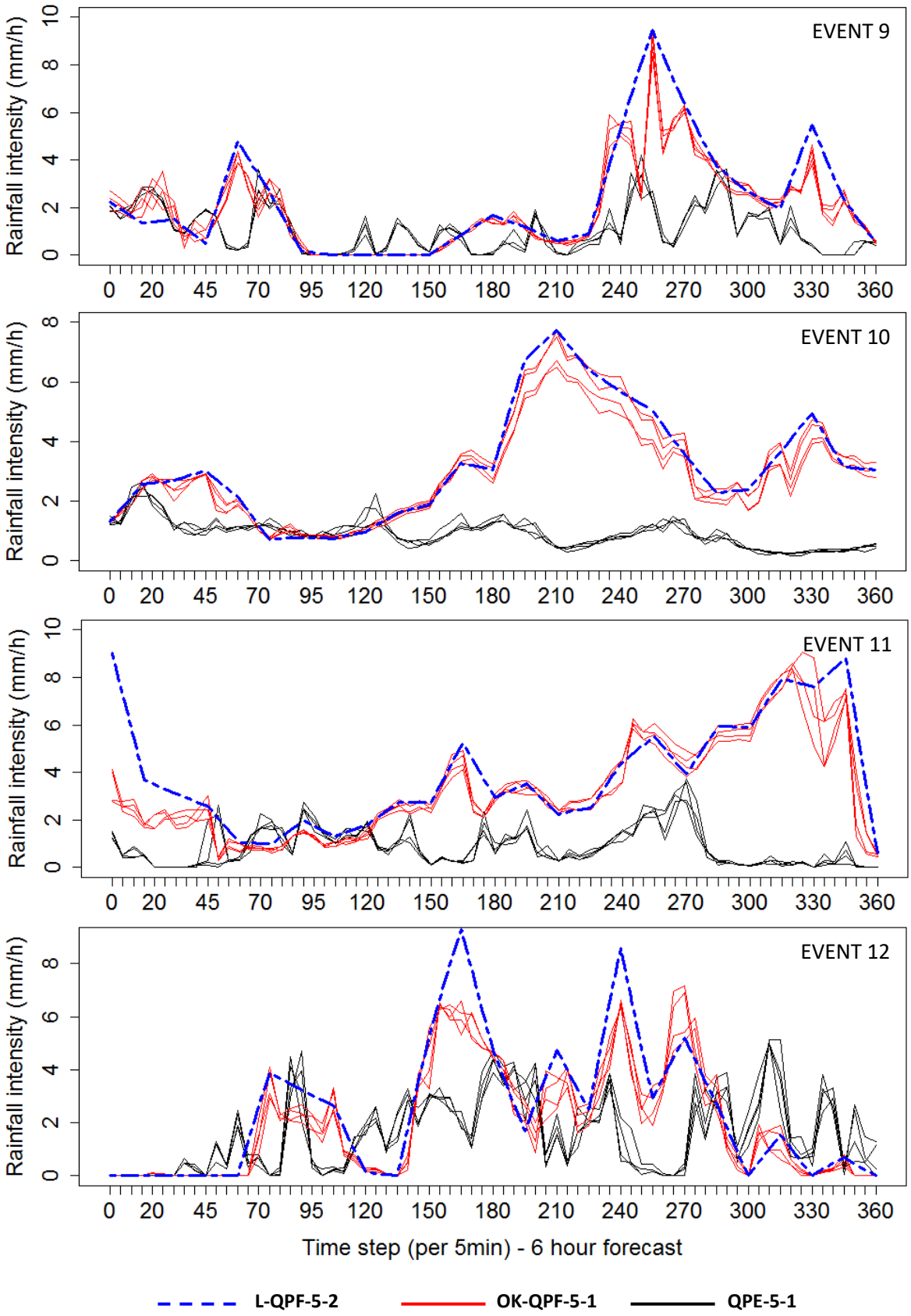

Figure 3.14. Hyetographs showing L-QPF-5-2, four OK-QPF-5-1 and QPE-5-1 data at a selected single QPF grid for autumn events 9 - 12.

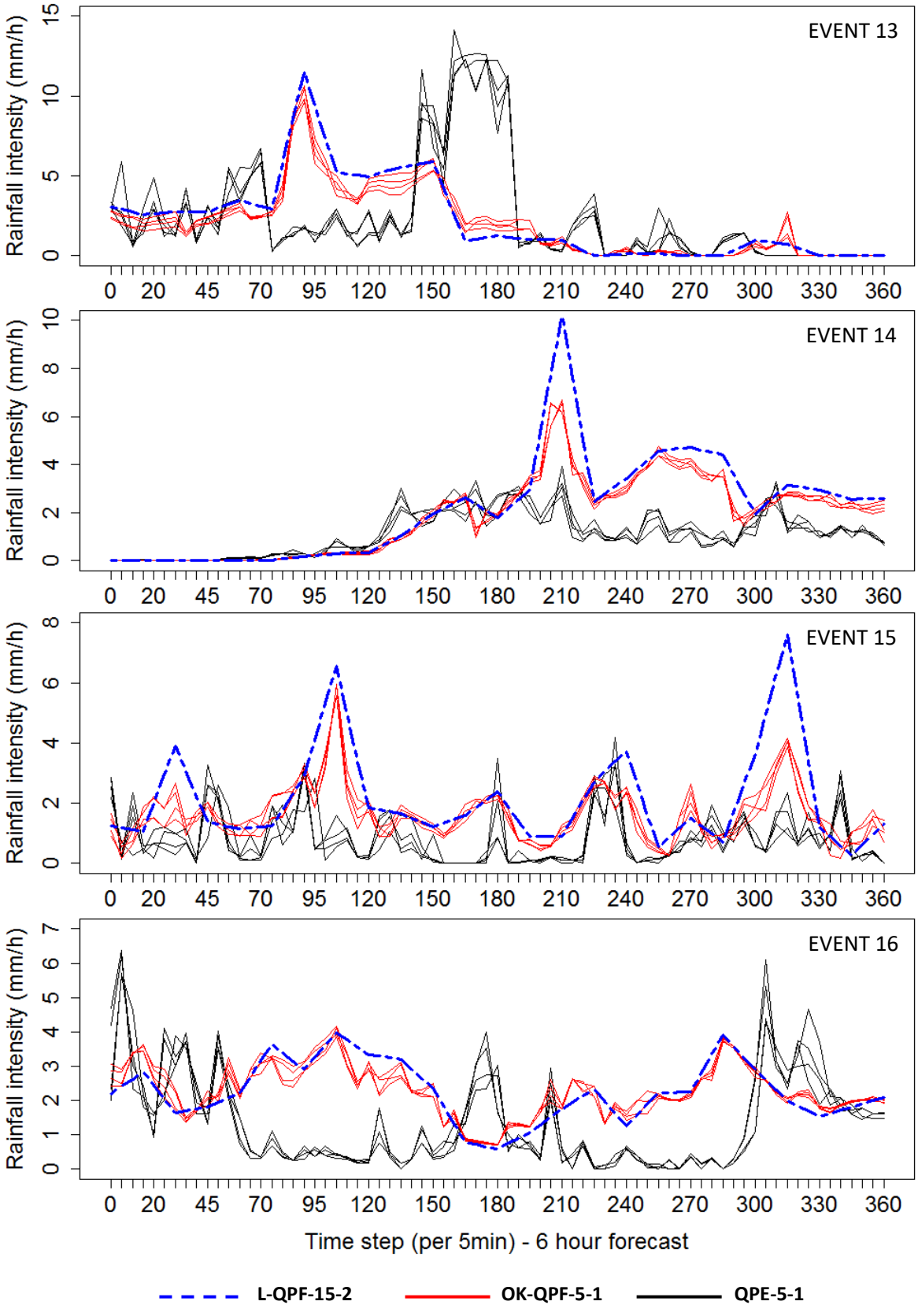

Figure 3.15. Hyetographs showing L-QPF-5-2, four OK-QPF-5-1 and QPE-5-1 data at a selected single QPF grid for winter events 1 - 16.

The outputs of temporal and spatial interpolation of QPF-15-2 are visually demonstrated in the rainfall maps in Figure 3.11 and the hyetographs in Figure 3.15**,** Figure 3.13**,** Figure 3.14 and Figure 3.15. In Figure 3.11, these snapshots of the study area are shown for Events 3 and 4 in a time window of 45 mins. Thus, four rainfall maps are shown for the QPF-15-2 and it shows the rainfall values with its native 2-km spatial resolution. The two events primarily differ in terms of rainfall intensity as Event 4 has generally higher rainfall values. For Event 4, it is seen in QPF-5-1 that the spatial interpolation procedure does reasonably well to produce different values for individual 1-km grids interpolated within the 2-km QPF grid. Particularly, in the rainfall maps at 12:00, the bottom-right region of OK-QPF-5-1 shows heavier rainfall values which more resembles the colour region in the same region of the rainfall map of QPE-5-1. This is despite the bottom-right grid of QPF-15-2 showing lighter rainfall values, which indicates that the spatial interpolation produces more accurate results. This is also seen in the maps of Event 3 between times 03:15 and 03:30 where the interpolation phases show noticeably higher rainfall values in the top region of the study area, whereas the maps of QPF-15-2 don't present this information. The temporally interpolated rainfall maps demonstrate accurate results in terms of capturing similar rainfall values overall in the maps. This is particularly seen in Event 4 at times 12:10 and 12:20. Although, a small number of peaks at QPE grids have not been captured during the temporal interpolation process. This is seen at times 11:50 and 11:55. However, this is a difficult exercise for the interpolation process as further analysis would be required to preserve these types of peaks that usually necessitate a post processing technique coupling with the interpolation method (Wang *et al.*, 2015b). Nonetheless, the temporal interpolation of the QPF has more accurately captured the rainfall patterns at a higher resolution. This is better seen in Figure 3.15**,** Figure 3.13**,** Figure 3.14 and Figure 3.15 where the OK-QPF-5-1 data are visually closer to the QPE-5-1. The interpolation of QPF-15-2 is thus showing more information compared to its lower native temporal and spatial resolutions. This highlights the use of movement vectors in the optical flow technique as these influences the value of the interpolated points. This has particular effect on peaks in L-QPF-5-2 as these are lowered towards QPE-5-1 (time steps 110 to 200 in Event 3, time steps 210 to 285 in Event 5 and time steps 240 to 290 in Event 9).

OK-QPF-5-1 verses LS-QPF-5-1

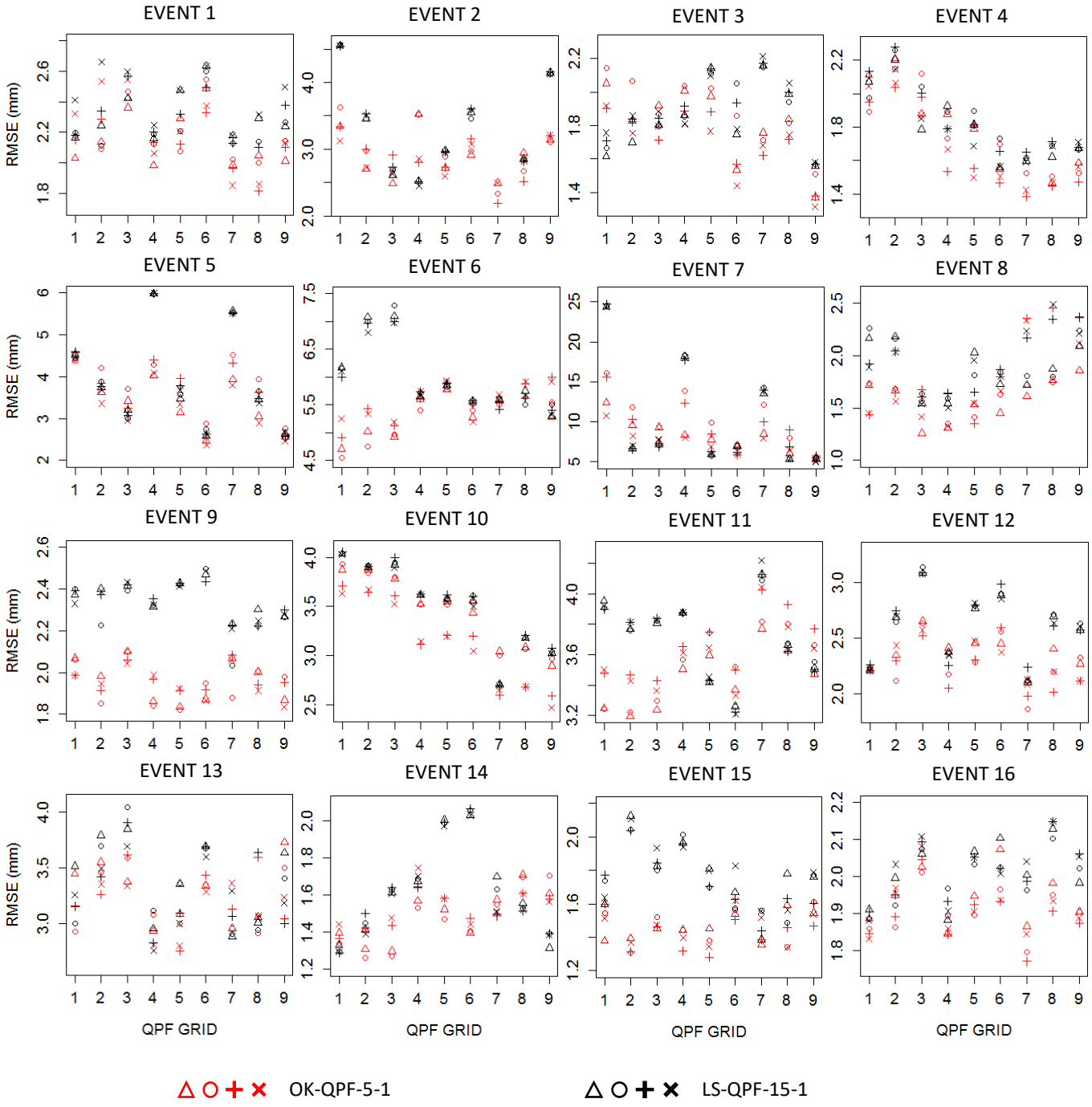

Figure 3.16. Scatter graphs showing the RMSE values of OK-QPF-5-1 and LS-QPF-5-1 over the six-hour forecast period across all the QPF grids in the study area for events 1-4 (spring), 5-8 (summer), 9-12 (autumn) and 13-16 (winter).

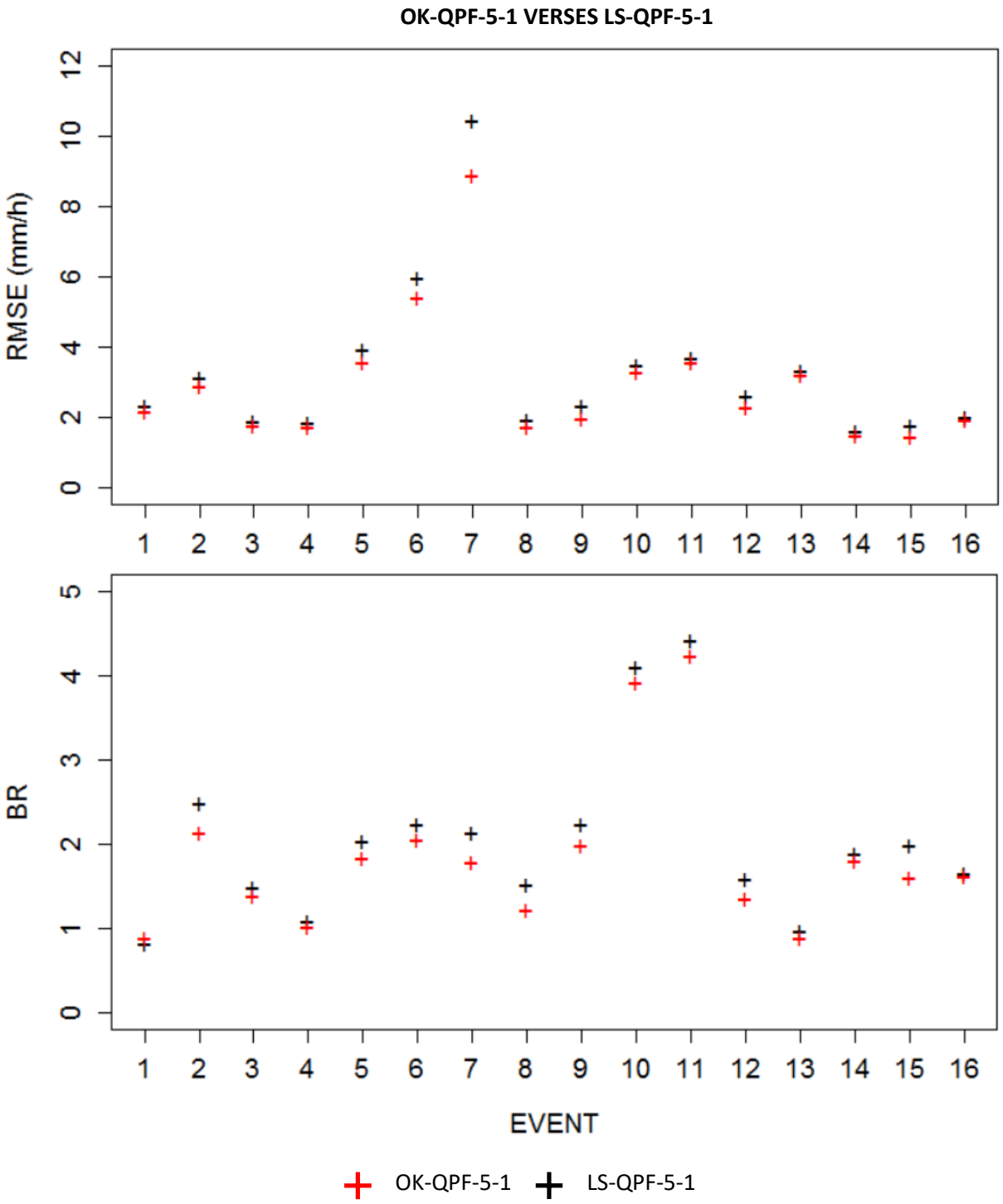

Figure 3.17. Scatter graphs showing the overall RMSE (top) and Bias Ratio (BR) (bottom) values of OK-QPF-5-1 and LS-QPF-5-1 against coincidental QPE-5-1 data for all verification events 1- 16.

Figure 3.16 shows the accuracy of the spatial interpolation of QPF-15-2. These show RMSE values of OK-QPF-5-1 and LS-QPF-5-1 against QPE-5-1 over the

six-hour forecast period over the individual QPF grids in the study area. Figure 3.16 and Figure 3.17 show that OK-QPF-5-1 is generally more accurate than LS-QPF-5-1. Overall, the average RMSE value across all 16 events has reduced by 8.86% from 3.27 mm to 2.95 mm. To compare the performances of the RMSE reduction over different seasons, it would require analysis of many events per season. This is due to various anomalies including highly spatially varied events or events that show extremely high peaks, which may produce a notably large reduction in the RMSE values for any season. Hence, this may not produce realistic comparisons. This is actually seen in Event 7 (summer) where the first QPF grid shows huge bias between the QPF and QPE values due to a very large peak in time steps 30 - 65. The RMSE for OK-QPF-5-1 at this location for this event has reduced by nearly 10 mm, which is the largest reduction compared to other events. Therefore, a broader performance between the warmer (spring and summer) and cooler (autumn and winter) seasons of the year is considered which includes more events per category (8 events). The average reduction of Events 1 – 8 (spring and summer) is 8.74% whereas the average reduction of Event 9 – 16 (autumn and winter) is 8.98%. By removing Event 7 (i.e. the only anomalous event in terms of magnitude of reduction of RMSE values), the average reduction of Events 1 – 8 reduces to 8.08%. Hence, based on this analysis, it is concluded that OK-QPF-5-1 performs marginally better for rainfall events in the cooler periods of the year. Reasons for this include that there is less spatial variation in this period, which makes interpolating points more accurate.

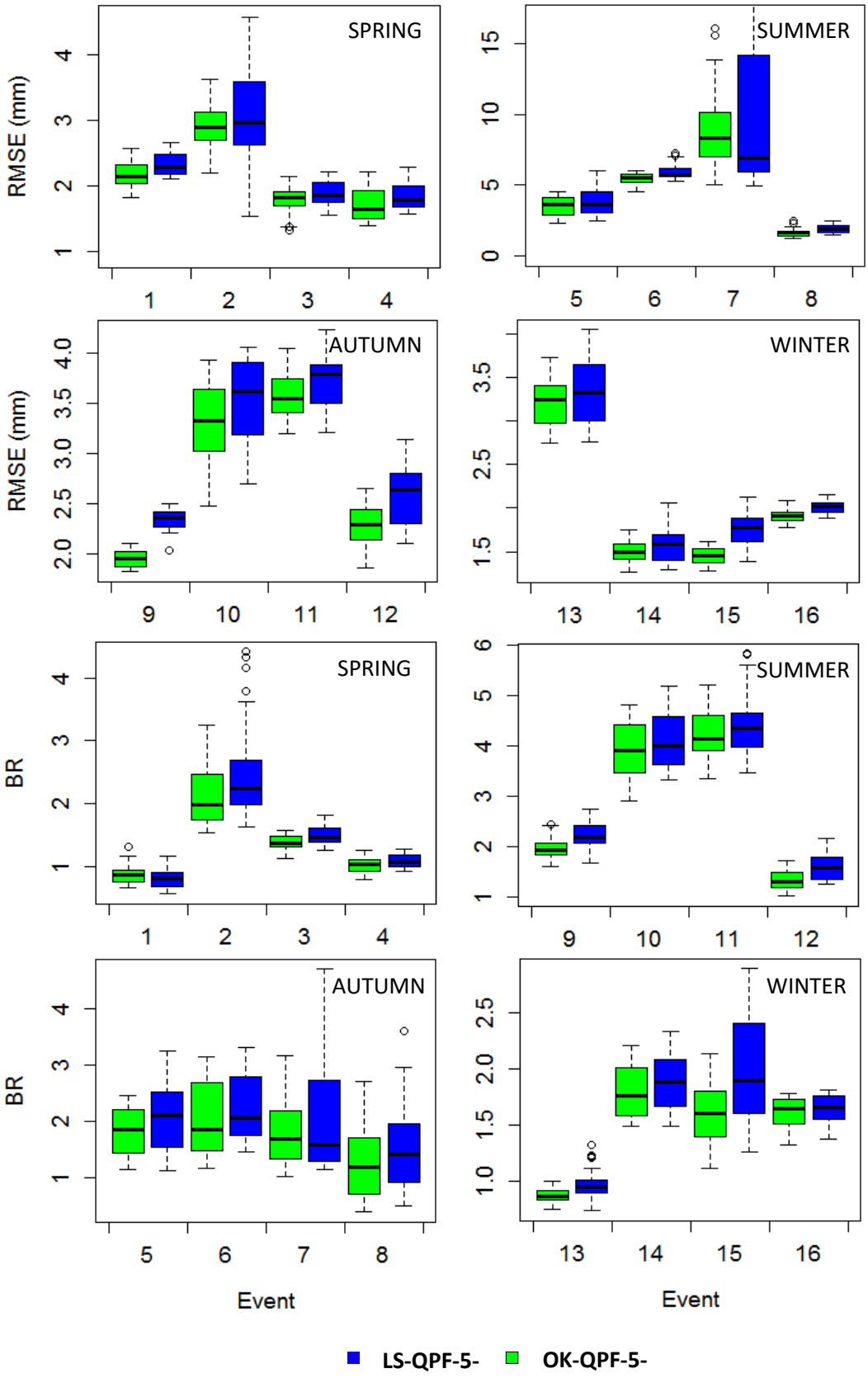

Figure 3.18. Boxplots of the RMSE and Bias Ratio (BR) of OK-QPF-5-1 and LS-QPF-5-2 across the six-hour forecast period over the 36 km² (6 x 6 km²) region for all 16 verification events (four seasons).

Figure 3.18 provides another visualisation demonstrating the accuracy of OK-QPF-5-1. The RMSE and BR values are shown for OK-QPF-5-1 and LS-QPF-5-1 across the entire 36 km^2 (6 x 6 km^2) study area (i.e. all data from the 36 grids are included as members of the boxplots).

The RMSE and BR values for nearly all of the events show improvement for OK-QPF-5-1 and therefore OK-QPF-5-1 is more accurate than LS-QPF-5-1 overall. The only event whose RMSE value is worse is event 7 (summer). This is due to the large peak seen in the QPE of this event and although the OK-QPF-5-1 has highlighted the peak, some QPF grids in the study area for this event show a temporal 'lag', which means that the peak is shown at a later time step. This would produce inaccurate results when comparing the data sets on a temporal scale, hence showing worse RMSE scores. This anomaly could be studied closely as further work which requires further analysis of the temporal interpolation process. However, despite the median RMSE value for this event being worse, the interquartile range has decreased. This highlights the success of the spatial interpolation because the four data points are each closer to the coincidental QPE data compared to the LS-QPF-5-1.

Where RMSE/BR values are worse for OK-QPF-5-1, in the low likelihood that optical flow shows a peak that linear interpolation is unable to show, occasionally, the peak might be very large in comparison to the observed data. In this case, the linear interpolated value may be closer to the observed value in comparison to the peak. But this is not to say that overall linear interpolation is a better approach than optical flow, especially when this is seen in just a small number of events (e.g. Event 7 and 13).

To briefly summarise this section, OK-QPF-5-1 is more accurate than LS-QPF-5-1. Therefore the methods presented in this chapter are recommended over simple linear temporal interpolation and spatially aggregating 2-km values to four 1-km values.

OK-QPF-5-1 verses OI-QPF-5-1

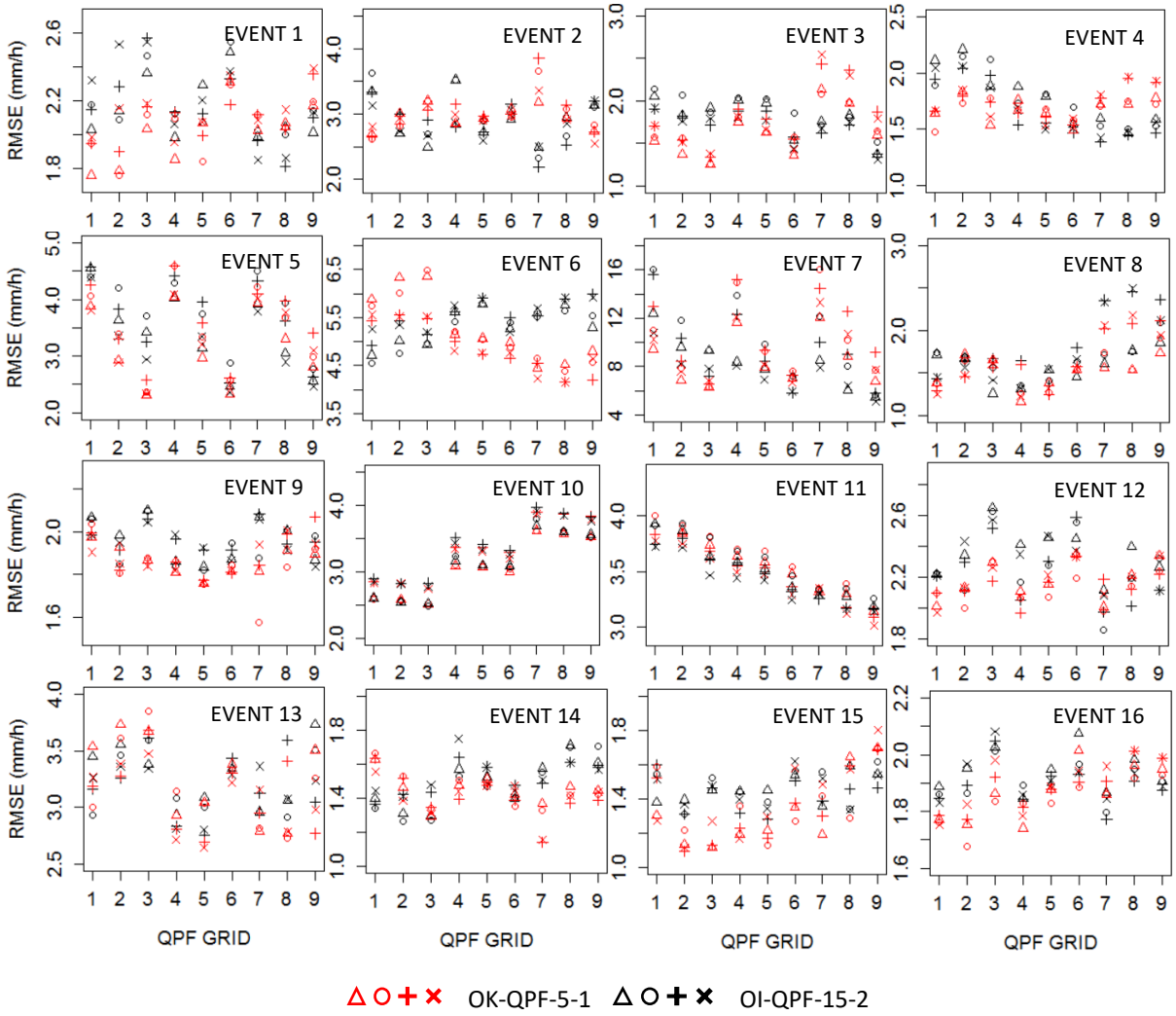

Figure 3.19. Scatter graphs showing the RMSE values of OK-QPF-5-1 and OI-QPF-5-1 over the six-hour forecast period across all the QPF grids in the study area for events 1-4 (spring), 5-8 (summer), 9-12 (autumn) and 13-16 (winter).

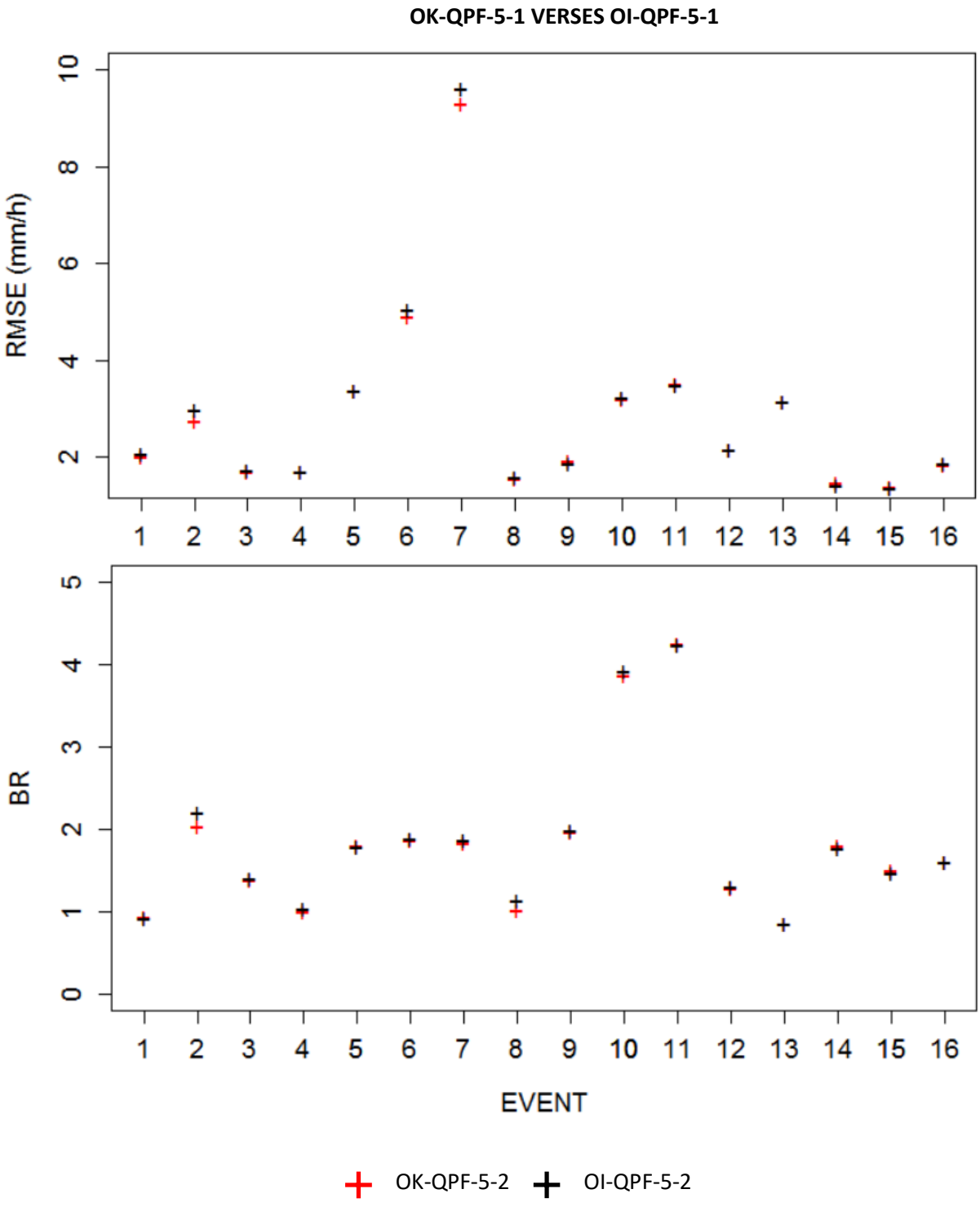

Figure 3.20. Scatter graphs showing the overall RMSE (top) and Bias Ratio (BR) (bottom) values of OK-QPF-5-1 and OI-QPF-5-1 against coincidental QPE-5-1 data for all verification events 1- 16.

Figure 3.19 and Figure 3.20 show comparisons of the RMSE and BR values of OK-QPF-5-1 and OI-QPF-5-1 for all the validation events. As two different spatial interpolation techniques follow a dataset that has been temporally interpolated

using the same technique (i.e. via optical flow estimation), this comparison directly compares the performance between UKR and IDW. Figure 3.19 shows the performance of OK-QPF-5-1 over individual 1-km grids over the study area. Based on this figure, differences between spatial interpolation by UKR is distinguished between the performance of IDW. For some grids, OK-QPF-5-1 performs worse. Some of these worse performing grid locations are clustered in a particular region of the study area. For example, in Event 4 and 10, OK-QPF-5-1 performs better for the top region of the study area (i.e. grids 1,2 and 3) and gradually perform worse for regions near the bottom of the study area (i.e. grids 7,8 and 9). The opposite trend is observed in Event 11 (i.e. better performing grid locations near the bottom of study area). Reasons for this include that the variogram generated for UKR may require more data points near worse performing grid locations to better represent the uncertainties in interpolated points. It just so happens that at these worse performing grids locations, the simple spatial interpolation method, IDW, has produced better estimates direct usage of the measured rainfall intensities around the interpolated points. Nonetheless, overall, nearly all 16 verification events show that OK-QPF-5-1 is more accurate than OI-QPF-5-1. This is observed in the RMSE and BR values in Figure 3.20, which also show that spatial interpolation by UKR is better at reducing the overall overestimation/underestimation of the QPF than IDW.

However, the performance differences between OK-QPF-5-1 and OI-QPF-5-1 is small. The average improvement of RMSE values of OK-QPF-5-1 over OI-QPF-5-1 across all 16 verification events is 1.38%. For events in the cool seasons (Events 1 – 8), this figure is higher at 1.59% and lower for events in the warm seasons (Events 9 – 16) at 1.17%. This shows that based on the case study used, the performance of UKR is marginally better than IDW.

OK-QPF-5-1 verses LI-QPF-5-1

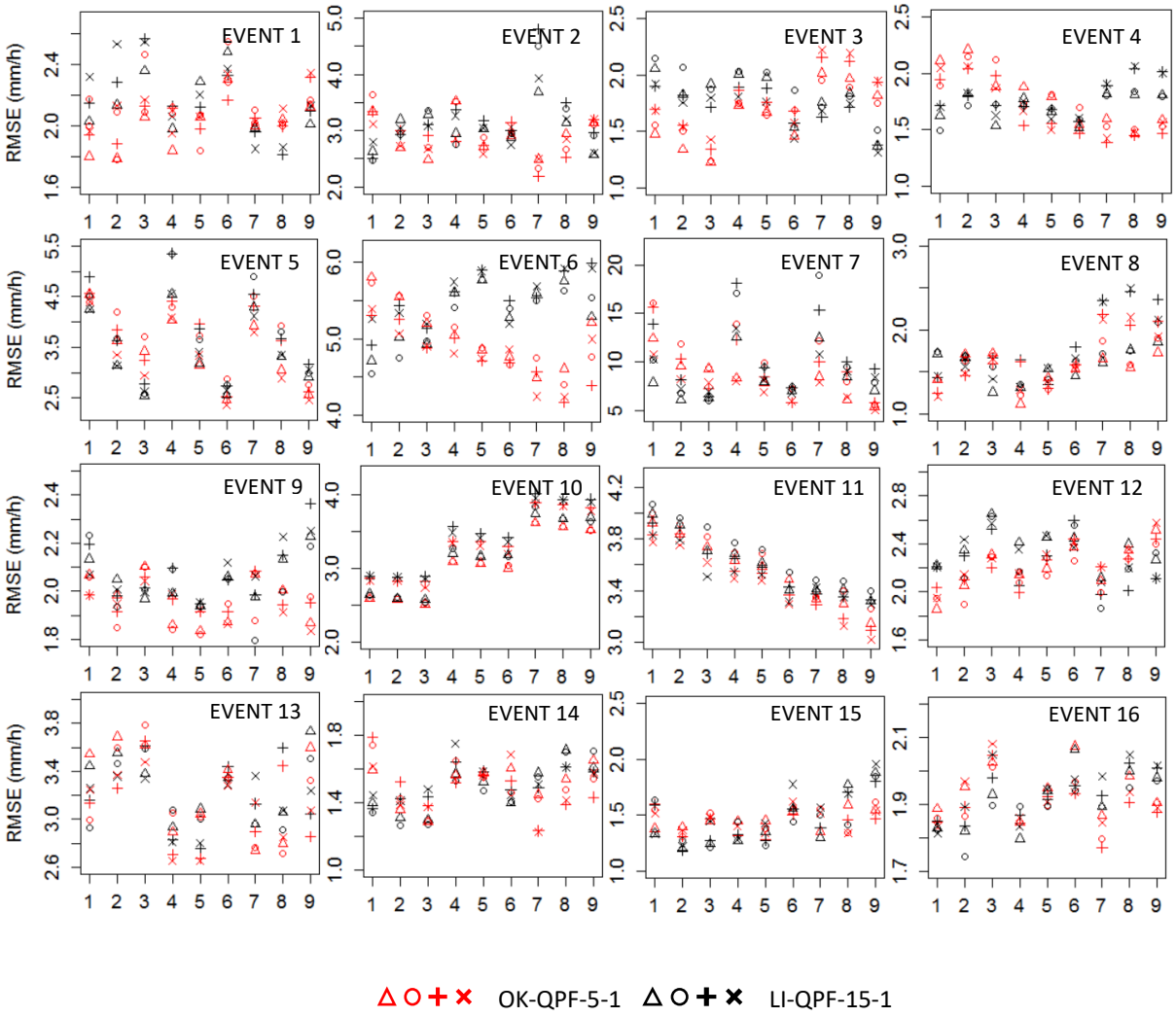

Figure 3.21. Scatter graphs showing the RMSE values of OK-QPF-5-1 and LI-QPF-5-1 over the six-hour forecast period across all the QPF grids in the study area for events 1-4 (spring), 5-8 (summer), 9-12 (autumn) and 13-16 (winter).

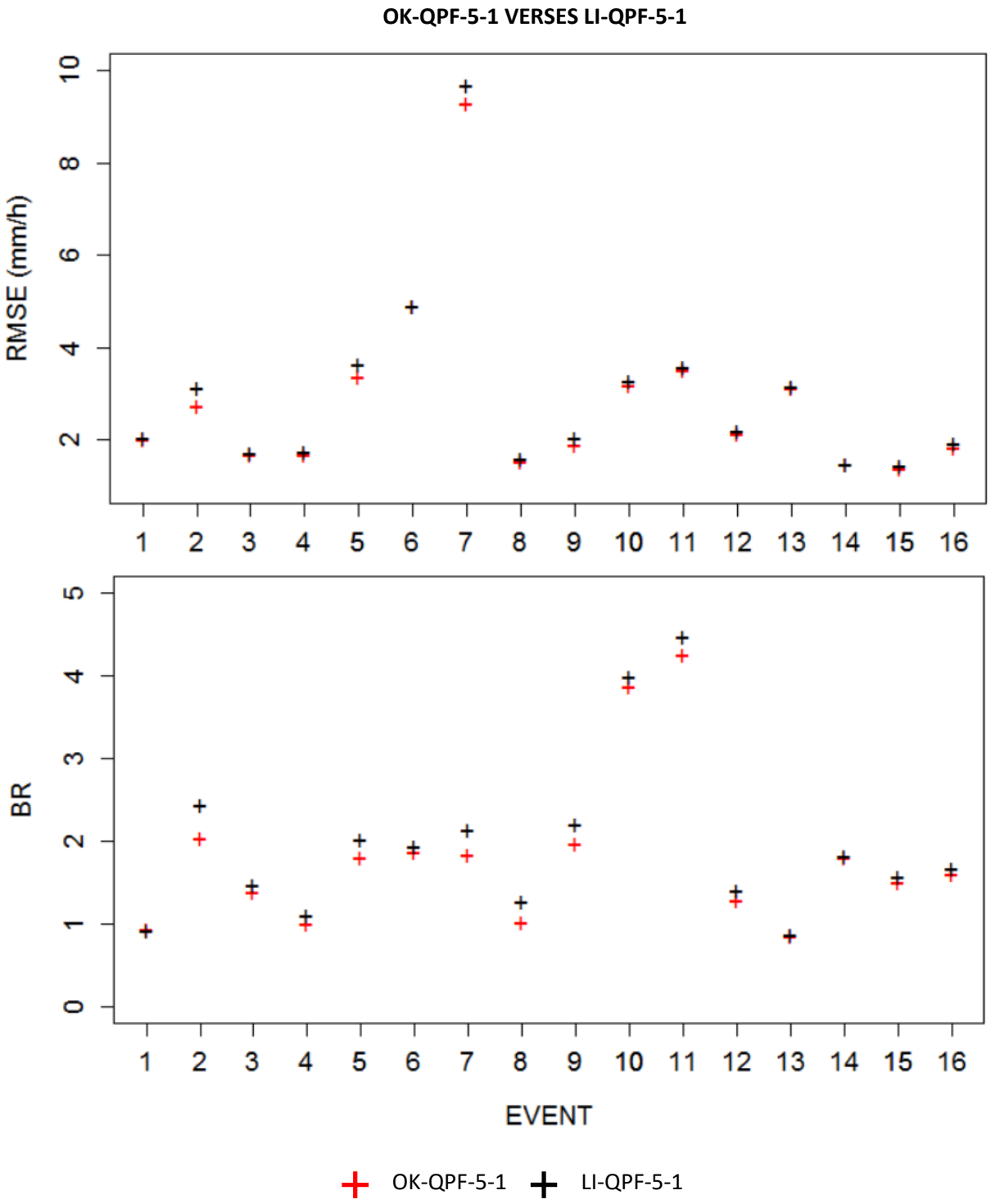

Figure 3.22. Scatter graphs showing the overall RMSE (top) and Bias Ratio (BR) (bottom) values of OK-QPF-5-1 and LI-QPF-5-1 against coincidental QPE-5-1 data for all verification events 1- 16.

Figure 3.21 and Figure 3.22 show comparisons between OK-QPF-5-1 and LI-QPF-5-1. Figure 3.21 shows the RMSE values at individual 1-km grids in the study area and Figure 3.22 shows the average RMSE and BR values of all 16

verification events. The two QPF data used in this comparison have different temporal and spatial interpolation methods applied. It has been shown that temporal interpolation by optical flow estimation performs better than simple linear temporal interpolation (see *O-QPF-5-2 verses L-QPF-5-2*). It has also been shown that UKR performs better than IDW for spatial interpolation of O-QPF-5-2 (see *OK-QPF-5-1 verses OI-QPF-5-1*). Therefore, it is expected that OK-QPF-5-1 performs better than LI-QPF-5-1. This is clearly observed in Figure 3.22 where OK-QPF-5-1 outperforms LI-QPF-5-1 in all 16 verification events. The overall RMSE value of OK-QPF-5-1 across the verification events has been reduced by 4.58% - this is higher for events in the cool seasons (Events 1 – 8) with a reduction of 5.15% and lower for events in the warm seasons (Events 9 – 16) with a reduction 4.01%.

This confirms that temporal interpolation by optical flow and spatial interpolation by UKR is recommended for producing more accurate higher resolution QPFs in comparison to simple linear temporal interpolation and spatial interpolation by IDW.

OK-QPF-5-1 verses LK-QPF-5-1

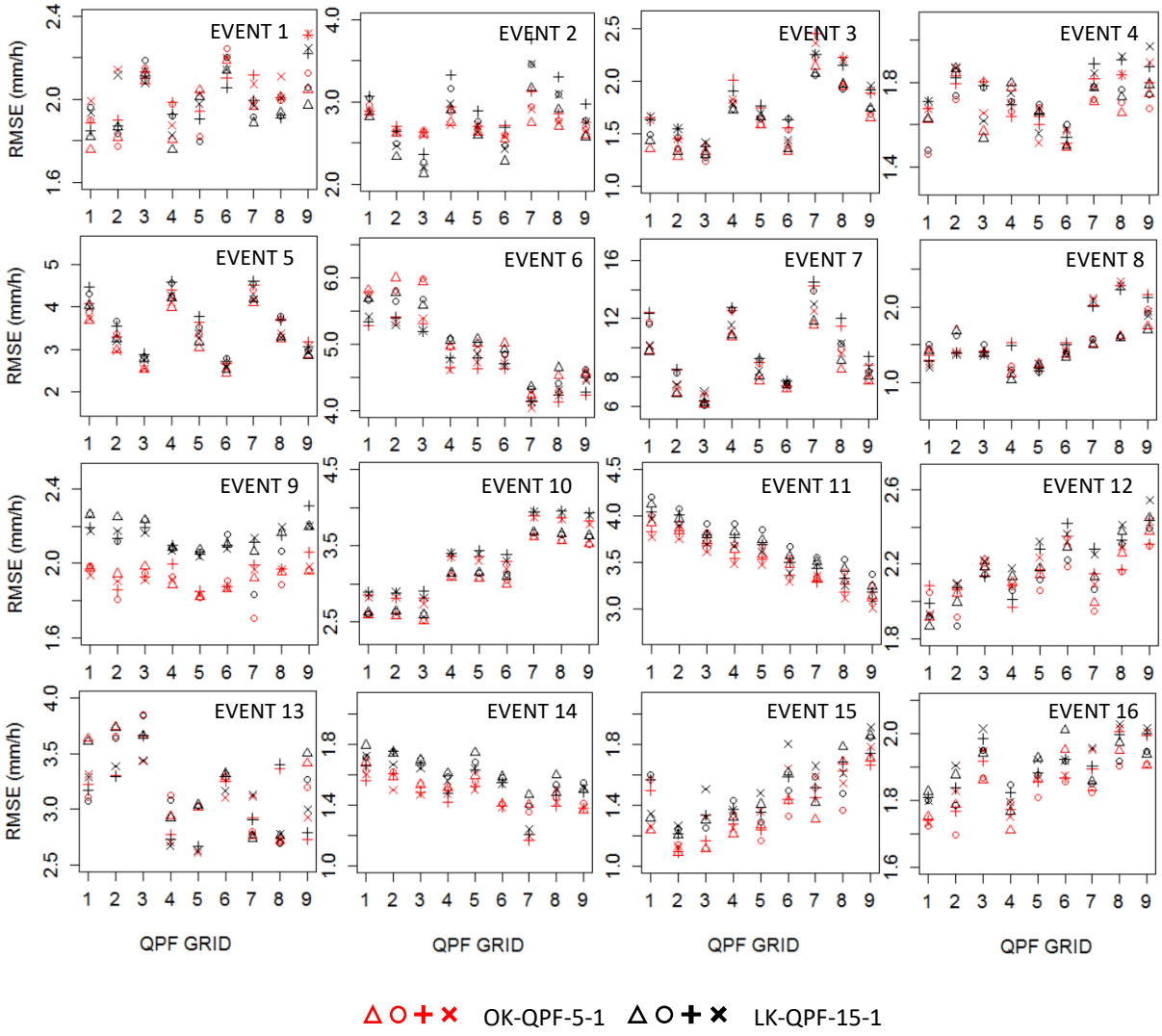

Figure 3.23. Scatter graphs showing the RMSE values of OK-QPF-5-1 and LK-QPF-5-1 over the six-hour forecast period across all the QPF grids in the study area for events 1-4 (spring), 5-8 (summer), 9-12 (autumn) and 13-16 (winter).

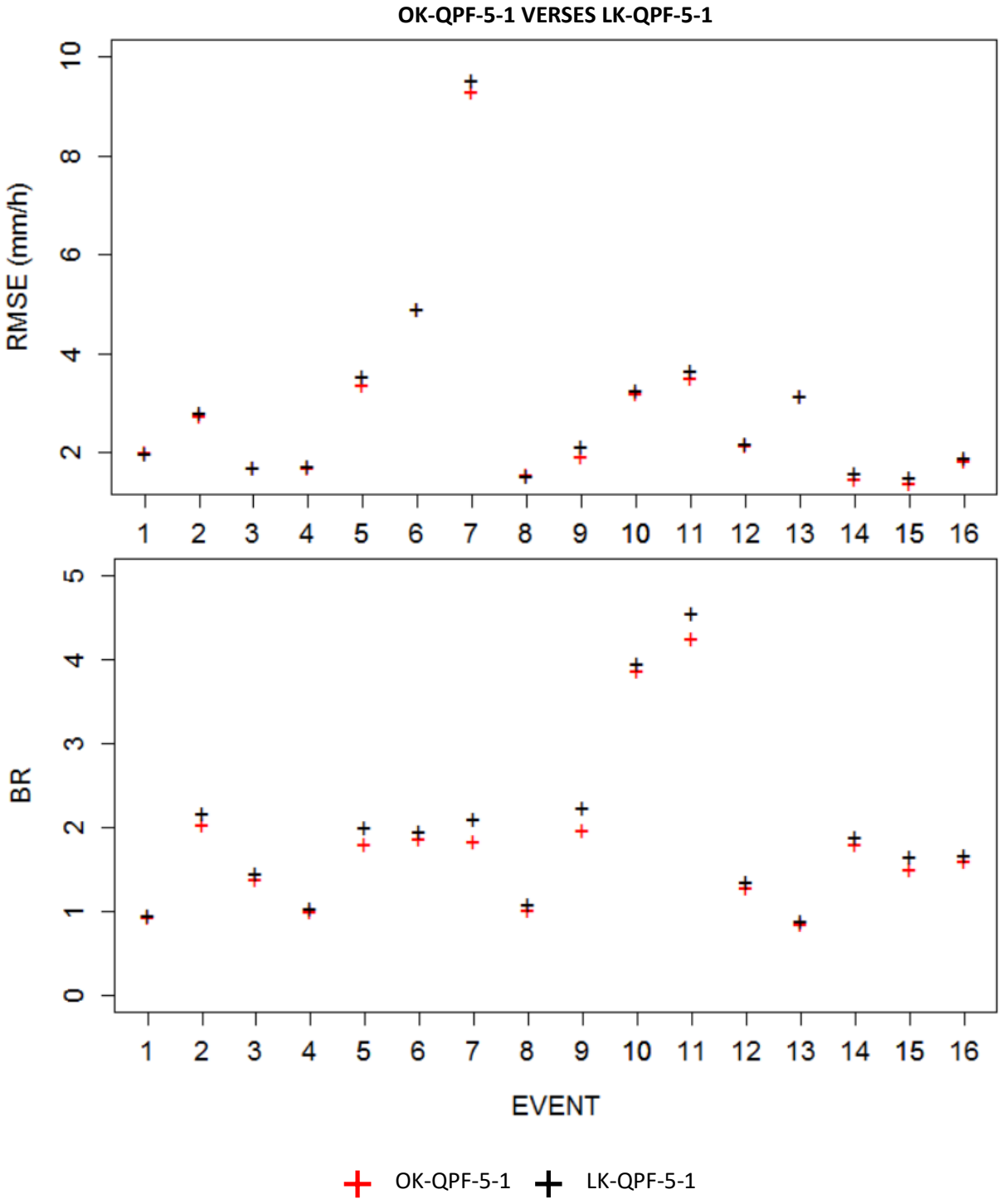

Figure 3.24. Scatter graphs showing the overall RMSE (top) and Bias Ratio (BR) (bottom) values of OK-QPF-5-1 and LK-QPF-5-1 against coincidental QPE-5-1 data for all verification events 1- 16.

Figure 3.24 Shows RMSE and BR values of OK-QPF-5-1 and LK-QPF-5-1 against coincidental QPE-5-1 data. Particularly, this analysis draws comparison between the temporal interpolation techniques. This is because the two different

temporal interpolation techniques are followed with the same spatial interpolation technique (i.e. UKR spatial interpolation). Similar analysis could be conducted for OI-QPF-5-1 and LI-PF-5-1. However, it is sufficient to show comparisons for one of them as O-QPF-5-2 and L-QPF-5-2 have already been compared. Based on a previous comparison of the two temporal interpolation techniques, temporal interpolation by optical flow estimation showed to outperform simple linear temporal interpolation. Figure 3.24 supports this result as OK-QP-5-1 outperforms LK-QPF-5-1 with lower RMSE values and better BR values that suggest that OK-QPF-5-1 is better at reducing the overestimation/underestimation of the QPF against the QPE.

The overall RMSE value of OK-QPF-5-1 across the verification events has been reduced by 2.56% - this is higher for events in the cool seasons (Events 1 – 8) with a reduction of 2.81% and lower for events in the warm seasons (Events 9 – 16) with a reduction 2.31%.

Table 3.2. Summary of average RMSE and BR values over all 16 verification events, against coincidental QPE-5-1 data, of each QPF data listed in Table 3.1

	O-QPF-5-2	L-QPF-5-2	OK-QPF-5-1	OI-QPF-5-1	LK-QPF-5-1	LI-QPF-5-1	LS-QPF-5-1
RMSE (mm/h)	**6.37**	**6.35**	**2.87**	**2.92**	**2.95**	**2.99**	**3.27**
BR	**0.64**	**0.58**	**1.81**	**1.84**	**1.93**	**1.96**	**2.04**

Table 3.2 shows a summary of all the RMSE and BR values derived from this study. This draws comparisons between each QPF data other than comparisons with OK-QPF-5-1. Furthermore, Figure 3.25 shows the RMSE and BR values for OK-QPF-5-1, OI-QPF-5-1, LK-QPF-5-1 and LI-QPF-5-1 summarised in one figure.

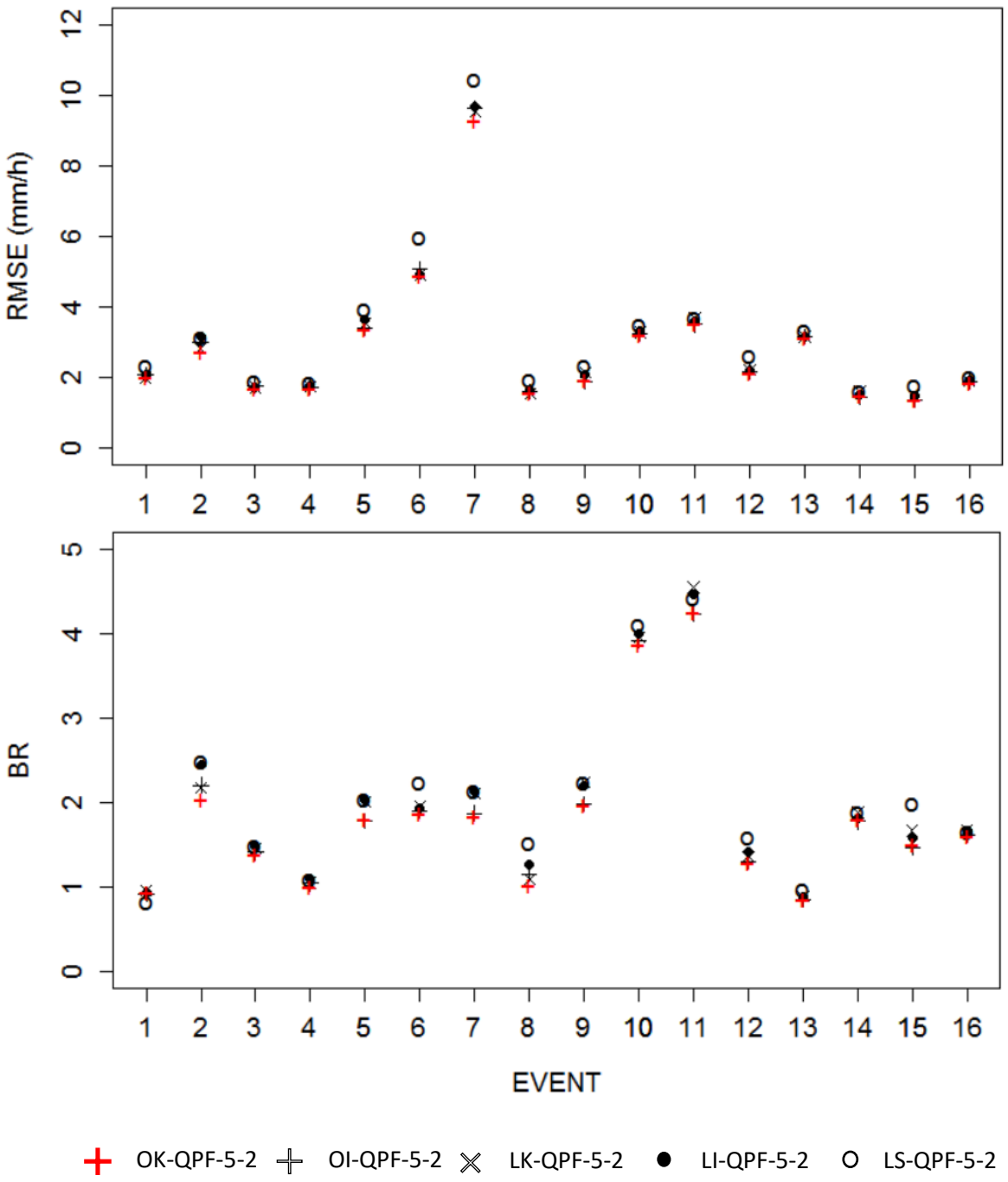

Figure 3.25. Scatter graphs showing the overall RMSE (top) and Bias Ratio (BR) (bottom) values of OK-QPF-5-1, OI-QPF-5-1, LK-QPF-5-1 and LI-QPF-5-1 against coincidental QPE-5-1 data for all verification events 1- 16.

3.5 Summary and conclusions

In this chapter, an interpolation process involving temporal and spatial interpolation has been developed to improve radar-based QPFs. This process was tested on NIMROD based Nowcast QPFs for the North-East England. 16 verification events across four meteorological seasons are obtained between June 2016 and May 2017 to validate the interpolation process of this study. These verification events are temporally interpolated using optical flow and then spatially interpolated using UKR. Comparisons are made with simple temporal and spatial interpolation approaches to validate the methodology. The following conclusions can be drawn from the case study:

- Across all the verification events, the RMSE values against the QPE of the temporally and spatially interpolated QPF against QPF data that had been interpolated temporally by linear methods and spatially by parting have reduced by 8.74% in warm periods and 8.98% in cool periods.
- Across all the verification events, the RMSE values against the QPE of the temporally and spatially interpolated QPF against QPF data that had been interpolated temporally by linear methods and spatially by IDW have reduced by 4.01% in warm periods and 5.15% in cool periods.
- Across all the verification events, the RMSE values against the QPE of the temporally and spatially interpolated QPF against QPF data that had been interpolated temporally by linear methods and spatially by UKR have reduced by 2.31% in warm periods and 2.81% in cool periods.
- Across all the verification events, the RMSE values against the QPE of the temporally and spatially interpolated QPF against QPF data that had been interpolated temporally by optical flow and spatially by IDW have reduced by 1.17% in warm periods and 1.59% in cool periods
- The BR values of temporally and spatially interpolated QPFs outperform those of other QPF that had been applied simple interpolation techniques in nearly all of the verification events.

Therefore, the temporal and spatial interpolation method presented in this chapter proves to show better results for increasing the resolution of radar QPF for hydrological applications.

There is considerable uncertainty between the forecast and observed data sources used in this study and in order to verify the results, it would be reasonable to use different sets of QPF and QPE data. For future work, the preservation of peak magnitudes (so called ‘singularities’) in the QPF could further be investigated. Furthermore, the accuracy of the interpolated QPF could further be demonstrated by comparing it to extrapolated QPF (from QPE) at similar resolutions. For example, the OK-QPF-5-1 could be compared against Nowcast data from the UKMO with identical temporal and spatial resolutions.

Overall, using the interpolation processes proposed in this study it is able to make comparisons of the hydrological outputs should the forecasts be used in real-time hydrological applications. Whilst such techniques could be implemented by, and acquired from, meteorological services this way of adjusting the data enables the user to explore different variables in the interpolation method to tailor it to different hydrological modelling purposes. Moreover, it is a cost effective and convenient manner of obtaining higher resolution – and thus more accurate – forecasts, especially as the higher resolution data may not readily be available.

4 Updating probabilistic radar Quantitative Precipitation Forecasts

4.1 Introduction

Whilst deterministic QPFs are used for flood forecasting, they do not present any information on the uncertainty of the rainfall forecast. Therefore, probabilistic QPFs are used in flood forecasting models as it provides information about the uncertainty of the deterministic rainfall forecast (Krzysztofowicz and Kelly, 2000; Nogueira and Barros, 2015; Regonda *et al.*, 2013; Zhao *et al.*, 2015). Rainfall data are considered to be the most influential inputs into hydrological models (Mizukami and Smith, 2012). Hence, if the uncertainty of a QPF is propagated through a hydrological model, it could have significant effect on flood variables, particularly defining thresholds of these variables that cause flooding. The uncertainty estimates from these probabilistic model outputs can then be incorporated into decision-making systems, for example, to issue an emergency flood warning based on flood risk assessment or to perform appropriate intervention strategies (Khan and Valeo, 2015).

Stochastic methods have been used to generate probabilistic QPFs but they may not perform well in different rainfall characteristics. Probabilistic QPFs are typically accompanied with a measure of total uncertainty in the form of PDFs. These can be generated from historical data or revised on the basis of priori knowledge (Reggiani and Weerts, 2007; Wood and Schaake, 2007). Schaake *et al.* (2007) suggested a stochastic method to produce probabilistic QPFs from historical PDFs. Rene (2014) produced probabilistic QPFs from deterministic QPFs based on NWP forecasts with a lead time up to 12 hours. In this method, however, the temporal structure across individual timesteps (e.g. hourly) is fixed throughout a forecast period due to the QPE values being assigned a probability from the distributions. This may produce probabilistic QPFs that do not represent the patterns of the estimated rainfall temporally. This highlights the need to consider the temporal structure of probabilistic QPFs. Furthermore, the construction of the probabilistic QPFs using the stochastic approach estimates the uncertainty purely based on forecast errors in historical data, and this may not fully represent the uncertainty for extreme events, such as low and high

rainfall. As a result, Rene (2014) underestimates high rainfall events and overestimates low rainfall events.

Given the limitations discussed above, Bayesian inference methods can be used to post process probabilistic QPFs using the latest QPEs so that they are weighted against the historical rainfall data (Wasson, 2016). This would help better estimate the uncertainty of the deterministic QPF. The use of Bayesian methods for probabilistic QPFs is not in itself a new approach. Many studies have used Bayesian methods to quantify the uncertainty of deterministic QPFs for flood forecasting (Krzy, 1999; Krzysztofowicz and Herr, 2001; Reggiani and Weerts, 2007). For example, Sloughter *et al.* (2007) used a Bayesian model averaging approach to predict the full PDF of future rainfall. Zhao *et al.* (2015) explored BJP to estimate forecast uncertainty by post processing raw daily streamflow forecasts. However, a stronger focus is needed to update existing PDFs with the most recent QPE data using Bayesian methods. This would produce the more accurate probabilistic QPFs by using the temporal structure of the latest rainfall storms.

The use of Bayesian methods for post processing supports an application of a statistically self-calibrating system (i.e. updating model parameters with the latest input data), which is conducive for an operational flood forecasting system (Yu *et al.*, 2016; (Krzy, 1999). Furthermore, probabilistic QPFs generated from a stochastic model using Bayesian methods produce reliable estimates over small temporal and spatial scales (Biondi and De Luca, 2012). This is particularly beneficial for applying radar rainfall data over small catchments, which is a feasible exercise due to the high temporal and spatial resolutions typically seen in this source of rainfall data (Einfalt *et al.*, 2004). It is therefore clearly advantageous to explore post processing PDFs generated from stochastic models in order to increase the accuracy of the radar probabilistic QPFs. A disadvantage of post processing with a Bayesian approach is the increased computational effort. For this reason, it is noted that a bulk of any post processing should be conducted offline (Reggiani and Weerts, 2007)

The aim of this chapter is to develop a two-stage Bayesian method to post process probabilistic QPFs considering the temporal structure of the latest radar QPE data. First, PDFs are produced using the forecast errors between

coincidental QPE and QPF historical values using the stochastic model implemented by Rene (2014). Second, these PDFs are then refined independently using two applications of Metropolis Hastings (MH) Monto Carlo Markov Chain (MCMC) using recent radar QPE data preceding the deterministic QPF and that is not included in the historical QPF/QPE in the stochastic model. This two-stage process is an integral component of the posterior predictive distribution which is estimated in the final stage of the post processing method to provide new PDFs. Two applications of MCMC are necessary to estimate new PDFs using both historical and recent QPE. Finally, probabilistic QPFs are generated from the new PDFs. Also, a GLM is used to determine the conditional distributions of nonzero QPF values and it replaces the use of the bivariate distribution in the stochastic model.

Postprocessing probabilistic rainfall forecasts increases the accuracy of hydrological forecasts andhelps the preparedness for emergency response (Dottori *et al.*, 2015). Hence, outputs of this study would assist decision makers in flood risk management in real-time settings. Particularly, in flood risk management, postprocessing probabilistic rainfall forecasts would be useful to accurately determining threshold values for flood management.

4.2 Post processing method

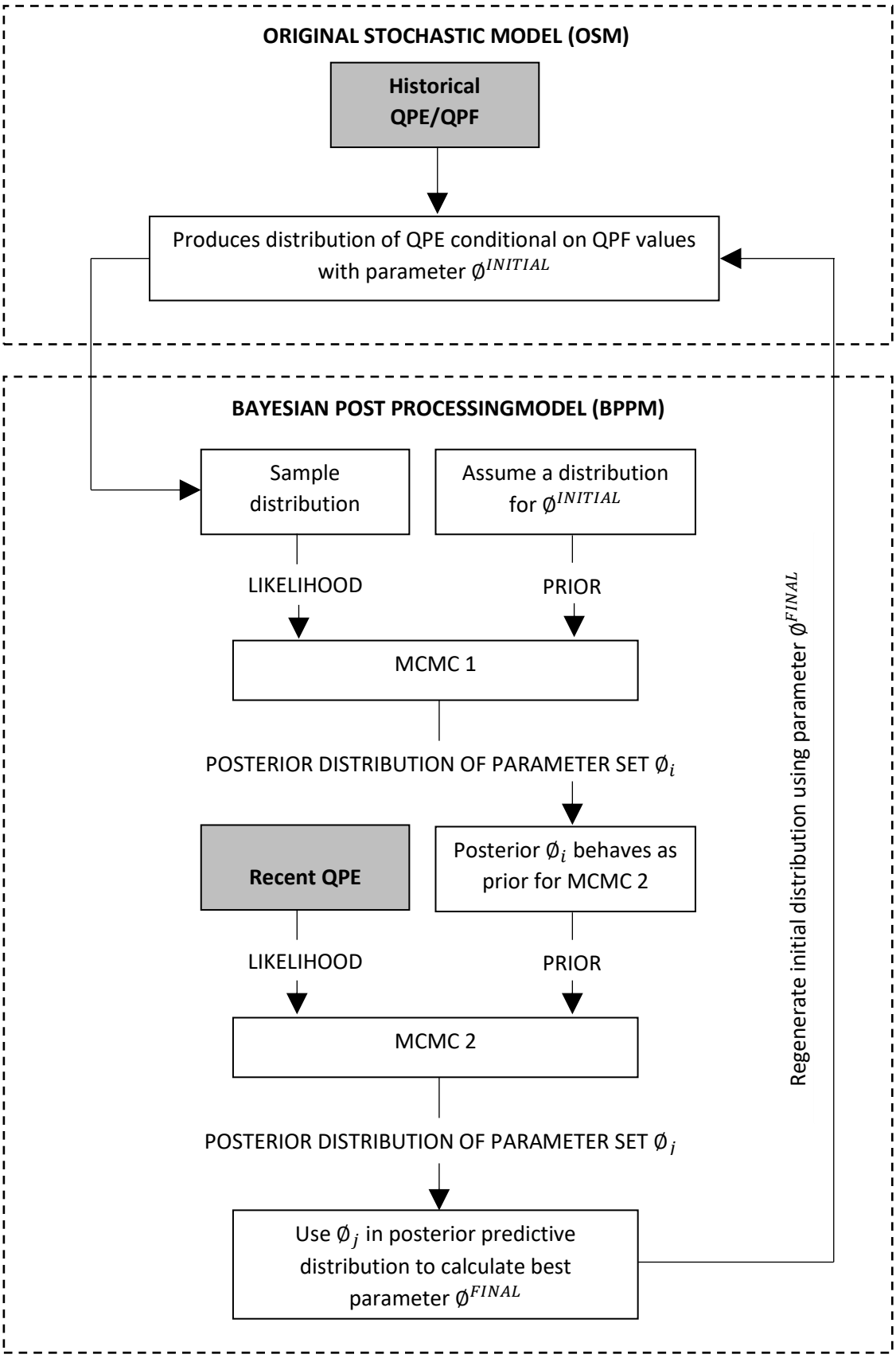

Figure 4.1. Flow chart showing the different stages of the post processing method described in this study (Shaded boxes represent datasets).

Figure 4.1 shows the different stages of the postprocessing method. They are described below:

Original Stochastic Model (OSM)

Full explanations of the OSM are provided in section 4.2.1. The summary of each process/dataset are provided below.

- *Historical QPE/QPF (dataset)* – coincidental temporal and spatial QPE and QPF values in a historical period are used to generate distributions based on the errors between the QPE/QPF
- *Produce a distribution of QPE conditional on QPF values with parameter* $\emptyset^{INITIAL}$ – Cumulative Distributions Functions (CDFs) are generated for QPE values conditioned on specific QPF values using the historical QPE/QPF data. Hence, depending on what QPF value is used, the parameter $\emptyset^{INITIAL}$ of the distribution is unique.

Bayesian Post Processing Model (BPPM)

Full explanations of the BPPM are provided in section 4.2.2, including why two applications of MCMC are required. The summary of each process/dataset are provided as follows:

- *Sample distribution* – the distribution is sampled using $\emptyset^{INITIAL}$ to produce a dataset (denoted H in this study) with a fixed size (see section 4.2.3 for more details). This dataset behaves as the likelihood of the first MCMC stage in the BPPM.
- *Assume a distribution for* $\emptyset^{INITIAL}$ – an appropriate distribution is chosen for $\emptyset^{INITIAL}$. This is used as the prior distribution for the first MCMC stage in the BPPM.
- *MCMC Stage 1* – the output of this stage produces a posterior distribution for the parameter $\emptyset^{INITIAL}$ conditioned on the sampled dataset from the distribution (i.e. dataset H).
- *Recent QPE (dataset)* – this is a dataset containing the latest QPE values that is not part of the historical QPE dataset. This is used to update the distribution. It is denoted D in this study.

- *Posterior* $\emptyset_i$ behaves as prior for MCMC 2 – the posterior distribution for $\emptyset^{INITIAL}$ in the first MCMC stage is used as the prior distribution for $\emptyset^{INITIAL}$ in the second MCMC stage.
- *MCMC Stage 2* – the output of this stage produces a posterior distribution for the parameter $\emptyset^{INITIAL}$ conditioned on the dataset representing the latest QPE (i.e. dataset D).
- *Use* $\emptyset_j$ *in posterior predictive distribution to calculate best parameter* $\emptyset^{FINAL}$ – the posterior distribution for the parameter $\emptyset^{INITIAL}$ produces a posterior parameter range $\emptyset_j$ which is used in a posterior predictive distribution to calculate $\emptyset^{FINAL}$. This is then used in the OSM to 'update' the CDFs.

4.2.1 Original Stochastic Model (OSM)

1.1.1.1 Stochastic models

The post processing method includes a stochastic model (i.e. OSM) implemented by Rene (2014) to generate initial probabilistic QPFs that would be further post processed using Bayesian methods. A QPF value could either be zero or nonzero, hence two separate stochastic models are implemented as part of this method. The stochastic models generate distributions (i.e. CDFs) of QPE conditional on specific QPF values. Each stochastic model is made up of three conditional probabilities that are calculated using historical forecast and observed rainfall data. Together, they are used to produce a CDF describing the exceedance probabilities of observing specific rainfall values conditioned on a zero QPF rainfall value (zero QPF model) or a nonzero QPF rainfall value (nonzero QPF model).

Assuming S and $\dot{S}$ are the QPE (observed) and QPF (forecast) rainfall intensity, respectively, and x is a random realisation. The nonzero and zero rainfall forecast can be calculated using Equations (4.1) and (4.2), respectively, depending on whether $\dot{S}$ is nonzero or zero. For a nonzero rainfall forecast $\dot{S}$ = y, where y > 0, the CDF is defined as:

$$P(S \leq x \mid \dot{S} = y) = P(S \leq x \mid S > 0, \dot{S} = y)P(S > 0 \mid \dot{S} = y) + P(S = 0 \mid \dot{S} = y) \quad (4.1)$$

For a zero-rainfall forecast $\dot{S}$ = 0, the CDF is defined as:

$$P(S \leq x \mid \dot{S} = 0) = P(S \leq x \mid S > 0, \dot{S} = 0)P(S > 0 \mid \dot{S} = 0) + P(S = 0 \mid \dot{S} = 0) \quad (4.2)$$

The full implementation of the OSM by Rene (2014) is described in Implementation of Original Stochastic Model.

The components for the zero-forecast model (Equation (4.1)) are estimated in the following way:

$P(S > 0 \mid \dot{S} = 0)$ and $P(S = 0 \mid \dot{S} = 0)$ are obtained empirically from the QPF/QPE data. $P(S \leq x \mid S > 0, \dot{S} = 0)$ is obtained by extracting datasets from the historical QPE and fitting it to a distribution.

The components for the nonzero forecast model (Equation (4.2)) are estimated in the following way:

$P(S = 0 \mid \dot{S} = y)$ is obtained by fitting the dataset $\{S = 0 \mid \dot{S} = y\}$ to a logistic regression or to a distribution. $P(S > 0 \mid \dot{S} = y)$ is thus estimated by calculating $1 - P(S = 0 \mid \dot{S} = y)$. The component $P(S \leq x \mid S > 0, \dot{S} = y)$ requires the dataset $\{S > 0, \dot{S} = y\}$ which could contain $\dot{S}$ values that do not have corresponding S rainfall values, such as intense rainfall values from extreme events, and therefore would not be fitted to a distribution. The study by Rene et al. (2014) used a bivariate normal distribution to predict the probabilities of observed rainfall, although, this may not accurately depict the probabilities for extreme forecast rainfall values (Katz *et al.*, 2002). In the case of the historical data used in this study, the nonzero QPE dataset did not follow a normal distribution ($p << 0.05$ using the Kolmogorov–Smirnov test) and was found to follow a Gamma distribution (at the 5% significance level using the Chi-Square Goodness-of-Fit Test). Given the reasons above, $P(S \leq x \mid S > 0, \dot{S} = y)$ is calculated using a gamma distribution (Albert, 2009),

$$\frac{\beta^{INITIAL}{}^{\alpha^{INITIAL}}}{\Gamma(\alpha^{INITIAL})} S^{\alpha^{INITIAL}-1} e^{-\beta^{INITIAL} S} \quad (4.3)$$

where Γ is the gamma function and $\alpha^{INITIAL}$ and $\beta^{INITIAL}$ are the gamma shape and rate parameters, respectively. The parameters $\alpha^{INITIAL}$ and $\beta^{INITIAL}$ are estimated using GLM as described below.

1.1.1.2 Generalised Linear Model

The GLM is used to calculate the shape and rate parameters of the gamma distribution, $\alpha^{INITIAL}$ and $\beta^{INITIAL}$, respectively (or $\emptyset^{INITIAL} = (\alpha^{INITIAL}, \beta^{INITIAL})$)(n.b. the rate parameter is the inverse of the scale parameter). A natural log link is used to set up the GLM:

$$\ln\big(E(S)\big) = b_0 + b_1\dot{S} \tag{4.4}$$

Where $E(S)$ is the expectation of S and b_0 and $b_1$are the coefficients of the GLM.

Values for coefficients b_0 and b_1 are calculated by finding the maximum likelihood estimate of the expectation of S. Similarly, the maximum likelihood estimate of the shape parameter $\alpha^{INITIAL}$ of the gamma distribution of S, is also derived using $E(S)$ in the GLM. the rate parameter $\beta^{INITIAL}$ can then be calculated using (De Smith, 2013):

$$\beta^{INITIAL} = E(S)\alpha^{INITIAL} \tag{4.5}$$

$$Var(S)\alpha^{INITIAL} = E(S)^2 \tag{4.6}$$

$$Var(S)\beta^{INITIAL} = E(S) \tag{4.7}$$

Implementation of modified OSM

The procedures to implement the modified OSM are described in this section.

For the nonzero QPF model (Equation (4.1)), the components are calculated as follows:

Step 1: Component $P(S = 0 \mid \dot{S} = y)$ is calculated by extracting $\{S = 0 \mid \dot{S} > 0\}$ and fitting the data to a gamma distribution. Then using the fitted gamma parameters, a PDF is generated and the value for $\dot{S} = y$ is derived.

Step 2: Component $P(S > 0 \mid \dot{S} = y)$ is calculated by performing $1 - P(S = 0 \mid \dot{S} = y)$

Step 3: Component $P(S \leq x \mid S > 0, \dot{S} = y)$ is calculated by extracting $\{S > 0,\ \dot{S} > 0\}$ and generating a GLM based on a gamma distribution where the predictor variable is $\dot{S}$ and the predicted variable is S. Then, using the outputs of the GLM, derive the maximum likelihood estimates of the expectation of S and the value of

the shape parameter, α. Use these values in equation (4) to obtain the rate parameter, β.

For the zero QPF model (Equation (4.2)), the components are calculated as follows:

Step 1: Calculate the joint probabilities (the size of $\{S, \dot{S}\}$ is denoted N):

1. $P(S = 0,\ \dot{S} = 0) = |\{S = 0,\ \dot{S} = 0\}|/N$
2. $P(S > 0,\ \dot{S} = 0) = |\{S > 0,\ \dot{S} = 0\}|/N$
3. $P(S = 0,\ \dot{S} > 0) = |\{S = 0,\ \dot{S} > 0\}|/N$
4. $P(S > 0,\ \dot{S} > 0) = |\{S > 0,\ \dot{S} > 0\}|/N$

Step 2: Estimate component $P(S = 0 \mid \dot{S} = 0) = \frac{P(S=0,\dot{S}=0)}{P(S=0,\dot{S}=0)+ P(S>0,\dot{S}=0)}$

Step 3: Estimate component $P(S > 0 \mid \dot{S} = 0) = \frac{P(S>0,\dot{S}=0)}{P(S=0,\dot{S}=0)+ P(S>0,\dot{S}=0)}$

Step 4: Component $P(S \leq x \mid S > 0, \dot{S} = 0)$ is calculated by extracting $\{S > 0,\ \dot{S} = 0\}$ and fitting the data to a gamma distribution. Then using the fitted gamma parameters, a CDF is generated.

4.2.2 Bayesian Post Processing Model (BPPM)

The BPPM is used to deduce a new value of the parameter of the distribution $\emptyset^{FINAL}$. This is done using two MCMC processes. The first MCMC stage extracts the range of parameters of $\emptyset^{INITIAL}$ based on the historical dataset. The second MCMC stage extracts the range of parameters within the parameter range of the first MCMC stage based on recent QPE. Hence, a new approximation of $\emptyset^{INITIAL}$ is evaluated together within the uncertainty range of the historical and recent QPE. It is expected that this two-stage implementation of MCMC updates the distribution of the historical datasets to more accurately represent the current rainfall uncertainties whilst still representing the uncertainties in the historical datasets.

Sampling the distribution with parameter $\emptyset^{INITIAL}$

In the historical QPE/QPF datasets, the size of S varies for different $\dot{S}$. So, if a large S is used as the likelihood of the first MCMC stage this would require more computational resources and thus the post processing method would take longer to execute. By sampling from the initial distributions of the stochastic model, the size of S is appropriately selected and kept the same across all values of $\dot{S}$ for which CDFs are to be generated for. Thus, the post processing method would take a shorter time to execute. Hence, a sampled dataset H from the distribution of S with parameters $\emptyset^{INITIAL}$ is used as the likelihood of MCMC stage 1 instead of using the historical dataset of S.

Post processing using the latest rainfall data

In this study, the shape and rate parameters are assumed to be independent.

The distributions $P(S \leq x \mid S > 0, \dot{S} = 0)$, for zero forecasted QPF, or $P(S \leq x \mid S > 0, \dot{S} = y)$ and $P(S = 0 \mid \dot{S} = y)$, for nonzero forecasted QPF, in the stochastic model (Equations (4.1) and (4.2)) are updated in a posterior predictive distribution described as follows:

$$P(S \leq x|D) = \int P(S \leq x|\emptyset_j) P\left(\emptyset_j \middle| D\right) d\emptyset_j \tag{4.8}$$

Where D is a set representing the most recent, consecutive timesteps of the QPE data and $\emptyset_j = (\alpha_j, \beta_j)$ is a set of gamma parameters after the second MCMC process (described later). This set is obtained by quantifying $P\left(\emptyset_j \middle| D\right)$ in a two-stage application of a MH MCMC algorithm described in section 2.2.1.

Introduction to MH

A popular numerical integration method to perform MCMC is the MH sampling technique (Han *et al.*, 2014). This method is especially useful in estimating the forecast uncertainty and is therefore necessary in revising the PDFs used to produce probabilistic QPFs (Montanari and Brath, 2004).

The MH algorithm is described as follows. By choosing a target distribution – or the posterior distribution – a specific function needs to be selected or derived, expressed as K, which is called the transition kernel. An arbitrary value for the sample variable is selected and the process is performed a large number of times

until the samples fit approximately in the target distribution (Chib and Greenberg, 1995; Flötteröd and Bierlaire, 2013; Renshaw, 2004).

The transition kernel is expressed as:

$$K(\emptyset^i, \emptyset^j) = q(\emptyset^i, \emptyset^j)v(\emptyset^i, \emptyset^j)d\emptyset^j + \bar{r}(\emptyset^j)\delta_{\emptyset^i}(d\emptyset^j) \quad (4.9)$$

Where $\emptyset^i$ and $\emptyset^j$ represent two different samples of the parameters, $q(\emptyset^i, \emptyset^j)$ is the proposal distribution, $\bar{r}(\emptyset^j) = 1 - \int q(\emptyset^i, \emptyset^j)v(\emptyset^i, \emptyset^j)d\emptyset^j$ and

$$\delta_{\emptyset^i}(d\emptyset^j) = \begin{cases} 1, & \emptyset^i \in (\emptyset^i, \emptyset^i + d\emptyset^i) \\ 0, & Otherwise \end{cases}$$

$v(\emptyset^i, \emptyset^j)$ is referred to as the acceptance probability and is expressed as:

$$v(\emptyset^i, \emptyset^j) = min\left[\frac{\pi(\emptyset^j)q(\emptyset^i, \emptyset^j)}{\pi(\emptyset^i)q(\emptyset^j, \emptyset^i)}, 1\right]$$

In both of the MCMC processes in this study, q is chosen in the implementation to be a multivariate normal distribution where samples representing the gamma distribution parameters are chosen. However, the posterior distribution, or the target distribution, will differ in the two MCMC processes.

MCMC Stage 1

In the first MH MCMC process, the posterior distribution is expressed as follows where $\emptyset_i = (\alpha_i, \beta_i)$ is a set of gamma parameters after running this process:

$$P(\emptyset_i|H) = P(\alpha_i, \beta_i|H) = P(\alpha)P(\beta)P(H|\alpha, \beta) \quad (4.10)$$

Here, $P(\alpha)$ and $P(\beta)$ are the prior distributions of the initial gamma parameters $\alpha^{INITIAL}$ and $\beta^{INITIAL}$ where α and β are random realisations of the gamma parameters. The exponential distribution is chosen for these prior distributions based on the outputs of deviance information criteria. Thus, the updated parameter values, denoted $\emptyset^{FINAL} = (\alpha^{FINAL}, \beta^{FINAL})$, would be better estimated.

The rates of the exponential distributions (for the prior distributions) are chosen by calculating the gamma shape and rate parameters of a set $A \subset H$ using the expectation of A, $E(A)$, and the variance of A, $Var(A)$, in equations 4.6 and 4.7.

α_A and β_A are the mean shape and rate values in the prior distribution. As an exponential distribution is chosen for the prior distribution the rate of $P(\alpha)$ is $\frac{1}{\alpha_A}$ and the rate of $P(\beta)$ is $\frac{1}{\beta_A}$ using the relationship $E(\alpha) = \frac{1}{\beta}$. (De Smith, 2013).

As in the GLM, the likelihood function $P(H|\alpha, \beta)$ is also gamma distribution where α and β are sampled from the prior distributions of equation (4.10).

1.1.1.3 MCMC Stage 2

The second MH MCMC process uses the posterior distributions in Equation (4.10) as the prior distributions so that the posterior distribution of the second MH MCMC process is represented as follows:

$$P(\emptyset_j|D) = P(\alpha_j, \beta_j|D) = P(\alpha_i|H)P(\beta_i|H)P(D|\alpha, \beta) \quad (4.11)$$

The likelihood function $P(D|\alpha, \beta)$ uses D and is also gamma distribution where α and β are sampled from the prior distributions in equation (4.11). In the posterior distribution of equation (4.8), we are only interested in the percentiles forming the set $\emptyset_j$ of parameters. The distribution itself is not essential for use in this study. Hence, after running this MH MCMC process the gamma parameters $\emptyset_j$ are inputted into the posterior predictive distribution stated earlier, in a computational estimation for $P(S \leq x|D)$:

$$\sum_{\bar{k}=1}^{N} P(S \leq x|\emptyset_{j_{\bar{k}}}) \quad (4.12)$$

Where N is equal to the number of parameter samples considered in the MCMC processes, which is 10,000 (after discarding the initial 500 results as “burn in”). This value is chosen in the case study of this study.

Equation (4.12) produces a distribution for a continuous set of x and the gamma parameters of this distribution,$\emptyset^{FINAL}$, are used in equations (4.1) and (4.2) to produce an updated CDF.

4.2.3 Producing probabilistic QPFs

In the OSM, the QPF is provided at each lead time at which CDFs are generated. The method of producing probabilistic QPFs is that rainfall values are sampled by the exceedance probabilities from each CDF at every lead time. These rainfall

values are put together to form another single QPF across the forecast period with the temporal resolution equal to the difference between the lead times. This single QPF generated is a probabilistic QPF. The same process is performed for different exceedance probabilities to form several probabilistic QPFs.

In this study, CDFs are generated in hourly lead times that are 1, 2, 3, 4, 5 and 6 hours, based on the maximum lead time of 6 hours of Nowcast QPFs. Using shorter lead times requires running the stochastic model more times and also post processing them which is computationally demanding. Hence, choice of hourly lead times would enable the methodology to be tested with reasonable computational effort.

Values represented by percentiles lower than 0.1 would not be sufficiently large enough to compare performance. Also, it is assumed that these percentiles and those above 0.95 would not normally be considered in operational settings due to them representing the extremities of the event. Hence, for measuring performance and presenting results, the CDFs are sampled using exceedance probabilities between 0.1 and 0.95 with an increment of 0.05 (i.e. 18 probabilistic forecasts are produced).

Hence 18 probabilistic QPFs are produced representing the uncertainty of a deterministic QPF.

4.2.4 Performance indicators

Hyetographs show the range of the rainfall intensities of the probabilistic QPF temporally generated from the OSM and the BPPM. For quantitative measurements of improvement, the accumulated rainfall of the probabilistic QPFs over the six-hour forecast period, RMSE and Pearson's r values are calculated.

The probabilistic QPFs represent the uncertainty range of the QPF and the QPE is expected to fall within this range. It is an indicator of performance if the QPE is closer to the mean probabilistic QPF as it shows that the QPE is less likely to fall outside of the updated uncertainty range. The mean probabilistic QPF is referred to as the mean rainfall intensity values of the probabilistic QPFs at each timestep.

The accumulated rainfall amounts of the probabilistic QPFs are compared against the QPE over the 6 hour forecast period. As the timestep of a probabilistic QPF is 1 hour (up to 6 hours), the accumulation, denoted $\bar{A}^p$, of the probabilistic QPF of the exceedance probability (or percentile), p, is calculated using the following expression:

$$\bar{A}^p = \sum_{i=1}^{6} S_i^p \tag{4.13}$$

Where S_i^p is the rainfall intensity of the probabilistic QPF of the p percentile at the ith timestep. Accumulated rainfall would be considered as a measurement of performance because it is a factor determining the flood extent over a catchment in hydrological modelling. A value that is closer to the accumulated rainfall of the QPE would indicate better performance.

RMSE in this study is described as the standard deviation of the difference between the probabilistic QPF of percentile p and the QPE, over the six-hour forecast period. This would indicate how close the magnitudes of the intensities are between the two data. RMSE values range from zero to infinity so the closer the value to zero the better the performance.

The fluctuating path of a QPF could also be measured against the fluctuating path of the QPE, which indicates the linear dependence of the two data. r calculates the strength of this linear dependence by using the covariance and standard deviations of two random variables (Zhou *et al.*, 2016). Values range between -1 and 1 and the closer r is to 1 the stronger the probabilistic QPF is positively correlated with the QPE. Negative values show that the probabilistic QPF is increasing over the forecast period whilst the QPE is decreasing, or vice versa.

Considering the fluctuating path over a time period is important in hydrological applications where forecasting of model variables would need to be performed in real time. This is particularly the case for flood forecasting where peaks occurring at specific timesteps would need to be forecasted early enough so that early decisions could be made within short time frames. In this study, a positive correlation between the probabilistic QPFs and the QPE is desired. However, in the case of negative correlation, a less negative correlation would indicate improvement despite weaker correlations. It is therefore an indicator of success if updated probabilistic QPFs have a higher r with the QPE.

4.3 Case studies

4.3.1 frontal and convective storms

The case study presented in section 3.3.1 is used in this chapter. Two studies are used in this chapter to test the post processing method described in this chapter. These studies are chosen by considering the differing storm characteristics in any given year. A distinct characteristic that is identifiable is whether the storm occurs in the warm seasons (spring and summer) or cool seasons (autumn and winter) of the year. Typically, convective storms are predominant in the warm seasons and frontal storms are predominant in the cool seasons (Rico-Ramirez *et al.*, 2015). Frontal storms are considered in this study as the QPFs of these storms evolve more linearly due to the large scale of such rainfall that develops slowly on a temporal scale (Barillec and Cornford, 2009). This would enable the methodology to be tested appropriately with the assumption that recent rainfall characteristics are indicatory of future rainfall within a Nowcast range. The post processing method is tested in order to draw comparison of performance between frontal and convective events. Hence, study events from each period are distinguished in this study:

Frontal storms - the historical data used to generate the CDFs in the OSM are sourced between September 2015 and February 2016. These are in line with the meteorological autumn and winter seasons in the northern hemisphere. Hence, the study events are also sourced from the same seasons but between September 2016 and February 2017.

Convective storms) – similar to how the historical and study events had been selected for frontal storms, the historical data for this case study are selected between June 2016 and August 2016. The study events are selected between June 2017 and August 2017. These periods represent the meteorological spring and summer seasons in the northern hemisphere.

The period sourced for historical and study events is short due to limited data availability. However, the spatial coverage of the data is 184 x 140km (see section 3.3). This ensures that there are many data points used in the historical QPF and QPE to extract the uncertainty of these two data.

4.3.2 Historical data used to generate CDFs

The historical QPE/F data are obtained from matching data sets in the warm/cool seasons where comparisons are made between the data sets. This is used to obtain the forecast errors in the stochastic model to generate the probability distributions for all of the components in the stochastic model. This requires obtaining QPE/QPF data points at every grid cell in the radar domain of dimensions 184 x 140 km. The temporal and spatial resolution of the historical QPE/F data is chosen to be that of the QPF, which is 15-min and 2-km, respectively. Spatially, there would be repeated statistical comparisons of the same 2-km QPF value against four 1-km QPE data points. Instead, the mean of these four values is used as the coincidental QPE data point against the 2-km QPF value. Therefore, across the whole QPF domain (92 x 70 km due to the 2-km resolution), there are in total 6440 (92 x 70) data points. Also, there are six subsets of the QPF historical data set that represent the six forecast periods of 1,2,3,4,5 and 6 hrs (i.e. each QPF value in a single subset has a fixed forecast horizon despite being a continuous period with 15 timesteps). Hence, with a total of 11,712 15-min timesteps in a warm/cool season, 452,551,680 (11,712 x 6440 x 6) QPE/F comparisons are performed for the stochastic model.

H is set to have a size of 1000 as this would allow the BPPM to be performed at reasonable computational speed. 48 previous timesteps of the QPE, prior to the QPF, representing the 6 hours of data, are used in the BPPM.

It is worth to note that a radar domain of 184 x 140 km is large that the specific location characteristics may not be distinguishable (i.e. rainfall in London may be very different to Edinburgh). However, it was not possible to conduct this type of analysis due to limited data. Data is only available for the North East of England. However, for future work this analysis is recommended.

4.3.3 Study events

A study event is defined to be a full QPF (to six hours in the future) at any point during a storm and it may have zero/nonzero values at the six forecast horizons. As the historical data uses QPE/F data during the warm or cool season, study

events are chosen in the respective period for consistency of performance. Periods of rainfall are identified in either the warm or cool season. Next, QPF grid cell is selected in the QPF radar domain that shows sufficient rainfall across the 6-hour forecast period. This procedure is used to extract four study events for each case study. Hence, there are eight study events that have been used as case studies.

In addition to the eight study events, a further two events are also used to verify the postprocessing method. These events show storm characteristics that are not pronouncedly observed in the eight study events and would present further information about the performance of the postprocessing method. The two events have been extracted from the warm seasons. This is due to this period showing more varying storm characteristic (which is typically expected of convective storms). Hence, in total ten study events are used to verify the postprocessing method.

Events 1 – 4 are representative of frontal storms (events from the cool seasons) and are part of frontal storm study. Events 5 – 8 are representative of convective storms (events from the warm seasons) and are part of convective storm study. Different characteristics of study events 1 - 8 are presented in Figure 4.2. These include the accumulated rainfall of the QPF and QPE data, the peak rainfall intensity of the QPE and the variance of the QPE data. The variance is calculated using all the data points of the QPE across the 6-hour forecast period (or storm duration). Hence it is a quantification of the temporal variance. In the bottom of figure of Figure 4.2 it is observed that events in case study 2 (from the warm seasons) present larger variance values in comparison to the events in frontal storm study (from the cool seasons). This shows that the warm events show more variance in rainfall intensities in any given duration of rainfall, which is commonly observed in convective rainfall storms. Secondly, these events (Events 5 – 8) also have larger peak intensities compared to Events 1 – 4 (see middle figure in Figure 4.2) which is another attribute of convective storms. This is also a reason why storms observed in the warm seasons are more difficult to predict. Interestingly, the accumulated rainfall of the QPF and QPE data sets are also generally distinguishable between the cool and warm seasons. Events from the cool seasons show QPFs that overestimate the QPE, whereas events from the warm seasons show QPFs that underestimate the QPE (see top figure of Figure

4.2). This explains the dynamic nature of convective storms as the actual rainfall is made more difficult to predict in comparison to the more linearly developing frontal storms. As the peaks in convective storms are commonly larger than peaks in frontal storms, it is hence more likely that the QPF of warm events under predict the QPE.

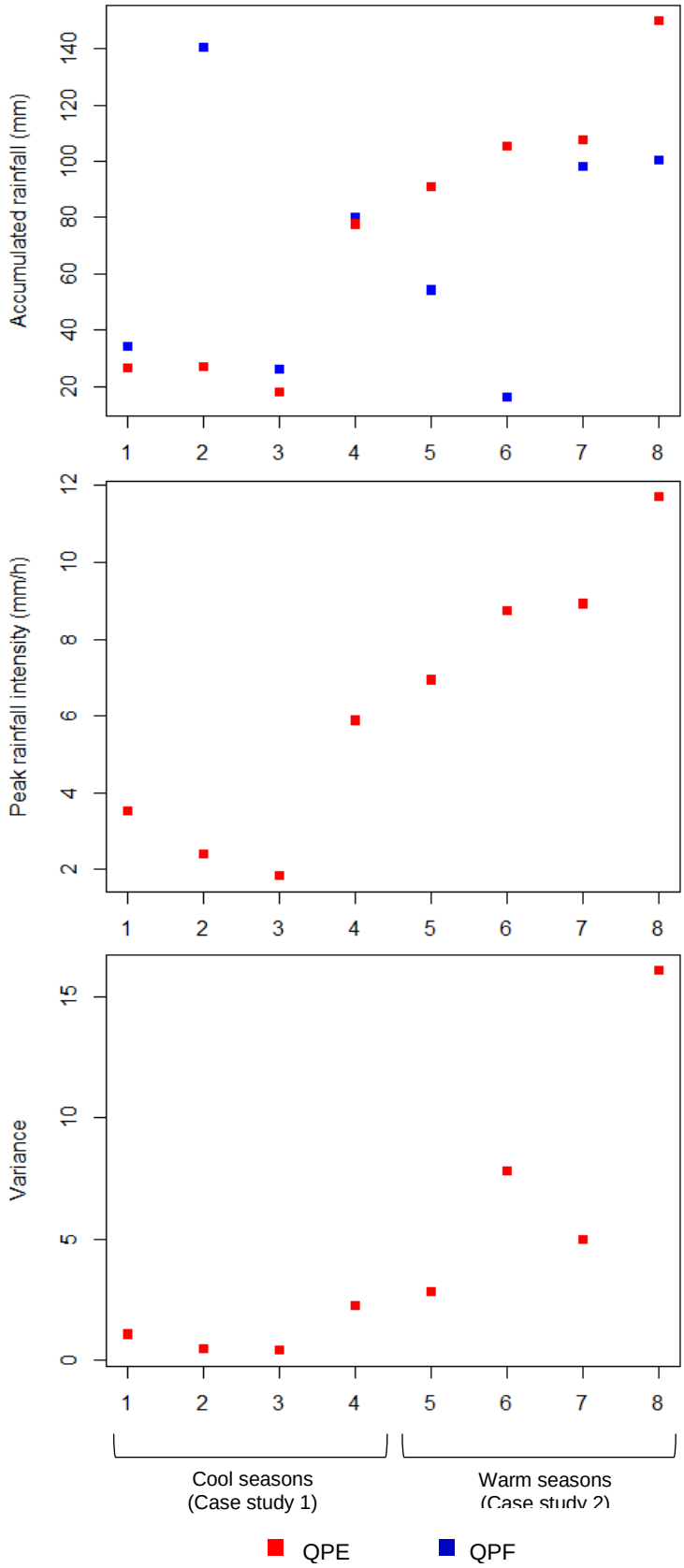

Figure 4.2. Accumulated rainfall amount of the QPF/QPE (top), peak rainfall intensity (middle) and variance (bottom) of the QPE across the 6-hour forecast period of study events 1 – 8.

4.4 Frontal storms

4.4.1 Hyetographs of probabilistic QPFs of OSM and BPPM

Figure 4.3 show the hyetographs of pQPFs of BPPM and OSM, QPE and QPF. Figure 4.4 shows the hyetograph of previous QPE preceding the QPE/QPF. This is used as the recent QPE used in the BPPM.

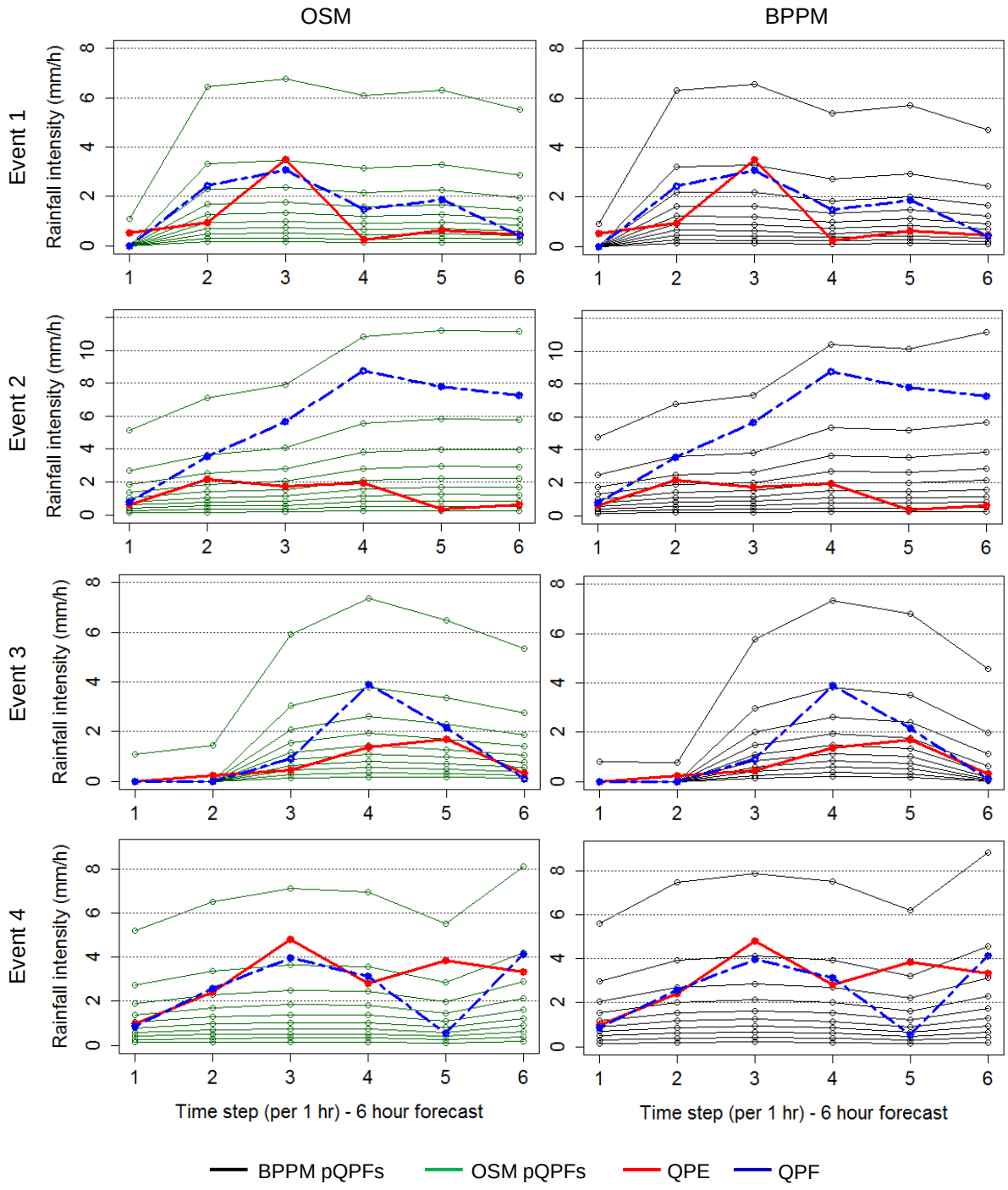

Figure 4.3. Hyetographs of the pQPFs of the OSM (left) and BPPM (right) with QPE and QPF across the 6-hour forecast period (hourly timesteps) for the four study events from the cool seasons.

The QPE in Event 1 (see **Fig. 3**) shows relatively low intensity with a peak on the third hour. The BPPM have reduced the pQPFs to lower intensity values (explained in Accumulation and RMSE section). This is better observed in **Fig. 4** where the mean pQPF is closer to the QPE by 13.3%.

The QPF in Event 2 (see Figure 4.3) heavily overpredicts the observed rainfall by 162.5% as the QPE shows. The QPF resembles the hyetograph of its pQPF between the 0.9 – 0.95 percentiles, which of all the events is situated at the top range of the pQPFs (this is better illustrated in section 4.4.3). Note that this demonstrates that for a high intensity QPF most of its pQPFs will be lower in intensity values compared to the QPF. This is the main reason why the stochastic model generally underestimates observed rainfall for this QPF, as a higher intensity QPE would be situated in a higher pQPF range. However, in this event, the BPPM shows pQPFs visually closer to the QPE despite expected underestimation of the pQPFs. Even with a low intensity QPE, the BPPM more accurately predicts the actual rainfall. The success of this is shown in Figure 4.5 and Figure 4.6 where the mean pQPF of the BPPM moves closer overall to the QPE by 10.2%. In Event 3 (in Figure 4.3Figure 4.4) the QPF overestimates the rainfall where the QPE doesn't exceed rainfall amounts of 2 mm/h and the QPF has a peak of around 4 mm/h. The previous QPE does not add much information to the Bayesian updating process as they are all zero rainfall values. Due to this, the QPF values have a bigger influence in the Bayesian updating process (i.e. dataset D would have no nonzero values from the previous QPE besides the QPF values). However, where zero values are predicted in the QPF, namely at lead times 1-hr, 2-hr and 6-hr, the Bayesian updating process decreases the pQPF intensity values.

Unlike in the other study events, the QPF in Event 4 underestimates the actual rainfall by 58.5%. This means that the QPE would fit in a range around the higher percentiles of the pQPFs. Despite the underestimation of rainfall, the pQPFs have noticeably increased in intensity values. This is indicated in Figure 4.5 and Figure 4.6 where the mean pQPF of BPPM has moved closer to the QPE by 1.6%. The OSM normally over estimates QPE of low-medium rainfall intensities but, despite this, the BPPM does not lower intensity values to reduce the overestimation of the pQPFs. Instead, it more accurately predicts the QPE (based on the mean pQPF) compared to the OSM. This clearly demonstrates the benefits of the BPPM compared to using a fixed stochastic model in a real-time flood forecasting system.

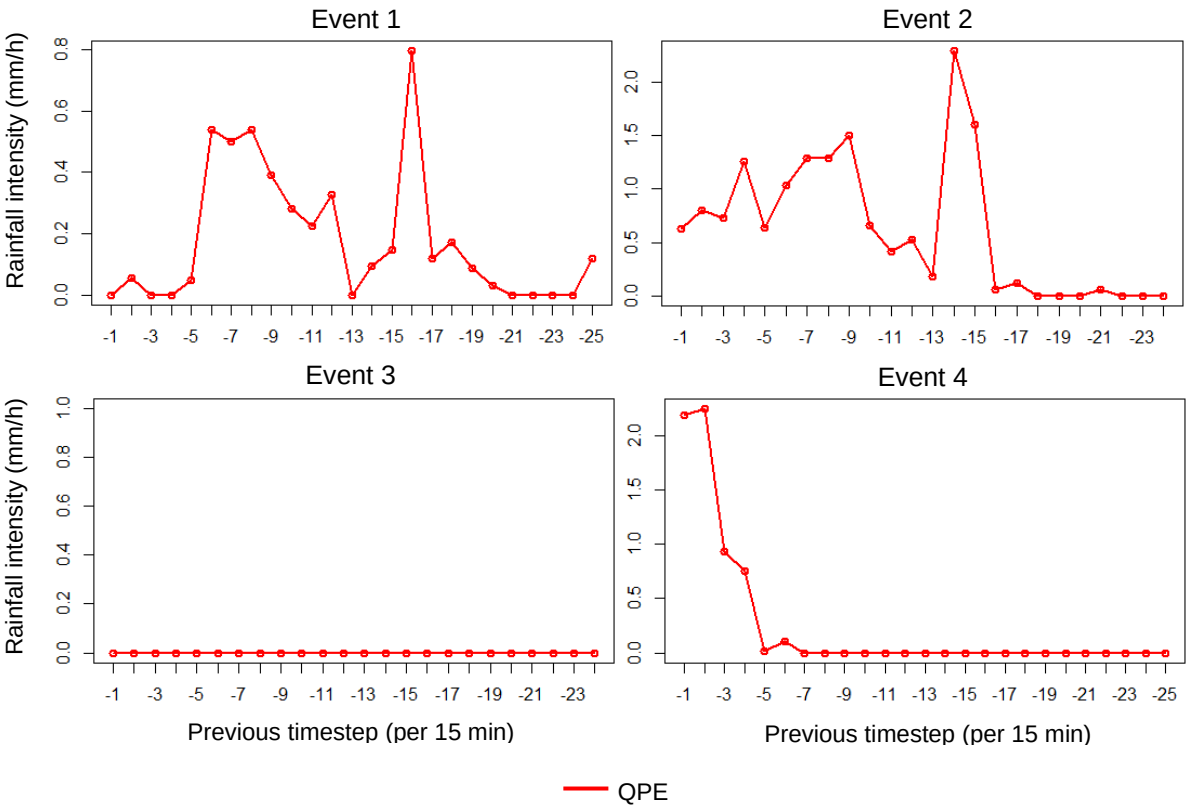

Figure 4.4. Hyetographs showing the QPE of the previous timestep (per 15-min) preceding the QPF in Events 1 - 4.

4.4.2 Measuring the accuracy of probabilistic QPFs of the BPPM using mean forecast

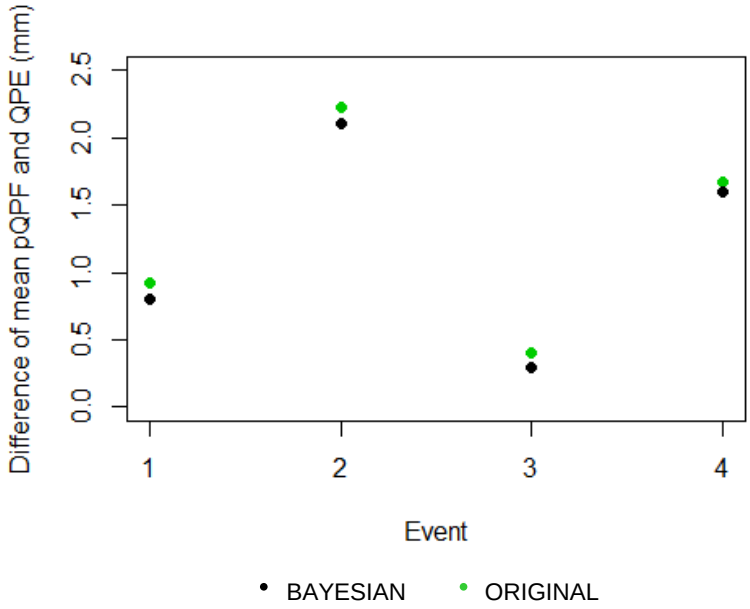

Figure 4.5. The average difference across the 6-hour forecast of the mean intensity values of the pQPFs and QPE of both the OSM and BPPM are shown for the four study events.

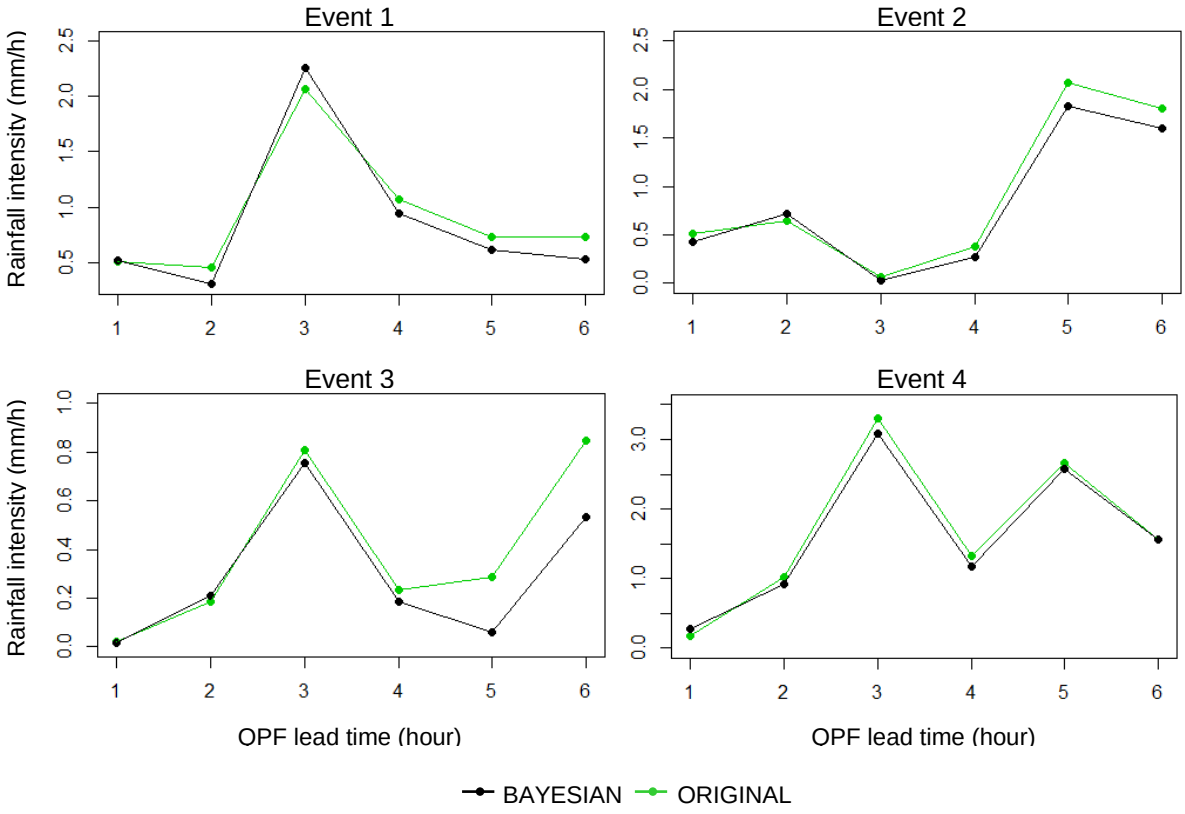

Figure 4.6. The difference of the mean intensity values of the pQPFs and QPE across the 6-hour forecast period of both the OSM and BPPM are shown for the four study events.

As explained in section 4.2.5, the accuracy of the pQPFs of the BPPM could also be measured by calculating the difference between the mean pQPF, at each timestep across the forecast period, with the QPE. The lower the difference, the more accurate the pQPFs.

Across the 6-hour forecast period, the mean pQPF of the BPPM has a smaller difference with the QPE compared to the OSM in all four study events (see Figure 4.5Figure 4.6). The average decrease of the mean pQPF is 8.2% from 1.31 mm/h to 1.19 mm/h. Although this isn't large, it clearly demonstrates that the BPPM alters the uncertainty range of the pQPFs so that the QPE is closer to the mean pQPF. This is beneficial as the QPE is less likely to fall outside of the uncertainty range shown by the pQPFs and therefore the uncertainty estimates are more accurate. Also, the small change is chiefly due to the latest QPE data resembling

the historical data sets in rainfall intensity values, and so a small alteration is expected.

The differences of the mean pQPF with the QPE are also done at different lead times (see Figure 4.6). Clearly, the pQPFs of the BPPM are generally visually closer to the QPE in the different lead times. In all the study events, the bigger differences between the BPPM and OSM are observed where the QPE has low rainfall intensity values. This is because most of the pQPFs would be updated to move closer to the QPE at these lead times. However, in Event 1, the BPPM has performed worse compared to the OSM at the 3-hr lead time. This is due to the QPE peak seen at this lead time even though the BPPM lowers the rainfall intensity values of the pQPFs. Moreover, a similar lowering of the rainfall intensity values is seen in Event 2 to account for the over prediction of the QPF. This has caused a smoothing affect between the 1 – 3 hr lead times (see BPPM for Event 2 in Figure 4.3) whereas the pQPFs in the OSM had small peaks at the 2-hr lead time. This explains the worsening of the performance of the BPPM in this lead time for this event. However, the decrease of average difference for Event 2 (Figure 4.5) again shows that the overall uncertainty range is better represented by the BPPM.

4.4.3 Accumulated rainfall and RMSE

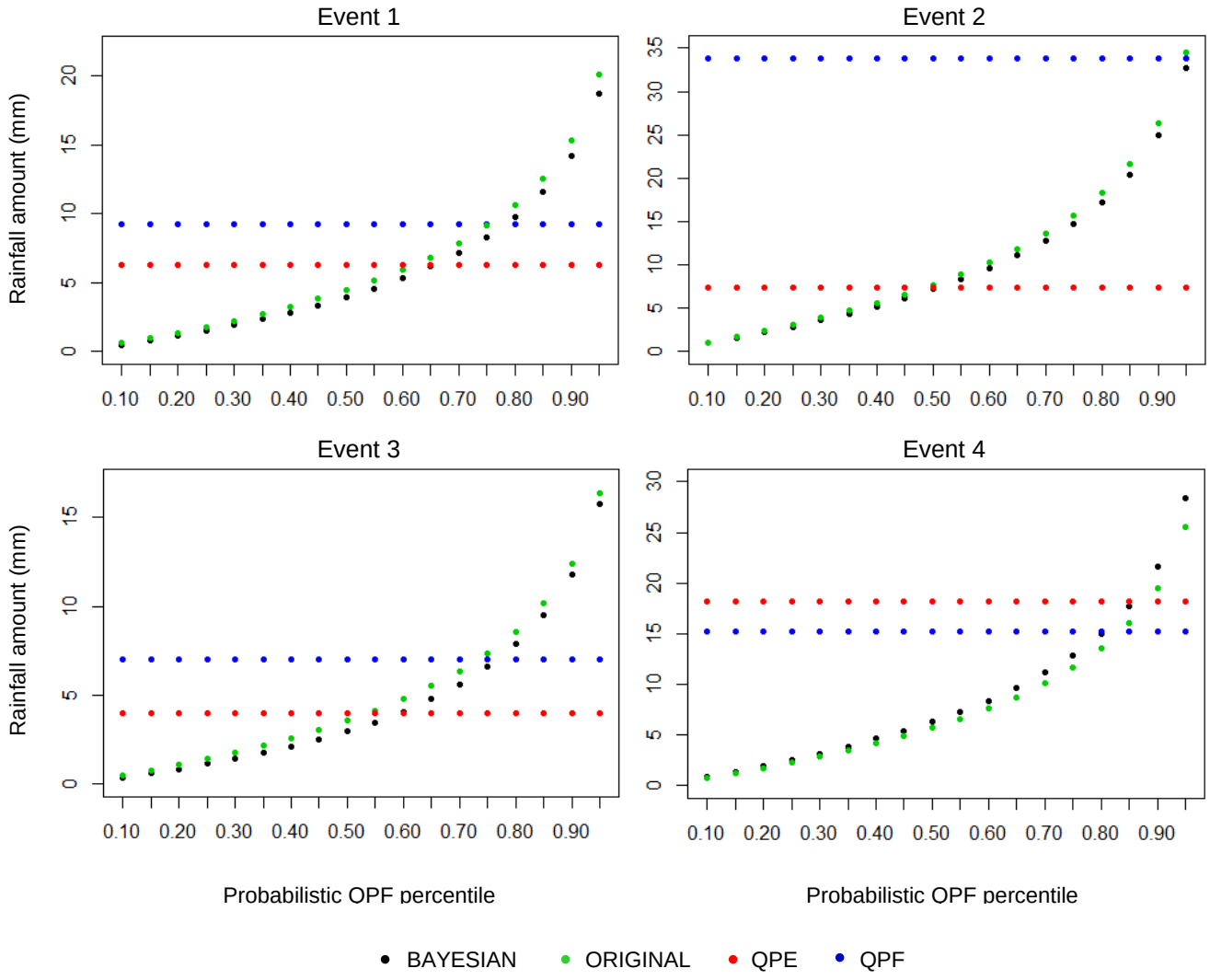

Figure 4.7. Accumulated rainfall amount across the 6-hour forecast period of the pQPFs of the OSM and BPPM, QPE and QPF for each percentile, for the four study events.

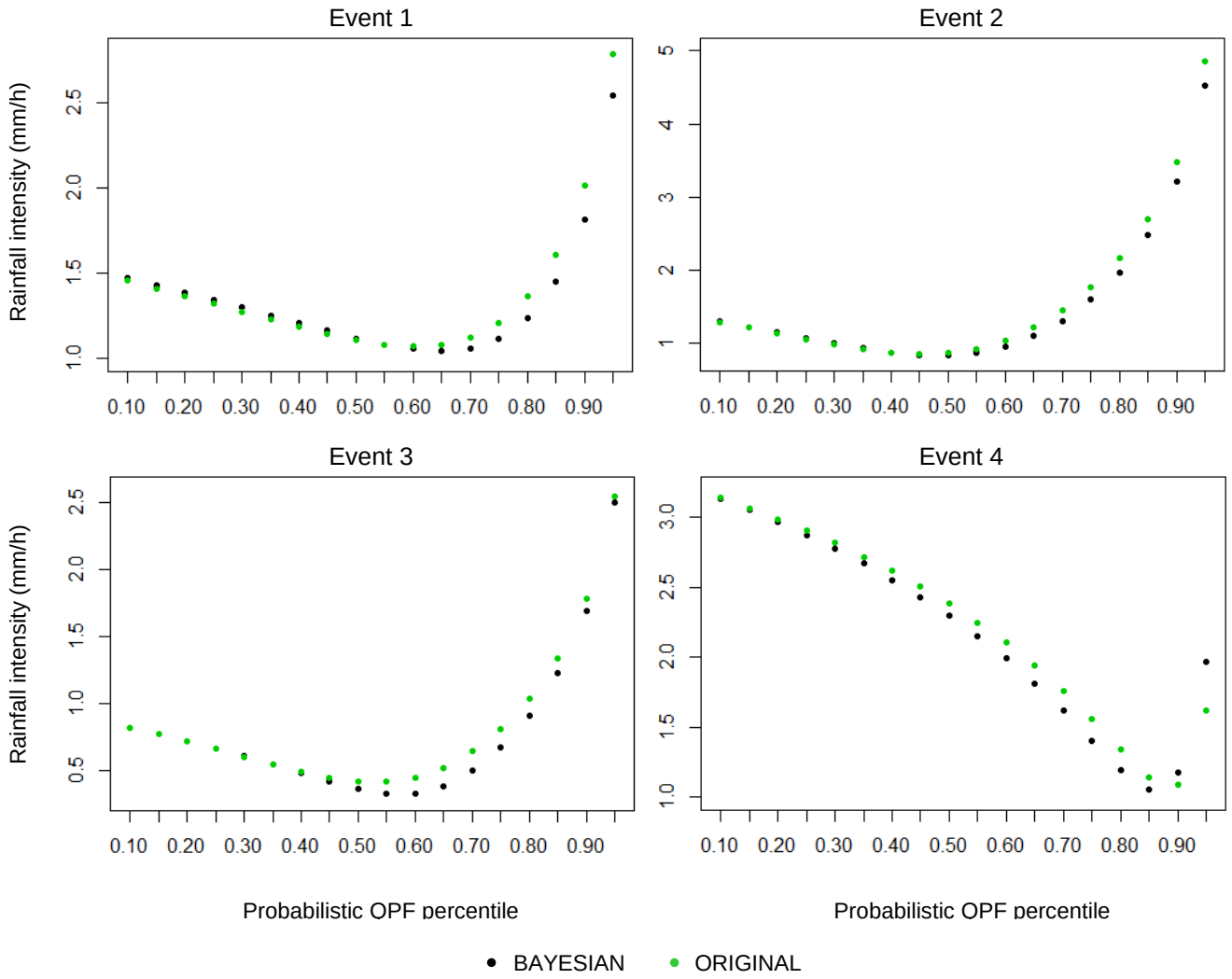

Figure 4.8. The mean RMSE values of the pQPF of the OSM and BPPM, across the 6-hour forecast period, against the QPE for each percentile.

Figure 4.7 shows the accumulated rainfall for all study events of pQPF of the OSM and BPPM against the QPE and QPF. The closer the value is to the QPE, the more accurate the particular percentile is in predicting the total rainfall amounts over the six-hour period. The QPF accumulation is shown as it indicates which percentile it closely matches. This would provide information on how the uncertainty range is generated around the QPF by the stochastic model. For example, in Event 2, the QPF has the highest 6-hour accumulation and it is situated nearest to the 0.95 percentile of its pQPF. This indicates that the pQPFs of this event are likely to underestimate the QPE.

In Event 1, whilst the percentiles above 0.6 show improvement, percentiles between 0.10 and 0.6 show worse accumulated rainfall values. As the

accumulated rainfall for these percentiles were initially lower than the accumulated QPE, they do not reflect the improvement of the updating process despite the mean pQPF being closer to the QPE. The same reason applies for the RMSE scores of the pQPF for the BPPM (see Figure 4.8). A likely cause of a high proportion of percentiles showing worse accumulation and RMSE values is the peak intensity observed (in the QPE) in the third timestep which is anomalous in that peaks in the previous QPE were not seen with similar magnitudes.

In Event 2, the benefit of the BPPM is clearly demonstrated where the accumulated rainfall is reduced for all the percentiles in the BPPM. Whilst this has not improved for the lower percentiles, 0.1 to 0.45, the improvement is seen in higher percentiles, 0.5 to 0.95. Also, the accumulation differences between the pQPFs of the two models are increasing over higher percentiles. This means that there's a smaller change for the 0.1 to 0.45 percentiles whilst there being a bigger change – and hence a larger improvement – for the remaining percentiles. The RMSE values demonstrate a similar trend (see Figure 4.8); however, there is not a noticeable difference in the RMSE values between the two models for the lower percentiles. The percentiles 0.5 to 0.95 show an increasingly bigger improvement where the 0.95 percentile shows the biggest improvement. The lower percentiles in both models commonly under predict the actual rainfall in pQPFs of both the OSM and BPPM. It is thus expected that, in this type of rainfall event, the lower percentiles are not vastly changed in the BPPM.

The RMSE values for the BPPM are better in Event 3 in that all of the percentiles, with the exception of the 0.95 percentile, show an improvement of the pQPF value against the QPE. For accumulated rainfall, percentiles above the 0.55 percentile show total rainfall closer to the accumulated rainfall of the QPE. However, note in that the middle percentiles have shown the biggest change in the BPPM where the RMSE values show that these percentiles have made the biggest improvement. This is chiefly due to the position of the QPE in the pQPF range in the hyetograph. It is situated approximately in the 0.55 – 0.60 percentile range, which means that pQPFs of percentiles near this range of the BPPM would be closest to the QPE. Moreover, due to the increased pQPF intensities in the BPPM, the higher percentiles deviate away from the QPE bringing out about less improvement compared with the middle percentiles. In Event 4, the percentiles below 0.9 are closer to the accumulated rainfall of the QPE which indicates that

the pQPFs are post processed so that the overestimation of the QPF is reduced. RMSE scores support the improvement of the pQPFs of the BPPM where all percentiles under 0.9 are closer to the QPE compared with those of the OSM.

4.4.4 Correlation Coefficient

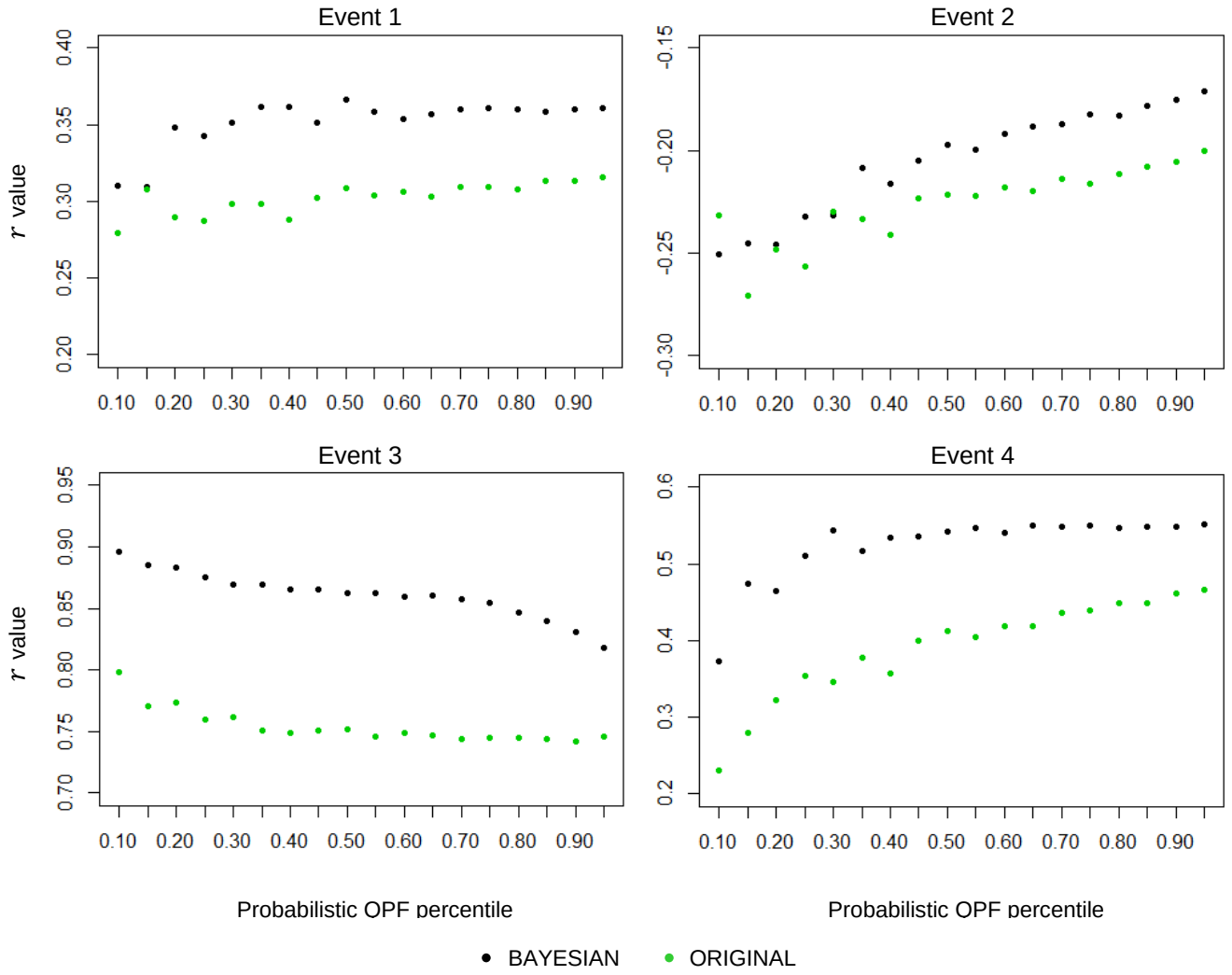

Figure 4.9. The mean r values of the pQPF of the OSM and BPPM, across the 6-hour forecast period, against the QPE for each percentile.

Figure 4.9 shows the r values for all the study events. The r values in all four events show that the pQPFs of the BPPM have a less negative (or stronger positive) relationship compared to those of the OSM. This is indicated by an increase of the value of r for all of the percentiles. The r values of Event 2 show that the pQPFs of the OSM have a negative linear relationship with the QPE. This means that they are not accurate on a temporal scale in predicting the fluctuating patterns of the QPE. After being post processed, the pQPFs have shown to reduce the strength to a weak negative relationship. Although this shows little correlation, the fluctuating path of the pQPFs is more random than before. It means that there is a lower likelihood of the paths diverging to the opposite path

of the QPE. The largest increase of r in all of the study events is seen in Event 4 where the mean r across the pQPFs in the BPPM increased by 34.3% to 0.52.

4.4.5 Summary of the results for the frontal events

In summary, the pQPFs of all four of the study events have improved so that the mean pQPF is closer to the QPE by 10.2%. This is due to the CDFs being updated using the latest QPE data, which would closely correspond to the magnitude and temporal path of the QPE. Hence, the pQPFs for the BPPM are overall better positioned around the QPE values which would provide a more realistic uncertainty range of the QPF. This is plausible despite some of the lower percentiles changing to further under predict the QPE, as is seen in Event 1.

Due to this improvement, the RMSE and Accumulation values have also altered for the post processed pQPFs. It is seen that the higher percentiles have shown the biggest improvement. This also shows that these percentiles would normally be closest to the QPE, which would provide an indication of thresholds if decision makers were to select a specific range of percentiles as the likely pQPFs that predict QPE. This would be considered for future work. The RMSE values show an improvement with an average decrease (across all the study events) by 2.2%. This is figure is small due to the data added to update the distributions having a similar variance to that of the likelihood data, or the historical data used to generate the initial distributions. Hence, this would result in minimal changes to the prior distribution of the second MCMC process. In fact, this is expected in Bayesian analysis (Gelman *et al.*, 2013).

Also, the r values of the pQPFs of the BPPM has increased in all of the study events. This is essential for hydrological purposes where modelling output using pQPFs would show to closer resemble the output using QPE based on simulations over particular time periods.

4.5 Convective storms

4.5.1 Hyetographs of probabilistic QPFs of OSM and BPPM

Figure 4.10 show the hyetographs of pQPFs of BPPM and OSM, QPE and QPF. Figure 4.11 shows the hyetograph of previous QPE preceding the QPE/QPF. This is used as the recent QPE used in the BPPM.

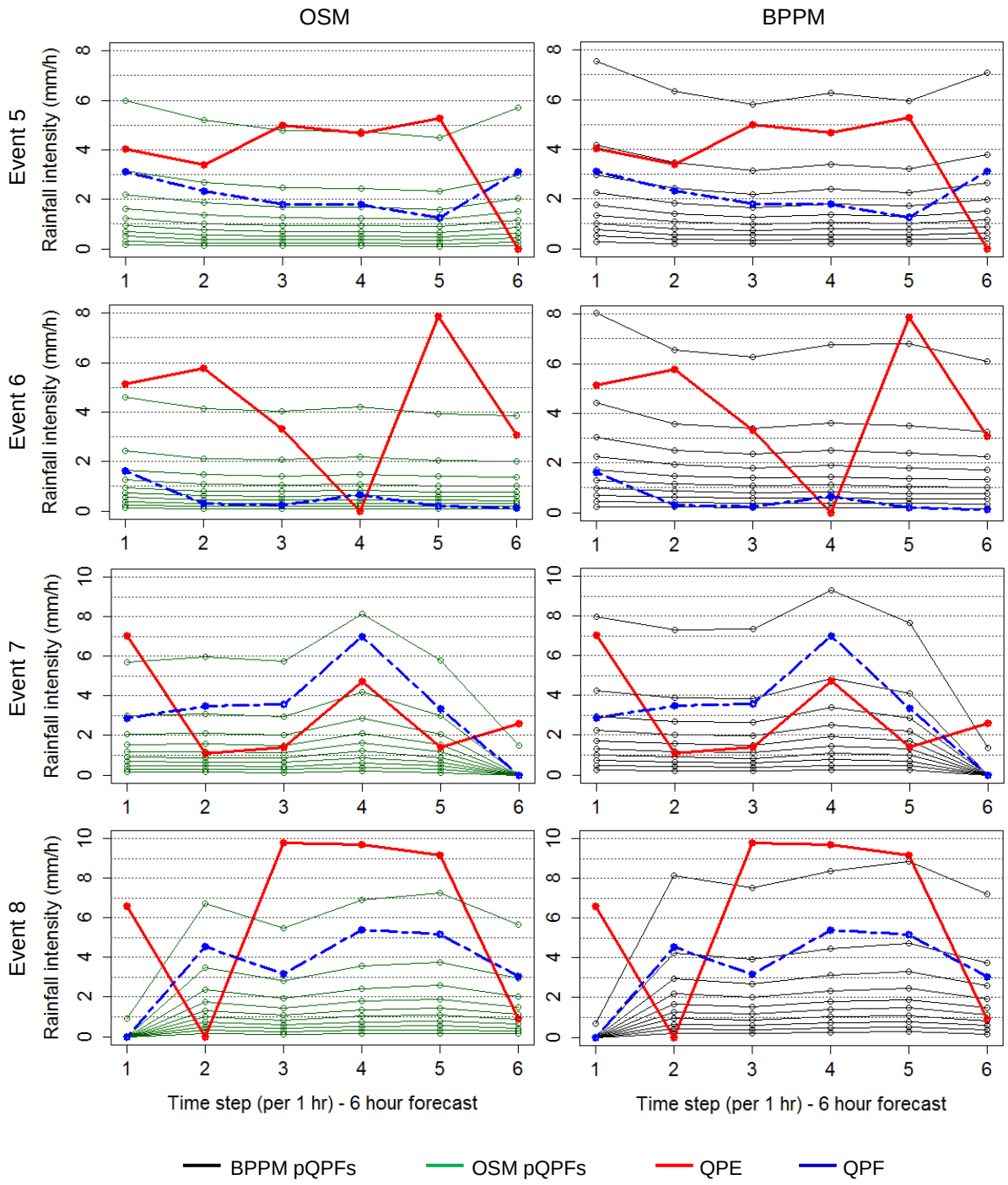

Figure 4.10. Hyetographs of the pQPFs of the OSM (left) and BPPM (right) with QPE and QPF across the 6-hour forecast period (hourly timesteps) for Events 5 – 8 (warm seasons).

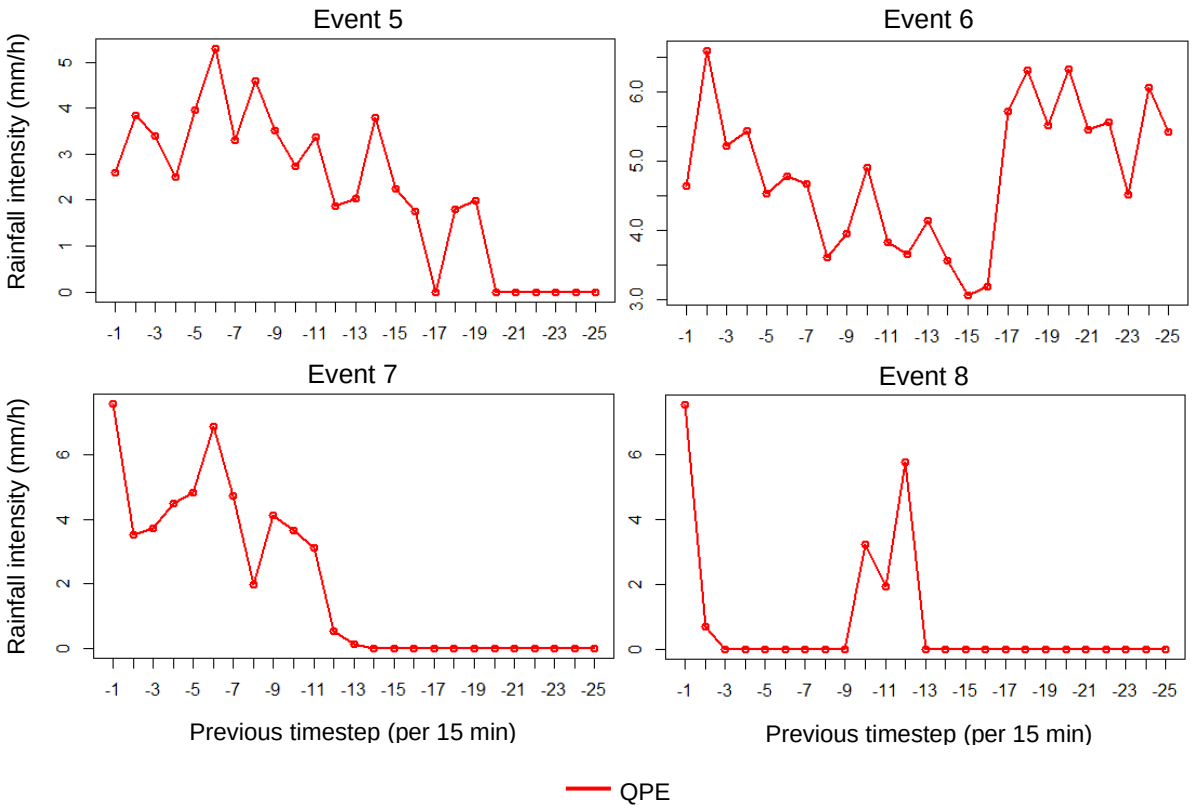

Figure 4.11. Hyetographs showing the QPE of the previous 6 hours preceding the QPF in Events 5- 8.

The QPF in Event 5 overestimates the QPE by 77% and the storm shows consistently large rainfall intensities over a prolonged period. This is normally observed in the spring season, as this is the period of the year the event had been extracted. As the QPF underestimates the QPE, the QPE falls outside of the uncertainty range. Based on the previous QPE (see Figure 4.11), the BPPM increases the rainfall intensities of the pQPFs. This produces an updated uncertainty range that the QPE is within at every temporal point. This also observed in the BPPM output of Events 6 and 7 where more of the temporal points of the QPE are within the updated uncertainty range of the pQPFs than the initial range. Visually, this makes the pQPFs of the BPPM more accurate than those of the OSM. Where the QPE shows large rainfall intensities (or peak intensities), such as in Event 6 and 8, these present challenges in that the updated pQPFs would not be able to predict them (see timesteps 3 – 5 hrs in Event 8). Although, the uncertainty range of the pQPFs of the BPPM better represent the QPE values (i.e. more accurate than the pQPFs of the OSM) this challenge highlights the requirement to study peaks of convective rainfall.

Note that events that show QPFs of large rainfall intensities (Events 7 and 8) show pQPFs of the OSM that are generally lower in rainfall intensities in comparison to the QPF. This demonstrates the problem of the OSM and in the case of convective rainfall where the QPF is likely to underestimate the QPE, the pQPFs are thus more likely to underestimate the QPE. The post processing method has therefore demonstrated to reverse this effect by increasing the rainfall intensities of the pQPFs in these events so that they are more likely to predict the QPE.

4.5.2 Measuring the accuracy of probabilistic QPFs of the BPPM using mean forecast

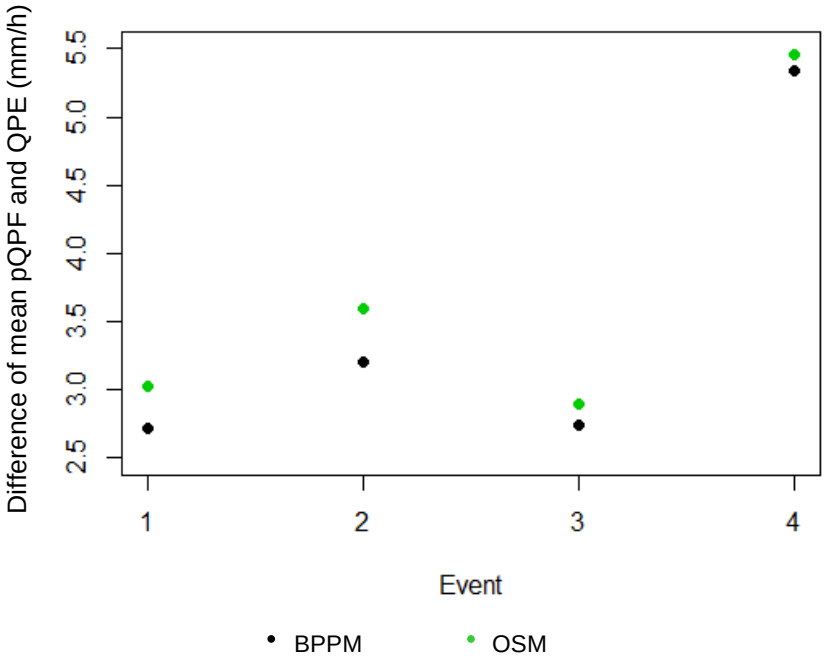

Figure 4.12. The average difference across the 6-hour forecast of the mean intensity values of the pQPFs and QPE of both the OSM and BPPM are shown for Events 5 – 8 (warm seasons).

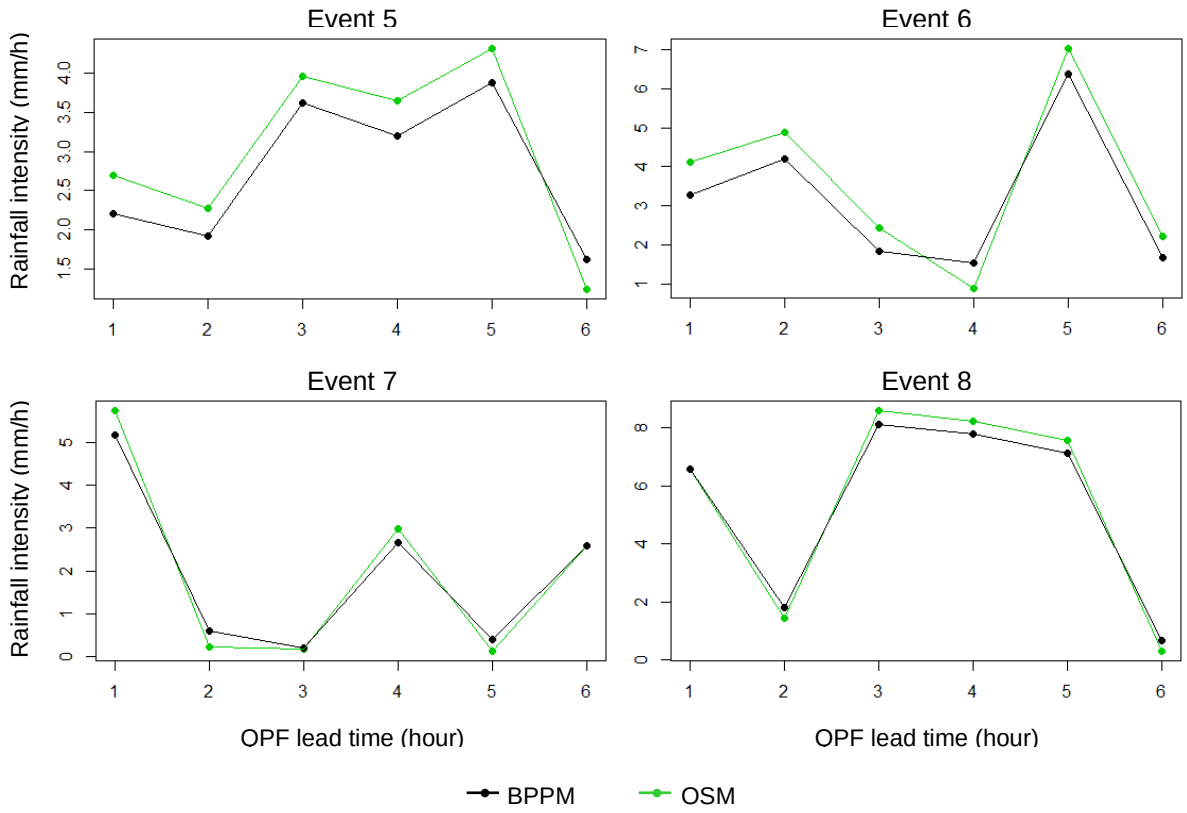

Figure 4.13. The difference of the mean intensity values of the pQPFs and QPE across the 6-hour forecast period of both the OSM and BPPM are shown for Events 5 – 8 (warm seasons).

Figure 4.12 shows the overall difference between the mean pQPF and the QPE of the OSM and BPPM and Figure 4.13 shows the differences at each timestep. Overall, the mean pQPF of the BPPM is closer to the QPE than that of the OSM. The signficance of this depends on how the pQPFs of the OSM have been updated in the BPPM. For Events 5 – 8, all of the pQPFs have generally increased in rainfall intensities. This means that the pQPFs of the OSM were generally underestimating the QPF, and hence underestimating the QPE. If the mean pQPF has moved closer to the QPE, the updated pQPFs have reduced the underestimation and thus produce an uncertainty range that is more accurate. This means the QPE in these events are more likely to fall within the uncertainty range indicated by the pQPFs of the BPPM than the OSM. At some timesteps of Events 5 – 8, the mean pQPF value of the BPPM is worser than the OSM (e.g. 6th timestep in Event 5 and 4th timestep in Event 6). This is due to the dynamic nature (i.e. highly fluctuating characterstics) of the warm events. For example, the 6th timestep of Event 5 and the 4th timestep of Event 6 show zero QPE values

with a nonzero QPF value. Furthermore, at these timesteps, these are the only points during the storm with the lightest/no precpitation. Hence, as the pQPFs overall show an underestimation of both the QPF and QPE, these points are not considered when the updated pQPFs generally increase precpitation intensities. Hence, the mean pQPF value at these points would be worse but not causing significant effect on the overall performance of the updated pQPFs.

4.5.3 Accumulated rainfall and RMSE

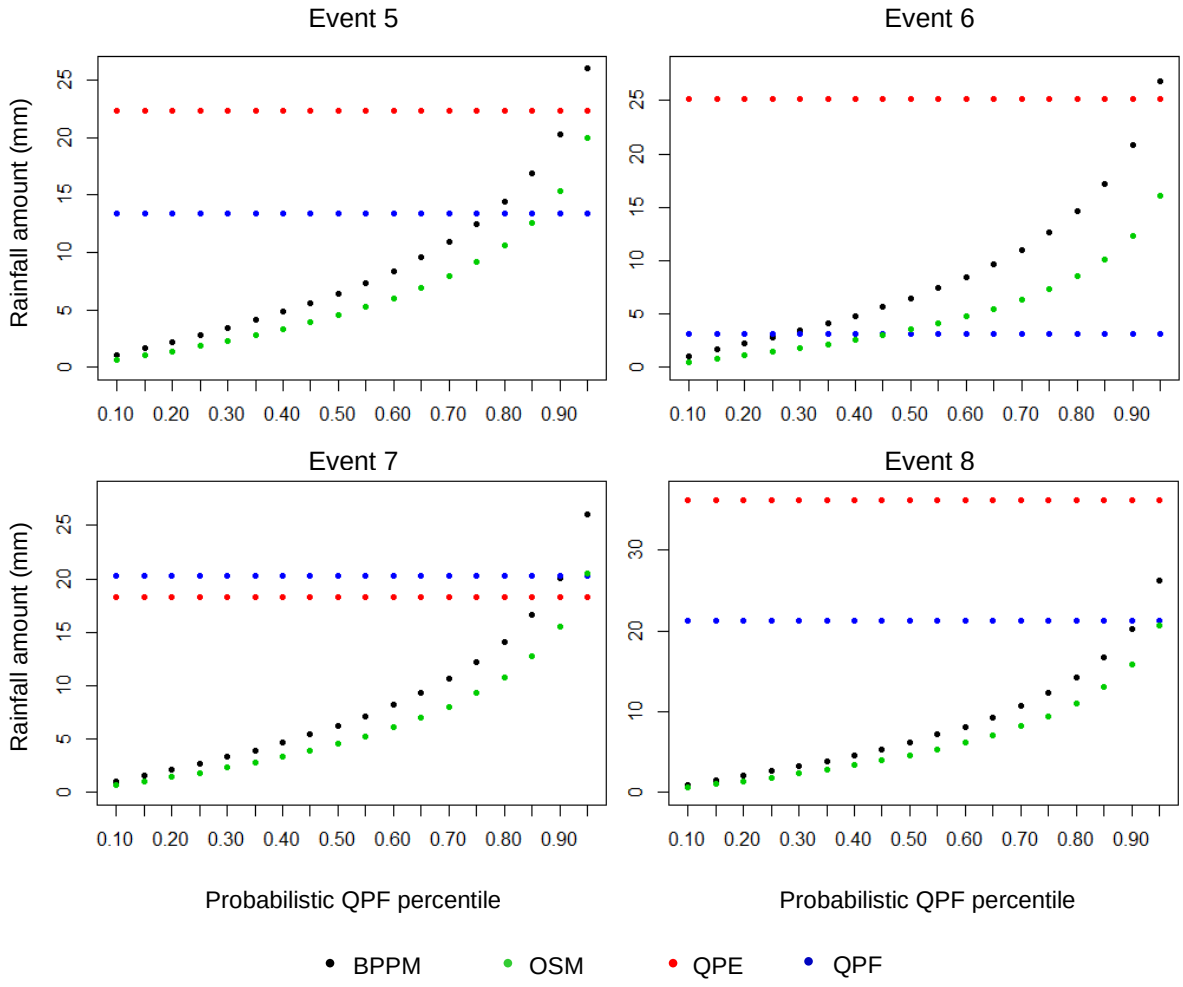

Figure 4.14. Rainfall accumulation across the 6-hour forecast period of the pQPFs of the OSM and BPPM, QPE and QPF for each percentile, for Events 5 – 8 (warm seasons).

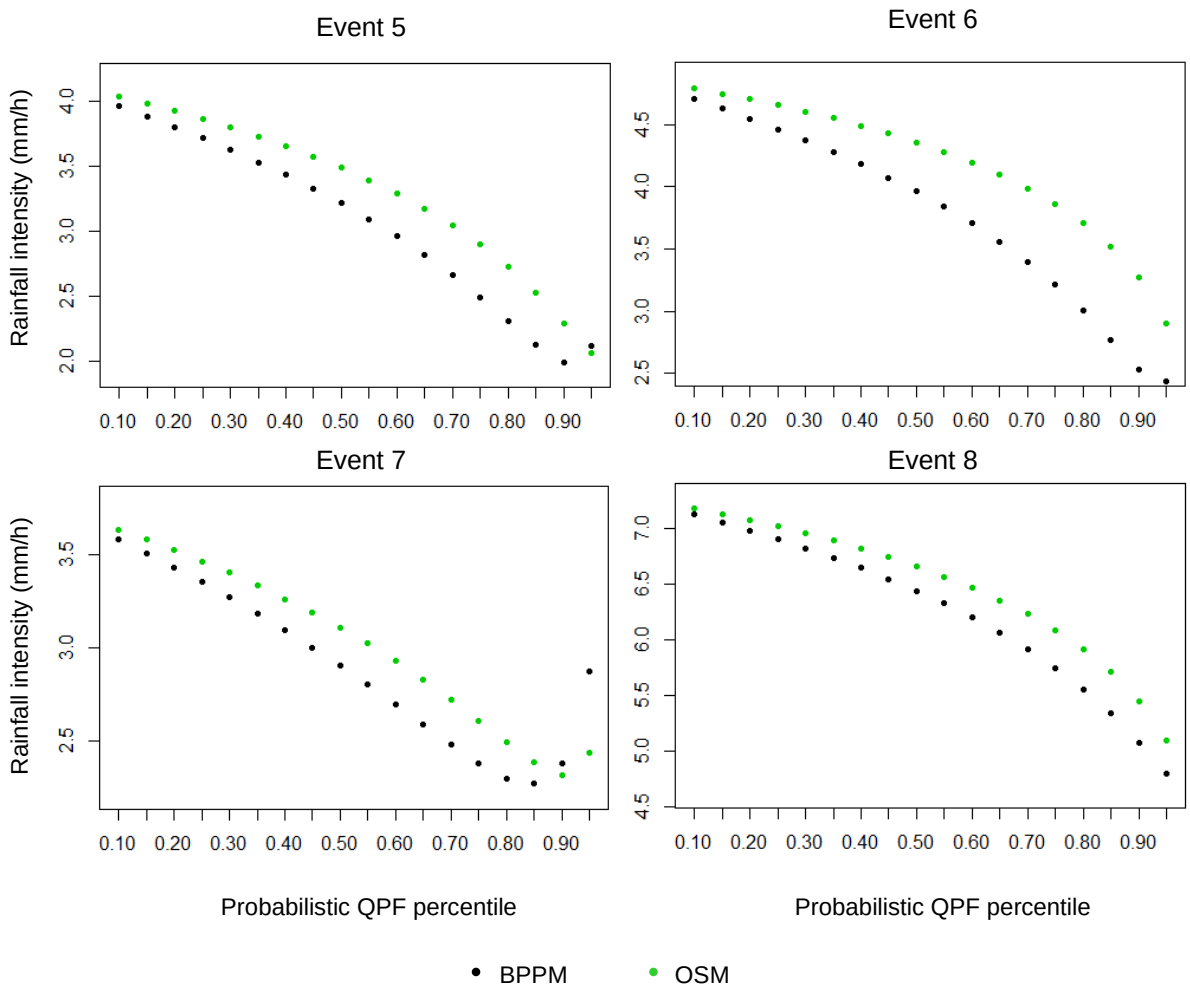

Figure 4.15. The mean RMSE values of the pQPF of the OSM and BPPM, across the 6-hour forecast period, against the QPE for each percentile.

Figure 4.14 shows rainfall accumulation of the pQPFs of the OSM and BPPM, the QPF and QPE across the 6-hour forecast period. In all four warm events, the rainfall accumulation of the pQPFs of the BPPM is closer to the QPE accumulation than those of the OSM. This indicates that all of the pQPFs of the BPPM are more accurate. Also, note that the QPE accumulation of all four events are large relative to the accumulations of the pQPFs of the OSM. This chiefly due to the two issues of the OSM: (1) the QPF of the event largely underestimates the QPE and (2) large rainfall QPFs produced pQPFs that generally underestimate the QPF. However, the output of the post processing methods described in this chapter clearly demonstrate that updating the pQPFs of the OSM tackle these two issues.

The RMSE values of each pQPF of the OSM and BPPM for all four warm events are given in Figure 4.15. Nearly all of the pQPFs of the BPPM show to have lower

RMSE values in comparison to those of the OSM. Exceptions include the largest percentiles (i.e. 90th and 95th percentiles) in Events 5 and 7. This is expected and has no significant effect on the overall performance of the post processing method.

4.5.4 Correlation Coefficient

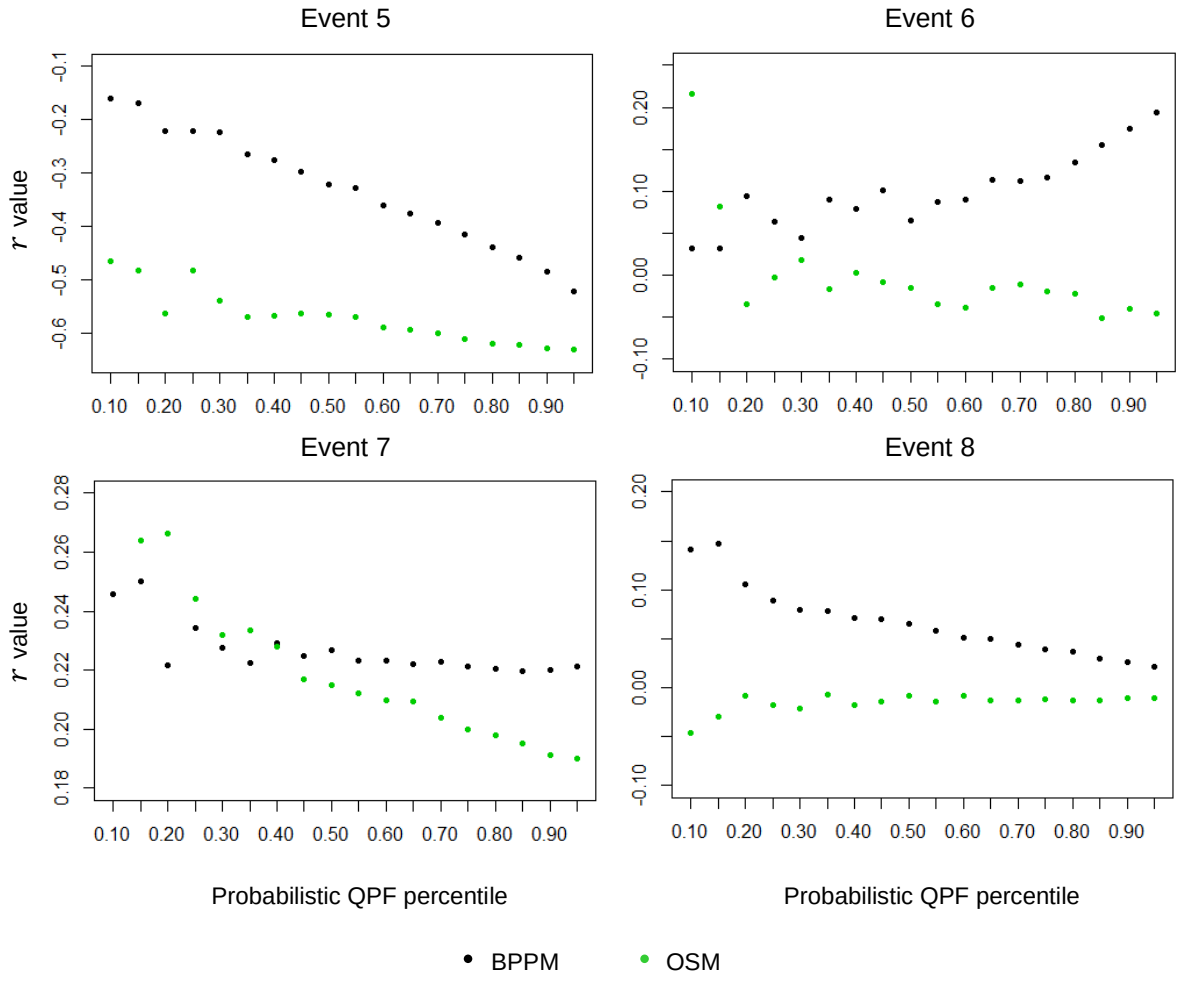

Figure 4.16. The mean r values of the pQPF of the OSM and BPPM, across the 6-hour forecast period, against the QPE for each percentile.

Figure 4.16 shows the r values of the pQPFs of the OSM and BPPM against the QPE. Similar to the performance of the post processing method with the cool events in case study 1, the pQPFs of the warm events also show mean r values closer to 1 in the BPPM compared to the OSM. This shows that the post processing reduces the negative relationship of the temporal path of the pQPFs against the QPE across the 6-hour forecast period. This highlights the success

of the post processing method in improving the temporal structure of the rainfall of the pQPFs even in convective rainfall. It is therefore important to consider using the latest QPE data that is not part of the historical data sets to update pQPFs as they would show more accurate information about the latest rainfall characteristics on a temporal scale.

4.6 Additional study events

An additional two rainfall events are used to verify the BPPM. These two rainfall events are not necessarily representative of the characteristics of the season of which they were sourced. The purpose of using them to verify the BPPM is to assess its performance in extreme or uncommon rainfall characteristics. The event presented in section 4.6.1 shows a rainfall storm from a warm season with a very large peak that presents a forecast error not observed in the historical datasets. The event presented in section 4.6.2 shows a rainfall storm from a warm season with relatively light and less temporally fluctuating rainfall (which the opposite is normally observed in warm seasons).

4.6.1 Rainfall storm with a large peak

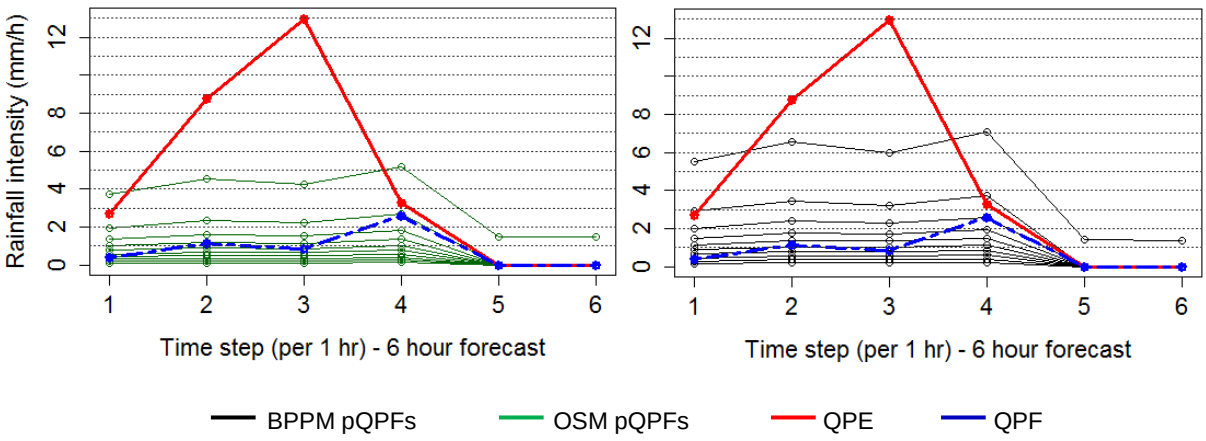

Figure 4.17. Hyetographs of the pQPFs of the OSM (left) and BPPM (right) with QPE and QPF across the 6-hour forecast period (hourly timesteps) for Event 9.

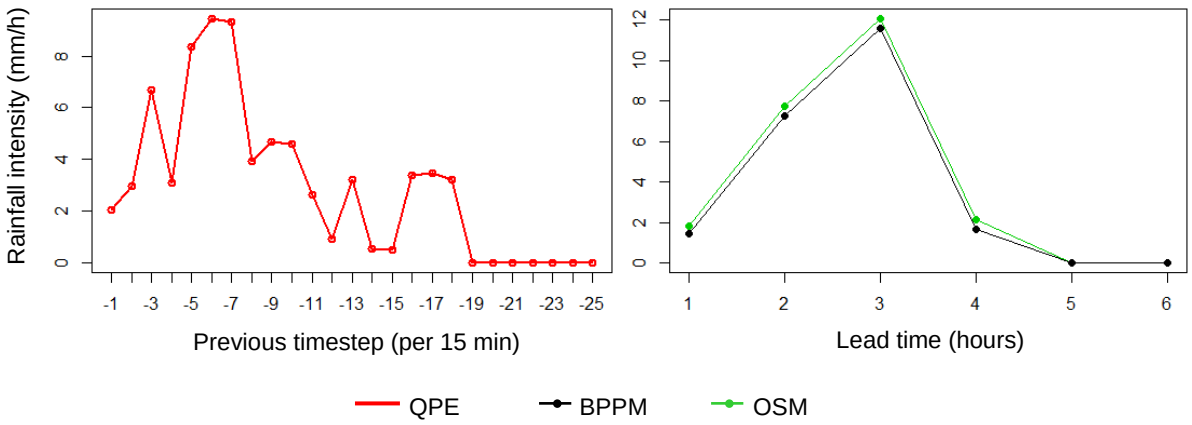

Figure 4.18. Hyetographs showing the QPE of the previous 6 hours preceding the QPF (left) and the difference of the mean intensity values of the pQPFs and QPE across the 6-hour forecast period of both the OSM and BPPM (right) for Event 9.

The purpose of using the Bayesian based post processing method is to update the distributions based on a different set of QPE data. This is because QPE data may fall outside of the uncertainty range presented by the pQPFs generated from a fixed set of historical QPF/QPE data. However, the QPE may largely be underestimated by the QPF so that the uncertainty range presented by the pQPFs of the OSM may be overwhelmingly small in comparison to it. This would occur due to the inaccuracies of the QPF data, which may not be remedied without further specific analysis, such as studying the preservation of peak rainfall in storm-specific (i.e. convective or frontal) rainfall. As this is outside the scope of the methods introduced in this chapter, it is sufficient to show that the post processing method is able to produce more accurate pQPFs by using the latest QPE as a way of improving pQPFs that do not accurately represent the magnitude of QPE values across the 6-hour forecast period.

In Event 9, the QPF underestimates the QPE by 82% (i.e. the accumulation of the QPE is 452% of that of the QPF) (see Figure 4.17). This shows an event that has a poor performing rainfall forecast and therefore would not be reliable for hydrological purposes. The QPE has temporal values that fall outside the magnitude range presented by the pQPFs of the OSM. Particularly, there is a large peak of 13 mm/h at the third timestep. As this forecast error had not been predominantly seen in the historical data sets, the OSM is not able to produce pQPFs with an uncertainty range to represent the extent of this peak intensity

value. Hence, this would be regarded as an ‘extreme’ or ‘anomalous’ value, and thus it is expected that both the pQPFs of the OSM and the BPPM may not accurately represent the QPE with these values. However, the pQPFs of the BPPM have increased in rainfall intensities to become closer to the QPE values across the 6-hour forecast period. At a temporal scale, the mean pQPF of the BPPM is closer to the QPE at all the timesteps (with the exception of the 5th and 6th timesteps as they have zero rainfall QPF/QPE values) (see right figure of Figure 4.18). Overall, the mean pQPF of the BPPM has moved closer to the QPE by 8.48%.

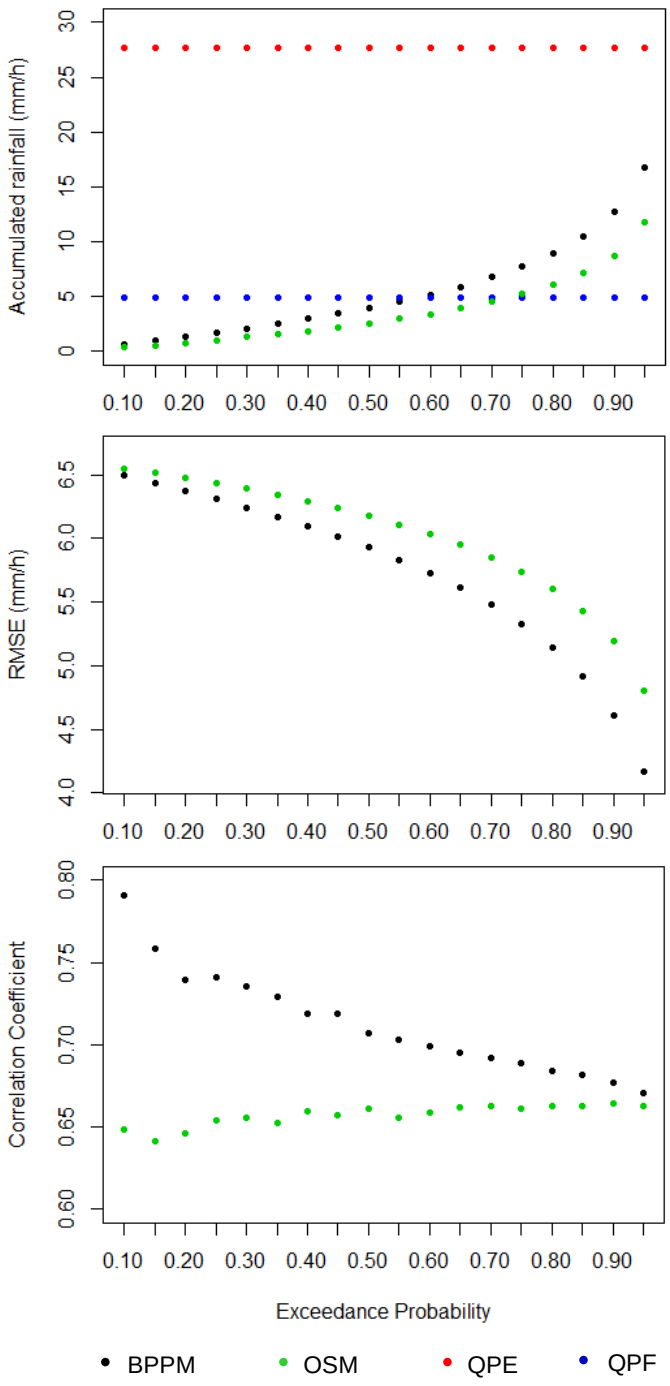

Figure 4.19. Rainfall accumulation (top), the mean RMSE values (middle) and the mean r values (bottom) of the pQPF of the OSM and BPPM, across the 6-hour forecast period, against the QPE for each percentile for Event 9.

Figure 4.19 further demonstrates the benefit of the post processing method to improve a poor performing QPF with a QPE showing a very large peak. The accumulated rainfall values of all the pQPFs of the BPPM move closer to the QPE. Also, the RMSE values of all these pQPFs have decreased and the magnitude by which they decrease increases over increasing percentiles.

Furthermore, their temporal paths across the 6-hour forecast period have changed so that they have a lower negative relationship with the QPE. Hence, the pQPFs of the BPPM are more accurate showing that the post processing method improves pQPFs even in poor performing QPFs.

4.6.2 Warm event with light rainfall

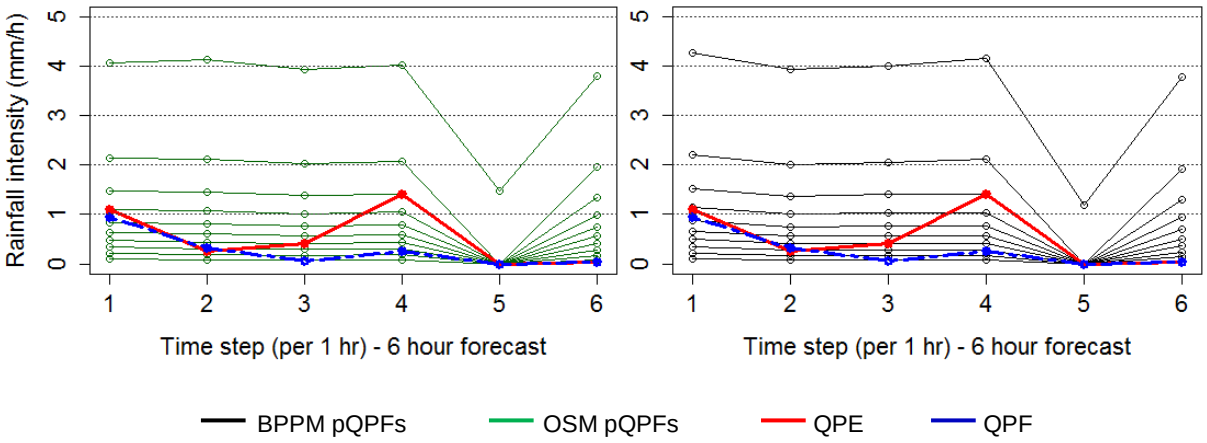

Figure 4.20. Hyetographs of the pQPFs of the OSM (left) and BPPM (right) with QPE and QPF across the 6-hour forecast period (hourly timesteps) for Event 10.

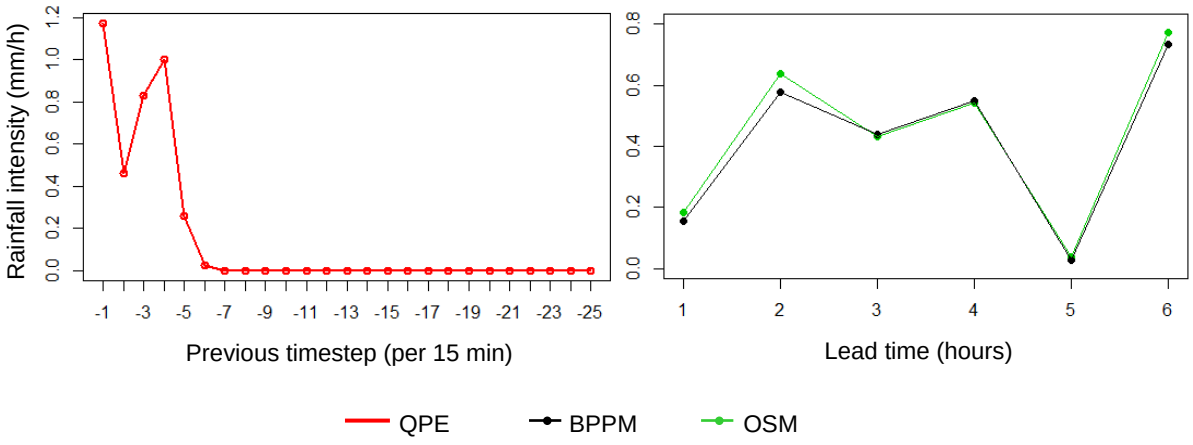

Figure 4.21. Hyetographs showing the QPE of the previous 6 hours preceding the QPF (left) and the difference of the mean intensity values of the pQPFs and QPE across the 6-hour forecast period of both the OSM and BPPM (right) for Event 10.

The hyetograph of Event 10 (see Figure 4.20) shows a light rainfall event extracted from the warm seasons. During most of the storm duration, the rainfall intensity doesn't exceed 1 mm/h and it has a peak intensity of around 1.4 mm/h.

The QPF of this event also underestimates the QPE by around 44%, as expected from an event from the warm seasons (similar to Events 5 – 8). Despite the underestimation of the QPF, the pQPFs of the BPPM have not been updated to the same extent as seen in the case studies, particularly at lead times 3 – 6 hours. The biggest change is observed between lead times 1 - 3 hours because at these timesteps in the right figure of Figure 4.21 the QPF more closely predicts the QPE. It indicates that in the forecast errors in the historical data (OSM) the QPE is normally underestimated by the QPF. Hence, if the latest QPE data contains values close to the QPF values (which are relatively low), this is then weighted against the QPE values in the historical data sets so that the rainfall values of the pQPFs are lowered slightly. This would have a bigger effect on QPE values that are closer to the latest QPE data updating the pQPFs and less on those that match the forecast errors in the historical data. This is the reason why less change is observed between lead times 3 – 6 hours. Nonetheless, the change in pQPF rainfall magnitudes signifies that they are more accurate after being post processed.

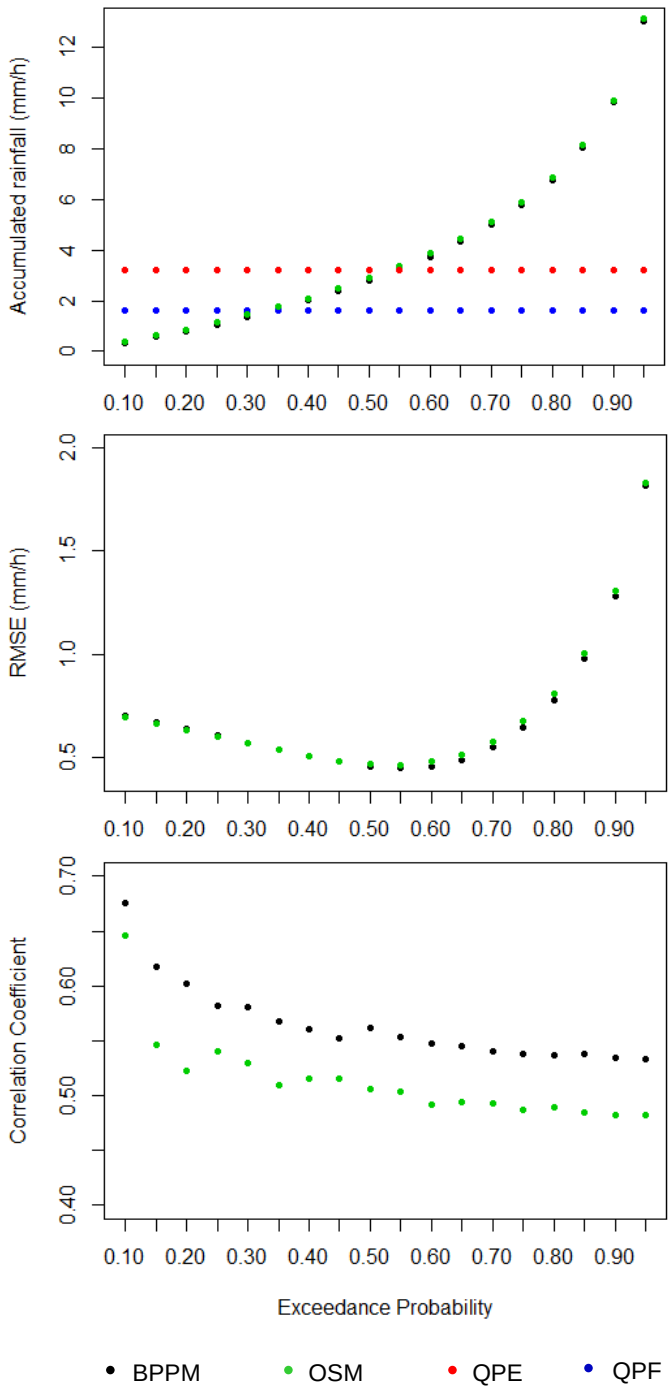

Figure 4.22. Rainfall accumulation (top), the mean RMSE values (middle) and the mean r values (bottom) of the pQPF of the OSM and BPPM, across the 6-hour forecast period, against the QPE for each percentile for Event 10.

Figure 4.22 shows rainfall accumulation, mean RMSE and mean r values of pQPFs of the OSM and BPPM. Due to there not being a large difference between the rainfall magnitudes of the pQPFs of the BPPM and OSM, the accumulated rainfall of the pQPFs have not changed to large extent. However, despite the small difference, the accumulated rainfall of the updated pQPFs have reduced to

be closer to the accumulated rainfall of the QPE. This is also the same case for the RMSE values of each pQPF against the QPE as the RMSE values have decreased for the BPPM.

The mean r values of the all the pQPFs, against the QPE, have increased (become more positive) for the BPPM. This shows that despite there not being a large change in the rainfall magnitudes of the pQPFs, their temporal paths across the 6-hour forecast period are more positively correlated with the QPE. This means their temporal structure is more accurate in comparison with that of the pQPFs of the OSM. This is an indicator of success.

4.7 Conclusions

This chapter has introduced a two-step post processing methodology for probabilistic QPFs using Metropolis Hastings (MH) Monto Carlo Markov Chain (MCMC) to consider recent QPE data. Using a stochastic model, CDFs are initially generated from historical comparisons between radar QPF and QPE data. The parameters of these CDFs are updated in two applications of MH MCMC where the posterior distribution of the first stage is the prior distribution of the second stage. The final parameter set after the second MH MCMC is used in a posterior predictive distribution which is used to generate updated CDFs. Finally, updated probabilistic QPFs are produced by sampling rainfall values by their exceedance probability on the CDFs.

Historical radar based Nowcast QPF and Rain Radar (i.e. QPE) data in the North East of England between September 2015 and February 2016 for frontal storms, and June 2016 and August 2016 for convective storms are used in the stochastic model to produce the initial probabilistic QPFs. The probabilistic QPFs are generated for 6-hour lead time with an hourly timestep. Four QPFs between September 2016 and February 2017 for case study 1 (frontal storms), four QPFs between June 2017 and August 2017 for case study 2 (convective storms) and two additional QPFs were chosen as study events (i.e. 10 study events). The Bayesian Post Processing Model is applied to the study events and the performance of the postprocessed probabilistic QPFs is evaluated against the probabilistic QPFs from the Original Stochastic Model. The main conclusions drawn from this study are as follows:

- The Bayesian updating process alters the probabilistic QPFs so that the mean probabilistic QPF is closer to the QPE by an average of 10.2%. This indicates that the probabilistic QPFs are better positioned so that the observed rainfall is less likely to fall outside of the uncertainty range, which makes them more accurate.
- Across all the study events, after being postprocessed the Pearson's r values show that the temporal paths of the post processed probabilistic QPFs are more positively correlated to the path of the QPE, or have reduced the negative dependence of the paths. In this way, the temporal structure of the probabilistic QPFs has improved.
- The RMSE has lowered especially for the higher percentiles of the pQPFs across all ten study events. Whilst this shows that these percentiles have updated to become more accurate, it also demonstrates that the higher percentiles have potential to indicate thresholds of the likely rainfall intensity values the QPE would equate to.

Overall, the approach described in this chapter attempts to fill the gaps of post processing radar based probabilistic QPFs. Therefore, this motivates the introduction of probabilistic rainfall forecasting in real time for bodies that manage flood risk, especially where the latest rainfall data is readily available. Therefore, this would provide a useful way of incorporating new rainfall data to make rainfall/flood forecasting more accurate and computationally feasible.

An area to explore is to perform this methodology for many study events. As the method produces more accurate pQPFs, specific percentiles could be used to define thresholds for rainfall intensities where the QPE would lie. This analysis would deepen understanding of the accuracy of specific QPF/QPE. Fnially, various parameters of the Bayesian Post Processing Model could be changed in order to further analyse the performance of the method. For example, different sizes of the recent QPE could be used to post process the probabilistic QPFs.

5 Estimating flood extent using spatial analysis of radar Quantitative Precipitation Estimates

5.1 Introduction

The spatial distribution of rainfall over a sewer catchment has an influence on flood dynamics of an urban catchment. It has been shown that spatial structure of the rainfall field was the main contributor to a flash food event studied by Lay and Saulnier (2007). Also, the spatial distribution of rainfall influenced the flood extent when considering the distribution of soil properties (Anquetin *et al.*, 2010; Delrieu *et al.*, 2005). However, the response of the sewer network is similarly influenced by the spatial variability of the storm. It has been shown by Schellart *et al.* (2012) that the spatial variability of radar data produced significance differences in the sewer flow predictions. This highlights that the impact of spatial variability of rainfall on sewer flooding should be considered.

In the previous chapter, probabilistic QPFs had been introduced in detail. When used as input to hydraulic models the model variables (i.e. sewer depth or flow) could then be interpreted probabilistically. The advantage of this is that the uncertainty range of a model variable (i.e. depth or flow) could be realised for a deterministic QPF. However, probabilistic QPFs would need to be generated for each radar grid over the sewer catchment to run hydraulic simulations. However, this would have implications on the spatial distribution of the rainfall over the catchment. Specifically, depending on what percentiles of the probabilistic QPFs are chosen at each grid, the spatial distribution of the field may significantly differ from the actual spatial distribution (i.e. from the deterministic QPFs at each grid). This means that using probabilistic QPFs as gridded rainfall forcing to a hydraulic model may not accurately depict the spatial structure of the rainfall field. Whilst spatial dependence could be assumed (e.g. use the nth percentile of probabilistic QPFs at each grid to produce the rainfall over the sewer catchment), using different percentiles at each radar grid may result in different flooding extents. This is because the spatial distribution of the probabilistic QPFs over the sewer catchment would be different. Hence, a spatial analysis should be accompanied with hydraulic sewer flood forecasting that use probabilistic QPFs.

Another limitation of using probabilistic QPFs in real-time sewer flood forecasting is that many hydraulic simulations would need to be performed for each probabilistic QPF simultaneously. This requires significant computational resources. Due to this limitation, simple hydraulic and mathematical models are used instead of computationally heavy hydraulic models (Kimura *et al.*, 2010). By using these models for simulating flood variables (i.e. flow or depth) the computational time is reduced.

This chapter introduces an approach that predicts sewer flooding based on a historical analysis of the spatially varying characteristics of radar QPE and hydraulically simulated flood variables. There are two components of this method; firstly, a spatial analysis of QPE events based on four spatial rainfall variables: mean rainfall, variance of the rainfall field and the use of two spatial indexes representing the 'spatial moments of rainfall'. Secondly, the development of two generalised linear models that use the spatial rainfall variables to predict total flood volume and total floods of four sewer catchments that are of different sizes. The benefits of the generalised linear models are that the hydraulically simulated flood volume and total floods could be estimated without running computationally expensive hydraulic simulations. This approach can be used to select the appropriate percentile combinations of probabilistic QPFs in each grid over a sewer catchment. This would be conducive for estimations of the flood extents directly from spatial information of probabilistic radar QPFs in a real-time sewer flood forecasting system.

5.2 Method for predicting model variables using spatial analysis

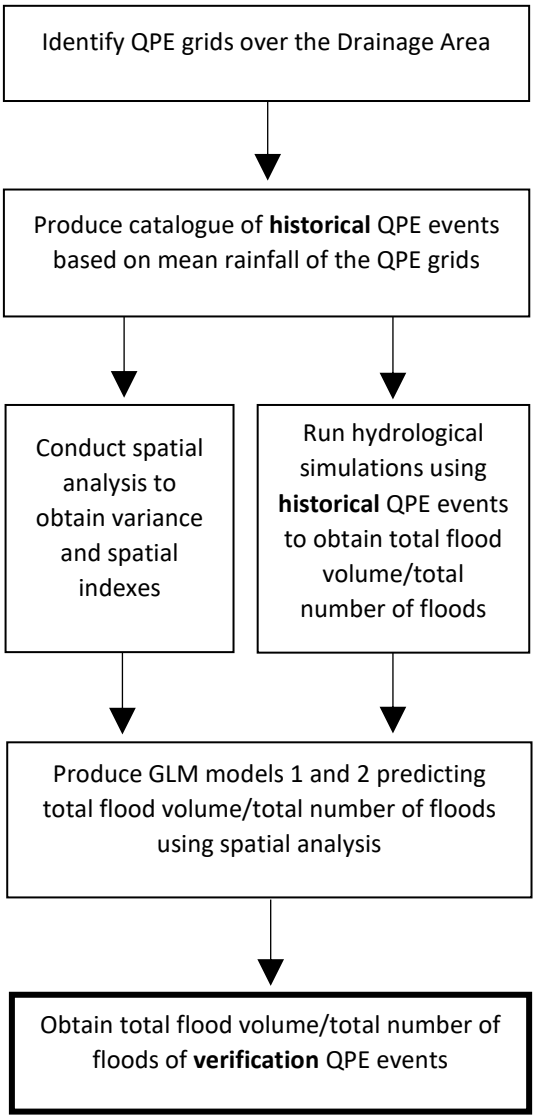

Figure 5.1. The method to predict flood volume/number of floods using spatial analysis of rainfall over the sewer catchment.

Figure 5.1 shows the method for predicting model variables using spatial analysis. Firstly, radar QPE grids over a sewer catchment are identified. Using rainfall from these grids, a catalogue of historical QPE events are extracted based on the mean rainfall of the QPE grids over the sewer catchment. Spatial analysis of the events is conducted to obtain mean rainfall, variance and values for two spatial indexes. The QPE events are used to produce hydraulic simulations to obtain total flood volume and total number of floods. Two GLM models are produced using different sets of spatial variables to predict the flood volume and total flood number. The GLMs are then verified by predicting total flood volume

and total number of floods using spatial information of verification QPE events. The sections 5.2.1 – 5.2.4 explain these processes in more detail.

5.2.1 Identify QPE radar grids over the sewer catchment

The QPE radar grids over the sewer catchment are identified in the sewer model that receive rainfall. For sewer catchments that are relatively small, there would be fewer QPE grids providing rainfall over the area and the opposite would be true for larger sewer catchments. Generally, it is expected that the more grids there are over the sewer catchment, a more accurate analysis of the spatial variation of the rainfall could be conducted. This is because they would present more information of the spatial distribution of rainfall. Hence, the method presented in this chapter would be more appropriately conducted on relatively larger sewer catchments, particularly when using the spatial indexes (introduced later).

5.2.2 Extracting historical QPE events based on mean rainfall over the QPE radar grids

The number of radar QPE grids N over a sewer catchment are identified. Per QPE event ev, six-hour rainfall accumulations over each grid j are calculated, denoted A_j^{ev}. A set of A_j^{ev} for the N QPE grids is produced, denoted AC^{ev}. The mean of AC^{ev}, denoted $E(AC^{ev})$, is then calculated:

$$E(AC^{ev}) = \frac{AC^{ev}}{N} \tag{5.1}$$

Based on $E(AC^{ev})$ for each ev, categories of mean rainfall are produced by discretising the values in 10 mm accumulated rainfall bins. Rainfall events ev are organised in this manner to produce a catalogue of 'historical' QPE events.

The 6 hour lead time corresponds to the maximum lead time of the radar QPF data source used in this study (i.e. Nowcast from UKMO). This is because the analysis done in this chapter could be applied to radar QPFs. A lead time of 6 hours has been applied across all the catchments irrespective of catchment size (and concentration times) for consistency purposes. Furthermore, should this method be used to estimate sewer flooding in real-time it would be most

beneficial to consider the maximum lead time of the QPF (which is 6 hours in this case).

5.2.3 Spatial analysis of individual events

Spatial analysis of AC^{ev} is performed by calculating the variance, standard deviation and the use of two spatial indexes from literature.

Variance and standard deviation are useful metrics for measurement errors and represent the spread of the data around the mean (Yu *et al.*, 2016). Large values indicate that the rainfall values at different grids are dissimilar and are highly varied, whereas smaller values indicate similar rainfall values and signify uniformity of rainfall over the catchment.

As AC^{ev} is a discrete dataset, the variance (Var) and standard deviation (SD) of AC^{ev} are calculated as follows:

$$Var(AC^{ev}) = \frac{1}{N}\sum_{j=1}^{N}\left(A_j^{ev} - E(AC^{ev})^2\right) \quad (5.2)$$

$$SD(AC^{ev}) = \sqrt{\frac{1}{N}\sum_{j=1}^{N}\left(A_j^{ev} - E(AC^{ev})^2\right)} \quad (5.3)$$

Two indexes are also used as measures of spatial variability, which have been introduced by Zoccatelli *et al.*, (2010) and used by Douinot *et al.*, (2016) for flash flood forecasting. These indexes describe the spatial moments of catchment rainfall that relate the spatial positioning of rainfall in relation to the catchment structure. These indexes are used to determine the spatial positioning of rainfall in relation to the distances of any point in a sewer catchment to its outlet node. Whilst the spatial indexes apply to a natural catchment with the flow pathways leading to the outfall, the sewer catchment could be characterised as a natural catchment with the sewer flow pathways leading to the outlet node. This assumption would enable the use of the indexes that could provide useful information of sewer catchments in spatially varying rainfall storms. The purpose of this analysis is to establish correlations between these indexes and the flood variables to identify sewer catchments that could use these indexes to predict sewer flooding.

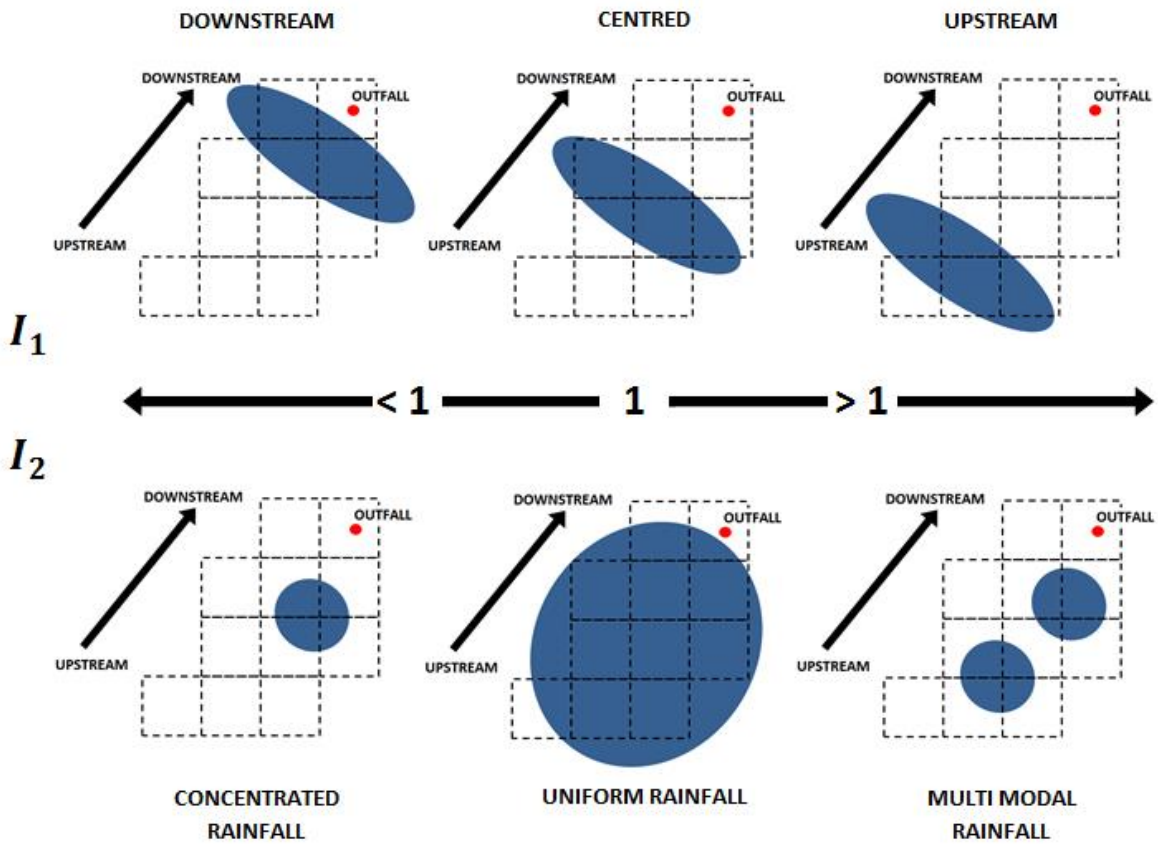

Figure 5.2. Interpretations of spatial indexes $\boldsymbol{I_1}$ *and* $\boldsymbol{I_2}$ *.*

Figure 5.2 describes the interpretations of the spatial indexes. The first index, denoted $\boldsymbol{I_1}$, describes the position of the rainfall over the sewer catchment. A value below 1 means that the rainfall is localised downstream of the sewer catchment whereas a value above 1 describes rainfall localised upstream. If this index has a value near or equal to 1 means that the rainfall is localised at the centre of the sewer catchment. The second index, denoted $\boldsymbol{I_2}$, describes the concentration of the rainfall over the sewer catchment. A value below 1 describes concentrated rainfall (which is characterised to be a convective type rainfall storm) whereas a value above 1 indicates rainfall with multiple concentrated regions. If the value is equal to 1 this indicates globally uniform rainfall over the sewer catchment. In equations 5.4 and 5.5, the flow distance from a QPE grid j to the outfall node is denoted F_j^{ev}, for event ev, A_{total}^{ev} is the total rainfall over the sewer catchment and B^{ev} is the total area of the catchment. In this study, B^{ev} is equal to the total area each QPE grid contributes to the rainfall over the sewer catchment. As the area of each QPE grid is 1 km^2, B^{ev} is equal to N.

$$\boldsymbol{I_1} = \frac{\frac{1}{A_{total}^{ev}}\sum_{j=1}^{N}\left(A_j^{ev} * F_j^{ev}\right)}{\frac{1}{N}\sum_{j=1}^{N} F_j^{ev}} \tag{5.4}$$

Here, $\frac{1}{A_{total}^{ev}}\sum_{j=1}^{N}\left(A_j^{ev} * F_j^{ev}\right)$ represents the average flow distance from the spread of rainfall in all the QPE grids to the outfall. $\frac{1}{N}\sum_{j=1}^{N} F_j^{ev}$ represents the average flow distance from the area distribution to the outfall.

Zoccatelli *et al.* (2011) described $\boldsymbol{I_2}$ to be the dispersion of the rainfall-weighted flow distances about their expectation values to the ratio of the dispersion of the flow distances, as below:

$$\boldsymbol{I_2} = \frac{\frac{1}{A_{total}^{ev}}\sum_{j=1}^{N}\left(A_j^{ev} * F_j^{ev2}\right) - \left(\frac{1}{A_{total}^{ev}}\sum_{j=1}^{N}\left(A_j^{ev} * F_j^{ev}\right)\right)^2}{\frac{1}{N}\sum_{j=1}^{N} F_j^{ev2} - \left(\frac{1}{N}\sum_{j=1}^{N} F_j^{ev}\right)^2} \tag{5.5}$$

where $\frac{1}{A_{total}^{ev}}\sum_{j=1}^{N}\left(A_j^{ev} * F_j^{ev2}\right) - \left(\frac{1}{A_{total}^{ev}}\sum_{j=1}^{N}\left(A_j^{ev} * F_j^{ev}\right)\right)^2$ represents the variance (or dispersion) of the flow distances F_j^{ev} weighted against the rainfall grid accumulations A_j^{ev}, and $\frac{1}{N}\sum_{j=1}^{N} F_j^{ev2} - \left(\frac{1}{N}\sum_{j=1}^{N} F_j^{ev}\right)^2$represents the variance (or dispersion) of the flow distances F_j.

$$\boldsymbol{I_2} = \frac{\frac{1}{A_{total}^{ev}}\sum_{j=1}^{N}\left(A_j^{ev} * F_j^{ev2}\right) - \left(\frac{1}{A_{total}^{ev}}\sum_{j=1}^{N}\left(A_j^{ev} * F_j^{ev}\right)\right)^2}{\frac{1}{N}\sum_{j=1}^{N} F_j^{ev2} - \left(\frac{1}{N}\sum_{j=1}^{N} F_j^{ev}\right)^2} \tag{5.6}$$

5.2.4 Generalised Linear Models

1D sewer flood simulations are produced using Infoworks ICM across the six-hour period of the historical events for selected catchments. The flood variables used in this study is the sum of the flood volume of flooded nodes in the model sewer catchment, denoted $\boldsymbol{V^a}$, and the number of flooded nodes, denoted $\boldsymbol{V^b}$. These variables are used as the response variable in two implementations of a GLM based on a Gaussian distribution for total food volume and Poisson distribution for total floods. For a random realisation, denoted x, the PDF of the Gaussian distribution is represented as

$$F(x) = \frac{1}{\sqrt{2\pi{\sigma_a}^2}} e^{\frac{-(x-\mu_a)^2}{2{\sigma_a}^2}} \tag{5.7}$$

and the Probability Mass Function (PMF) of Poisson distribution is:

$$\frac{1}{\sqrt{2\pi{\sigma_a}^2}} e^{\frac{-(x-\mu_a)^2}{2{\sigma_a}^2}} \frac{\beta_b^x e^{-\beta_b}}{x!} \tag{5.8}$$

Where $\mu_a$and σ_a are the gaussian mean and standard deviation, respectively, and β_b is the Poisson rate parameter.

Total number of floods is assumed to have a Poisson distribution and is treated as such to resemble count data. Furthermore, the number of floods can only be represented as a whole number.

The predictor variables in the two GLMs vary. There are four predictor variables altogether in the GLMs that are:

- Variance, denoted $\boldsymbol{VAR}$
- Mean Rainfall, denoted $\boldsymbol{MR}$
- Index 1, denoted $\boldsymbol{I_1}$
- Index 2, denoted $\boldsymbol{I_2}$

The first GLM, denoted $GLM1$, has the predictor variables $\boldsymbol{VAR}$ and $\boldsymbol{MR}$ whereas the second GLM, denoted $GLM2$, uses all the four predictor variables$GLM1\boldsymbol{I_1}\boldsymbol{I_2}$. The significance of using $GLM2$ is to highlight the benefit of using the spatial indexes in calculating predictions of $\boldsymbol{V^a}$ and $\boldsymbol{V^b}$ that could be used in addition to the variance and mean rainfall of the spatial radar field. Thus, the purpose of using the GLMs in this methodology is described as follows:

1. Predict the model flood volume and number of floods ($\boldsymbol{V^a}$ and $\boldsymbol{V^b}$) using mean rainfall ($\boldsymbol{MR}$), variance ($\boldsymbol{VAR}$) and spatial indexes ($\boldsymbol{I_1}$ and $\boldsymbol{I_2}$).
2. Compare the performance of the spatial indexes ($\boldsymbol{I_1}$ and $\boldsymbol{I_2}$) and variance ($\boldsymbol{VAR}$) in predicting the model flood volume/number of floods ($\boldsymbol{V^a}$ and $\boldsymbol{V^b}$)

Poisson and Gaussian based GLMs can have a natural logarithm canonical link function. Hence $GLM1_a$ (Equation (5.8)) and $GLM2_a$ (Equation (5.9)) are set up for total flood volume (V^a) using Gaussian based GLM:

$$\ln\left(E(\boldsymbol{V^a})\right) = b_0^{GLM1} + b_1^{GLM1}\boldsymbol{MR} + b_2^{GLM1}\boldsymbol{VAR} \quad (5.9)$$

$$\ln\left(E(\boldsymbol{V^a})\right) = b_0^{GLM2} + b_1^{GLM2}\boldsymbol{MR} + b_2^{GLM2}\boldsymbol{VAR} + b_3^{GLM2}\boldsymbol{I_1} + b_4^{GLM2}\boldsymbol{I_2} \quad (5.10)$$

Where b_0^{GLM1}, b_1^{GLM1} and b_2^{GLM1} are the coefficients of $GLM1_a$ and b_0^{GLM2}, b_1^{GLM2}, b_2^{GLM2}, b_3^{GLM2} and $b_4^{GLM2}$are the coefficients of $GLM2_a$.

Similarly, $GLM1_b$(Equation (5.10)) and $GLM2_b$ (Equation (5.11)) are set up for total number of floods (V^b) using Poisson based GLM:

$$\ln\left(E\left(\boldsymbol{V^b}\right)\right) = g_0^{GLM1} + g_1^{GLM1}\boldsymbol{MR} + g_2^{GLM1}\boldsymbol{VAR} \quad (5.11)$$

$$\ln\left(E\left(\boldsymbol{V^b}\right)\right) = g_0^{GLM2} + g_1^{GLM2}\boldsymbol{MR} + g_2^{GLM2}\boldsymbol{VAR} + g_3^{GLM2}\boldsymbol{I_1} + g_4^{GLM2}\boldsymbol{I_2} \quad (5.12)$$

Where g_0^{GLM1}, g_1^{GLM1} and g_2^{GLM1} are the coefficients of $GLM1_b$ and g_0^{GLM2}, g_1^{GLM2}, g_2^{GLM2}, g_3^{GLM2} and $g_4^{GLM2}$are the coefficients of $GLM2_b$.

For a Poisson based GLM, the expectation of $\boldsymbol{V^b}$ is equal to the Poisson shape parameter, which is the expected number of occurrences. This value is considered an estimate of $\boldsymbol{V^b}$. Similarly, the expectation of $\boldsymbol{V^a}$ in the Gaussian GLM is equal to the mean parameter of the distribution. This value is also considered as the estimate of $\boldsymbol{V^a}$.

5.2.5 Performance indicators

To demonstrate the benefits of the spatial analysis of the gridded QPEs, scatter graphs are produced illustrating the correlations of the flood volumes or number of floods against the spatial parameters described in section 5.2.3. Furthermore, Pearson's r is used to show the strength of the correlations between the spatial parameters and flood variables. Furthermore, the applications of the spatial indexes are visually presented in sections 5.4.

The performance and comparisons of the two GLMs are summarised using RMSE. This performance metric is used across different mean rainfall categories and overall across the sewer catchments (i.e. average values for $\boldsymbol{V^a}$ and $\boldsymbol{V^b}$). The average values for $\boldsymbol{V^a}$ and $\boldsymbol{V^b}$ of all verification events, with the total events denoted EV, are calculated as follows:

$$\frac{\sum_{ev}^{EV} \boldsymbol{V^a}}{EV} \tag{5.13}$$

$$\frac{\sum_{ev}^{EV} \boldsymbol{V^b}}{EV} \tag{5.14}$$

5.3 Case studies

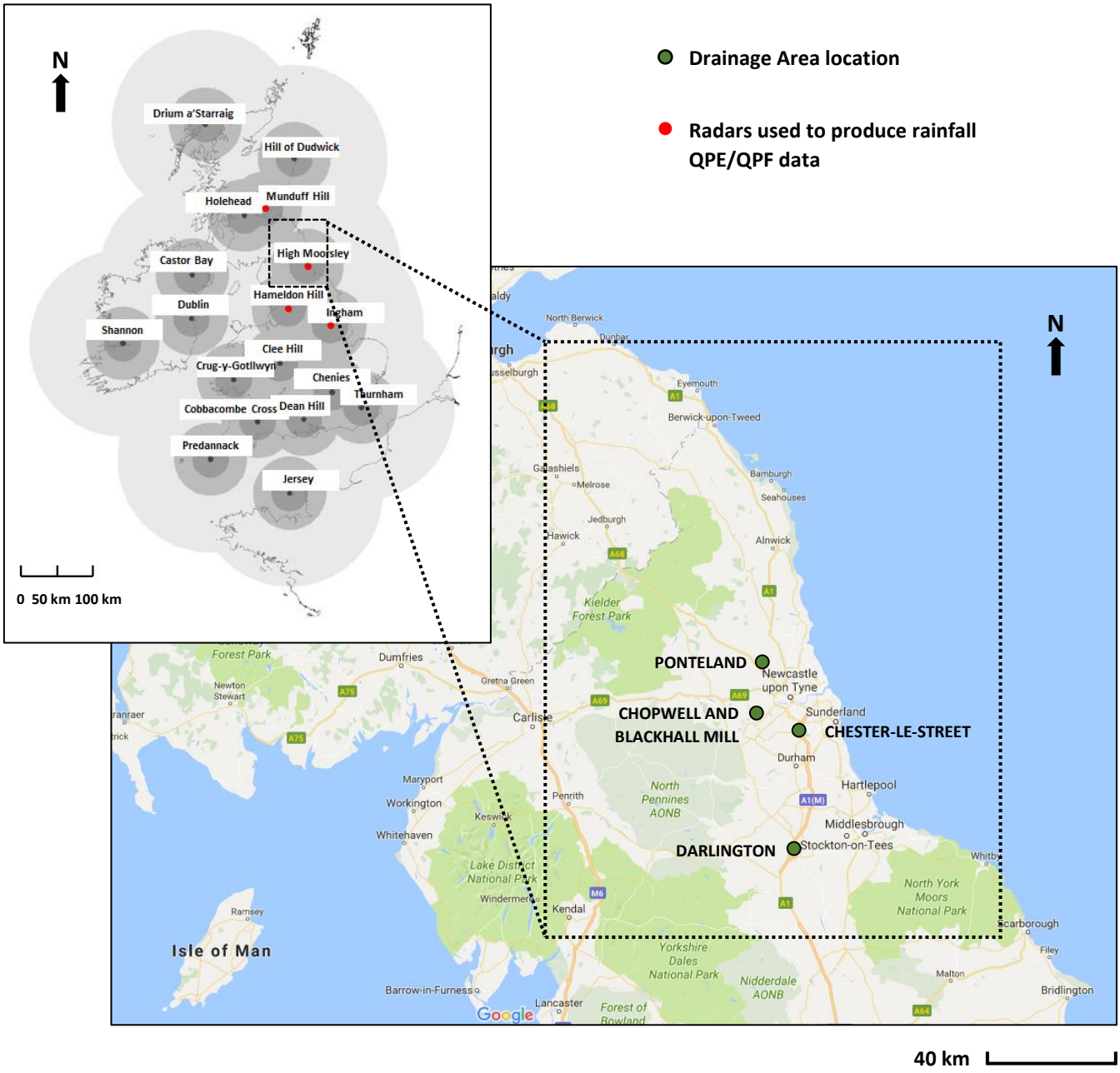

Figure 5.3. Map showing the boundaries of the radar domain of the North-East of England along with the four catchments for which the methodology is tested for: Ponteland, Chopwell and Blackhall Mill, Chester-le-Street and Darlington.

5.3.1 Catalogue of historical events

The radar QPE and QPF sources are the Rain Radar rain-rate and Nowcast products, respectively, both produced and available from the UK Met Office (see section 3.3.1). The region of the rainfall data is the North East of England (see Figure 5.3) and four sewer catchments from this region are used as case studies in this chapter. Two case studies represent small sewer catchments and a further two represent large sewer catchments. Distinctions are drawn between the results for these two categories of sewer catchments in section 5.6 and 5.7.

As explained in section 3.3.2, a rainfall event is defined to be a time series data up to 6 hours in duration. The spatial scale is based on the QPE spatial resolution of 1-km and thus 1-km grids over the sewer catchment model are used to study the spatial variation of accumulate rainfall on sewer flooding over the 6-hour period.

In this study, a 15-min temporal resolution has been selected as this matches the temporal resolution of the QPF source. This would enable the use of probabilistic QPFs using the spatial analysis presented in this chapter. However, a 2-km spatial resolution (which is the native resolution of the Nowcast data) is not used due to it not providing sufficient amount of information on the spatial variation over the sewer catchment compared to a 1-km scale. If probabilistic QPFs were to use the outputs of the spatial analysis in this chapter, it necessitates downscaling the QPF data to a 1-km spatial resolution. This type of interpolation has been explored in section 3.

The period sourced for the historical QPE events is between January 2012 and December 2016. As described in section 5.2.1, QPE events are categorised by the mean rainfall over a sewer catchment. Therefore, QPE events are chosen from the period by mean rainfall. Using this selection method, between 60 and 67 QPE events are organised to form a catalogue of historical QPE events. Catalogues for each sewer catchment are shown in Appendix AAppendix B.

5.3.2 Ponteland

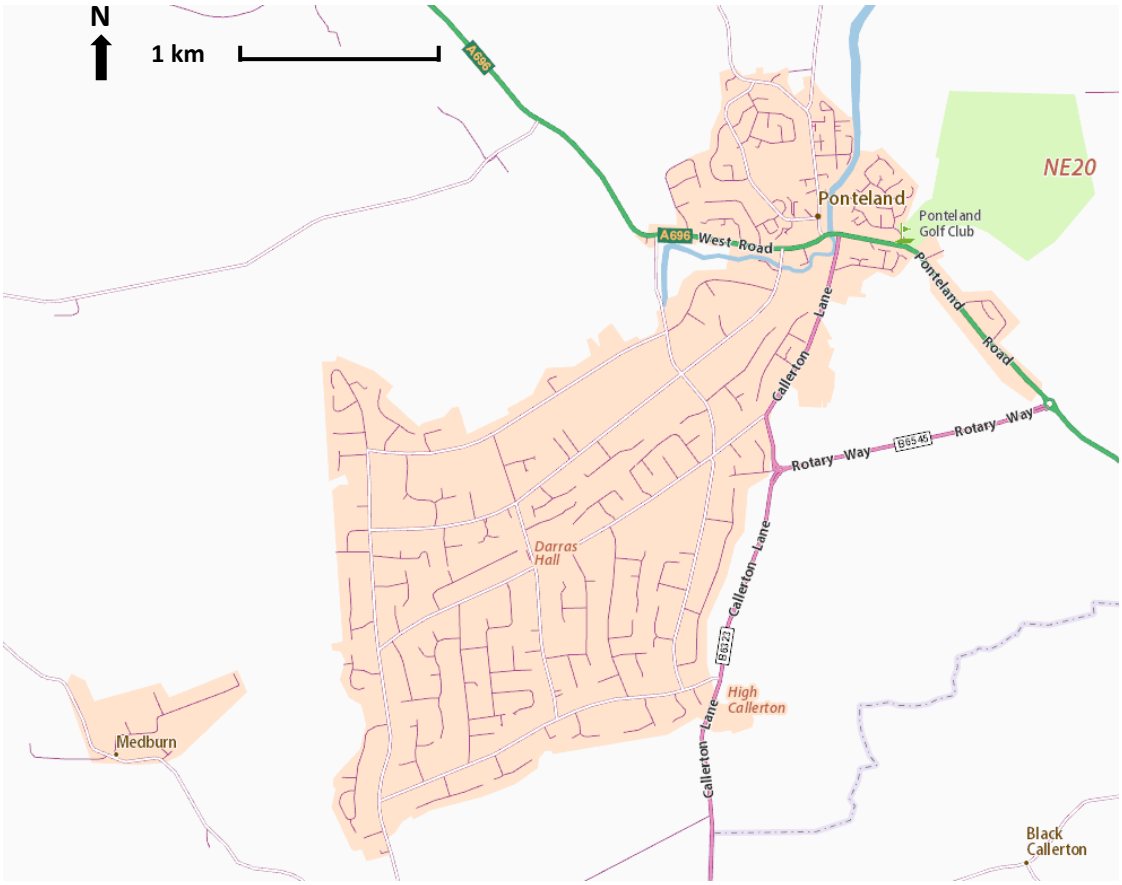

Figure 5.4. Map of the Ponteland sewer catchment.

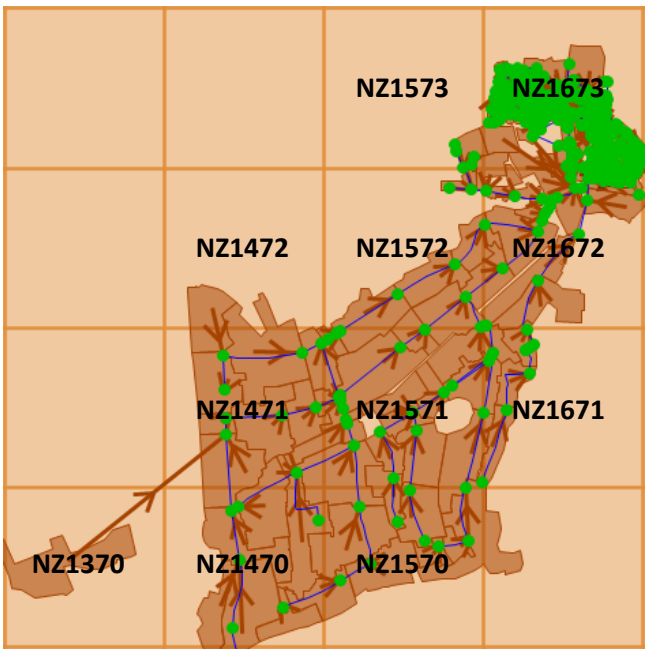

Figure 5.5. Sewer catchment model of Ponteland in Infoworks ICM showing the QPE 1-km grids that it overlaps with.

Figure 5.4 and Figure 5.5show the Ponteland drainage area and sewer catchment, respectively. The Ponteland sewer catchment model has 490 nodes, 473 links and 140 subcatchments. This is a relatively small catchment area and has 11 QPE grids over the region. The QPE accumulations at these grids are used to study the spatial distribution of the rainfall. Although, due to the relatively small size of the sewer catchment, the spatial distribution of QPE accumulation may be more challenging to ascertain. Therefore, the outputs of a small sewer catchment are compared to a larger sewer catchment to determine the benefits of the study across different sized sewer catchments.

Based on the QPE accumulations over the 11 QPE grids of this sewer catchment, 7 mean rainfall categories are identified and based on these 67 events are extracted in the historical QPE period. These events are summarised in Table B.1 in Appendix AAppendix B showing the $\boldsymbol{MR}$, $\boldsymbol{VAR}$, $\boldsymbol{I_1}$, $\boldsymbol{I_2}$, the $\boldsymbol{V^a}$ and $\boldsymbol{V^b}$ of each QPE event.

5.3.3 Chopwell and Blackhall Mill

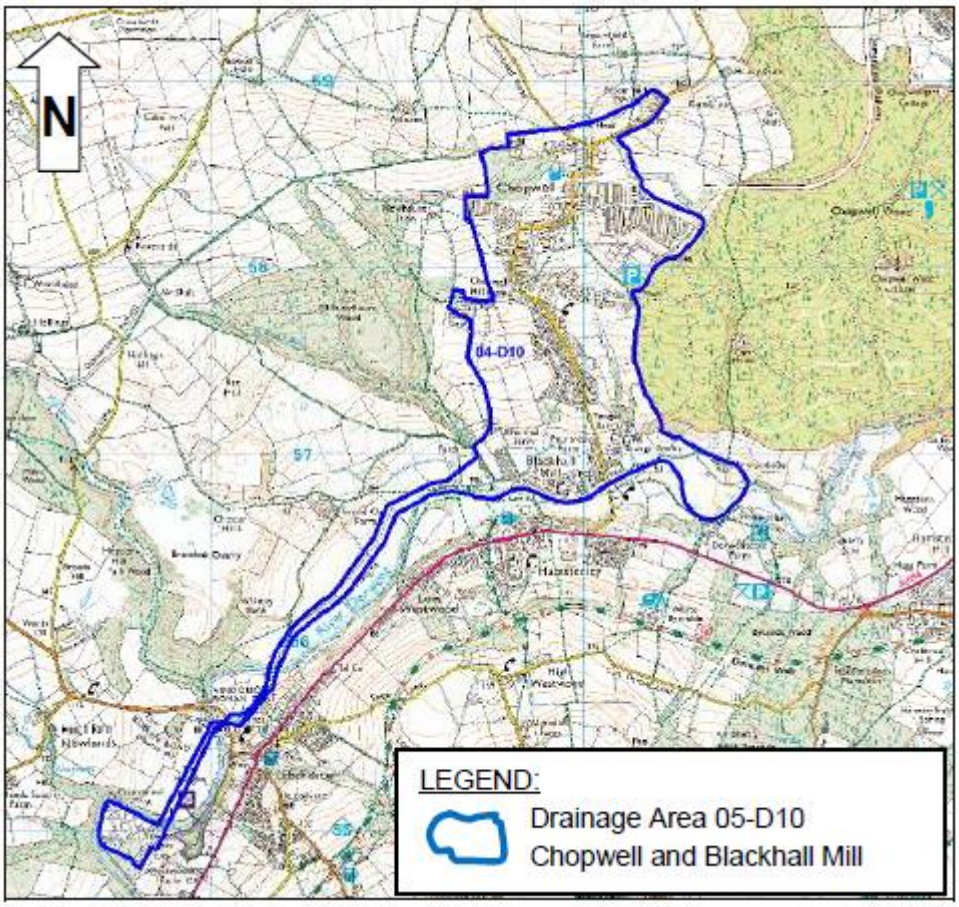

Figure 5.6. Map showing the boundaries of the Chopwell and Blackhall Mill drainage area (courtesy of AMEC Foster Wheeler).

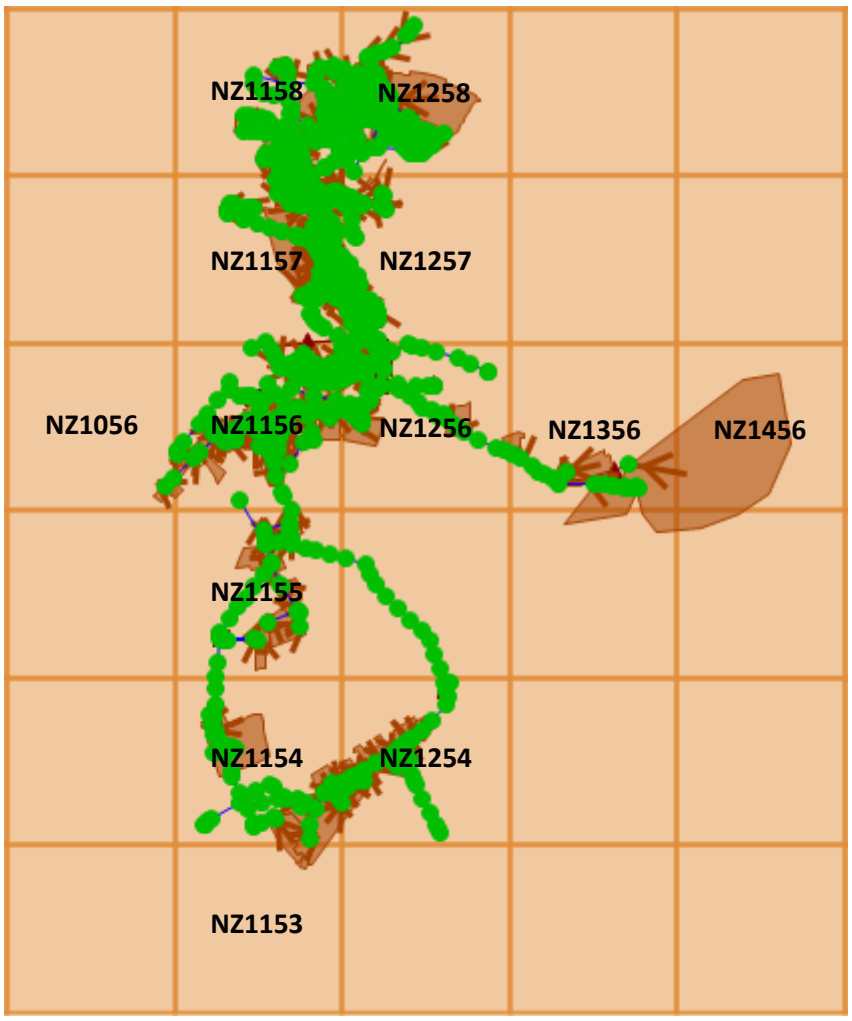

Figure 5.7. Sewer catchment model of Chopwell and Blackhall Mill in Infoworks ICM showing the QPE 1-km grids that it overlaps with.

Figure 5.6 and Figure 5.7 show the Chopwell and Blackhall Mill drainage area and sewer catchment, respectively. The Chopwell and Blackhall Mill sewer catchment consists of 1126 nodes, 1094 links and 252 subcatchments. Like Ponteland, this is a relatively small sewer catchment and is approximately 218 hectares. It is located within Tyne and Wear and is approximately 15 km south west of Newcastle upon Tyne city centre. The sewer network serves a population size of 4,246. The topography of the drainage is such that the land falls steeply from north to south (towards the centre of the sewer catchment). The bottom region consists of Blackhall Mill and the land of this region falls steeply from south to north.

The catalogue of historical QPE events consist of 50 events organised into 5 mean rainfall categories. These events are summarised in Table B.2 in Appendix AAppendix B showing the $\boldsymbol{MR}$, $\boldsymbol{VAR}$, $\boldsymbol{I_1}$, $\boldsymbol{I_2}$, the $\boldsymbol{V^a}$ and $\boldsymbol{V^b}$ of each QPE event.

5.3.4 Chester-le-Street

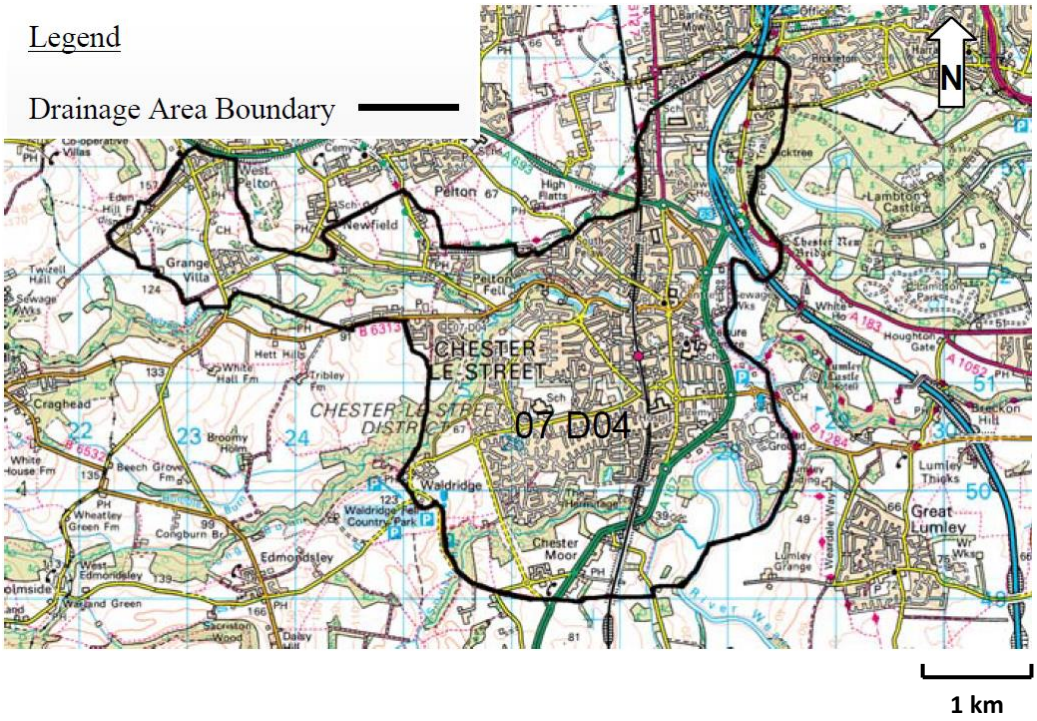

Figure 5.8. Map showing the boundaries of the Chester-le-Street drainage area (courtesy of AMEC Foster Wheeler).

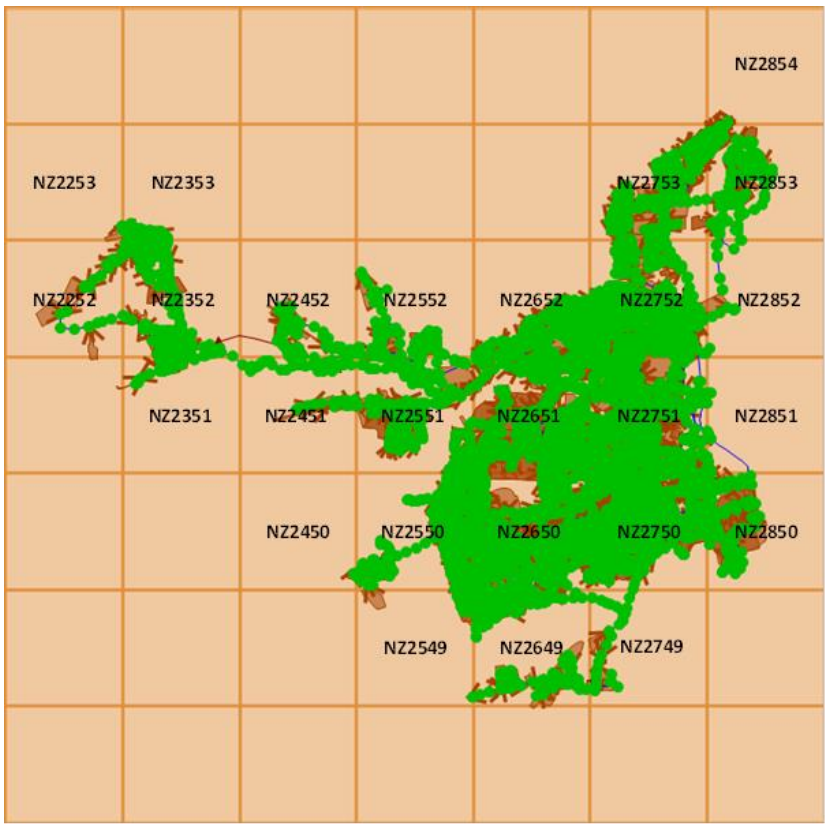

Figure 5.9. Sewer catchment model of Chester-le-Street in Infoworks ICM showing the QPE 1-km grids that it overlaps with.

Figure 5.8 and Figure 5.9 show the Chester-le-Street drainage area and sewer catchment, respectively. Chester-le-Street is located in County Durham and is approximately north 10 km from Durham City Centre. In the region, there are approximately 24,000 people based in a mostly urbanised area and the outer regions are rural agricultural areas. River Wear is located on the west side of the sewer catchment, which receives surface water directly from the east regions. The catchment is not wholly level as the catchment flow falls steeply towards the valleys of River Wear.

Most of the sewerage network is combined but there are several regions showing new sewerage development that are separate foul and surface water sewers. These separate sewers eventually join onto the combined systems.

There are in total 6278 nodes, 6244 links and 1307 sub catchments in the sewer catchment. The region covers in total 26 radar QPE 1-km grids (see Figure 5.9).

The QPE accumulations for these grids are used as the forcing to simulate sewer flooding for this sewer catchment.

Based on the selection method for producing the catalogue of historical QPE data, 7 categories of mean rainfall across the 26 QPE grids have been identified for which 67 QPE events have been extracted. Summaries of these QPE events along with the $\boldsymbol{MR}$, $\boldsymbol{VAR}$, $\boldsymbol{I_1}$, $\boldsymbol{I_2}$, the $\boldsymbol{V^a}$ and $\boldsymbol{V^b}$ of each event are shown in Table B.3 in Appendix AAppendix B**.**

5.3.5 Darlington (North)

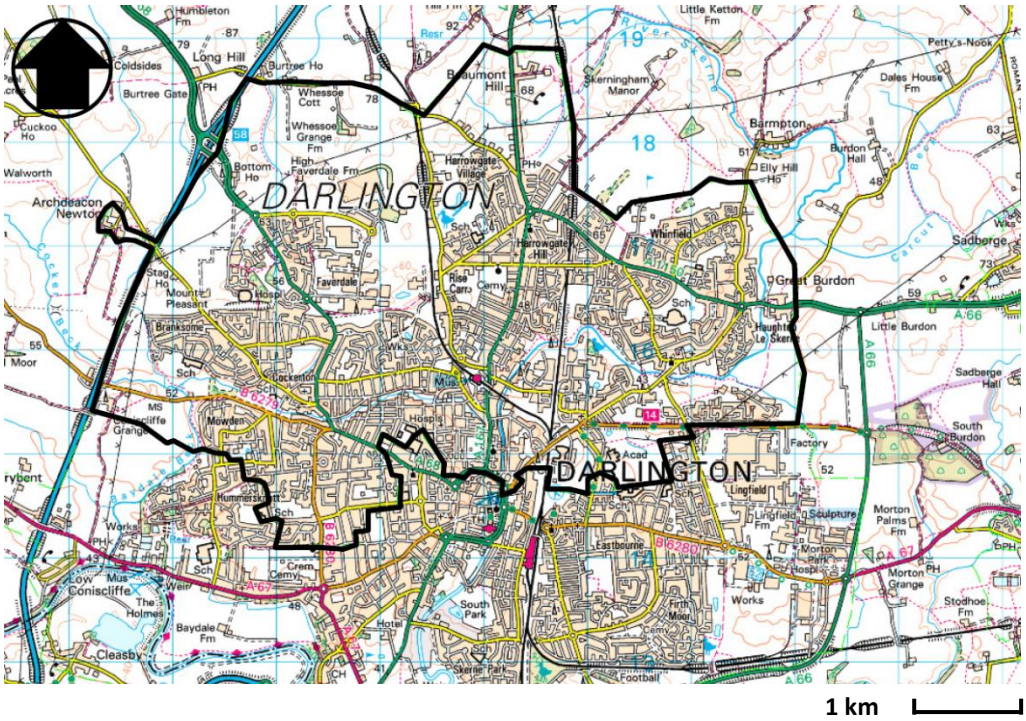

Figure 5.10. Map showing the boundaries of the Darlington (North) drainage area (courtesy of AMEC Foster Wheeler).

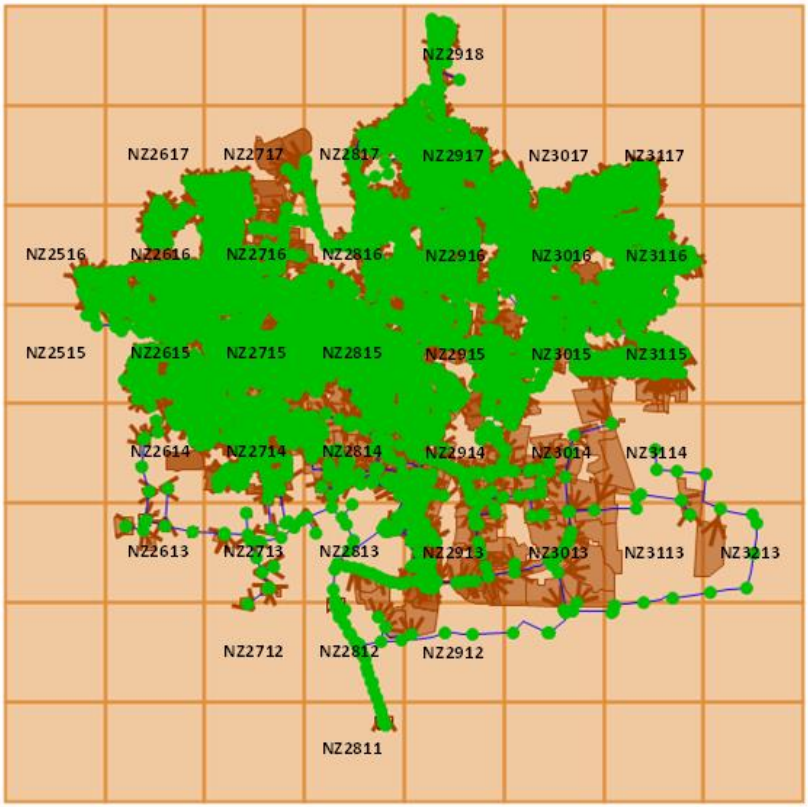

Figure 5.11. Sewer catchment model of Darlington (North) in Infoworks ICM showing the QPE 1-km grids that it overlaps with.

Figure 5.10 and Figure 5.11 show the Darlington (North) drainage area and sewer catchment, respectively. Darlington (North) is situated in Darlington which serves a community of 55,000 people. The catchment is relatively level with a sewerage network with roughly the same proportion of combined and separate sewer systems. The sewer catchment is located around the River Skerne and the outfall leads to the Stressholme STW which is located south of the sewer catchment.

The sewer catchment model of Darlington (North) represents the region with 9145 nodes, 9057 links and 3300 subcatchments. Based on this model, there are 38 QPE 1 km grids that cover the sewer catchment (see Figure 5.11). At these grids, 6 mean rainfall categories are identified in the historical QPE period and then using these categories 60 QPE events is extracted. Table B.4 in Appendix AAppendix B shows the catalogue of historical QPE events extracted for Darlington (North).

5.3.6 Verification events

For testing the performance of the two GLMs, a different set of QPE events are used (i.e. verification QPE events). The spatial parameters described in section 5.2.3 are calculated for the verification QPE events and these are used in the GLMs to predict $\boldsymbol{V^a}$ and $\boldsymbol{V^b}$ without running hydrological simulation. To establish that the GLMs perform accurately and consistently, QPE events of the same mean rainfall categories were required but with different spatial characteristics (i.e. different values for $\boldsymbol{VAR}$, $\boldsymbol{I_1}$ and $\boldsymbol{I_2}$). This is achieved by modifying the historical QPE events so that the mean rainfall value is different but kept within the respective mean rainfall category (i.e. QPE accumulations of the grids are scaled by a random factor) and the QPE accumulations of the grids are switched to other grid locations so that new values for $\boldsymbol{VAR}$, $\boldsymbol{I_1}$ and $\boldsymbol{I_2}$ are produced.

5.3.7 Predicting model flood variables using spatial rainfall variables

In a similar way of obtaining $\boldsymbol{V^a}$ and $\boldsymbol{V^b}$ for the historical QPE events, $\boldsymbol{V^a}$ and $\boldsymbol{V^b}$ are obtained for the verification QPE events. $\boldsymbol{V^a}$ and $\boldsymbol{V^b}$ are then used to test the predictive accuracy of the GLMs.

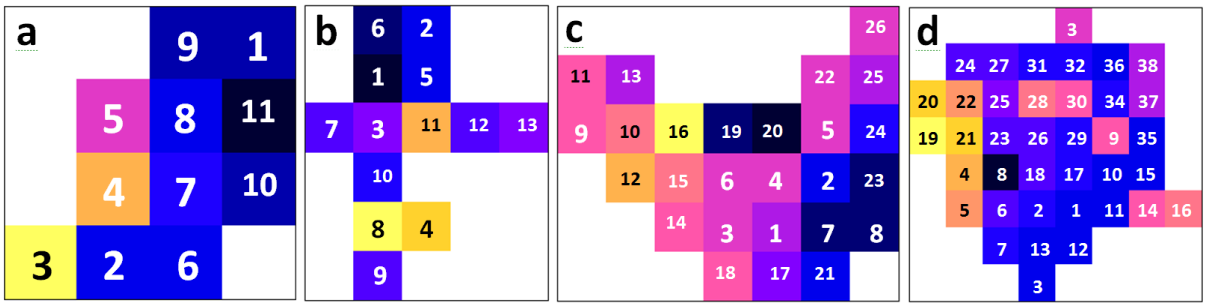

Figure 5.12. The grids of case studies: (a) Ponteland, (b) Chopwell and Blackhall Mill, (c) Chester-Le-Street and (d) Darlington (North) are numbered according to their grid references. The colours show rainfall accumulation (in mm).

In section 5.4 and 5.5, the outputs of each case study are presented based on three topics:

- **Extremities of the values of the spatial indexes** - there is no measure of the sensitivity of the values below or above 1 in relation to what they mean on the catchment (i.e. for $\boldsymbol{I_1}$, a value of 0.9 could have 40% of the

rainfall focused downstream and a value of 0.8 could have 99% of the rainfall focused downstream. However, there is no way of determining this directly from the values of the spatial indexes). Hence, to understand the sensitivities of the spatial indexes, the maximum and minimum values in the catalogue of historical rainfall events for each case study are visually represented. Figure 5.12 assigns numbers to the grid references of each sewer catchment and these are referred to for identifying the grids in explaining the proportion of rainfall.

- **Relationship between model flood variables and spatial variables** – for each spatial rainfall variable, the flood volume and total floods are plotted against them in order to visualise the relationships between them. This allows the general trend of predicting the flooding extent using the spatial rainfall variables to be deduced. Furthermore, these relationships are propagated in the GLMs to predict the flooding extent.
- **Generalised Linear Models** – the performances of $GLM1$ and $GLM2$ are then presented and analysed to demonstrate how well they can predict the flood volume and total floods. Particularly, the performance of $GLM2$ is reviewed against $GLM1$ for each case study to understand how accurate it is in different sized sewer catchments.

5.4 Case studies: small drainage areas

5.4.1 Extremities of spatial indexes

Ponteland

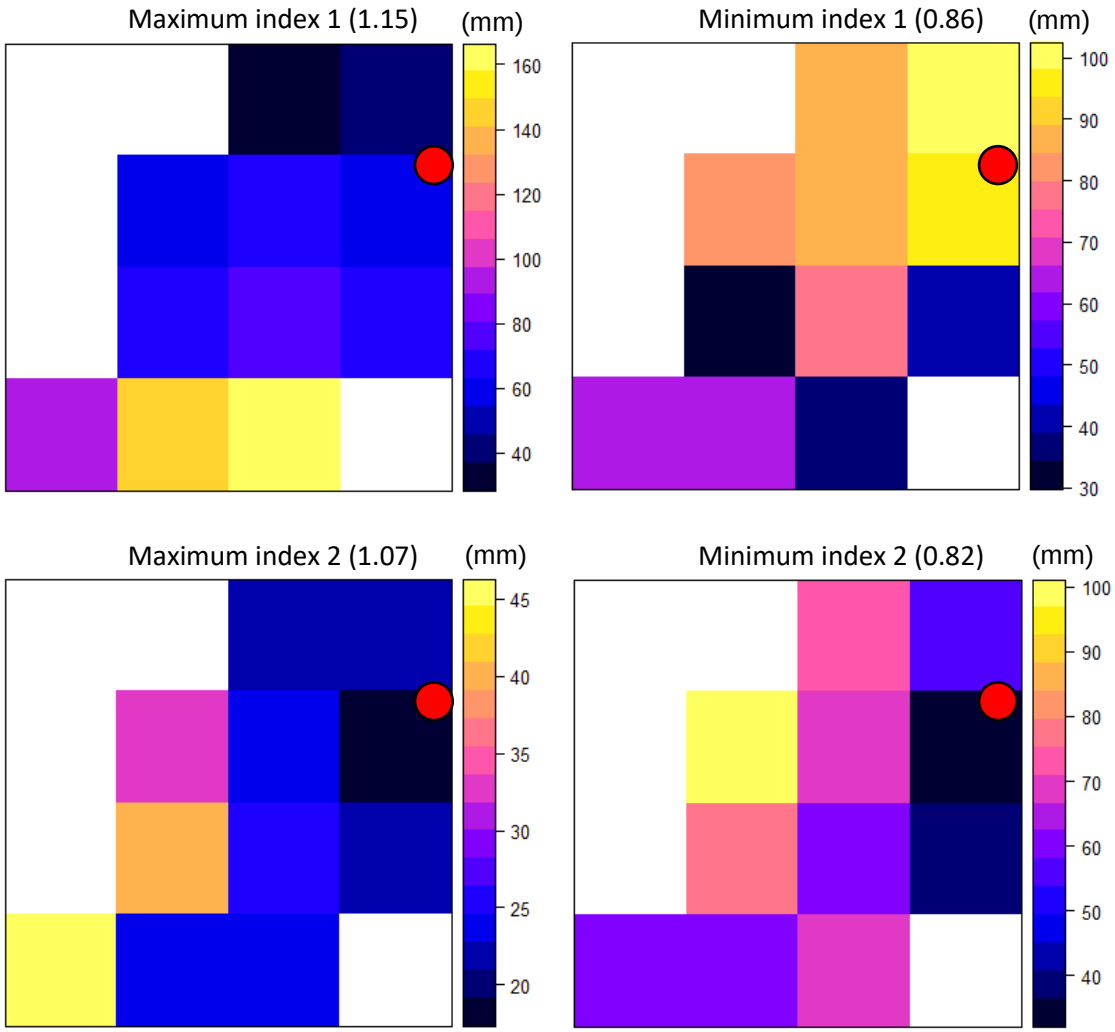

Figure 5.13. Maximum (left) and minimum (right) values for spatial indexes 1 (top) and 2 (bottom) across the catalogue of historical QPE events for Ponteland. The values are stated in brackets. Legend represents rainfall accumulation (in mm). Location of the main outlet is shown as a red filled circle.

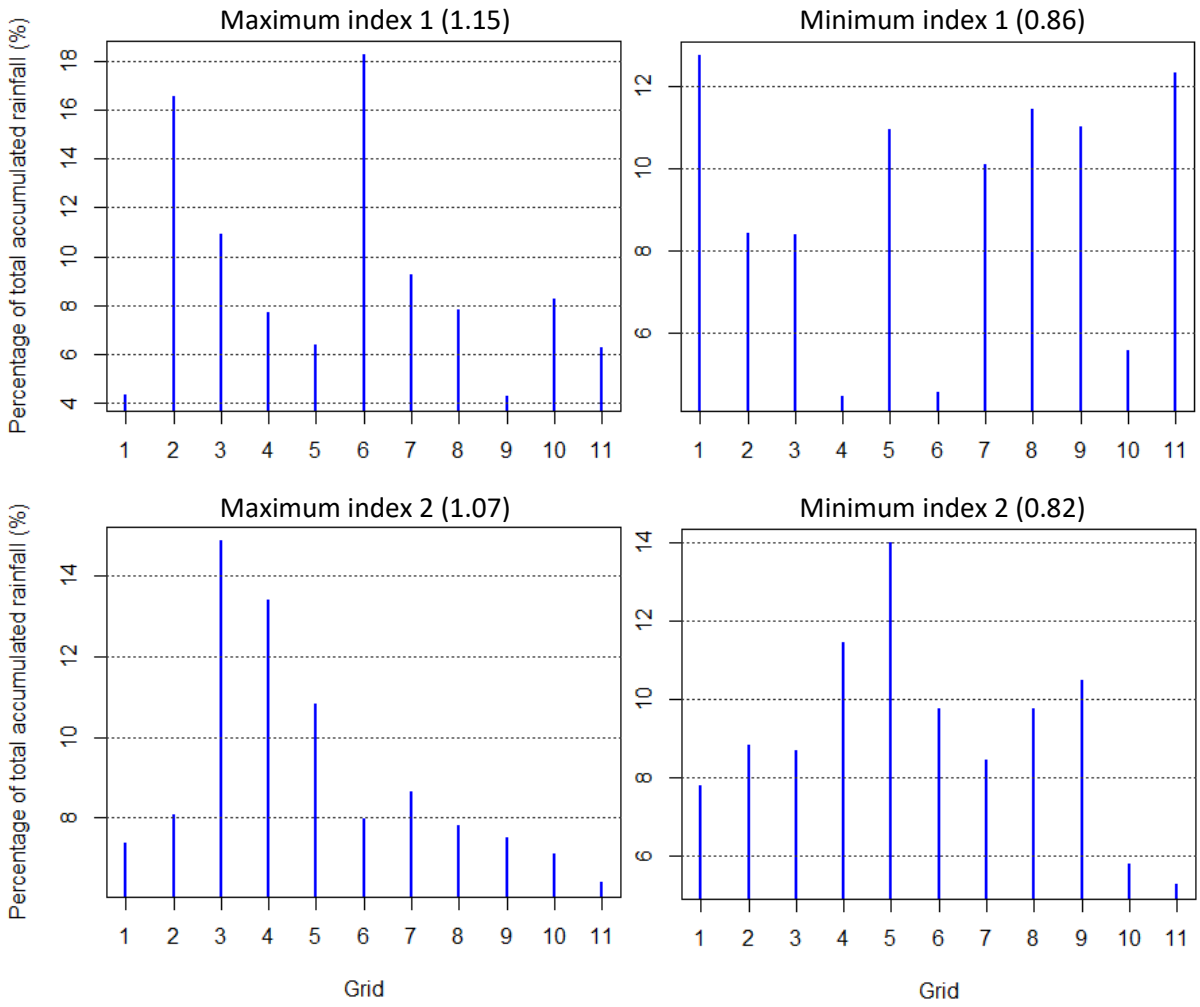

Figure 5.14. The percentage of total rainfall over the study region, Ponteland, is stated for each grid (see Figure 5.12) for events showing maximum/minimum spatial indexes.

Figure 5.13 and Figure 5.14 shows the maximum and minimum values for the spatial indexes across the entire catalogue of historical events for Ponteland. The purpose of this is to show how the rainfall is distributed across the study region for the extreme values existent in the historical events used to generate the GLMs. However, it would be ideal to extract many more events to derive the extreme values for the spatial indexes representing extreme events, which would show more information of the distribution of rainfall for a wider a range of values for the spatial indexes. Nonetheless, the precipitation maps in Figure 5.14 show the spatial distribution of rainfall described by the spatial indexes within a measurable range. For example, a value of 1.15 for spatial index 1 shows that most of the rainfall is situated upstream of the sewer catchment (grids coloured

in purple, orange and yellow). Based on this distribution, the average rainfall in this region equates to approximately 130 mm whereas the approximate average rainfall towards downstream/centre of the sewer catchment equates to 60 mm. Furthermore, the region where heaviest rainfall is observed (bottom three grids) roughly constitutes 46% of the rainfall in the study region (see top left figure of Figure 5.14). The lowest value for spatial index 1 in the catalogue of historical events is 0.86. Considering the four grids nearest to the outlet (grids 1,8,9 and 11), these have an average rainfall of 92 mm and constitute 51% of the rainfall in the study region. By considering the most downstream grids (grids 1, 9 and 11), these constitute 40% of the rainfall in the region. This indicates the level of sensitivity of spatial index 1 in terms of the distribution of the rainfall relative to the outlet for Ponteland sewer catchment. The event with the lowest spatial index 2 (value of 0.82) shows that one of the grids (grid 5) has the largest proportion of the rainfall over the study region (14% of total rainfall) followed by another grid adjacent to it. The event with the largest value for spatial index 2 also characterises convective-type of rainfall albeit being multimodal over the sewer catchment. This is vaguely observed in grids 3 and 4 as these grids show the largest proportion of rainfall in the study region. Due to the relatively small size of the sewer catchment, certain grids over the study area show heavier rainfall that may not fully represent the spatial distribution of the storm. In this case, a larger sewer catchment would better represent this distribution. But on a small spatial scale, the rainfall over the sewer catchment may characterise a multimodal storm even if the actual storm is differently distributed. Based on the relative rainfall over the sewer catchment, the large value for spatial index 2 demonstrates that the storm over the region is multimodal.

Chopwell and Blackhall Mill

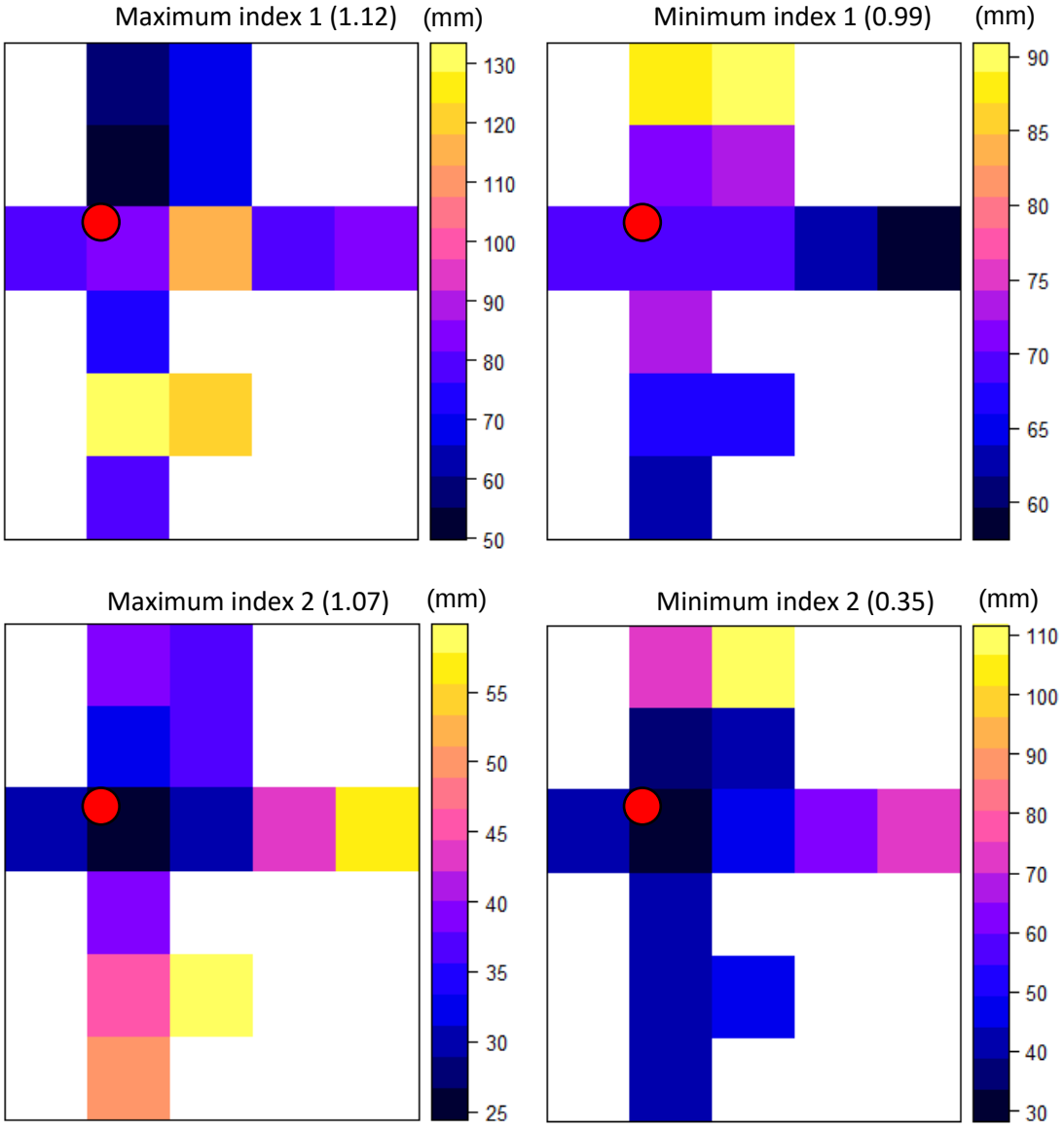

Figure 5.15. Maximum (left) and minimum (right) values for spatial indexes 1 (top) and 2 (bottom) across the catalogue of historical events for Chopwell and Blackhall Mill. The values are stated in brackets. Legend represents rainfall accumulation (in mm). Location of the main outlet is shown as a red filled circle.

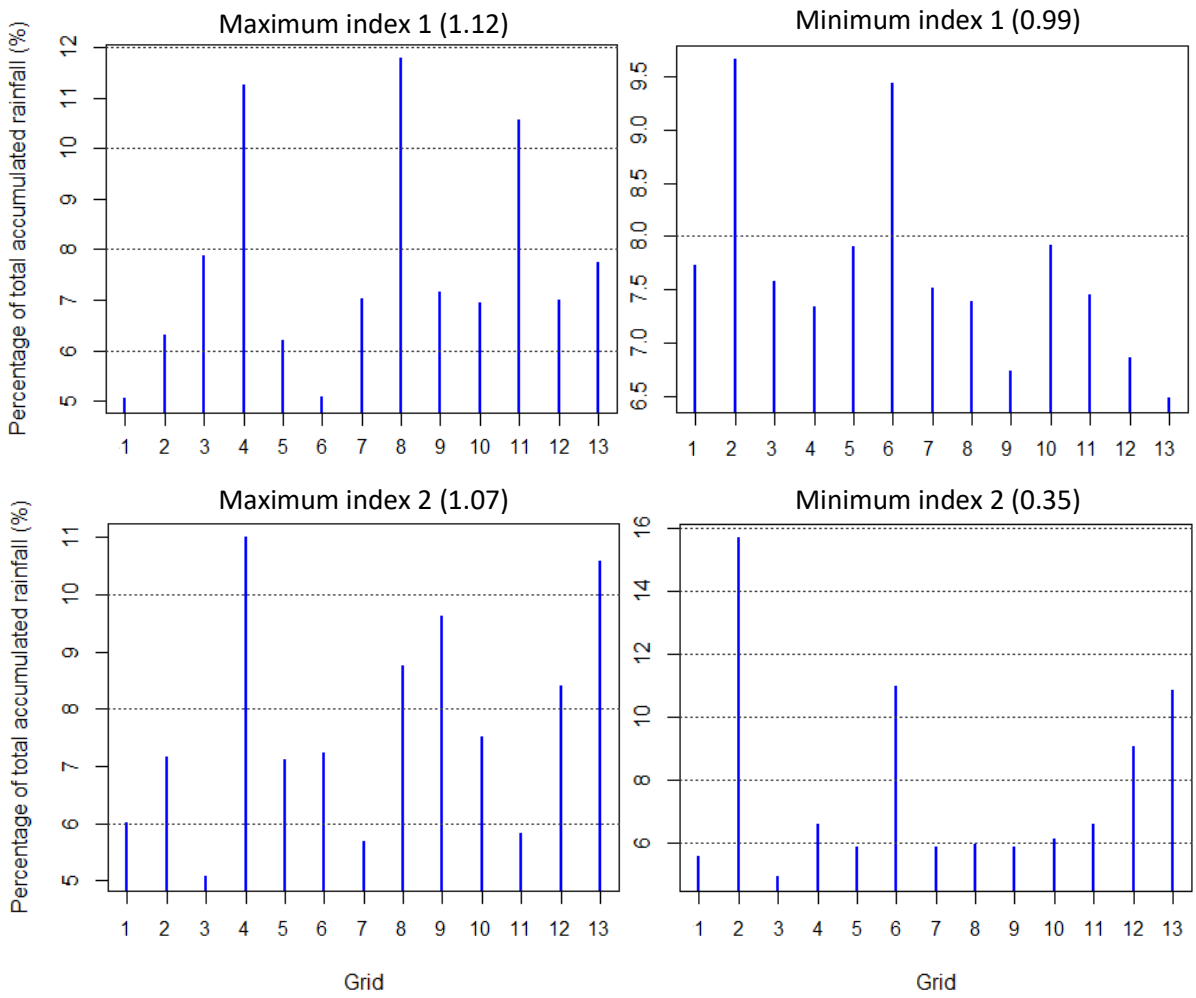

Figure 5.16. The percentage of total rainfall over the study region, Chopwell and Blackhall Mill, is stated for each grid (see Figure 5.12) for events showing maximum/minimum spatial indexes.

This sewer catchment is relatively small and the radar grids used to obtain the rainfall over the area are spatially distributed so that there are not many grids adjacent to each other. In fact, only one grid has four adjacent grids and most of the grids have only one adjacent grid. The consequence of this is that studying the spatial variation of the rainfall in relation to the sewer catchment is made more difficult, particularly when understanding the location and distribution of where most of the rainfall is situated over the area. This is the primary challenge of a sewer catchment of this size and structure.

Nonetheless, the maximum and minimum values for the spatial indexes for Chopwell and Blackhall Mill present some reasonable information related to the

spatial characteristics of rainfall over the study area. For example, in Figure 5.15 the maximum value for spatial index 1 (value of 1.12) suggests that the heavier rainfall is observed upstream of the sewer catchment. Specifically, grids 4 and 8 located upstream of the sewer catchment constitute around 23% of the total rainfall over the area (see Figure 5.16). In the catalogue of historical events, the lowest value for spatial index 1 is 0.99 which is expected to closely resemble a storm where most of the rainfall over the sewer catchment is situated at the centre of the area. Although this is not visibly clear in Figure 5.15 the two grids with the highest proportion of rainfall are situated roughly midway between upstream and downstream of the sewer catchment (i.e. heaviest rainfall is neither situated at the furthest or nearest point from the outlet). For spatial index 2, the lowest value suggests a convective type of storm where a singular region over the sewer catchment has relatively the highest rainfall. Based on Figure 5.15 and Figure 5.16, the event with the lowest value (value of 0.35), grids 2 and 6 show the highest proportion of rainfall (around 27%). These grids show notably higher rainfall in comparison to the other grids, which means that there is greater spatial variation in this event. Based on this, the concentration of rainfall in these regions is more pronounced that result in the value for the spatial index 2 being notably low.

5.4.2 Relationship between model flood variables and spatial variables

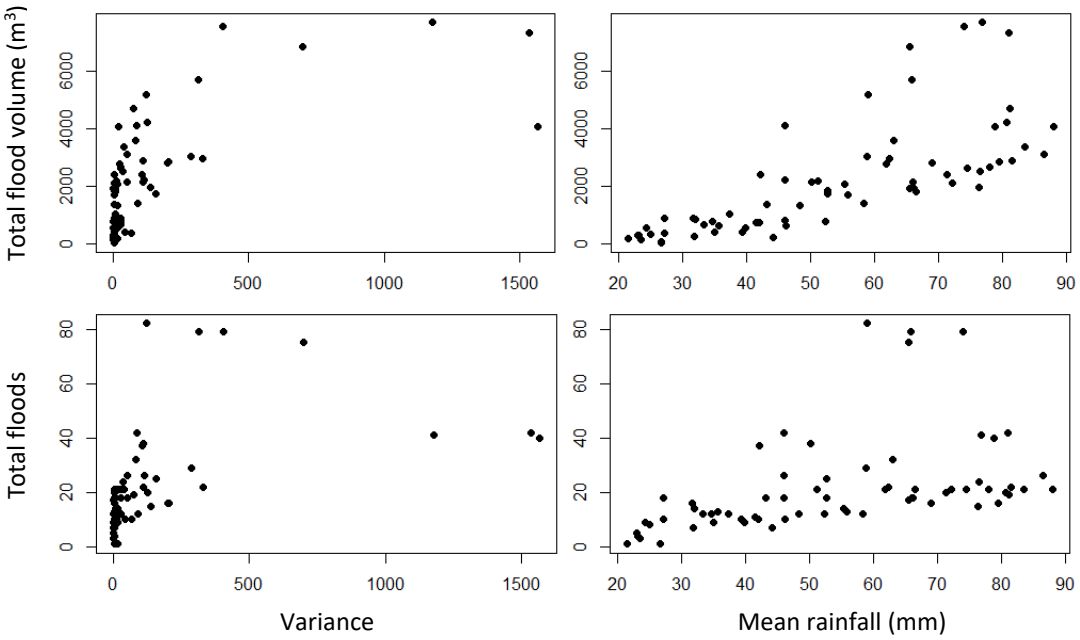

Figure 5.17. Scatter graphs showing the correlation of the $\boldsymbol{V^a}$ (total flood volume) (top) and $\boldsymbol{V^b}$ (total floods) (bottom) against the variance (left) and mean rainfall (right) of Ponteland.

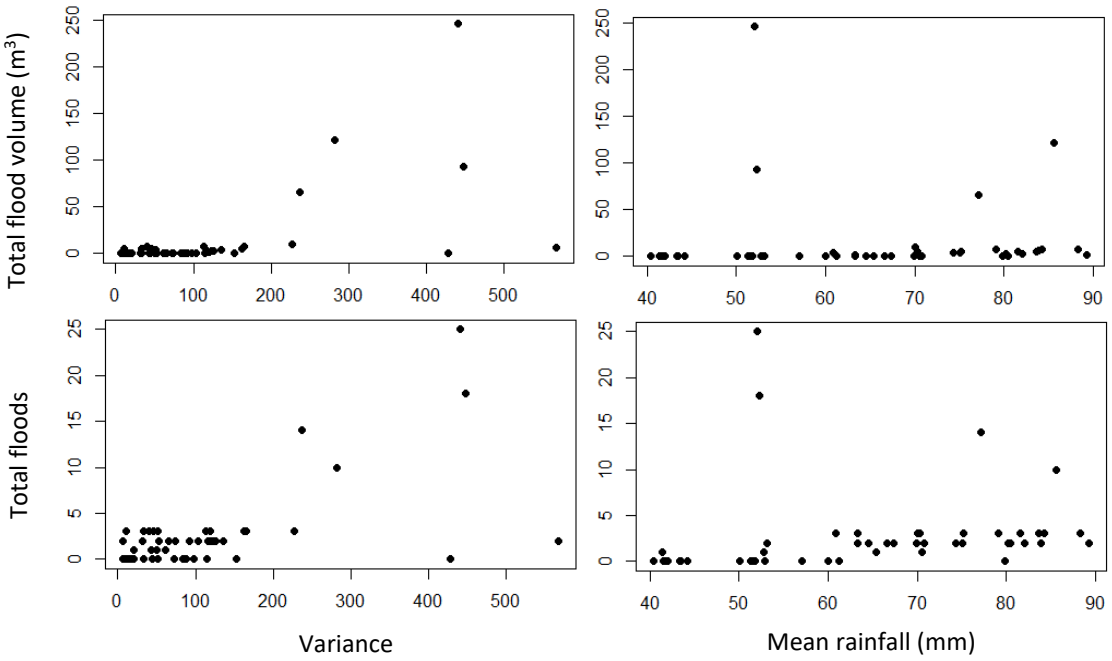

Figure 5.18. Scatter graphs showing the correlation of the total flood volume ($\boldsymbol{V^a}$) (top) and total number of floods ($\boldsymbol{V^b}$) (bottom) against the variance (left) and mean rainfall (right) of Chopwell and Blackhall Mill.

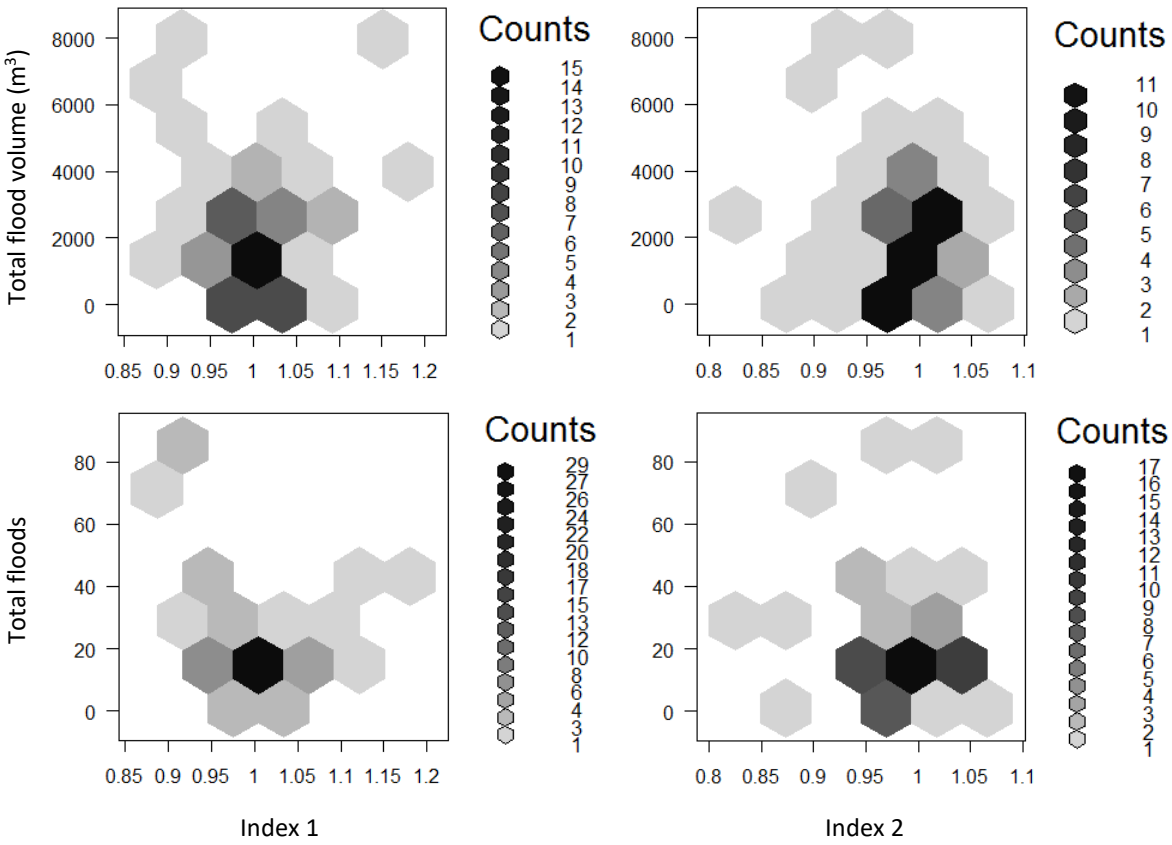

Figure 5.19. Hex bin charts showing the density of events per value of index 1 (left) and index 2 (right) for $\boldsymbol{V^a}$ (total flood volume) (top) and $\boldsymbol{V^b}$ (total floods) (bottom) of Ponteland.

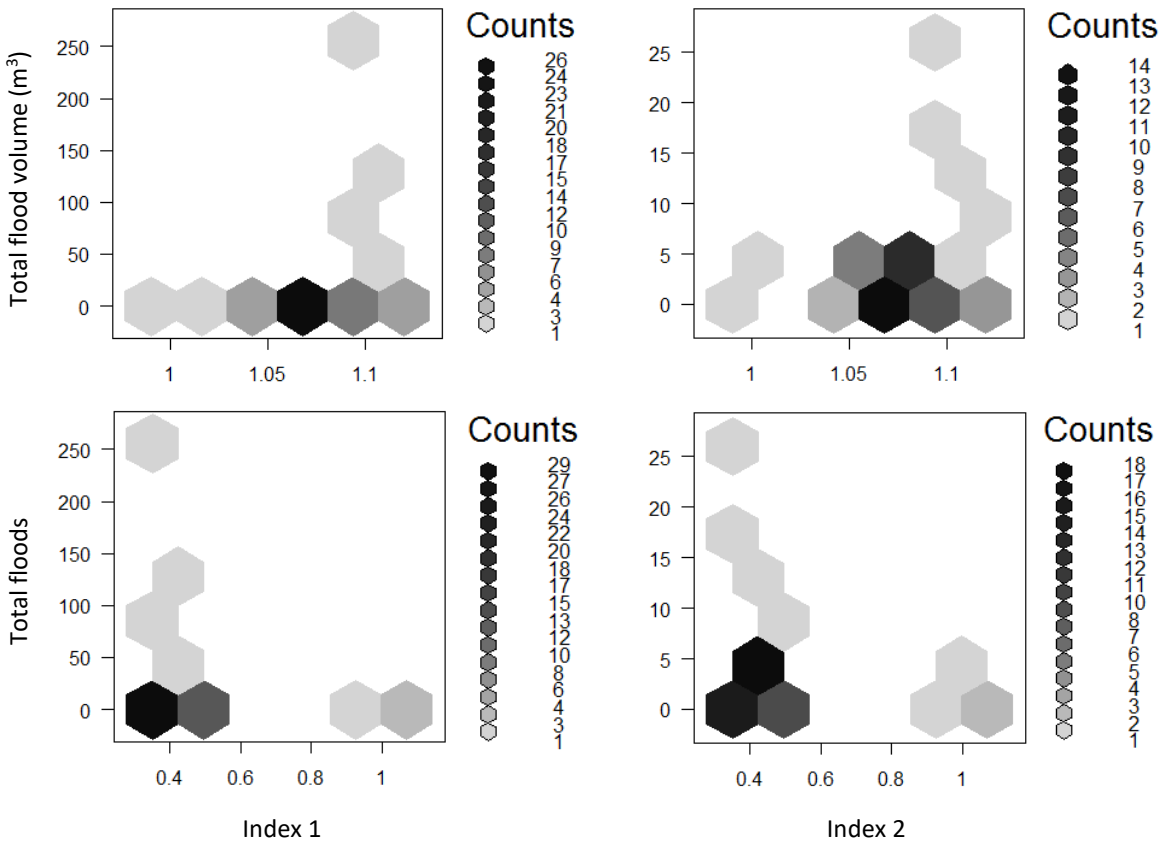

Figure 5.20. Hex bin charts showing the density of events per value of index 1 (left) and index 2 (right) for $\boldsymbol{V^a}$ (total flood volume) (top) and $\boldsymbol{V^b}$ (total floods) (bottom) of Chopwell and Blackhall Mill.

Ponteland

Figure 5.17 and Figure 5.19 show the relationships between $\boldsymbol{V^a}$ or $\boldsymbol{V^b}$ and variance, mean rainfall, spatial indexes 1 and 2 for Ponteland. Generally, $\boldsymbol{V^a}$ and $\boldsymbol{V^b}$ increase as the spatial variance and mean of the rainfall over the study region increases. For mean rainfall, this is an expected outcome as the more rainfall that enters the sewer network, the more likely the system would reach full capacity that would causes the sewage to escape through the manholes. Furthermore, the quantity of sewage escaping the network would also increase with increasing rainfall. The correlation coefficients for $\boldsymbol{V^a}$ and mean rainfall, and $\boldsymbol{V^b}$ and mean rainfall are 0.73 and 0.55, respectively. The correlation coefficients for the $\boldsymbol{V^a}$ and variance, and $\boldsymbol{V^b}$ and variance are 0.66 and 0.49, respectively. The relationship established for variance shows that the more disproportionate the distribution of the rainfall over the study region, the more flooding would occur. This means that

a uniformly distributed rainfall is less likely to cause sewer flooding or would produce a smaller quantity of flooding.

As a relationship has been established between $\boldsymbol{V^a}$ and variance, and $\boldsymbol{V^b}$ and variance, the spatial indexes present the opportunity to further analysis these relationships with spatial parameters related to storm type and positioning over the sewer catchment. Figure 5.19 shows that events that have the lowest values for $\boldsymbol{V^a}$ and $\boldsymbol{V^b}$ have values for spatial index 1 close to 1. This shows that rainfall situated at the centre of the sewer catchment (relative to the outlet) causes the least flooding. However, rainfall situated either upstream or downstream causes more flooding in terms of total flood volume (see top left figure of Figure 5.19). However, in terms of number of flooded nodes, more flooding occurs when rainfall is situated downstream of Ponteland sewer catchment. Physically, when most of the rainfall is situated upstream, the rainfall would enter the network as it travels towards downstream. When it does so, it would overload the network in the process in addition to the rainfall falling directly over the various locations in the sewer catchment. This would increase the flood volumes of already flooded nodes at these locations without necessarily causing an unflooded node to become flooded.

The left figures of Figure 5.19 show the relationships of total flood volume/total floods and spatial index 2. These figures show that when the rainfall is generally uniform (i.e. values of spatial index 2 are centred close to 1) the total flood volume and total floods are relatively low. This less pronounced for total flood volume as most events with a value for spatial index 2 close to 1 shows relatively medium flooding. However, values for this index marginally lower than 1 show the largest flooding volumes, although this cannot clearly be concluded for total floods. This shows that rainfall over the catchment that has a distribution resembling a convective storm (i.e. having a singular region in the radar field over the sewer catchment with the highest proportion of total rainfall) would generally be expected to show higher quantities of flood volumes. As this index describes characteristics of the storm over the study region with detailed distributions indicating singular or multimodal storms, smaller study regions would make this more difficult to show. This is the reason why conclusions cannot easily be

derived for this index, especially in the case of multimodal storms (i.e. values of spatial index 2 over 1). This is later confirmed in the other case studies.

Chopwell and Blackhall Mill

Figure 5.18 shows scatter graphs of $\boldsymbol{V^a}$ and $\boldsymbol{V^b}$ against variance and mean rainfall over the study area. There isn't a strong positive correlation between $\boldsymbol{V^a}$ and mean rainfall, and $\boldsymbol{V^b}$ and the mean rainfall. This means that even if more rainfall falls on the sewer catchment, there is no significant effect on the number of manholes flooded or the volume of flooding. There could be several reasons for this including that the sewer model used in the case study factored in sustainable urban drainage systems in the design of the model. This would be performed by engineering consultancies for wastewater companies to support construction of new development. Usually, the model is modified to reduce sewer flooding. The solutions include incorporating larger storage components or diverting flow so that the amount of rainfall entering the sewer network is reduced. These modifications may alter the correlations expected in the case that higher rainfall over the sewer catchment causes higher flood volumes/more flooded manholes. In the case of the sewer catchment in this case study, the flooding extent is weakly correlated with the rainfall amounts over the network. However, the relationship between $\boldsymbol{V^a}$ and variance, and $\boldsymbol{V^b}$ and the variance of the gridded rainfall is more positively correlated (r value of 0.58 and 0.61 for $\boldsymbol{V^a}$ and $\boldsymbol{V^b}$ against variance, respectively). This shows that the flooding extent in this sewer catchment is sensitive to the distribution of the rainfall spatially over the study area. This is clearly observed in Figure 5.20 where higher $\boldsymbol{V^a}$ values are observed for events with a large proportion of the rainfall over the area situated upstream of the sewer catchment. Furthermore, where two regions (or grids) show higher proportions of rainfall over the area (i.e. characterised a storm that is multimodal in spatial distribution) and having values for spatial index 2 above 1, $\boldsymbol{V^a}$ is higher in comparison to an event with with a more uniformly distributed rainfall over the area, or an event with only one region (or grid) with the highest proportion of rainfall. However, for $\boldsymbol{V^b}$, the opposite is the case. This means that there are more flooded nodes for events where the rainfall over the region is situated mostly downstream of the sewer catchment and for events that have a singular region (or grid) with the highest proportion of rainfall. This indicates the

characteristic of the sewer network that few flooded nodes may excessively flood in large quantities. For example, based on Figure 5.20**,** there might be a large cluster of nodes situated downstream of the sewer catchment that sensitive to rainfall falling directly over them. So, when the rainfall is mostly situated downstream, these nodes would become flooded. However, when the rainfall is mostly situated upstream, various nodes in the pathway towards downstream of the sewer catchment may have significantly lower hydraulic capacities causing them to become flood easily as rainfall runs over the surface entering prior nodes as the sewer flow travels downstream. Due to the flow pathway, these sensitive nodes would flood larger quantities of sewage without flooding the nodes further downstream. This would possibly explain the large flood volumes without causing many nodes in the sewer catchment to be flooded.

5.4.3 Generalised Linear Models

Ponteland

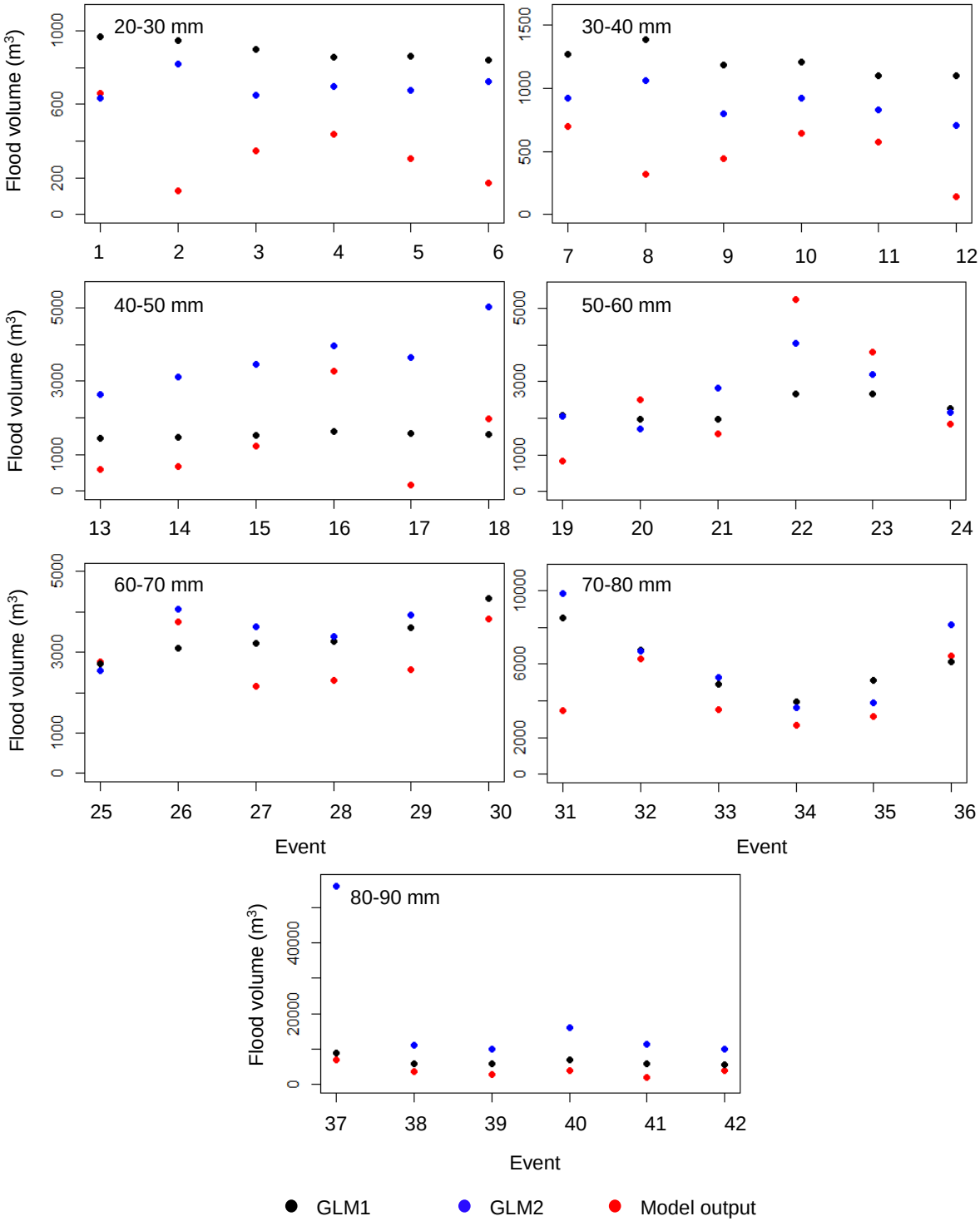

Figure 5.21. The values of flood volume ($\boldsymbol{V^a}$) of all verification QPE events across the different mean rainfall ranges over the sewer catchment for $GLM1$, $GLM2$ and the hydraulic model for Ponteland.

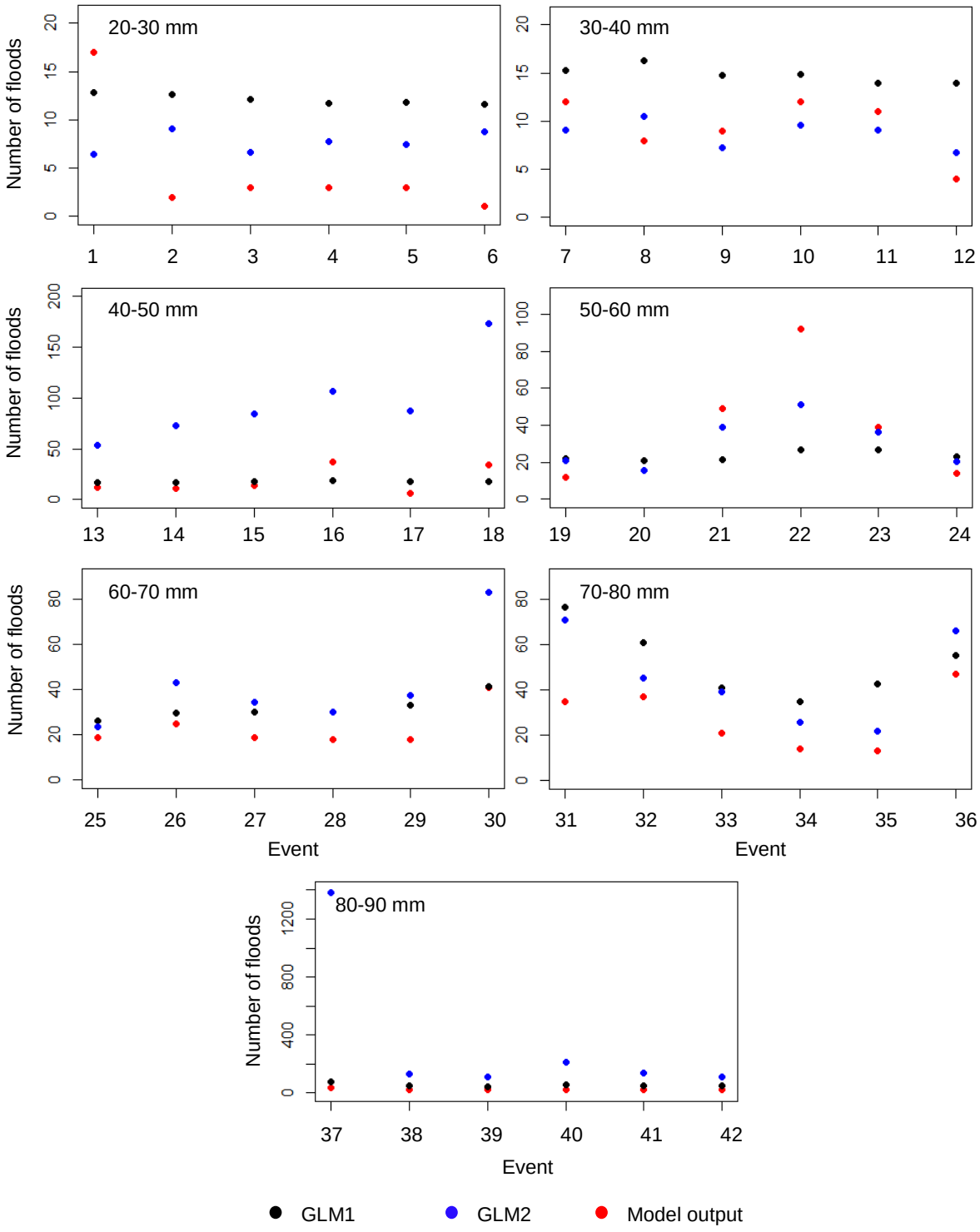

Figure 5.22. The total number of floods ($\boldsymbol{V^b}$) of all verification QPE events across the different mean rainfall ranges over the sewer catchment for $GLM1$, $GLM2$ and the hydraulic model for Ponteland.

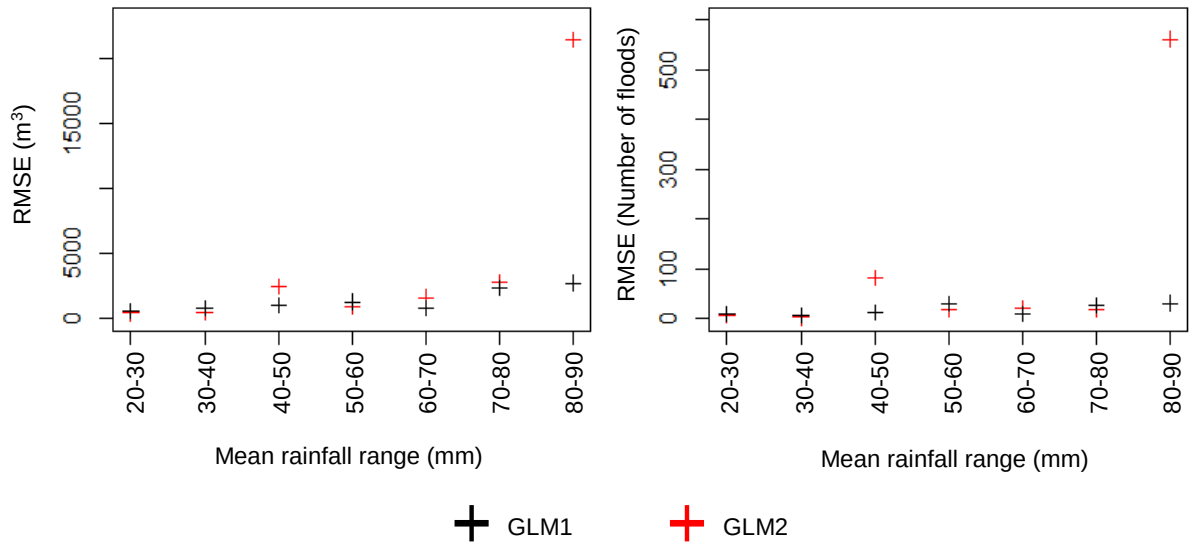

Figure 5.23. The RMSE values for the total flood volume ($\boldsymbol{V^a}$) (left) and total number of floods ($\boldsymbol{V^b}$) (right) across each mean rainfall range are presented for $GLM1$ and $GLM2$ against the model output for Ponteland.

The performances of $GLM1$ and $GLM2$ for Ponteland are presented in Figure 5.21, Figure 5.22 and Figure 5.23. Across the study events, the GLMs both over and under predict the model flood volume and number of floods (see Table 5.6.1 and

Table 5.6.2). Interestingly, the performance of $GLM2$ is better than $GLM1$ when the values for $\boldsymbol{V^a}$ and $\boldsymbol{V^b}$of $GLM1$ under-predict the model values for these variables. The average $\boldsymbol{V^a}$ for GLM1 under predicts the model value by 35% whereas the value for $GLM2$ under predicts $\boldsymbol{V^a}$ by 9%. For $\boldsymbol{V^b}$, the value for $GLM1$ under predicts the model value by 51% whereas the value for $GLM2$ over predicts the model value by 48%. Despite the overall performance of $GLM2$ being worse than $GLM1$, the specific analysis of the over/under prediction of model flood variables presents useful information for hydrologists in that where $GLM1$ under predicts the model output, the $GLM2$ is likely to perform better.

However, for Ponteland sewer catchment, $GLM1$ is overall more reliable for predicting $\boldsymbol{V^a}$ and $\boldsymbol{V^b}$. This is chiefly due to the relatively small area of the sewer catchment which reduces the clarity of spatial information of the rainfall storm relative to the area (i.e. for the same spatial grid dimension, the spatial 'resolution' of the rainfall field is reduced for a smaller sewer catchment. This coarseness of

the rainfall field data will provide less clear information of the spatial variability across the sewer catchment. Hence, the spatial index values will not accurately depict the extent of spatial variability according to their definitions).

However, based on the individual mean rainfall ranges, $\boldsymbol{V^a}$ and $\boldsymbol{V^b}$ of verification QPE events in the mean ranges 20-30, 30-40 and 50-60 mm for $GLM2$ show lower RMSE values in comparison to those of $GLM1$. A justification for this could be that for certain events in the catalogue of historical QPE events for Ponteland the values of the spatial indexes correlate with $\boldsymbol{V^a}$ or $\boldsymbol{V^b}$ within their respective mean rainfall range. However, events within higher mean rainfall ranges may not correlate strongly with these variables. Although more historical events within the mean rainfall range would better represent the correlations between the spatial index values and the $\boldsymbol{V^a}$ or $\boldsymbol{V^b}$ within the respective range, it may just be the case that the spatial indexes reduce in accuracy of representing spatial information at higher intensity/more spatially varied events. This is likely the reason why for higher mean rainfall ranges 60-70, 70-80 and 80-90 mm the RMSE values are higher for $GLM2$ for both $\boldsymbol{V^a}$ and $\boldsymbol{V^b}$.

Furthermore, whilst some study events show more accurate $\boldsymbol{V^a}$ and $\boldsymbol{V^b}$ values from $GLM2$ than $GLM1$, other events may show extremely inaccurate results from $GLM2$ (e.g. event 37). Hence, the performance of $GLM2$ fluctuates largely across all verification QPE events. This is also the case within each mean rainfall range, such as in the 40-50 mm range where event 15 has a $\boldsymbol{V^a}$ from $GLM2$ to have increased from the $GLM1$ value from approximately 1600 m^3 to 3500 m^3, when the model flood volume is approximately 1300 m^3. However, in event 16, $\boldsymbol{V^a}$ from $GLM2$ shows an improvement where the $\boldsymbol{V^a}$ of $GLM2$ increases from the $GLM1$ value from 1700 m^3 to 4000 m^3 when the model flood volume is approximately 3250 m^3.

Chopwell and Blackhall Mill

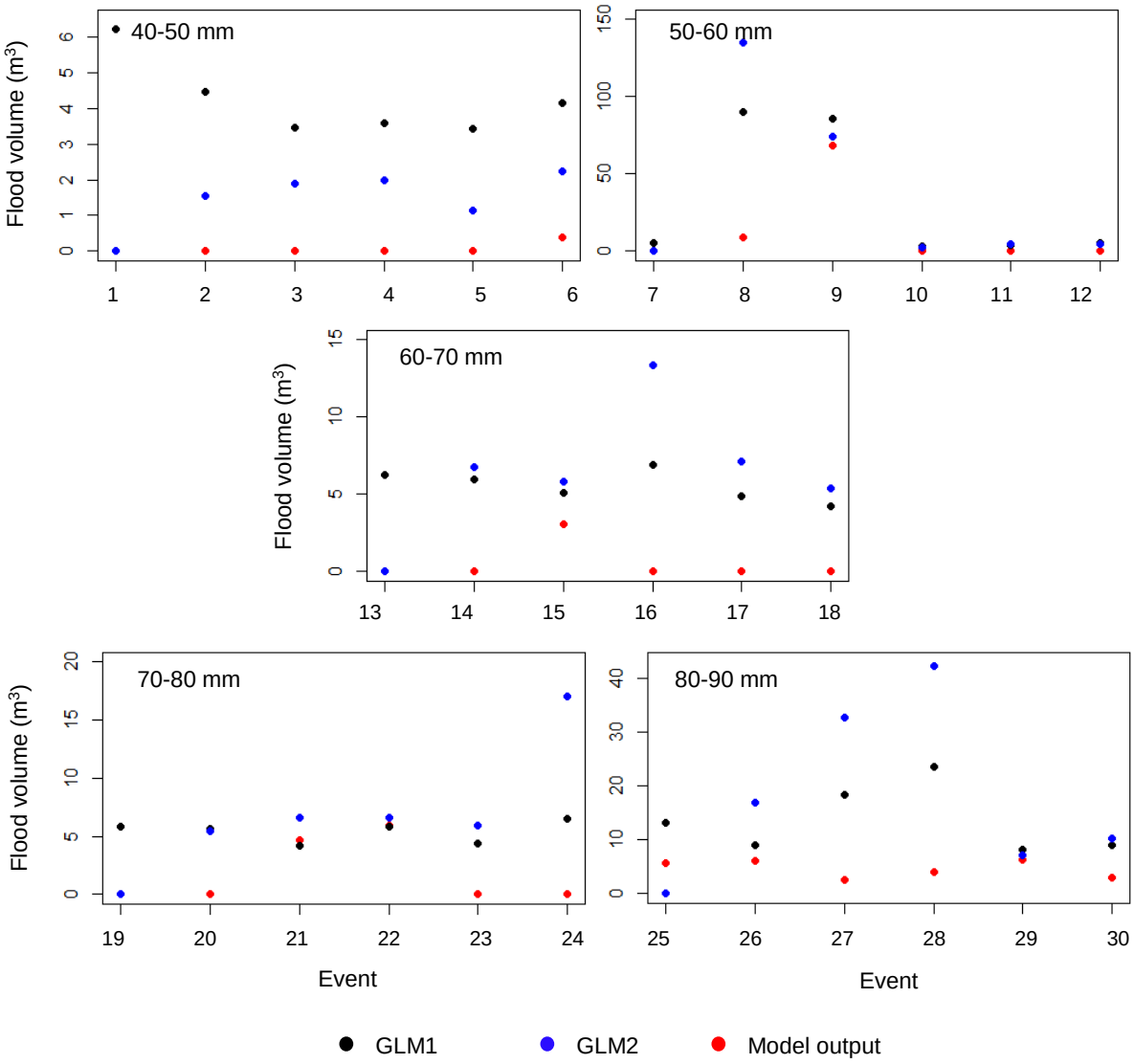

Figure 5.24. The flood volumes ($\boldsymbol{V^a}$) of each test event across the different mean rainfall ranges over the sewer catchment for $GLM1$, $GLM2$ and the hydraulic model for Chopwell & Blackhall Mill.

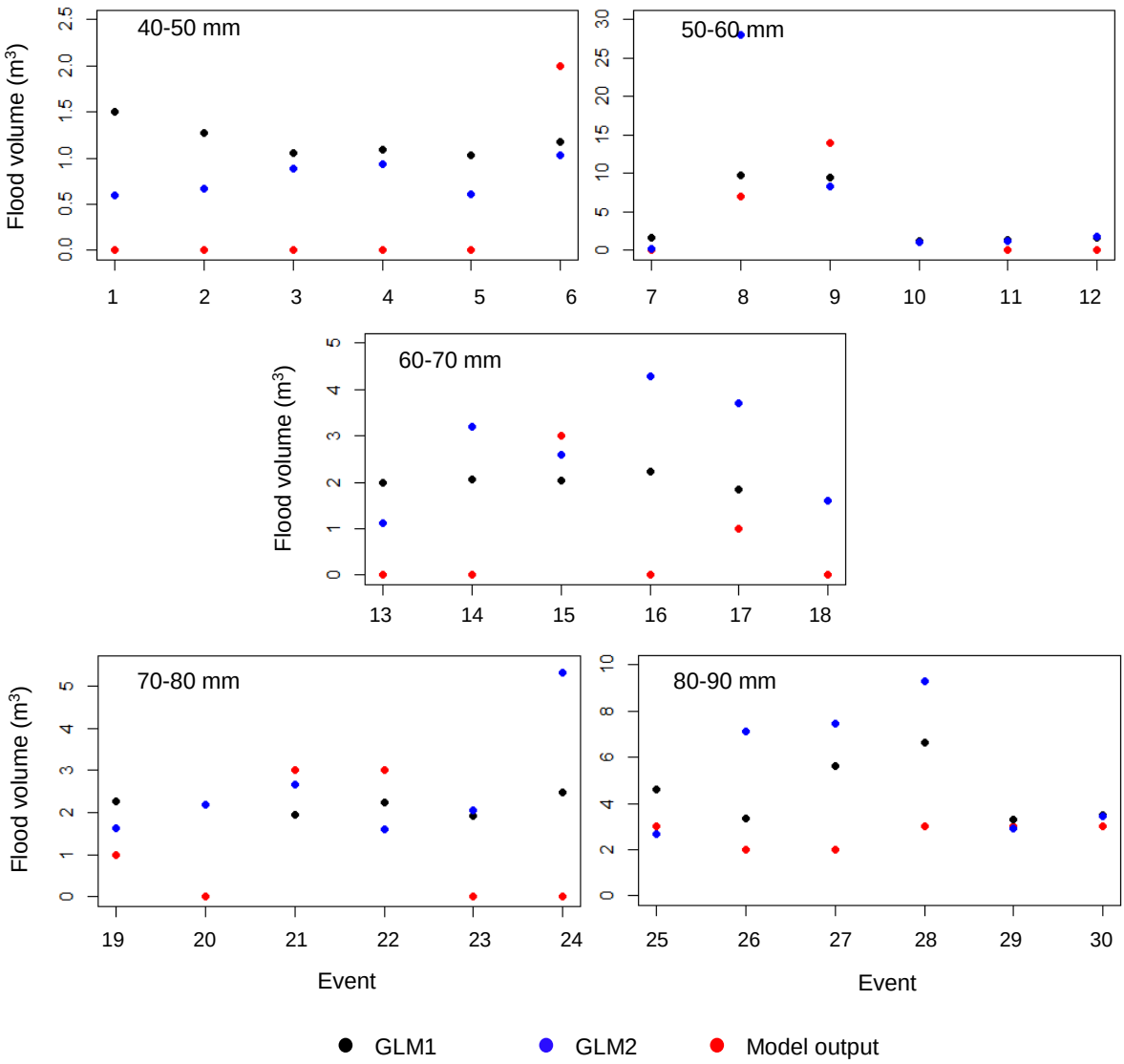

Figure 5.25. The total number of floods ($\boldsymbol{V^b}$) of each test event across the different mean rainfall ranges over the sewer catchment for $GLM1$, $GLM2$ and the hydraulic model for Chopwell & Blackhall Mill.

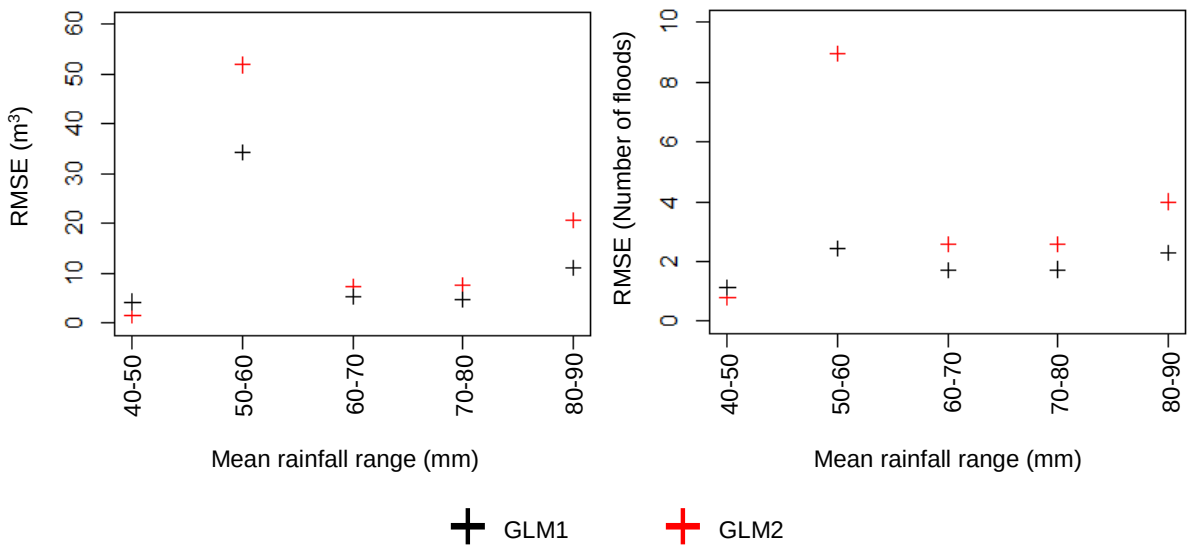

Figure 5.26. The RMSE values for the total flood volume ($\boldsymbol{V^a}$) (left) and total number of floods ($\boldsymbol{V^b}$) (right) across each mean rainfall range are presented for $GLM1$ and $GLM2$ against the model output for Chopwell & Blackhall Mill.

$\boldsymbol{V^a}$ and $\boldsymbol{V^b}$ showed relatively weak relationships with the mean rainfall, variance and the spatial indexes. When these variables are used in a GLM they will not accurately predict $\boldsymbol{V^a}$ and $\boldsymbol{V^b}$. This is observed in Figure 5.24, Figure 5.25 and Figure 5.26 where $\boldsymbol{V^a}$ and $\boldsymbol{V^b}$ are presented for $GLM1$, $GLM2$ and the hydraulic model as simulated. The verification QPE events used in this case study show that across the mean rainfall ranges, the sewer network does not flood extensively. This is observed from the values for $\boldsymbol{V^a}$ and $\boldsymbol{V^b}$ from Figure 5.24 and Figure 5.25 as they show relatively low values. For events that over and under-predict the model $\boldsymbol{V^a}$, GLM1 is better performing than $GLM2$. The average value for $GLM1$ over predicts the model $\boldsymbol{V^a}$ by 229% whereas the value for $GLM2$ overpredicts the model $\boldsymbol{V^a}$ by 275%. Where $GLM1$ under-predicts the model $\boldsymbol{V^b}$, the average value of $GLM2$ from $GLM1$ doesn't change (underprediction of 40%). However, where the values of $GLM1$ overpredict the model $\boldsymbol{V^b}$, the GLM1 performs better than $GLM1$ where the average value for $GLM2$ worsens from $GLM1$'s overprediction of 200% to 300%. Whilst these percentages are high, the average values for the flood variable is not large and so are not vastly inaccurate (see Table 5.6.2). Nonetheless, this analysis shows that $GLM2$ is less accurate than $GLM1$ for predicting the model $\boldsymbol{V^a}$ and $\boldsymbol{V^b}$ for

this sewer catchment. These outputs of $GLM2$ had been expected based on the explanations of how the spatial indexes perform for small sewer catchments.

Like the Ponteland case study, the performance of $GLM2$ performed better for study events in the lower mean rainfall ranges. Particularly, $\boldsymbol{V^a}$ and $\boldsymbol{V^b}$ of $GLM2$ show to be better for most of the events in the 40-50 mm mean rainfall range. This is also observed from the RMSE values in Figure 5.26 where overall the events in the first mean rainfall range (40-50 mm) shows better result for $GLM2$. However, for the events in the remaining mean rainfall ranges, $GLM1$ performs better as the RMSE values are lower in comparison to $GLM2$. Also, the primary reason the RMSE values for $GLM2$ in the 40-50 mm mean rainfall range are lower compared to $GLM1$ is that events 1 – 5 have no flooding, hence a value of 0 for $\boldsymbol{V^a}$. Only event 6 shows flooding (i.e. 2 floods) with less than 1 m^3 of flooding. However, both the $GLM1$ and $GLM2$ values for $\boldsymbol{V^a}$ and $\boldsymbol{V^b}$ are much above this and the values for $GLM2$ reduces the overestimation of the values of $GLM1$ thus being closer to the model values. Otherwise, $GLM2$ is generally less accurate than $GLM1$.

5.5 Case studies: large drainage areas

5.5.1 Extremities of spatial indexes

Chester-le-Street

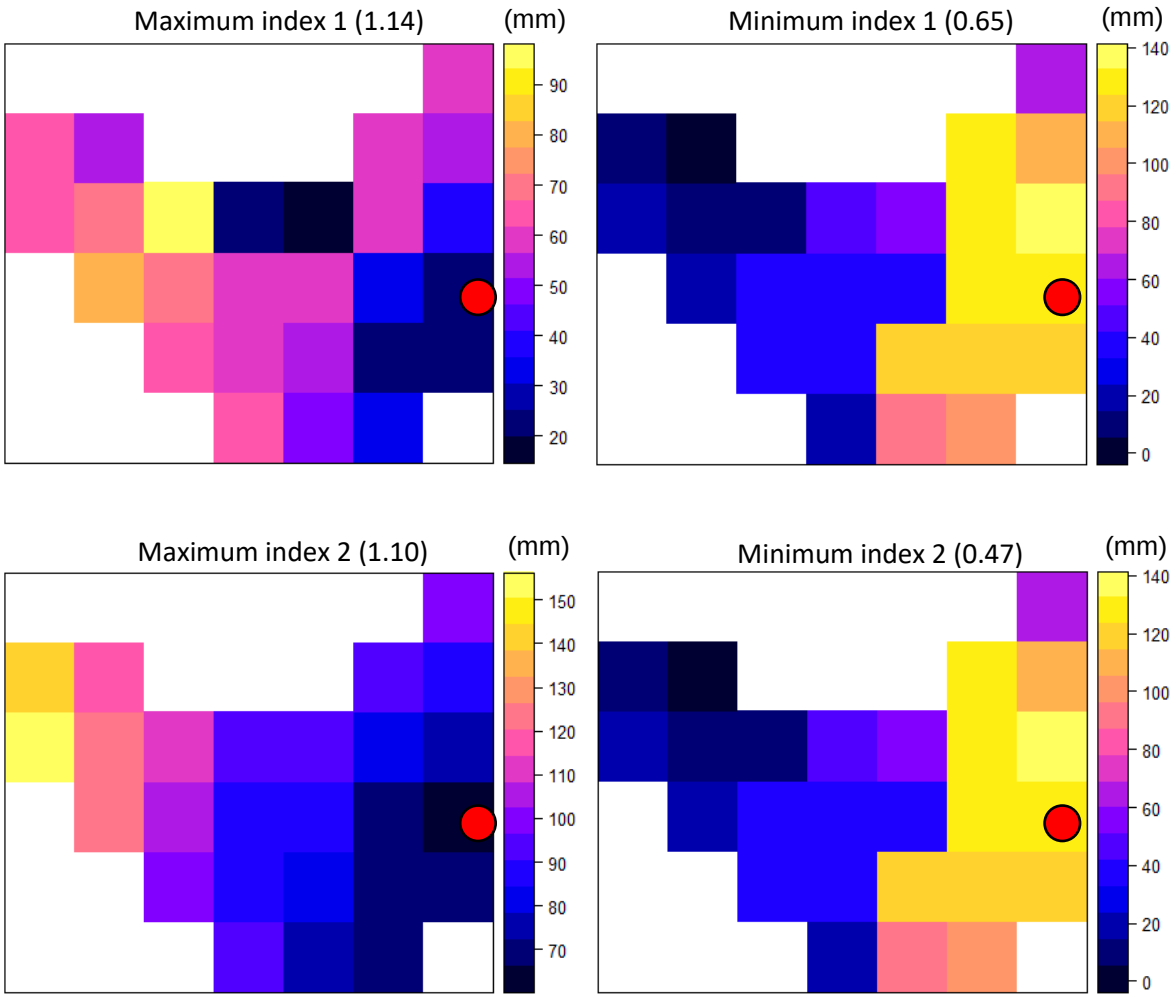

Figure 5.27. Maximum (left) and minimum (right) values for spatial indexes 1 (top) and 2 (bottom) across the catalogue of historical events for Chester-le-Street. The values are stated in brackets. Legend represents rainfall accumulation (in mm). Location of the main outlet is shown as a red filled circle.

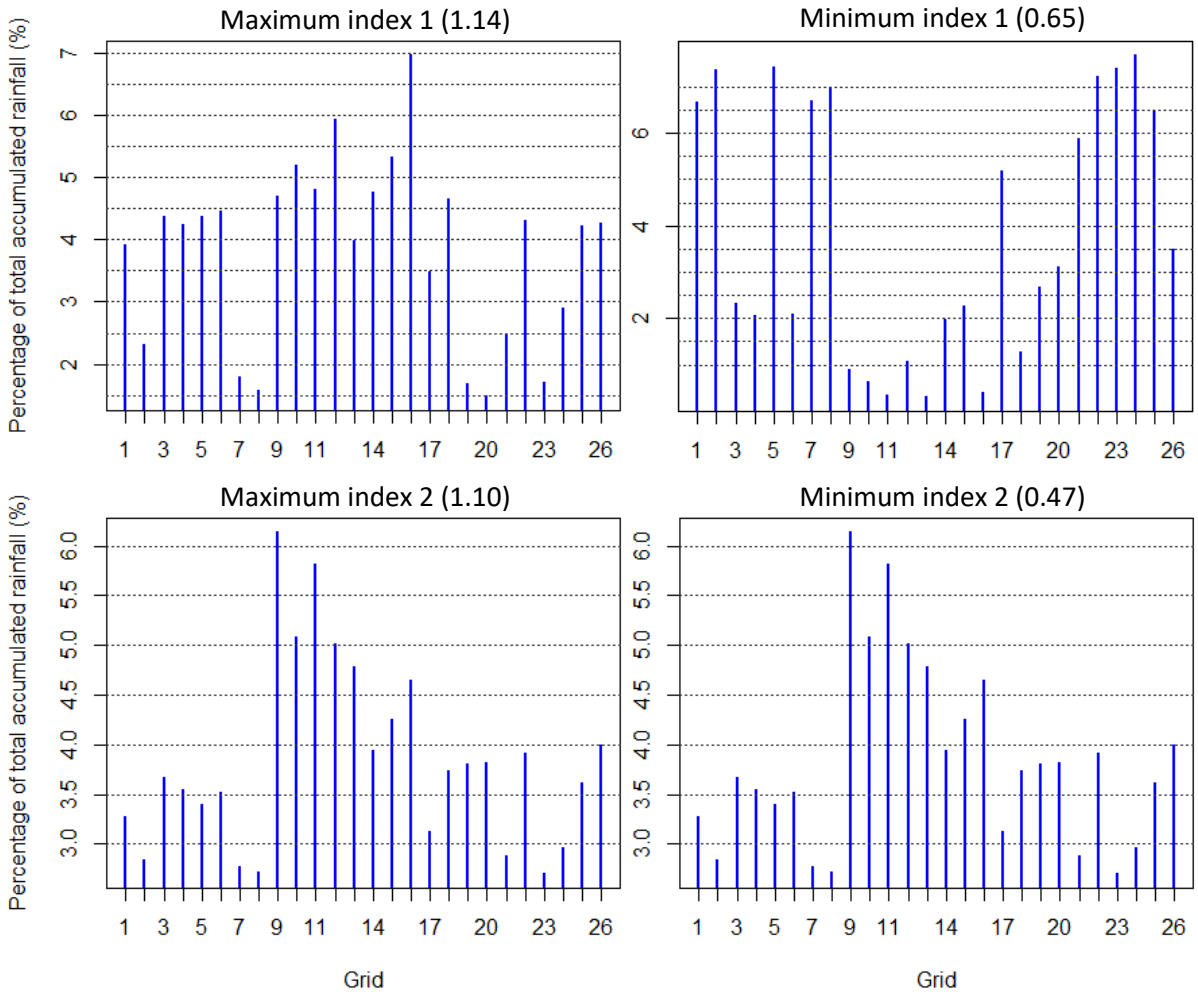

Figure 5.28. The percentage of total rainfall over the study region, Chester-Le-Street, is stated for each grid (see Figure 5.12) for events showing maximum/minimum spatial indexes.

Chester-Le-Street is relatively a larger sewer catchment in comparison to Ponteland and Chopwell & Blackhall Mill. Hence, the implications of the largest and smallest values for the spatial indexes are more visibly noticed. In Figure 5.27 these values are provided for spatial indexes 1 and 2. It is observed that the largest value for spatial index 1 shows that most of the rainfall is situated furthest away from the sewer catchment outfall (i.e. upstream) with the level of rainfall gradually decreasing towards it. This is better observed in Figure 5.28 where in the figure for maximum index 1(1.14) the grids with the highest rainfall are grids 12 and 16, followed by grids 15 and 10, all of which are situated upstream of the sewer catchment and all of which are adjacent to each other. Conversely, the event with the smallest value for spatial index 1 (0.65) has many grids

downstream of the sewer catchment that have the largest proportion of the rainfall over the area. In fact, the six grids that have the largest proportions of the rainfall are situated downstream and constitute 37.5% of the total rainfall over the sewer catchment. This event (i.e. event with the smallest value for spatial index 1) also has the smallest value for spatial index 2 in the catalogue of historical events. The six grids with the highest proportions of total rainfall are clustered together in a singular region of the sewer catchment. As this region in the sewer catchment consists of around 37.5% of the total rainfall, the storm for this event is characterised to be of convective type.

Darlington (North)

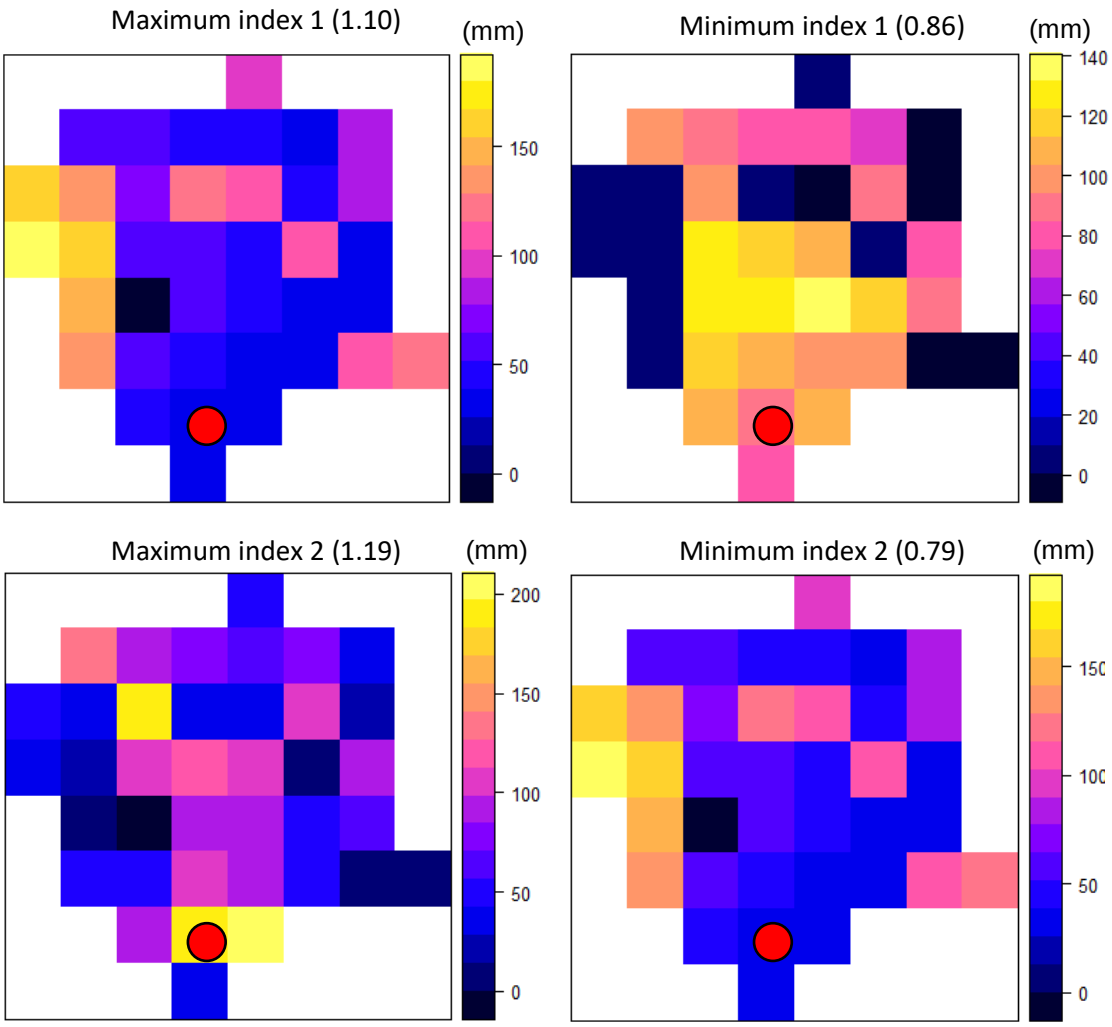

Figure 5.29. Maximum (left) and minimum (right) values for spatial indexes 1 (top) and 2 (bottom) across the catalogue of historical events for Darlington (North). The values are stated in brackets. Legend represents rainfall accumulation (in mm). Location of the main outlet is shown as a red filled circle.

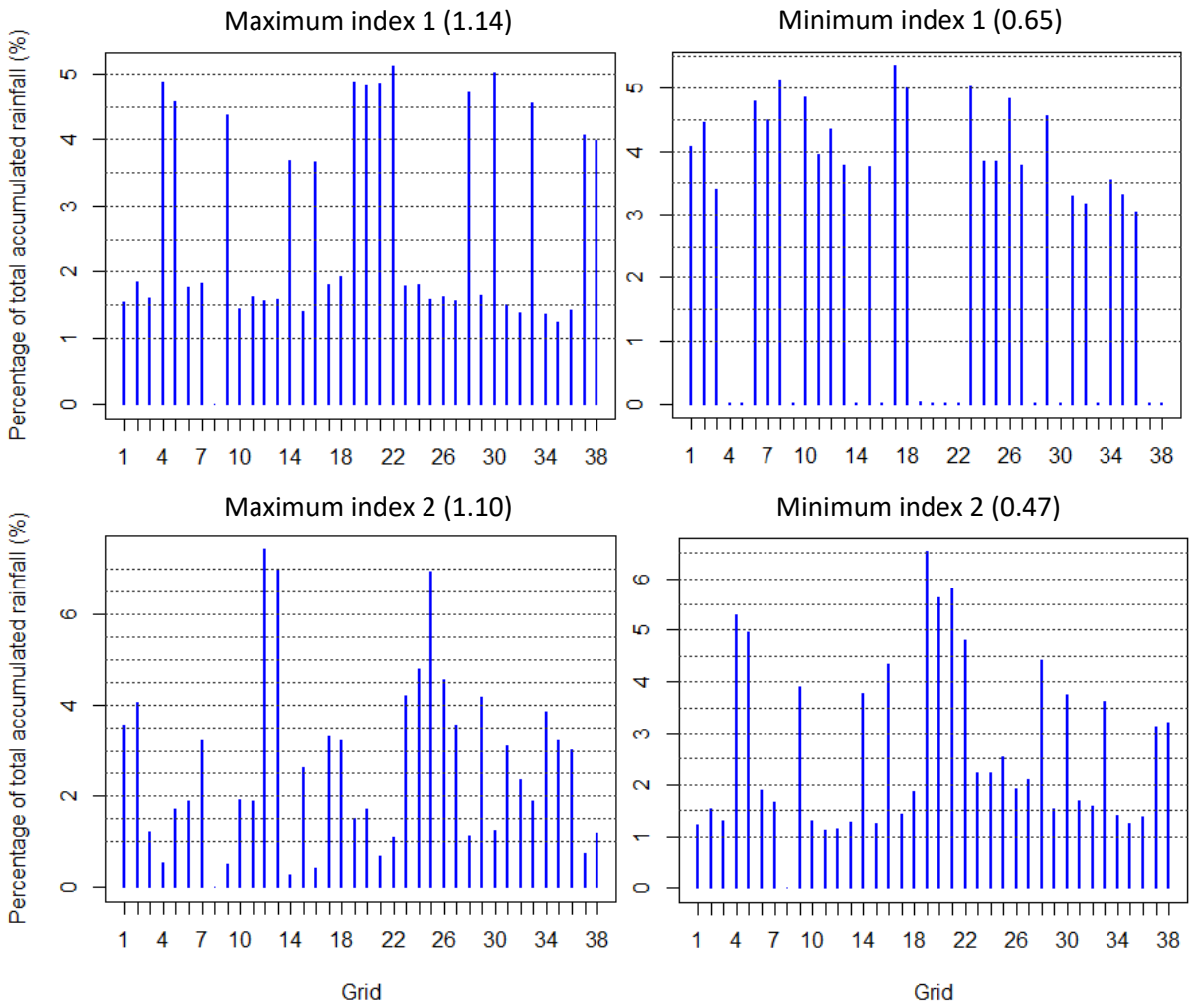

Figure 5.30. The percentage of total rainfall over the study region, Darlington (North), is stated for each grid (see Figure 5.12) for events showing maximum/minimum spatial indexes.

The main outlet for the sewer network of Darlington (North) is situated at bottom of the sewer catchment. Based on this, the extremities of the values of the spatial indexes can be visualised. For example, the value of 1.10 for spatial index 1 is the maximum value for an event found in the catalogue of historical QPE event. As is seen in Figure 5.29, the grid map shows heavier rainfall generally towards upstream of the sewer catchment. Although, there are regions at the northern boundaries upstream of the sewer catchment show less rainfall, whereas regions on the left boundary show the heaviest rainfall. More rainfall is seen towards the central and right regions of the sewer catchment. This is supported in Figure 5.30 where grids 1,2,3,6,7,12 and 13, all that are located downstream of the sewer catchment, show minimum rainfall. The event with the smallest value for spatial

index 1 has a value of 0.86. The grid map for this is different in that most of the rainfall is situated near the outlet (i.e. downstream of the sewer catchment). In fact, grids 6, 8, 10, 17, and 18 shows to have the highest proportions of the total rainfall and are all located downstream of the sewer catchment (these grids constitute around 25% of the total rainfall). However, several grids over the sewer catchment that have high proportions of rainfall are situated in the centre of catchment (grids 23, 26 and 29 constitute around 14.5% of the total rainfall). The event that has the lowest value for spatial index 1 also has the lowest value for spatial index 2 (value of 0.79), which suggests that the spatial distribution of the rainfall in this event is not only situated mostly upstream, but is focussed in a concentrated region over the sewer catchment indicating that the rainfall is from a convective type storm. The main difference between this event and another event with the largest value for spatial index 2 (value of 1.19) is that spatial distribution of the rainfall of the latter indicates a multimodal type of rainfall storm. This is suggested from the grid map in Figure 5.29 where there are two distinct regions in the sewer catchment that have the highest proportions of the total rainfall. The first region consists of grid 25 and this has 7% of the total rainfall (see Figure 5.30). The second region consists of grids 12 and 13 and they both make up 14.5% of the total rainfall. In comparison to the other 35 grids, the rainfall over these three grids is markedly higher and so explains why the large value of 1.19 for spatial index 2.

5.5.2 Relationship between model flood variables and spatial variables

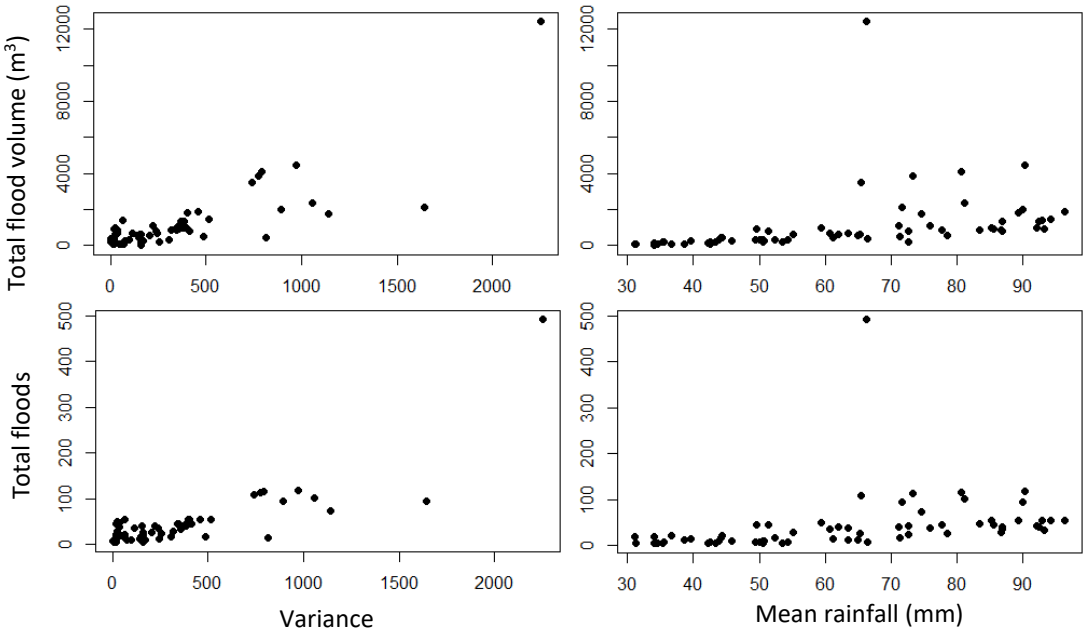

Figure 5.31. Scatter graphs showing the correlations of the total flood volume ($\boldsymbol{V^a}$) (top) and total number of floods ($\boldsymbol{V^b}$) (bottom) against the variance (left) and mean rainfall (right) of Chester-le-Street.

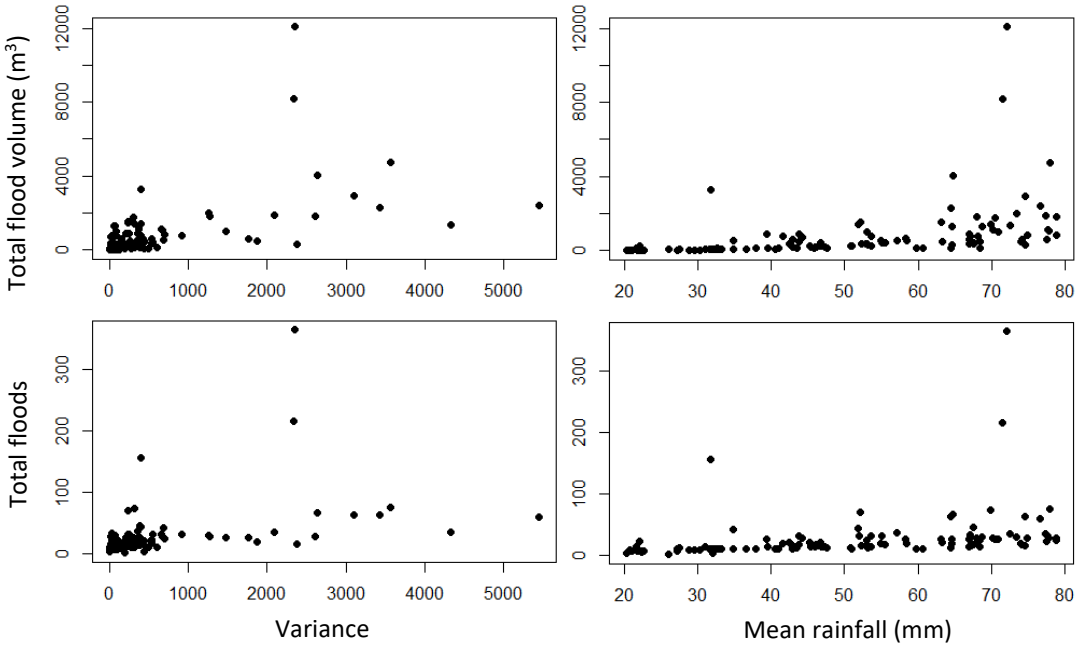

Figure 5.32. Scatter graphs showing the correlation of the total flood volume ($\boldsymbol{V^a}$) (top) and total number of floods ($\boldsymbol{V^b}$) (bottom) against the variance (left) and mean rainfall (right) of Darlington (North).

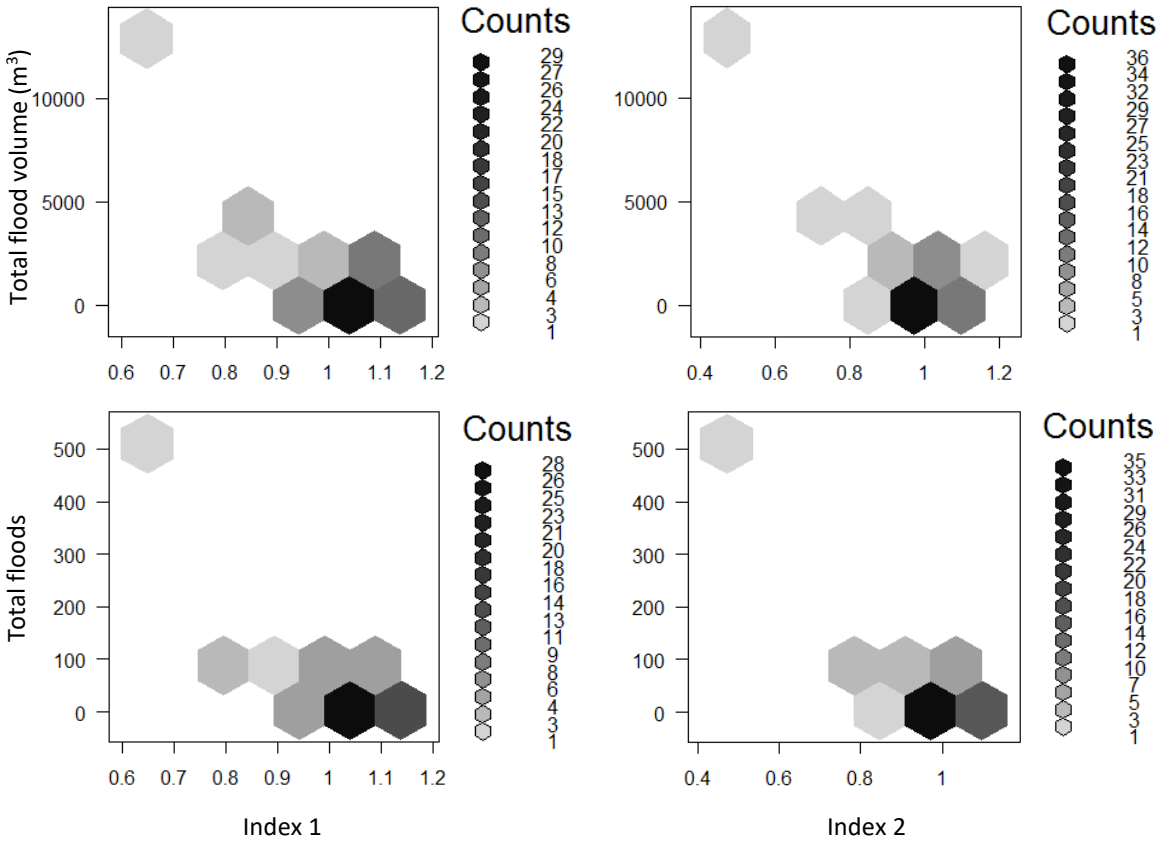

Figure 5.33. Hex bin charts showing the density of events per value of index 1 (left) and index 2 (right) for $\boldsymbol{V^a}$ (total flood volume) (top) and $\boldsymbol{V^b}$ (total floods) (bottom) of Chester-le-Street.

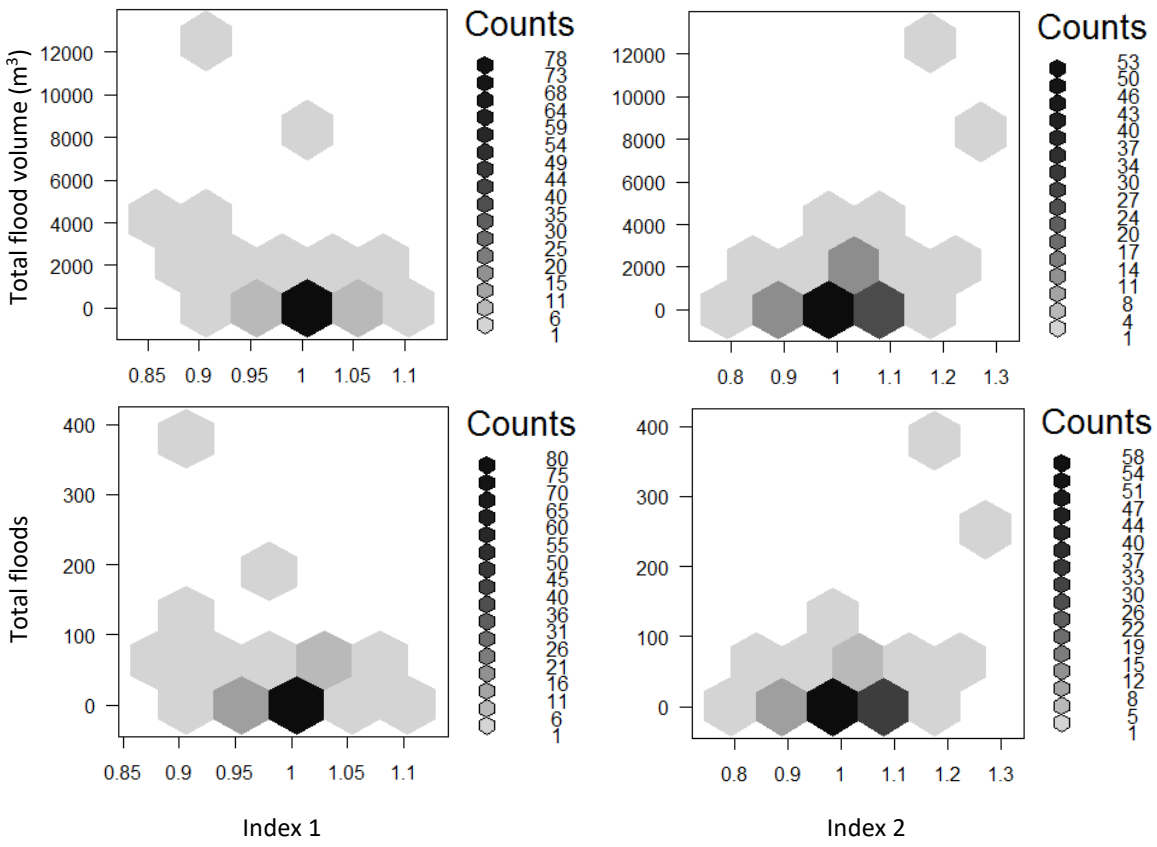

Figure 5.34. Hex bin charts showing the density of events per value of index 1 (left) and index 2 (right) for $\boldsymbol{V^a}$ (total flood volume) (top) and $\boldsymbol{V^b}$ (total floods) (bottom) of Darlington (North).

Chester-le-Street

$\boldsymbol{V^a}$ and $\boldsymbol{V^b}$ have moderate/strong positive correlations with variance and mean rainfall over the sewer catchment. The scatter graphs in Figure 5.31 show these relationships where the r values for mean rainfall are 0.47 and 0.51 for $\boldsymbol{V^a}$ and $\boldsymbol{V^b}$, respectively, and for variance are 0.82 and 0.81 for $\boldsymbol{V^a}$ and $\boldsymbol{V^b}$, respectively. The r value for the relationships of $\boldsymbol{V^a}$ and $\boldsymbol{V^b}$ with variance is particularly strongly positively correlated. This means that the higher the variance of the rainfall over the sewer catchment, the higher the total flood volume or more nodes in the network would be flooded. There is one event in the catalogue of historical QPE events showing mean rainfall that is not very high relative to the other events (in the range of 60 – 70 mm) and shows a markedly high value of $\boldsymbol{V^a}$ and $\boldsymbol{V^b}$in comparison to other events in the same mean rainfall category. In fact, this anomalous event shows the largest values of $\boldsymbol{V^a}$ and $\boldsymbol{V^b}$ (491 floods and 12411 m^3 of flooding, respectively). However, this event has the largest

value for variance. Furthermore, this event has the lowest value for spatial index 1 and 2 (see Figure 5.31). Based on this, it is concluded that highly convective rainfall over nodes situated downstream of this sewer catchment would result in the most flooded nodes with large flood volumes. Furthermore, this would not able to be predicted using the linear model (or a nonlinear model). However, for future work a separate analysis studying 'peaks' in flood data that cannot be predicted using linear or nonlinear models could be done. Work such as Wang et al. (2015) study singularities in rainfall and the concept used could also be applied to find anomalous peaks in flood data.

The hex bins in Figure 5.33 show the relationships between $\boldsymbol{V^a}$ and $\boldsymbol{V^b}$ with spatial indexes 1 and 2. It is observed that values of spatial index 1 below 1 generally show large $\boldsymbol{V^a}$ and $\boldsymbol{V^b}$. This means that more flooding would occur when the rainfall is situated mostly downstream of the sewer catchment. A similar trend is observed for spatial index 2 where larger values of $\boldsymbol{V^a}$ and $\boldsymbol{V^b}$ are observed for values below 1 for spatial index 2. Hence, it is expected that when rainfall is situated mostly in a concentrated region in the sewer catchment, more flooding is expected.

Darlington (North)

Like Chester-le-Street, Darlington (North) shows moderate to strong correlations of $\boldsymbol{V^a}$ and $\boldsymbol{V^b}$ with variance and the mean rainfall over the sewer catchment. The correlations for variance are 0.69 and 0.50 for $\boldsymbol{V^a}$ and $\boldsymbol{V^b}$, respectively, and for mean rainfall are 0.54 and 0.40 for $\boldsymbol{V^a}$ and $\boldsymbol{V^b}$, respectively. The relationships of $\boldsymbol{V^a}$ and $\boldsymbol{V^b}$ with the spatial indexes are similar to the Chester-le-Street sewer catchment. Values below 1 for spatial index 1 generally tend to show higher flood volumes or more flooded nodes (see Figure 5.34). This means that when most of the rainfall is situated downstream of the sewer catchment, more flooding would typically be observed in such events. However, where the spatial distribution of the rainfall indicates a multimodal storm or where more than one region in the drainage has the highest proportion of total rainfall (i.e. values above 1 for spatial index 2) more flooding is observed in contrast to singular regions in the sewer catchment that have the highest proportion of total rainfall. This

indicates that there are several regions in the sewer network that are sensitive to flooding, especially downstream of the sewer catchment.

5.5.3 Generalised Linear Models

Chester-le-Street

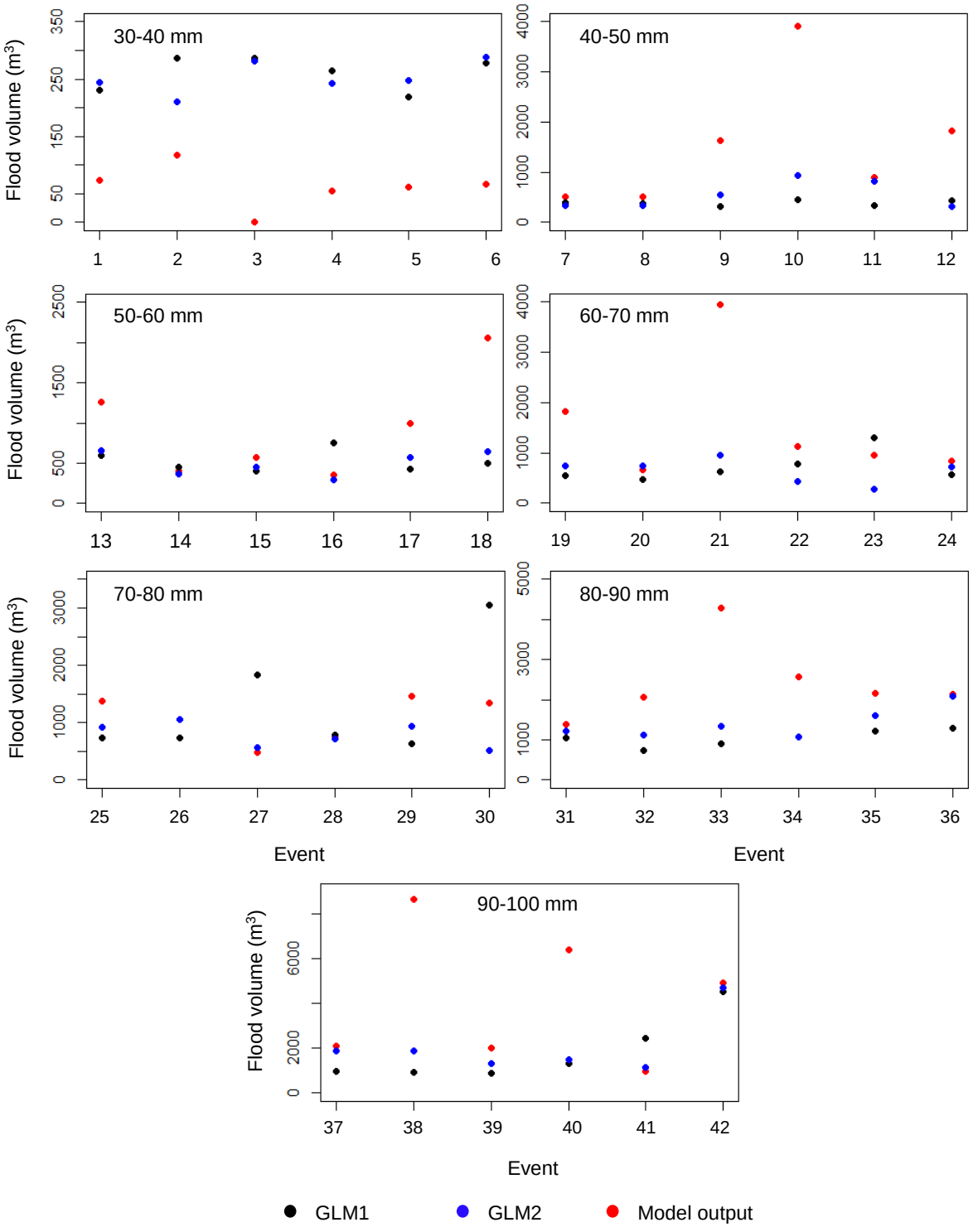

Figure 5.35. The flood volumes ($\boldsymbol{V^a}$) of each test event across the different mean rainfall ranges over the sewer catchment for $GLM1$, $GLM2$ and the hydraulic model for Chester-Le-Street.

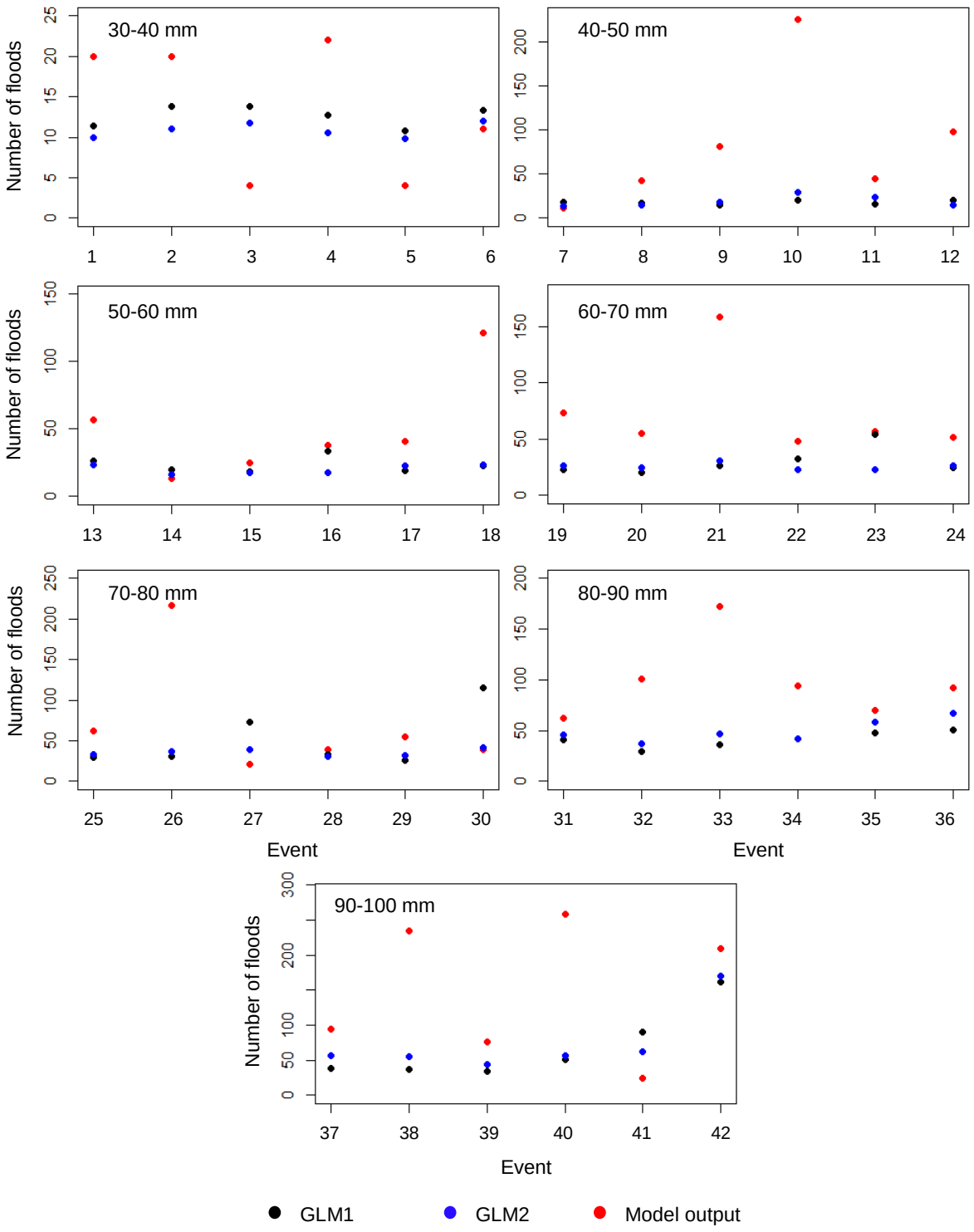

Figure 5.36. The total number of floods ($\boldsymbol{V^b}$) of each test event across the different mean rainfall ranges over the sewer catchment for $GLM1$, $GLM2$ and the hydraulic model for Chester-le-Street.

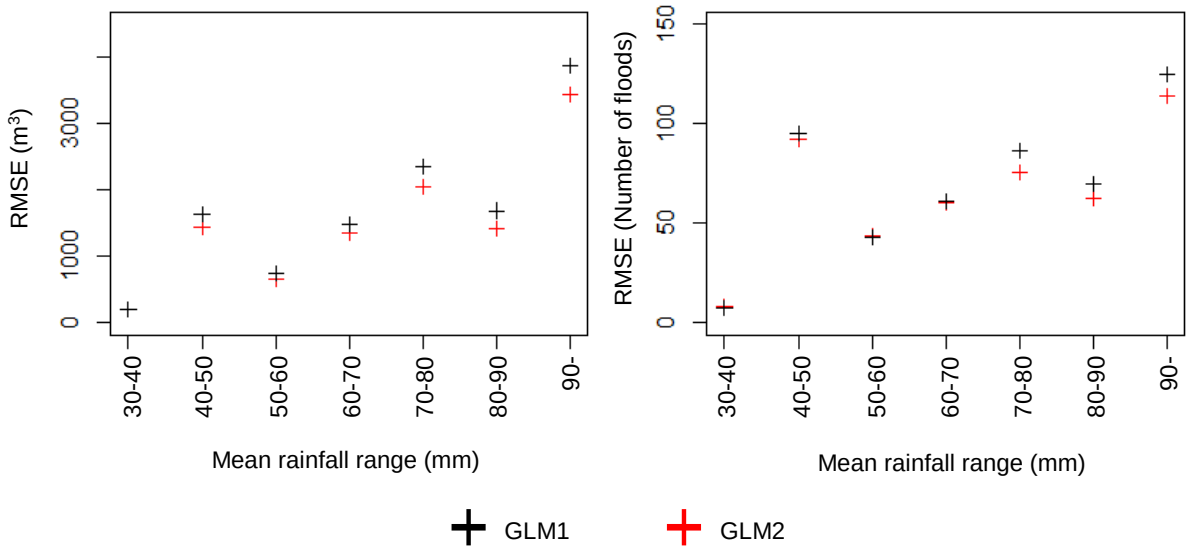

Figure 5.37. The RMSE values for the total flood volume ($\boldsymbol{V^a}$) (left) and total number of floods ($\boldsymbol{V^b}$) (right) across each mean rainfall range are presented for $GLM1$ and $GLM2$ against the model output for Chester-le-Street.

The performance of $GLM1$ and $GLM2$ for this sewer catchment is shown in Figure 5.35, Figure 5.36and Figure 5.37**.** Across all the verification QPE events, it is observed that values for $\boldsymbol{V^a}$ and $\boldsymbol{V^b}$ for $GLM1$ generally underestimate the model values. However, for some events values for $GLM1$ overestimate the model values. For example, values for $\boldsymbol{V^a}$ of $GLM1$ for all events in the 30-40 mm mean rainfall range overestimate the model values. For events that underestimate model $\boldsymbol{V^a}$, the average value for $GLM1$ underestimate the model $\boldsymbol{V^a}$ by 63%. For $\boldsymbol{V^b}$, the $GLM1$ underestimates the model $\boldsymbol{V^b}$ by 65%. However, when considering spatial indexes 1 and 2 in addition to variance and mean rainfall, the underestimation is reduced so that the predicted $\boldsymbol{V^a}$ and $\boldsymbol{V^b}$ from the GLM are closer to the model values. The average $\boldsymbol{V^a}$ for $GLM2$ reduces the overestimation of the values of $GLM1$ to 56%. For $\boldsymbol{V^b}$, the underestimation is reduced to 62%. When considering events where the values of $GLM1$ overestimate the model values, they overestimate these values to a large degree. The average values of $GLM1$ for $\boldsymbol{V^a}$ and $\boldsymbol{V^b}$ overestimate the model values by 119% and 175%, respectively. However, the values for $GLM2$ reduce this overestimation greatly where the average values reduce the overestimation of $\boldsymbol{V^a}$ and $\boldsymbol{V^b}$ to 0% and 56%, respectively. The average value of $\boldsymbol{V^a}$ for $GLM2$ equates to the average

model $\boldsymbol{V^a}$ (hence the 0%). Clearly, $GLM2$ is a better predictor than $GLM2$ for deducing values close to the hydraulically simulated $\boldsymbol{V^a}$ and $\boldsymbol{V^b}$.

By considering the spatial index values in addition to the variance and mean rainfall, the predictions of $\boldsymbol{V^a}$ and $\boldsymbol{V^b}$ improve over just considering variance and mean rainfall. This is because specific spatial information indicated by spatial indexes 1 and 2 is more accurately depicted in larger sewer catchments where several grids over the region are used to extract rainfall data. Chester-le-Street is a larger sewer catchment in comparison to Ponteland and Chopwell & Blackhall Mill, and so the results show that the spatial indexes are more reliable for a sewer catchment of this size.

Events in individual mean rainfall ranges demonstrate that $GLM2$ performs consistently well in each of them, for both $\boldsymbol{V^a}$ and $\boldsymbol{V^b}$. Also, the performance of $GLM1$ (and hence $GLM2$) progressively worsens for events higher up the mean rainfall ranges. This is better illustrated in Figure 5.37 where the RMSE values are provided for each mean rainfall range. Despite the RMSE values fluctuating in performance between the 40-50 and 80-90 mm mean rainfall range, the average difference between these two categories show that the RMSE has marginally increased. Also, the final mean rainfall range of 90-100 mm shows the largest RMSE value.

Darlington (North)

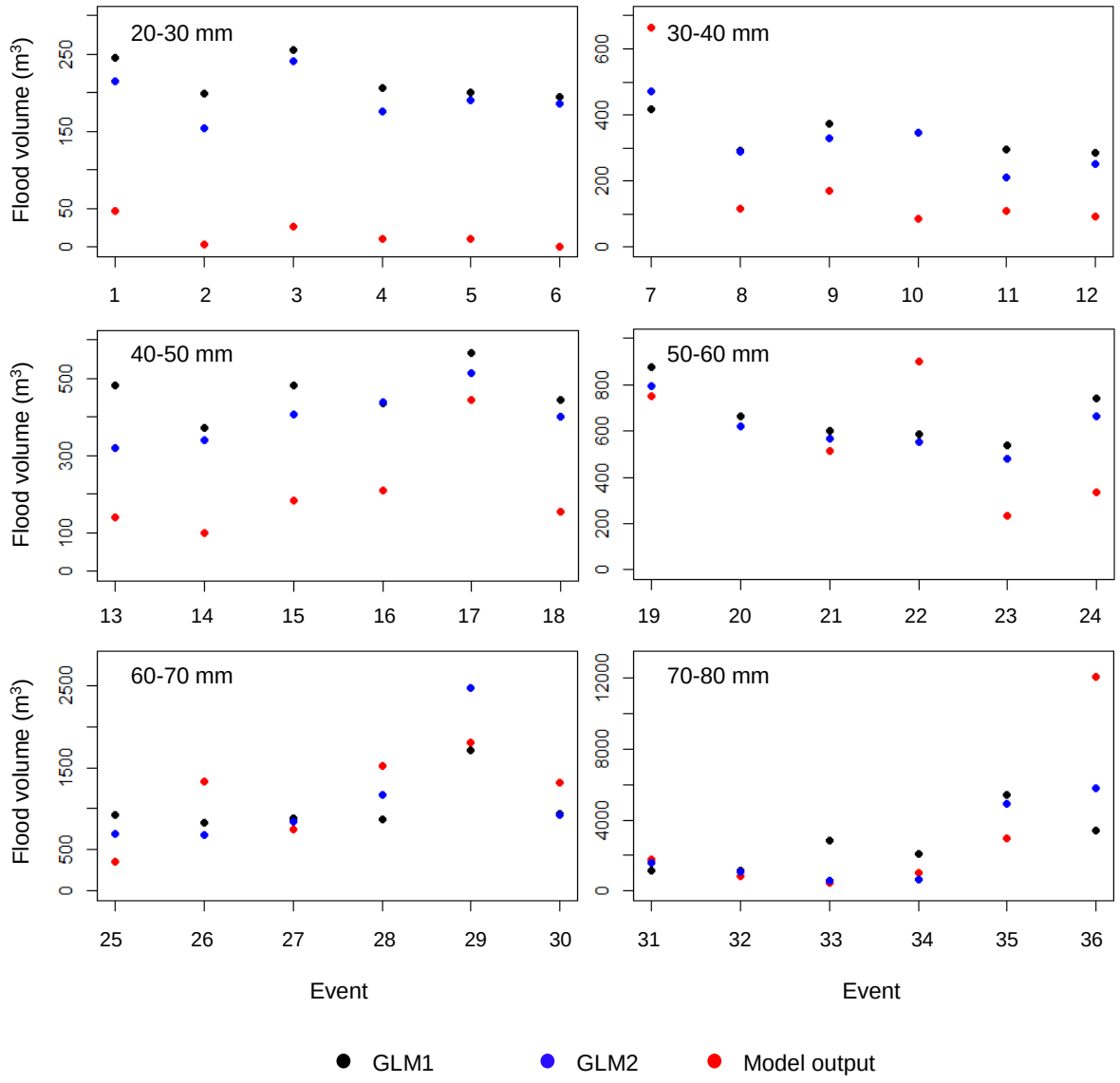

Figure 5.38. The flood volumes ($\boldsymbol{V^a}$) of each test event across the different mean rainfall ranges over the sewer catchment for $GLM1$, $GLM2$ and the hydraulic model for Darlington (North).

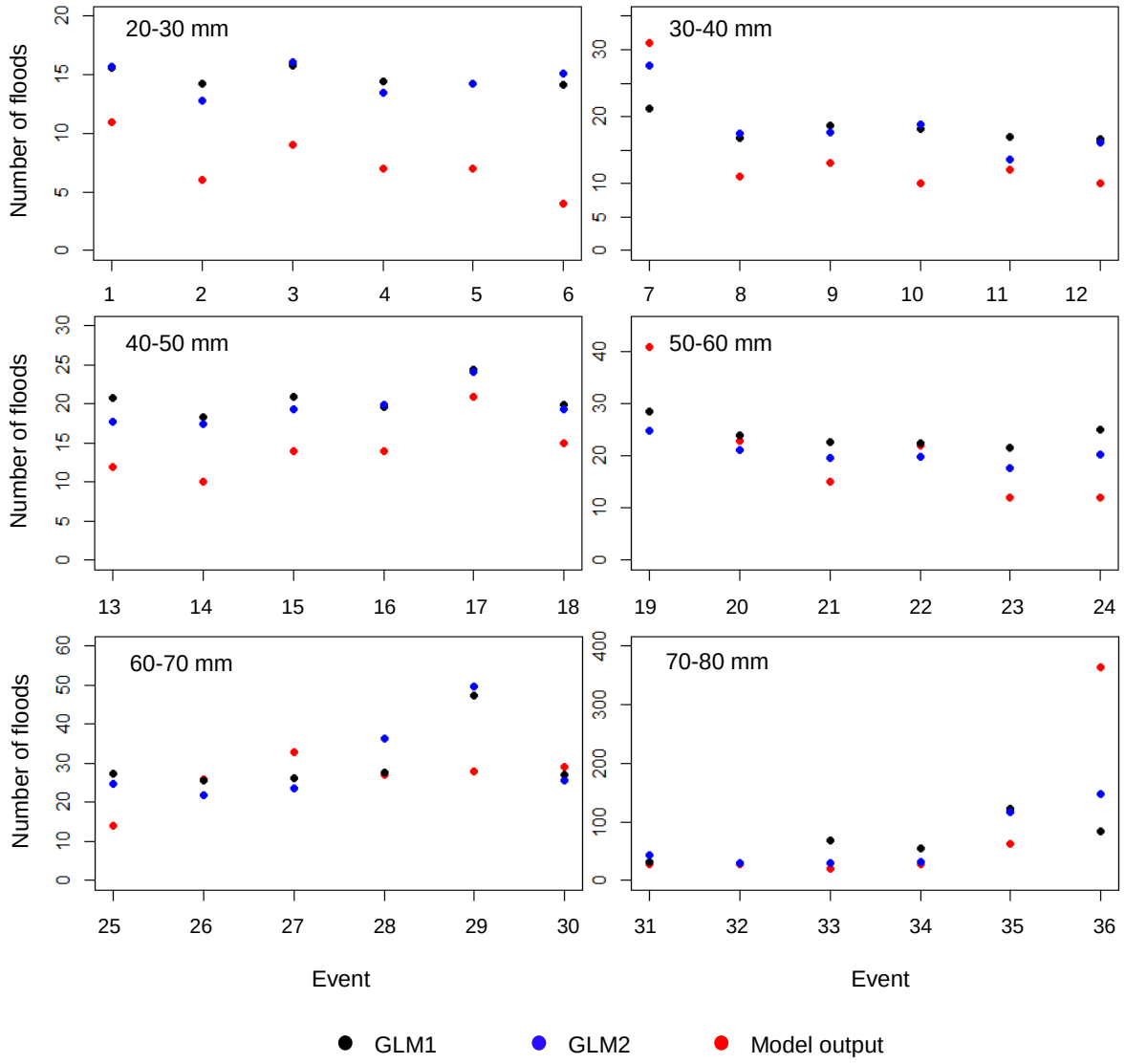

Figure 5.39. The total number of floods ($\boldsymbol{V^b}$) of each test event across the different mean rainfall ranges over the sewer catchment for $GLM1$, $GLM2$ and the hydraulic model for Darlington (North).

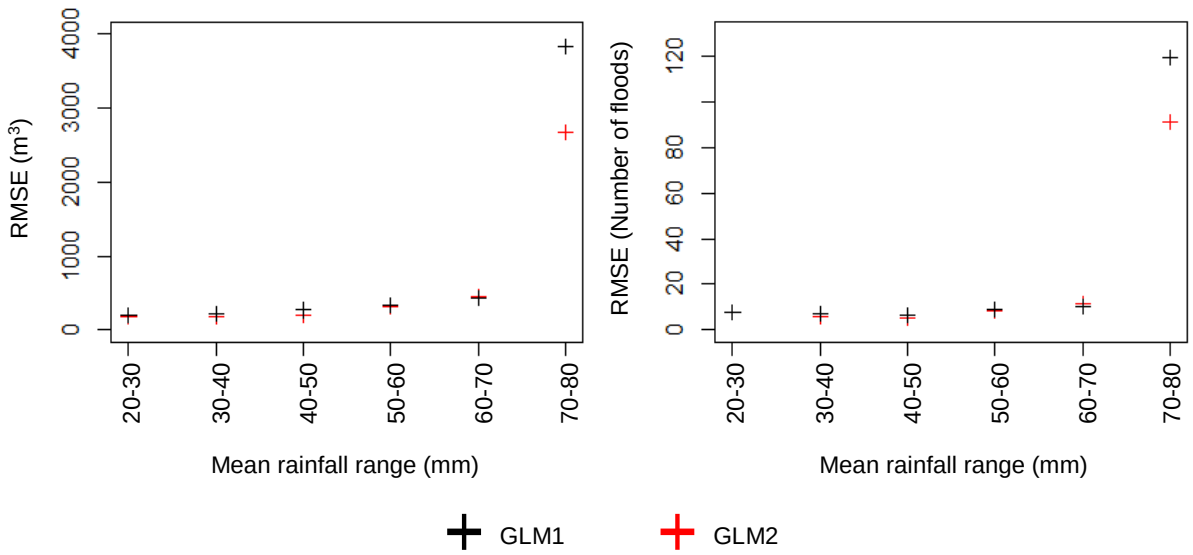

Figure 5.40. The RMSE values for the total flood volume ($\boldsymbol{V^a}$) (left) and total number of floods ($\boldsymbol{V^b}$) (right) across each mean rainfall range are presented for $GLM1$ and $GLM2$ against the model output for Darlington (North).

The performance of $GLM1$ and $GLM2$ for Darlington (North)'s sewer catchment performs similarly to the Chester-Le-street case study. Based on Figure 5.38 and Figure 5.39 for most the events $\boldsymbol{V^a}$ and $\boldsymbol{V^b}$ of $GLM1$ overestimate the mode values. Particularly, events in the 20-30 mm mean rainfall range have $GLM1$ values that overestimate the model values the most. For those events that overestimate the model values, $\boldsymbol{V^a}$ and $\boldsymbol{V^b}$ of $GLM1$ overestimate the model values by 115% and 59%, respectively. This particularly shows that just considering the variance and mean rainfall as predictors for $\boldsymbol{V^a}$ and $\boldsymbol{V^b}$ show that the GLM featuring these predictors would provide estimations more than double of the model output. However, when considering spatial index values as in $GLM2$, the average values for $\boldsymbol{V^a}$ and $\boldsymbol{V^b}$ reduce the overestimation to 61% and 41%, respectively. This highlights a major improvement for events where $GLM1$ greatly overpredicts the flood extents. For events that have values of $GLM1$ underestimating the model values, the average values given by $GLM1$ underestimate $\boldsymbol{V^a}$ and $\boldsymbol{V^b}$ by 53% and 60%, respectively. However, this underestimation is reduced by $GLM2$ where average values of $\boldsymbol{V^a}$ and $\boldsymbol{V^b}$ show underestimations of 37% and 48%. Similarly, to the trends of the results seen in the Chester-le-Street case study, $GLM2$ is clearly a more accurate model to predict $\boldsymbol{V^a}$ and $\boldsymbol{V^b}$ in comparison to $GLM1$. This is because the sewer catchment

of Darlington (North) is relatively large albeit being larger than Chester-Le-street. However, both sewer catchments are notably larger than Ponteland and Chopwell & Blackhall Mill sewer catchments whose performance of $GLM2$ is worse than $GLM1$.

Values of $\boldsymbol{V^a}$ observed in all the verification QPE events except for the 70-80 mm category are relatively low in comparison to some of $\boldsymbol{V^a}$ values observed in events in the 70-80 mean rainfall range (see Figure 5.38). In fact, the event with the highest $\boldsymbol{V^a}$is event 36 which is has an approximate value of 12000 m^3 whereas the values of $GLM1$ and $GLM2$ don't exceed 6000 m^3. However, based on the very large improvement of $\boldsymbol{V^a}$ predicted by $GLM2$ over the value of $GLM1$ for this event, the RMSE value for $GLM2$ for this mean rainfall range shows the largest improvement in Figure 5.40. Also, based on the relatively small values of $\boldsymbol{V^a}$ seen in the other events as described, the improved RMSE values of $GLM2$ in this figure are not very large compared the improvement seen in the 70-80 mean rainfall range. However, similarly as in the Chester-le-Street case study, the average RMSE value for each mean rainfall range has improved (i.e. $GLM2$ is more accurate than $GLM1$ in predicting flood volume across each mean rainfall range). A similar reasoning is applied for total floods (see Figure 5.39).

5.6 Summary of results and conclusions

The results for the four case studies are summarised in Table 5.6.1 which provides average values of the $\boldsymbol{V^a}$ and $\boldsymbol{V^b}$ (based on Equations (5.12 and 5.13)) for $GLM1$, $GLM2$ and the model output for the study events. Two sets of results are stated: one set is where the $\boldsymbol{V^a}$ and $\boldsymbol{V^b}$ of $GLM1$ overestimate the model values, and another set where the $\boldsymbol{V^a}$ and $\boldsymbol{V^b}$of $GLM1$ underestimate the model values. As $GLM2$ contains the two spatial indexes as predictor variables in addition to the mean and variance that $GLM1$ has as its only two predictor variables, the change of overestimation/underestimation could directly be attributed to the additional predictor variables in $GLM2$. Therefore, this would enable comparisons between $GLM1$ and $GLM2$ to be made to indicate whether $GLM2$ is indeed a better predictor. Furthermore, it would indicate the performance of $GLM2$ in two different cases where $GLM1$ overestimates or underestimates model output. Table 5.6.2 indicates the percentages of over/underestimation of

the values of $GLM1$ and $GLM2$ with the model values. The lower the percentages the better the result.

Table 5.6.1. The average values of $\boldsymbol{V^a}$ and $\boldsymbol{V^b}$ of $GLM1$, $GLM2$ and model output for each case study are provided. They are organised on values of $GLM1$ over/underestimating the model value to better see the improvement of $GLM2$.

		$\boldsymbol{V^a}$ (m^3)		$\boldsymbol{V^b}$(no. of floods)	
		Overestimate (GLM1 > Model)	Underestimate (GLM1 < Model)	Overestimate (GLM1 > Model)	Underestimate (GLM1 < Model)
Ponteland	$GLM1$	3425.4	2174.2	31	20
	$GLM2$	5683.8	3048.1	87	61
	Model	2046.5	3337.1	17	41
Chopwell & Blackhall Mill	$GLM1$	12.7	5.0	3	3
	$GLM2$	14.5	6.6	4	3
	Model	3.9	5.3	1	5
Chester-Le-street	$GLM1$	954.7	883.7	44	32
	$GLM2$	435.9	1074.4	25	35
	Model	435.4	2417.5	16	92
Darlington (North)	$GLM1$	805.7	1173.4	27	35
	$GLM2$	603.2	1590.4	24	45
	Model	375.1	2504.6	17	87

Table 5.6.2. Percentage of over/underestimate of average $\boldsymbol{V^a}$ and $\boldsymbol{V^b}$ of $GLM1$ and $GLM2$ with model value for each case study.

		Percentage of over/underestimate with model value (%)			
		$\boldsymbol{V^a}$		$\boldsymbol{V^b}$	
		Overestimate (GLM1 > Model)	Underestimate (GLM1 < Model)	Overestimate (GLM1 > Model)	Underestimate (GLM1 < Model)
Ponteland	$GLM1$	67	35	82	51
	$GLM2$	178	9	412	48*
Chopwell & Blackhall Mill	$GLM1$	226	6	200	40
	$GLM2$	272	25*	300	40
Chester-Le-street	$GLM1$	119	63	175	65
	$GLM2$	0	56	56	62
Darlington (North)	$GLM1$	115	53	59	60
	$GLM2$	61	37	41	48

* These values show percentage overestimation instead of percentage underestimation

For Ponteland case study (small sewer catchment):

- The overall RMSE values for total flood volume and total number of floods for $GLM1$ are 1270.9m^3 and 18, respectively.
- The overall RMSE values for total flood volume and total number of floods for $GLM2$ are 1963.2m^3 and 45, respectively.

For Blackhall Mill case study (small sewer catchment):

- The overall RMSE values for total flood volume and total number of floods for $GLM1$ are 4.55m^3 and 2, respectively.
- The overall RMSE values for total flood volume and total number of floods for $GLM2$ are 5.95m^3 and 3, respectively.

Hence, for small sewer catchments, use of spatial indexes together with mean rainfall and variance are not useful for predicting flood extents.

For Chester-le-Street case study (large sewer catchment):

- The overall RMSE values for total flood volume and total number of floods for $GLM1$are 1026.6m^3 and 44, respectively.
- The overall RMSE values for total flood volume and total number of floods for $GLM2$ are 671.8m^3 and 33, respectively.

For Darlington (North) case study (large sewer catchment):

- The overall RMSE values for total flood volume and total number of floods for $GLM1$ are 880.9m^3 and 31, respectively.
- The overall RMSE values for total flood volume and total number of floods for $GLM2$ are 571.2m^3 and 24, respectively.

Hence, for large sewer catchments, use of spatial indexes together with mean rainfall and variance are useful for predicting flood extents.

Whilst $GLM2$ performs worse overall compared to $GLM1$ for predicting $\boldsymbol{V^a}$ and $\boldsymbol{V^b}$ in cases studies Ponteland and Chopwell and Blackhall Mill, where $GLM1$ underestimate the model outputs $GLM2$ reduces this underestimation (apart from

predicting $\boldsymbol{V^b}$ in Chopwell and Blackhall Mill, which doesn't show a difference in values) (see

Table 5.6.2). In fact, the value for $\boldsymbol{V^a}$ of $GLM2$ in Ponteland is more accurate than the value of $GLM1$. Furthermore, $GLM2$ results in overestimating the model output where $GLM1$ underestimates for $\boldsymbol{V^a}$ Chopwell and Blackhall Mill and $\boldsymbol{V^b}$ in Ponteland (negative values in

Table 5.6.2). This shows that for the small sewer catchments, $GLM2$ has the tendency to overestimate $\boldsymbol{V^a}$ and $\boldsymbol{V^b}$ when $GLM1$ underestimates these values. For Chester-le-Street and Darlington (North), $GLM2$ performs better for predicting the model $\boldsymbol{V^a}$ and $\boldsymbol{V^b}$ when $GLM1$ overestimate these values in contrast to when $GLM1$ underestimate these values.

Conclusions

This chapter has developed an approach to estimate hydraulic model flood variables without running online hydraulic simulations using generalised linear models and a spatial analysis of radar QPE over sewer catchments. Spatial analysis involves extracting mean rainfall, variance and values for two spatial indexes from a 'catalogue' of historical rainfall events over a sewer catchment. Offline hydraulic simulations are performed to obtain flood volume and number of flooded nodes. Two generalised linear models are produced from the predictor variables mean rainfall, variance and values for two spatial indexes and response variables flood volume and number of flooded nodes. The first model, $GLM1$, includes mean rainfall and variance as predictor variables. The second model, $GLM2$, includes mean rainfall, variance and the two spatial indexes as predictor variables.

The study uses radar QPE/QPF sources from section 3.3.1 and introduces four sewer catchments in the region where the radar QPE/QPF are sourced that are used as case studies. Six-hour QPE events are extracted between January 2012 and December 2016 and used to produce a catalogue of historical QPE events. These events are edited to produce verification QPE events that are used to test the flood forecasting approach.

The main conclusion of this chapter is that the spatial indexes are more accurate predictors of the flooding extent than just using mean rainfall and variance for large sewer catchments. Using these four variables estimation of the flood extents could be obtained within a degree of uncertainty.

This approach could be used as part of probabilistic flood forecasting system to directly predict flood extents without running computationally expensive hydraulic simulations using probabilistic QPFs. Moreover, the approach to spatial analysis is useful for using probabilistic QPFs over a sewer catchment. This would improve probabilistic sewer flood modelling and forecasting at a spatial scale, thus improving the way probabilistic hydraulic variable forecasts are understood for supporting decision making. As the method presented in this chapter focuses on spatial distribution of rainfall fall, the temporal distribution of the rainfall is not included. Temporal distribution of rainfall is a specific area of research that could be explored as future work.

An area of exploration in the regression lines show in section 5.4 and 5.5 is that the upper envelopes could be used in the linear models instead of the regressed line. The rationale of this is that the model would consider worse flood scenarios and therefore would provide higher estimations. This would increase preparedness in the case that this method is used to estimate sewer flooding in real-time.

Furthermore, this study doesn't consider dry weather flow as this could be considered for combined sewers, which is what the sewer type is for the case studies used in sections 5.4 and 5.5.

6 Business case

6.1 Introduction

It has been realised that there are ample weather forecast data that are not being used for urban flood management. Important is the prediction of sewer flooding as it is a specific type of flood that could result from urban flooding. Several studies have used sewer models to produce predictions of sewer variables from rainfall forecasts (Achleitner *et al.*, 2009; Loewe *et al.*, 2014; Schellart *et al.*, 2012). However, rainfall forecasts can be uncertain which produce inaccurate flood predictions. Modelling uncertainties also exist which include verifying models against the most recent flood data. Furthermore, running computationally heavy hydraulic models for sewer flood forecasting in real-time is impractical. These are the main reasons why sewer operation teams in wastewater companies do not rely on rainfall forecasts and hydraulic models in online settings to inform decision making.

The results of this project provide a more accurate means to use short range weather forecasts by the wastewater company's operations team to give them the confidence to introduce the necessary interventions that are specific, resourceful and efficient in execution to reduce the risk of damage from a sewer flood or to prevent the event from occurring. This chapter presents a business case to use probabilistic sewer flood forecasting using probabilistic radar Nowcasts to reduce the costs of mitigating sewer floods.

6.1.1 Objectives

The aim of the business project is to predict sewer flooding with reasonable accuracy and efficiency to better inform decision making in tackling sewer floods.

Methods in Chapter 4 and Chapter 5 are used to develop the sewer flood forecasting process described in this business case.

The objectives of the project are as follows:

- Apply probabilistic sewer flood forecasting in real-time settings
- Reduce expenditure of mitigating sewer flooding

The project supports Northumbrian Water's core values, particularly:

- Creative – introducing a probabilistic approach provides a holistic and innovative way of tackling sewer flooding
- Results driven – improving rainfall forecasts is a way of producing better data from worse data. The additional benefits highlight a results-driven approach

6.1.2 Scope and interdependencies

Rainfall forecasting to predict sewer flooding is expected to be applied in Northumbrian Water's sewer operations to supplement the decision-making process in choosing appropriate interventions. Specifically, the class of interventions is considered 'reactive' as oppose to 'proactive'. Reactive interventions are used to mitigate imminent or direct consequences of flooding, which are normally deployed within a short time span. Proactive interventions are conducted to tackle potential sewer flooding in the future. However, these interventions produce long term changes to the drainage area that don't normally include short term mitigations affecting the network. Therefore, the proposed sewer flood forecasting system is expected to inform the selection of reactive interventions before the flood occurs.

Methods have been produced to improve and explore the uncertainties in radar rainfall forecasts. This has been solely applied to sewer flood modelling. However, these methods could also be applied to CSO management, leakage detection and blockage detection. The following projects within Northumbrian Water have potential independencies with the outputs of this thesis:

- SNIPER project – monitoring CSO spills with more accurate and postprocessed Nowcast data.

6.1.3 Blockage detection – forecasting methods could be used to conduct sensitivity analyses of blockages using hydrological models Benefits and drawbacks

The benefits of using the methods of this thesis are:

- Introduction of sewer flood forecasting system –the key consequence of this is that Northumbrian Water would be able to use Nowcast data to tackle sewer flooding before it occurs.

- Changing the way decisions is made by sewerage operations with the introduction of a ‘probabilistic’ approach to flood forecasting.
- Increased knowledge of rainfall forecasts and sewer catchment behaviour –the probabilistic methodology enables Northumbrian Water to understand the sensitivity of sewer flooding various hydraulic models by identifying the ‘clustering’ of sewer floods based on varying rainfall intensities.
- Cost savings

The potential drawbacks are as follows:

- Forecasting sewer floods increases preparedness. However, more resources could be used to mitigate predicted floods which is costlier.
- Forecasting some sewer floods based on the location and scale may not bring any more benefit than traditional approaches
- Forecasting is an integral part of a warning system which is dependent on the interventions used to mitigate sewer flooding. Hence, the forecasting system should be co-dependent on the efficiency of intervention management.

As radar QPEs are estimates of rainfall and do not show direct measurements of rainfall, this business case requires that rain gauge data is sourced and used to correct the radar QPE. This is included in the initial capital costs.

6.2 Planning

6.2.1 Product description

Probabilistic sewer flood forecasting – a simple approach

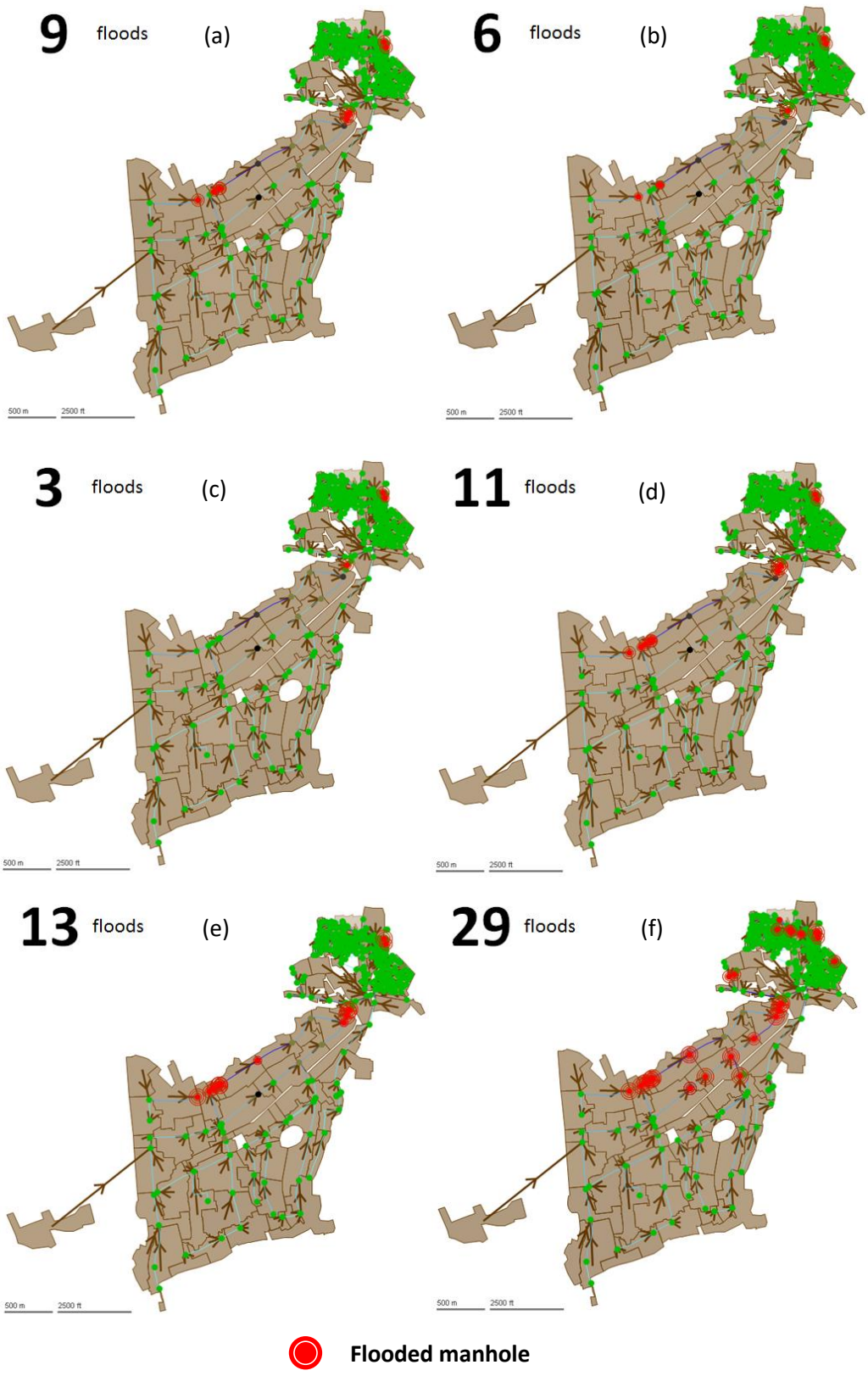

Figure 6.1. Hydraulic simulations using Infoworks ICM of a sewer model representing Ponteland, Newcastle using (a) QPE (b) QPF (c) 70 % prob. QPF (d) 80 % prob. QPF (e) 90% probabilistic QPF (f) 99% prob. QPF

A sewer model in a catchment of approximately 8 km^2 in area representing Ponteland, Newcastle is tested with a Nowcast (QPF source) on 14th November 2015, 6pm – 12am along with the observed rainfall, Rain Radar rain-rate (QPE source) and the probabilistic QPFs (see Figure 6.1). Assuming the QPE is an accurate source of observed rainfall, the QPF modelling output had under-predicted the number of manholes flooded, demonstrating that deterministic QPF is not reliable in this event. The 80th percentile of the probabilistic QPFs shows flooded manholes that most closely match the observed model with 11 floods. However, from the first percentile (70th percentile) that shows flooding, the 'growth' patterns of flooded manholes are generally seen, even though the 80th percentile is most accurate. This would highlight the region of manholes that are at most risk of being flooded, which a deterministic QPF would not show.

6.2.2 Risk assessment

The risks associated to setting up a real-time sewer flood forecasting system are described as follows:

- The project had aimed to explore the uncertainties of the Nowcast data and use this to develop flood forecasts. However, there is always a possibility that the methods presented in this thesis do not fully exploit the uncertainties for different storms. This is chiefly due to the dynamics of storm development and the complexity of predicting the development patterns cannot always be modelled or quantified statistically or hydrologically. In this case, it is imperative that the methods of this research project are thoroughly tested with different method parameters and with different data sets.
- Nowcasts postprocessed using methods described in this thesis may show worse predictions of the sewer flood. It reinforces the point that the methods need to be rigorously tested and should be tailored for specific drainage areas (as some storms would interact with various catchments differently).
- A good forecast doesn't necessarily require actions to be taken, and where action is to be taken the consequences of them should be holistically reviewed. For example, a warning of a large flood in a cluster of properties should be carefully communicated as if the actual event isn't so

destructive, the customer would lose trust or not take future warnings seriously.

- By having a functional sewer flood forecasting system, the methods of predicting sewer flooding from non-rainfall causes could potentially be evaluated. However, the risk is that the flood predictions may not be realistically represented due to non-rainfall causes of the sewer flood.

6.3 Financial appraisal

This section presents a financial appraisal showing the cost effectiveness of the proposed probabilistic sewer flood forecasting system. This is evaluated using projected cash flow based on cost savings and then deriving the Net Present Value (NPV) and Internal Rate of Return (IRR). Furthermore, a sensitivity analysis is conducted on the projected cash flow to evaluate the sensitivity of NPV and IRR based on increasing capital investment.

Formally, a reliable financial appraisal requires accurate data. However, due to limited data availability not all figures in the appraisal are representative of the cost effectiveness. As such, the appraisal is not comprehensive and necessitates introducing assumptions. These are explained in section 6.3.1.

6.3.1 Assumptions and definitions

Definitions

Net Present Value – the summation of the present value of the cash inflow over a period of time is termed net present value. It shows the profitability of an investment based on assumptions made on future cash flows. The NPV formula is given below:

$$NPV = \sum_{month}^{periods} \frac{CASH_{month}}{(1+dis)^{month}} \quad (6.1)$$

Where $CASH_{month}$ is the cash inflow per period, denoted $month$. The discount rate is denoted dis and the total number of periods is denoted $periods$.

Internal Rate of Return – this is the discount rate dis when the NPV is at zero value. It indicates what discount rate is suitably above the rate used in the NPV when the lowest value (i.e. NPV of zero) of the capital is used for investing.

Assumptions

The financial appraisal is applied to multiple drainage areas used in the sewer flood forecasting system. Therefore, the collective cost effectiveness is compared for different number of drainage areas.

The following assumptions have been made for the financial appraisal:

- The discount rate in the NPV formula is chosen to be 4.3%. This had been justified by Northumbrian Water (A Moore 2017, personal communication, 13 September). Investing in projects could provide water utilities ways of demonstrating innovation but these are considered higher risk. Therefore, a larger discount rate is used to compensate for potential losses in comparison to using a lower discount rate. A rate of 4.3% assumes that investing into this project is safely regulated and is not considered risky.
- The cash flow is defined for an annual period on a monthly basis.
- The number of drainage areas used in the appraisal are 1,2,4,8 and 16.
- The investment capital is assumed to be £5,000 per drainage area requiring monitoring for sewer flood forecasting in an annual period. This justifies labour and resource for operating the warning system. Specifically:
    - Assume a labour cost of £5,000 to conduct a historical analysis as part of setting up a sewer flood forecasting framework for one drainage area.
- Profit in the cash flow is represented as cost savings in terms expenditure of sending out crew members to tackle three types of sewer flooding: internal, external and highway/other. They are described as follows:
    - Internal flood: sewer flooding that had occurred within customer's household where sewage typically escapes through toilets.
    - External flood: sewer flooding that had occurred outside properties in gardens, driveways streets etc. where sewage escapes through the manhole.
    - Highway/other: sewer flooding that had occurred on a busy road or highway.

- Unit cost of sending out crew members vary monthly and thus an average is calculated and assumed for the cost of this expenditure. This is done for the three types of sewer flooding.
- The ratio of sewer flood incidents of the three types of sewer flooding have been derived. These are used to calculate the approximate floods per month
- The ratio of the average sewer floods (all types) occurring in each month of the year is used as a scaling factor to calculate the cost savings for each sewer flood for every month. This is used to derive the cash flows of all months in a year.
- Crew numbers reduced across multiple drainage areas are scaled by a factor of 1.9 when doubling the number of drainage areas in the sewer flood forecasting system (instead of simply doubling this figure). This accounts for any single drainage area not showing improvement in cost savings using the forecasting system.

6.3.2 Net Present Value and Internal Rate of Return

Summary of the cash flow, NPV and IRR for an example annual period is shown in Table 6.3.1 for different number of drainage areas.

Table 6.3.1. Summary of monthly cash flow, NPV and IRR of sewer flood forecasting system

MONTH	CASH FLOW (NET SAVINGS)				
	1 DA	2 DA	4 DA	8 DA	16 DA
0	-£5,000.00	-£10,000.00	-£20,000.00	-£40,000.00	-£80,000.00
1	£2,789.50	£5,300.05	£10,070.10	£19,133.18	£36,353.04
2	£658.00	£1,250.20	£2,375.38	£4,513.22	£8,575.12
3	£866.50	£1,646.35	£3,128.07	£5,943.32	£11,292.31
4	£190.00	£361.00	£685.90	£1,303.21	£2,476.10
5	£1,317.50	£2,503.25	£4,756.18	£9,036.73	£17,169.79
6	£641.00	£1,217.90	£2,314.01	£4,396.62	£8,353.58
7	£225.50	£428.45	£814.06	£1,546.70	£2,938.74
8	£1,282.00	£2,435.80	£4,628.02	£8,793.24	£16,707.15
9	£1,126.00	£2,139.40	£4,064.86	£7,723.23	£14,674.14
10	£415.50	£789.45	£1,499.96	£2,849.91	£5,414.84
11	£1,161.50	£2,206.85	£4,193.02	£7,966.73	£15,136.78
12	£380.00	£722.00	£1,371.80	£2,606.42	£4,952.20
NPV	**£3,856.10**	**£6,826.58**	**£11,970.51**	**£20,743.97**	**£35,413.53**
IRR	**20%**	**18%**	**16%**	**15%**	**13%**
4.3%					

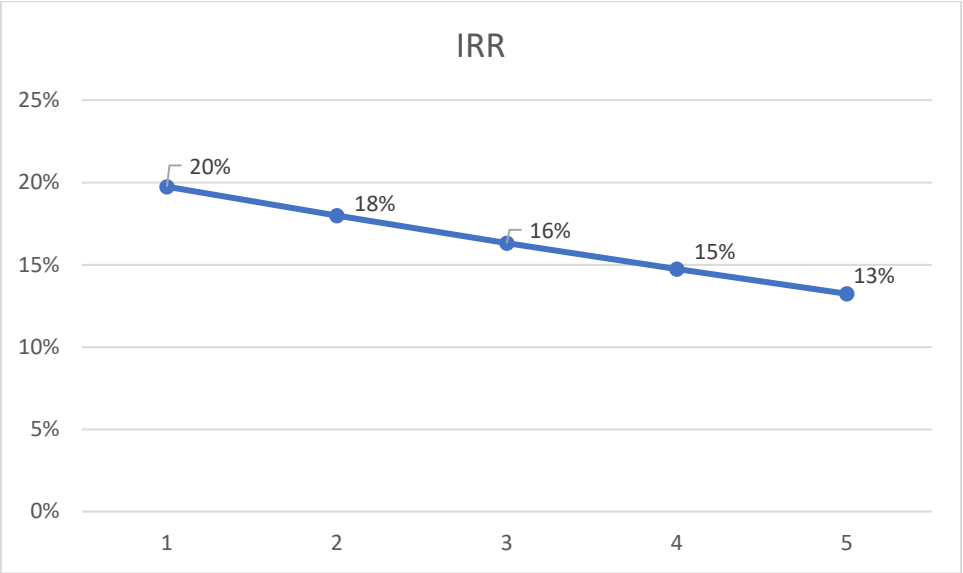

Figure 6.2. Internal Rate of Return (IRR) of sewer flood forecasting system (x axis represents number of drainage areas (DA)).

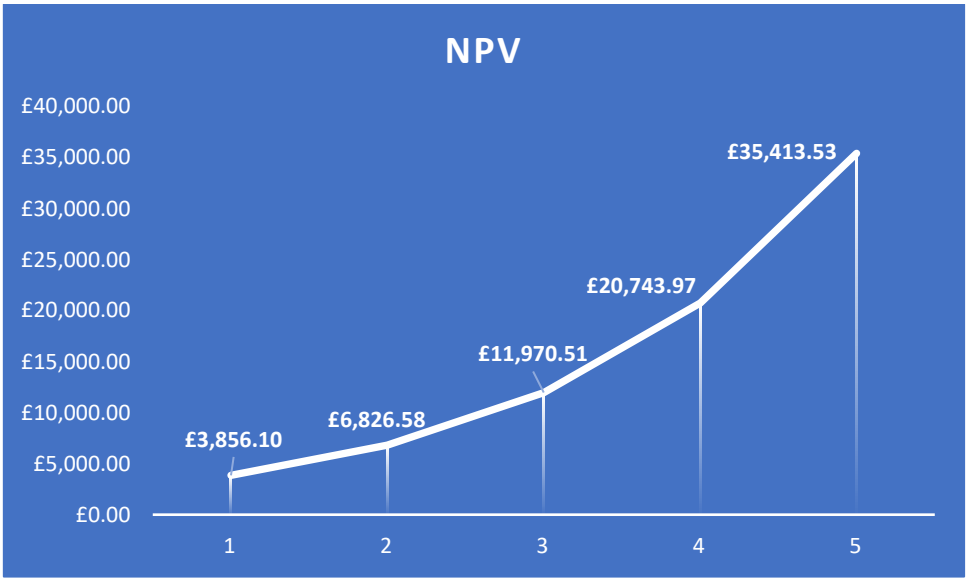

Figure 6.3. Net Present Value (NPV) of sewer flood forecasting system (x axis represents number of drainage areas (DA)).

Table 6.3.1 shows the capital investment of £5,000 per drainage area at month 0. This is scaled appropriately for multiple drainage areas used in the sewer flood forecasting system. The monthly cash flow values are based on the ratios of flood incidents occurring monthly (see Appendix C). This is main reason why the net cash flow for each month fluctuate in value (and so don't necessarily increase over monthly periods). For months 1 – 12, the cash flow in terms of net savings

are shown and these are used to calculate the NPV and IRR for each scenario (i.e. number of drainage areas).

Figure 6.2 and Figure 6.3 show the IRR and NPV values in Table 6.3.1 graphically, respectively. Although the IRR reduces over increasing number of drainage areas, the IRR values range between 13– 20% which is high. This shows that the discount rate needs to be high for capital to be invested when the future cash inflow equals cash outflow. In other words, it represents a high value investment because the investor should consider an IRR that high to ensure there would be no loss in the investment. This is supported with the NPV values for the different number of drainage areas used in the sewer flood forecasting system. Figure 6.3 shows that over increasing numbers of drainage areas, the NPV also increases. This indicates increasing profitability in terms of cost savings.

6.3.3 Sensitivity analysis

Increasing capital investment

Figure 6.4 shows the IRR and NPV values for monthly cash flows in Table 6.3.1 but with increasing capital from £5,500 to £7,000 per drainage area. Full details are provided in Appendix C.

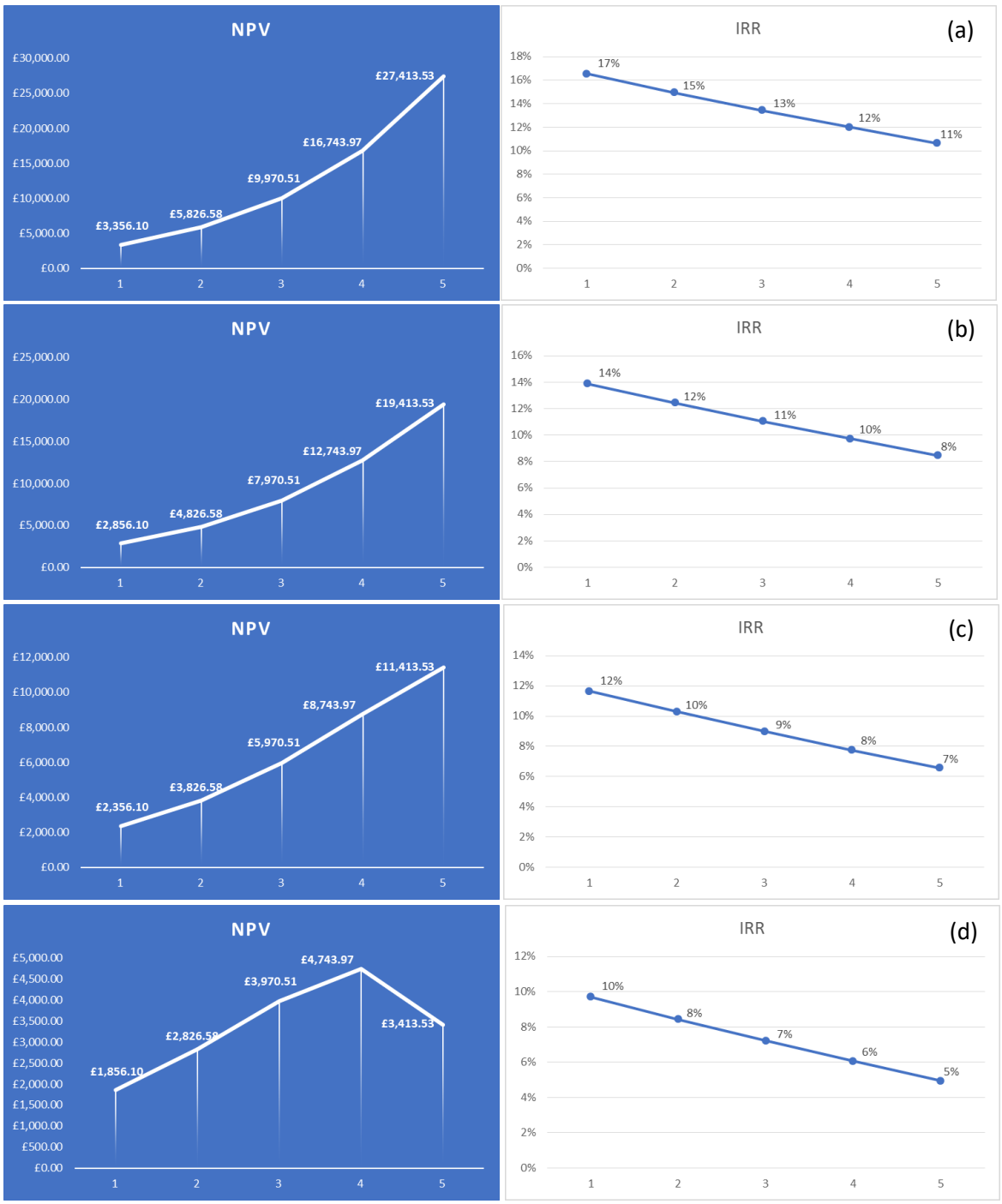

Figure 6.4. Sensitivity analysis for IRR and NPV showing increasing capital investment from £5,500 to £7,000 per drainage area: (a) £5,500 (b) £6,000 (c) £6,500 and (d) £7,000

Figure 6.4 shows the IRR and NPV values for multiple drainage areas with increasing capital investment between £5,500 and £7,000. Clearly, as the capital investment increases the IRR values across the different number of drainage areas decreases, which is expected. However, the decreasing trends for increasing numbers of drainage areas remain similar. For NPV values, there is a

gradual decrease of values over increasing capital investment. Whilst this is expected, the NPV values for 16 drainage areas for an investment capital of £7,000 drops to a value of £3,413.53. This indicates loss of increasing cost performance should £7,000 be invested and 16 drainage areas were monitored. However, monitoring 1 – 4 drainage areas still indicate profitability in terms of cost savings even if £7,000 is invested per drainage area. Overall, investing between £5,500 and £7,000 is most likely going to show cost savings when deploying crew members to mitigate sewer floods using the sewer flood forecasting system in a yearly period.

6.4 Conclusions

A key outcome of this project is producing accurate probabilistic radar rainfall forecasts which could produce probabilistic sewer flood forecasts. This chapter had introduced a business case to show cost effectiveness of forecasting sewer floods using the probabilistic methodologies presented in this project. One of the objectives of the business case is to reduce the costs associated to mitigating sewer flooding via crew members in sewer operations. the main conclusions associated to the financial appraisal are as follows:

- Analysis of Internal Rate of Return and Net Present Value has been conducted based on assumptions of the financial figures. Results show very high IRR values between 13% and 20% showing that investing to the business case has high value. Based on a capital investment of £5,000, NPV values show profit in terms of cost savings between £3,856 and £35,314.
- Based on a capital investment of £5,000 per drainage area, the more drainage areas monitored the more cost savings are expected
- A sensitivity analysis on the IRR and NPV values based on increasing capital investment shows that an investment between £5,500 and £7,000 shows profitability for all numbers of drainage areas. However, the threshold where decrease of performance for monitoring many drainage areas is expected to be near £7,000 as monitoring more than 8 drainage areas incurs loss.

Further additions for this business case could include the following scenarios related to false alarms and underestimated flood forecasts:

Cost of flooding due to underestimated flood forecast: this describes a scenario where a sewer flood occurs above a threshold that had been predicted from a probabilistic sewer flood forecast. If this occurs, the cost of mitigating the sewer flood would be underestimated and would mean the wastewater company would pay more after the flood occurs.

Cost of flooding due to overestimated flood forecast: this describes a scenario where a forecast over predicts the flood extent and issues a severe warning but the actual flood is less severe. The consequences are that more money would be spent to mitigate the flood before it occurs.

To obtain costs for these two scenarios, the forecasting system would need to be implemented for a period of time to gather cost data for the number of floods underestimated and overestimated for each probabilistic QPF (or range of probabilistic QPFs). This historical analysis would also ascertain the threshold of probabilistic QPFs that causes sewer flooding, which would be tailored to each drainage area.

7 Summary, conclusions and future work

7.1 Summary

Radar rainfall is increasingly used in urban hydrology for a vast range of applications. Recent studies have identified that inherent uncertainties of radar technology is a major issue in providing accurate estimates of rainfall and outputs of hydrological applications. Particularly, radar rainfall forecasts have several uncertainties because forecast accuracy is dependent on a range of factors such as lead time, rainfall intensity and catchment size. Radar rainfall forecasts are an integral component of flood forecasting systems and various models describe the uses of the forecasts as part of these systems. However, radar rainfall forecasts could also be used to predict sewer flooding. This type of flooding is of major concern to the UK water sector as it is disruptive, costly and affects hundreds of customers every year.

The aim of the research project was to investigate the uses of radar QPF and QPE to support short term decisions in sewer operational networks in reducing the risk of sewer flooding. A literature review was conducted to review the techniques, issues and solutions of rainfall estimation, uncertainty estimation and hydrological applications of radar rainfall data. This motivated the developments of the following components: increasing the accuracy of deterministic radar QPFs, postprocessing probabilistic radar QPFs and estimating flood extents using spatial analysis of radar QPE.

Accuracy requirements in hydrological applications are dependent on the resolution of deterministic rainfall forecasts. It had been identified that increasing the temporal and spatial resolutions of forecasts increases the accuracy of hydrological output. Therefore, an interpolation method was proposed to increase temporal and spatial resolutions of deterministic radar rainfall forecasts. This method was evaluated for rainfall events for all seasons of the year. This method could be used to match rainfall forecasts to coincidental observed rainfall. This is particularly useful in hydrological and statistical analysis.

Deterministic forecasts do not provide information of the uncertainty. However, probabilistic forecasts do provide information of this. This is the reason why

probabilistic methodologies have become popular. Therefore, the next step was to explore the usefulness of probabilistic radar QPFs. A method generating probabilistic QPFs was applied to radar QPFs and a new technique had been developed to postprocess these forecasts to better represent latest rainfall characteristics. This approach had been tested for both convective and frontal rainfall events.

Probabilistic radar QPFs present challenges at a spatial scale when used in hydraulic modelling due to the choice of percentiles over the catchment. Particularly, the issue is related to preserving the spatial structure of the rainfall. Furthermore, simulating many forecasts concurrently is computationally impractical in real-time settings. Therefore, a separate spatial analysis was conducted and a simple model was used to support probabilistic radar flood modelling.

Finally, a business case had been developed to support the UK water sector in actively tackling sewer flooding before it occurs using radar rainfall forecasts. This is discussed in Chapter 6 and outputs show that the methods presented in this thesis are promising for application at Northumbrian Water Limited. Further development is recommended to realise the full benefits of the forecasting capabilities.

7.2 Conclusions

The main findings of this research project are summarized below.

7.2.1 Improving radar deterministic quantitative precipitation forecasts

Chapter 3 develops an approach to temporally and spatially interpolate radar QPFs. The techniques used include the use of optical flow estimation and Kriging methods. In addition to the conclusions section of Chapter 3, the key findings of this analysis are as follows:

- Temporal interpolation via optical flow estimation can predict peaks for interpolated timesteps of the QPF better than simple linear temporal interpolation.

- Spatial interpolation via Universal Kriging produces more accurate estimates of the upscaled QPF with the QPE in comparison to simpler interpolation techniques including Inverse Distance Weighting.
- The temporally and spatially interpolated QPF is more accurate than the lower resolution QPF.
- The temporal and spatial interpolation method developed in Chapter 3 is recommended for use by hydrologists for obtaining higher resolution datasets. Another advantage is adjusting the resolution outputs due to more control over interpolation parameters. This is particularly useful for hydrologists for conducting historical analysis on forecast and observed datasets.

7.2.2 Increase the accuracy of radar probabilistic quantitative precipitation forecasts

Postprocessing techniques show that probabilistic QPFs could be improved. Chapter 4 focusses on postprocessing probabilistic QPFs using a Bayesian approach involving two applications of MCMC. Forecast errors in historical QPF/QPE datasets produce initial probabilistic QPFs. However, recent QPE data not part of the historical QPE is used in the postprocessing method to increase the accuracy of the probabilistic QPFs. The main conclusions for this study are as follows:

- Based on the performance indicators used in Chapter 4, the postprocessed probabilistic QPFs are more accurate than the pre-processed ones in all study events. Particularly, the percentiles are closer to the QPE and the temporal path of the percentiles are more positively correlated or are less negatively correlated with the QPE.
- Due to larger rainfall intensities seen in warm events (events from spring and summer), the benefit of the postprocessing method is more visually demonstrated compared to the cool events (events from autumn and winter). Moreover, the biggest changes are quantitatively seen for warm events. Thus, the postprocessing method is adaptable and performs well for events in both the warm and cool seasons.

- In some events, particularly those from the cool seasons, the postprocessing method demonstrates little change (or improvement). This mainly due to the statistical assumptions made in the Bayesian method. One assumption is that if the recent QPE resembles the statistics of that of the historical datasets, little change is observed. Whilst this is expected in Bayesian analysis, it may also show that the pre-processed probabilistic QPFs are sufficiently accurate and may not need much postprocessing.
- Overall, the use of two applications of the Bayesian method used in the methodology of Chapter 4 demonstrates consistent and more accurate results across any event in a year.

7.2.3 Conduct analysis of the spatial variation characteristics of radar quantitative precipitation data associated to the sewer network model

A method to analyse spatial variability of radar rainfall has been introduced in Chapter 5. The use of a spatial index previously used in literature had been used to characterise the spatial variability of the rainfall field over sewer model. The method includes two generalised linear models that use variance and mean value of the accumulated rainfall over the sewer model. The second generalised linear model includes spatial indexes as additional variables to draw distinction in the performance in comparison to just using variance and mean rainfall.

The outputs of this study are highlighted as follows:

- Spatial indexes provide useful information on the spatial variability of radar rainfall over the sewer model. By using the outlet as a reference point, the storm characteristics and location over the sewer model can be realised.
- Both generalised linear models can predict sewer flood volume and number of floods with a degree of uncertainty. However, the generalised linear model that includes spatial indexes performs worse for the two case studies featuring small area sewer models. But this model performs better for the two case studies featuring large area sewer models. Due to the higher clarity of spatial information in larger areas, the spatial indexes provide more accurate information and thus make good predictors in the generalised linear model.

- The appropriate generalised linear model (or similar simplified/statistical/ANN model) could be applied for specific sized drainage areas to make estimations of the flooding extent without running computationally expensive detailed models. Hence, by studying the spatial variability of the rainfall field over a sewer model, flood predictions could be made in real-time, which is conducive for real-time flood forecasting.

7.2.4 Develop business case for methodologies developed in the project

Chapter 6 establishes a business case for the methodologies developed in this project appropriate for UK wastewater companies to consider should real-time sewer flood forecasting be put in operation. The main points highlighted in this chapter include:

- Early decision making could reduce costs mitigating sewer flooding by reducing the number of crew members sent out to deal with the sewer network, which would help save costs to the business.
- Probabilistic sewer flood forecasting and rainfall forecasting could also be applied to managing CSO and bathing waters
- A financial appraisal shows that probabilistic sewer flood forecasting is a cost-effective way of mitigating sewer flooding before it occurs. IRR values show investment into the project has high value and NPV values show high cost savings especially when monitoring many drainage areas.
- The financial appraisal recommends that capital investment should be between £5,000 and £8,000 to gain benefit of the project in an annual period.

7.3 Recommendations for future work

In addition to the methods explored and developed in this research project, future work to consider has been identified and recommended. Specific points for future work has been briefly explained at the end of Chapters 3,4 and 5. However, comprehensive explanations are provided in the following areas: further increasing the accuracy of deterministic radar quantitative precipitation forecasts,

further development of the Bayesian-based postprocessing method for real-time forecasting applications, further development of estimating model flood variables using spatial analysis of radar rainfall over a sewer model, development of spatial radar probabilistic rainfall forecasts, and modelling the risk of sewer flooding and development of intervention framework.

7.3.1 Further improvement of deterministic radar quantitative precipitation forecasts

The temporal and spatial interpolation methods show that the accuracy of radar QPFs could be increased. Particularly, the optical flow technique used provides good estimates of movement vectors that prove to be useful to accurately predicting values for interpolated rainfall values temporally. It is recommended that the optical flow technique be applied to different radar QPF sources to ensure the robustness of the method. Kriging methods are proven to be useful to estimating spatial points in several hydrological studies. However, whilst univariate Kriging methods (i.e. simple, ordinary, universal Kriging) may produce results with small dissimilarities, the spatial interpolation technique in this study was limited to Universal Kriging. Thus, a detailed comparison of different univariate Kriging methods is recommended. Particularly, a wide range of assumptions could be tested. For example, the influence of the number of rainfall grids used to estimate interpolated spatial grids could be tried to ascertain the optimal number of grids to provide good estimates.

Further work is recommended for increasing the accuracy of deterministic radar QPFs by conducting historical analysis of coincidental forecast and observed rainfall after the interpolation process had been applied. Particularly, the preservation of spatial rainfall field structure is crucial. This requires analysis of the variance of the rainfall field and to identify peaks temporally and spatially. It is recommended that using techniques in the field of geostatistcs should accompany a regression approach so that the accuracy of spatial QPFs are vastly improved whilst preserving the spatial distribution of the rainfall field. Furthermore, the regression approach is linear based. A nonlinear approach is a potential area to explore for increasing the accuracy of the temporally and

spatially interpolated QPF. Polynomial regression or the use of functional relationships are potential techniques to explore. Lastly, radar QPE which is used as the observed data in this project is not assessed for its accuracy. However, in practice, radar QPE has uncertainties as they are estimates of rainfall. Thus, rain gauge adjustment is recommended.

7.3.2 Further development of the Bayesian-based postprocessing method for real-time forecasting applications

Bayesian methods require statistical assumptions for the estimation of a variable. Examples include the choice of distribution for the prior in the Markov Chain Monto Carlo method. The choice of distribution would have an influence on the variable outputs. Hence, different prior distributions could be tried in future studies. Furthermore, the choice of distribution for the QPF/QPE datasets was dependant on the empirical datasets. The datasets in this study followed a gamma distribution. However, this may change for different QPF/QPE sources. Hence, testing the postprocessing method on different QPF/QPE sources is a potential area of research. The size of the recent QPE data used to update the probabilistic QPFs may be an influencing factor determining the ability of the method to adjust the forecasts to accurately depict the recent rainfall characteristics. Furthermore, the recent QPE is made up of data sourced from the same location as the historical data used to generate the probabilistic QPFs (i.e. the forecasts are location specific). A potential area of research is to explore recent QPE in neighbouring grids which may influence the postprocessed forecasts. This area considers the spatial location of the probabilistic QPFs, which is an important area of exploration.

The postprocessing method presented in this project shows to update the probabilistic QPFs to more accurately represent recent rainfall characteristics. However, further work is required to study the output of the postprocessing method on a temporal scale. This involves running the method iteratively over consecutive time periods to analyse the performance for rainfall forecasts at different forecast horizons. This would potentially bridge the gap of applying the postprocessing method to real-time operational settings.

7.3.3 Further development of estimating model flood variables using spatial analysis of radar rainfall over a sewer model

The outputs of Chapter 5 show that spatial variability of rainfall over a sewer model can be used to make predictions of model flood variables. However, to more accurately establish correlations between the spatial parameters and the flood variables, it is necessary to analyse many different combinations of spatial rainfall distributions. Whilst sourced from actual rainfall events, the number of historical rainfall events used are limited in showing these combinations. Hence, to confirm or refine correlations between the spatial parameters and flood variables many more rainfall events need to be included. Alternatively, spatial distributions of the historical events could be altered and modelled separately. Secondly, a statistical model had been chosen as the alternative predictor to the detailed model used to produce the flood variables (i.e. Infoworks ICM). Whilst this requires less computational resources, other simple models could be explored as a potential research area. For example, the use of Artificial Neural Networks is useful as an alternative to generalised linear model due to capturing nonlinearity in the correlations between the spatial parameters and flood variables. By considering nonlinearity of the variables there is potential to further increase the accuracy of the flood estimates.

Furthermore, the techniques developed in Chapter 5 focus on spatial variation of accumulated rainfall over a six-hour period, which is representative of the maximum lead time of the QPF used in the case study of this project. However, the temporal variability is not considered during this period. Therefore, there is potential to extend the methodology to focus on both spatial and temporal variability of rainfall over sewer models.

7.3.4 Development of spatial radar probabilistic rainfall forecasts

The techniques used to produce probabilistic QPFs are location specific. Hence, probabilistic QPFs are required to be produced independently for each grid over

a sewer model or catchment. However, this would be problematic when selecting percentiles over the catchment due to the spatial representation of the storm (i.e. the spatial distribution is influenced by the selection of the percentiles over the catchment). Therefore, this clearly requires further research especially in studying the spatial distribution of rainfall over the region. Percentiles could be selected by varying spatial distributions and the combinations of percentiles would be referred to as spatial probabilistic rainfall forecasts.

7.3.5 Modelling the risk of sewer flooding and development of intervention framework

Though outside the scope of this research project, the probabilistic methodologies presented are very useful for sewer risk modelling for decision making in sewer network operations. Probability is a component of risk and therefore probabilistic rainfall forecasting could be used to quantify risk for sewer flood forecasting. Potential work includes developing a framework for risk management which quantifies risk via quantifying the consequences associated to the flood extent associated to each probabilistic rainfall forecast. Subsequently, the risk level could be mapped to a practical, short term intervention that could be used by a wastewater company or another mitigating body to tackle sewer flooding. This ‘intervention framework’ describes algorithms and guidelines to efficiently deal with sewer flooding in specific drainage areas. Thus, frameworks could be generated for different drainage areas depending on what interventions available.

Appendices

Appendix A Implementation of Original Stochastic Model

The following shows the implementation of the method by Rene (2014).

Split data according to lead time and perform the following for each lead time:

1 Compute number of observations N

2 Compute the joint probabilities:

a. $P(S=0,\hat{S}=0) = \#\ of\ events\ \{S=0,\hat{S}=0\}/N$

b. $P(S>0,\hat{S}=0) = \#\ of\ events\ \{S>0,\hat{S}=0\}/N$

c. $P(S=0,\hat{S}>0) = \#\ of\ events\ \{S=0,\hat{S}>0\}/N$

d. $P(S>0,\hat{S}>0) = \#\ of\ events\ \{S>0,\hat{S}>0\}/N$

2. Compute the conditional probabilities:

a. $P(S=0|\hat{S}=0) = P(S=0,\hat{S}=0)/P(S=0,\hat{S}=0) + P(S>0,\hat{S}=0)$

b. $P(S>0|\hat{S}=0) = P(S>0,\hat{S}=0)/P(S=0,\hat{S}=0) + P(S>0,\hat{S}=0)$

c. $P(S=0|\hat{S}>0) = P(S=0,\hat{S}>0)/P(S=0,\hat{S}>0) + P(S>0,\hat{S}>0)$

d. $P(S>0|\hat{S}>0) = P(S>0,\hat{S}>0)/P(S=0,\hat{S}>0) + P(S>0,\hat{S}>0)$

3. Model 1: when $\hat{S}=0$

The probability conditioned on a zero rainfall forecast:

$$P(S\le x|\hat{S}=0) = P(S\le x|S>0,\hat{S}=0)P(S>0|\hat{S}=0) + P(S=0|\hat{S}=0)$$

Extract data = $\{S>0|\hat{S}=0\}$ and estimate marginal probability distribution $P(S\le x|S>0,\hat{S}=0)$

Outputs are parameter estimates of marginal distribution

4. Model 2: when $\hat{S}>0$

The probability conditioned on a forecast $\hat{S}=x^*$

$P(S\le x|\hat{S}=x^*) = P(S\le x|S>0,\hat{S}=x^*)P(S>0|\hat{S}=x^*) + P(S=0|\hat{S}=x^*)$

Consider $P(S=0|\hat{S}=x^*)$

Split data $\{S=0|\hat{S}=x^*\}$ into equal intervals and estimate the probability of observing zero, then using the mid-point of the interval and the probability estimate, fit to logistic regression function or any other functional relationship.

Outputs are parameter estimates of logistic regression

Then the $P(S>0|\hat{S}=x^*) = 1 - P(S=0|\hat{S}=x^*)$

For describing $P(S\le x|S>0,\hat{S}=x^*)$, extract data $\{S>0|\hat{S}=x^*\}$ and transform from original domain to normal domain using Box Cox transformation or other method.

Outputs are parameters of transformation

Then estimate bivariate distribution of transformed data.

Outputs are parameter estimates of bivariate distribution

Appendix B Catalogue of historical QPE events

Table B.1. Historical QPE events categorised by mean rainfall over Ponteland sewer catchment. $\boldsymbol{MR}$, $\boldsymbol{VAR}$, $\boldsymbol{I_1}$ *and* $\boldsymbol{I_2}$ *are shown along with model simulated* $\boldsymbol{V^a}$ *and* $\boldsymbol{V^b}$ *values.*

CATEGORY	*EVENT REF*	*MR (mm)*	*VAR*	I_1	I_2	V^a *(m³)*	V^b
20-30	**8000**	27.22	67.99	1.11	1.07	372	10
	9565	26.59	6.84	0.96	0.96	56	1
	11344	24.92	5.57	0.99	0.96	317	8
	12622	23.01	3.23	1.01	0.97	287	5
	13390	23.49	3.03	1.03	1.00	138	3
	14321	21.51	16.80	0.96	0.89	181	1
	16204	24.28	18.77	1.03	1.02	531	9
	19933	23.06	4.36	1.01	0.96	277	4
	35016	27.07	30.89	0.93	0.97	872	18
	40460	26.69	3.81	0.99	0.97	11	1
30-40	**1795**	37.33	7.86	1.02	0.99	1008	12
	3206	39.84	3.21	1.02	1.03	548	9
	5272	33.31	28.29	0.94	1.03	654	12
	7087	34.67	29.19	1.02	0.97	773	12
	7385	31.96	10.20	1.03	0.98	838	14
	7541	31.82	3.20	1.00	0.98	248	7
	8949	31.64	7.56	1.00	0.96	874	16
	9525	35.72	13.72	0.97	0.93	619	13
	10544	35.05	7.16	1.00	0.97	375	9
	14310	39.33	45.64	0.95	0.93	410	10
40-50	**1783**	41.46	13.84	1.03	0.99	724	11
	3214	41.96	6.66	1.02	1.04	728	10
	4875	43.14	4.85	0.99	0.99	1372	18
	5010	45.99	88.31	0.96	0.99	4099	42
	5596	44.18	6.39	1.00	0.98	216	7
	7030	42.17	107.25	0.94	1.04	2395	37
	7409	45.96	3.95	1.02	0.99	790	18
	9500	48.28	17.46	1.03	1.00	1329	12
	10550	46.06	13.57	1.00	0.96	614	10
	14295	45.95	116.48	0.91	0.95	2213	26
50-60	**5605**	52.36	2.52	0.99	0.98	748	12
	5936	51.14	13.48	1.02	1.01	2156	21
	7018	50.14	112.25	0.94	1.03	2140	38
	8086	58.99	123.81	0.93	1.00	5171	82
	8970	58.77	287.66	1.08	0.99	3021	29
	9502	55.80	5.30	1.01	0.99	1698	13
	10479	58.29	90.95	1.05	1.03	1409	12
	14308	52.59	158.10	0.91	0.89	1728	25
	33170	52.57	4.47	1.00	1.01	1840	18
	3233.2	55.31	17.67	0.99	1.03	2064	14

60-70	**5940**	61.75	24.46	1.03	1.02	2763	21
	6182	63.00	85.53	0.98	1.01	3592	32
	8243	66.20	9.37	1.01	1.03	1912	18
	9516	66.39	9.72	0.99	0.98	1813	21
	10492	69.00	201.87	1.07	1.03	2813	16
	34974	65.71	315.15	0.93	0.98	5708	79
	34995	65.50	699.59	0.86	0.88	6846	75
	41404	65.48	3.21	1.00	1.01	1918	17
	3220.2	65.99	53.07	0.95	0.96	2138	18
	14495.2	62.35	329.90	1.04	0.82	2964	22
70-80	**5420**	78.70	1566.27	1.15	0.93	4051	40
	5440	76.72	1178.32	1.13	0.93	7672	41
	8245	77.89	29.58	1.01	1.04	2654	21
	9513	72.18	5.68	1.00	0.99	2088	21
	10485	79.42	206.43	1.06	1.02	2823	16
	34981	73.99	405.94	0.91	0.97	7532	79
	41375	76.48	36.11	0.99	1.03	2518	24
	41403	71.27	4.76	1.00	1.01	2381	20
	13505.3	76.29	138.09	0.94	0.93	1936	15
80-90	**34504.3**	74.53	30.16	1.01	0.97	2620	21
	5428	81.00	1533.34	1.15	0.93	7335	42
	8248	83.41	40.70	1.00	1.04	3366	21
	41376	86.41	52.86	0.99	1.02	3115	26
	41402	87.98	19.91	1.01	1.01	4070	21
	13508.3	81.40	110.20	0.95	0.95	2858	22
	21045.3	80.60	127.20	1.04	0.99	4220	20
	21058.3	81.11	74.69	1.02	0.98	4705	19

Table B.2. Historical QPE events categorised by mean rainfall over Chopwell and Blackhall Mill sewer catchment. $\boldsymbol{MR}$, $\boldsymbol{VAR}$, $\boldsymbol{I_1}$ *and* $\boldsymbol{I_2}$ *are shown along with model simulated* $\boldsymbol{V^a}$ *and* $\boldsymbol{V^b}$ *values.*

CATEGORY	***EVENT REF***	***MR (mm)***	***VAR***	I_1	I_2	$\boldsymbol{V^a}$ ***(m^3)***	$\boldsymbol{V^b}$
40-50	1881	40.41	98.17	1.06	1.07	0.001	0
	1903	43.42	32.60	1.08	0.42	0.001	0
	3208	41.55	11.15	1.09	0.42	0.001	0
	4878	42.04	19.07	1.05	0.40	0.001	0
	5590	40.44	10.41	1.08	0.41	0.001	0
	6181	41.38	42.81	1.11	0.44	0.001	1
	6198	41.79	44.59	1.11	0.44	0.001	0
	10530	41.77	11.62	1.10	0.44	0.001	0
	30078	43.35	114.37	1.09	0.39	0.001	0
	31526	44.16	427.23	1.12	0.40	0.001	0
50-60	1884	51.82	72.36	1.04	1.05	0.001	0
	5419	52.28	447.65	1.09	0.35	92.6	18
	5435	52.00	440.95	1.09	0.36	245.9	25
	5605	51.44	7.09	1.08	0.42	0.001	0
	8264	52.80	21.01	1.06	0.41	0.001	1
	9500	53.17	65.74	1.05	0.40	0.1	2
	10488	51.26	152.62	1.06	0.39	0.001	0
	10492	50.06	83.18	1.07	0.40	0.001	0
	16175	52.91	12.87	1.07	0.42	0.001	0
	41371	57.05	20.26	1.07	0.42	0.001	0
60-70	1892	60.06	87.29	1.04	1.05	0.001	0
	8238	63.31	118.20	1.09	0.41	1.6	3
	8262	69.96	52.19	1.07	0.41	0.8	2
	9505	63.34	92.44	1.05	0.40	0.1	2
	9518	65.38	50.58	1.06	0.40	0.001	1
	16182	61.25	14.36	1.07	0.43	0.001	0
	33162	64.60	6.72	1.08	0.43	0.7	2
	33181	60.86	51.10	1.06	0.42	4.5	3
	41405	66.57	31.29	1.06	0.41	0.7	2
	23751.2	67.39	52.78	1.08	0.42	0.3	2
70-80	9510	70.79	73.73	0.99	0.95	0.001	2
	9516	70.52	61.89	1.06	0.41	0.001	1
	33165	75.24	10.51	1.07	0.43	4.6	3
	33171	70.31	33.23	1.07	0.42	4.6	3
	41372	79.84	51.34	1.09	0.43	0.001	0
	7166.2	79.11	113.72	1.08	0.42	7	3
	12755.2	75.12	135.78	1.09	0.45	4.2	2
	12770.2	74.34	116.45	1.09	0.45	4	2
	16531.2	77.20	236.87	1.11	0.44	65.5	14
	30925.2	70.07	226.48	1.11	0.44	9.4	3

80-90	8241	84.28	164.85	1.01	0.97	7.3	3
	8261	80.24	126.53	1.08	0.41	2.3	2
	41403	88.34	40.36	1.06	0.41	7.5	3
	7164.2	83.63	162.04	1.08	0.41	5.2	3
	7184.2	81.64	46.47	1.08	0.42	5.5	3
	13042.2	82.05	123.10	1.07	0.41	3.3	2
	13060.2	89.33	120.52	1.10	0.45	1.5	2
	20670.2	85.58	281.98	1.11	0.46	121.9	10
	23742.2	80.48	103.41	1.08	0.42	0.3	2
	30933.2	83.90	567.08	1.12	0.46	6.1	2

Table B.3. Historical QPE events categorised by mean rainfall over Chester-le-Street sewer catchment. $\boldsymbol{MR}$, $\boldsymbol{VAR}$, $\boldsymbol{I_1}$ *and* $\boldsymbol{I_2}$ *are shown along with model simulated* $\boldsymbol{V^a}$ *and* $\boldsymbol{V^b}$ *values.*

CATEGORY	***EVENT REF***	***MR (mm)***	***VAR***	I_1	I_2	$\boldsymbol{V^a}$ ***(m^3)***	$\boldsymbol{V^b}$
30-40	**375**	39.66	17.13	0.99	0.97	244	15
	1790	35.30	5.42	0.97	0.99	175	5
	1870	31.11	49.60	1.03	1.01	74	20
	3204	35.57	3.08	1.01	0.99	217	8
	6445	34.52	17.22	0.97	0.95	98	5
	7094	33.96	157.28	1.13	0.96	118	20
	9591	31.09	6.47	1.03	1.01	1	4
	10470	36.66	63.58	1.07	1.04	55	22
	11402	31.22	13.09	1.03	1.01	61	4
	16210	38.57	68.53	1.05	1.00	67	11
40-50	**366**	42.60	21.43	0.99	0.98	64	8
	1908	44.14	147.79	1.04	1.03	450	16
	3210	49.39	10.07	1.00	0.98	326	8
	3940	44.36	18.12	1.03	1.00	469	22
	4880	43.93	17.93	1.04	1.02	320	9
	5585	42.15	6.72	0.99	0.98	148	5
	7402	43.43	9.04	0.99	0.98	182	5
	9605	42.61	5.65	0.99	0.98	177	8
	10561	45.85	75.38	1.09	1.03	279	10
	30084	49.54	19.80	1.02	1.01	911	44
50-60	**3214**	50.05	10.93	1.00	0.97	332	8
	5590	53.48	6.47	0.99	0.98	217	5
	5615	54.33	11.65	1.02	1.00	309	7
	5940	59.41	27.29	1.04	1.04	963	50
	7398	50.61	8.35	0.99	0.97	199	5
	9500	52.36	304.61	1.09	0.99	326	16
	10551	50.58	100.32	1.09	1.04	304	9
	10527	50.70	170.99	1.11	1.01	231	9
	30209	55.16	21.88	0.99	0.98	617	29
	4230	51.46	415.02	1.14	1.04	808	44
60-70	**1879**	65.28	161.69	1.09	1.06	617	25
	5600	66.47	4.87	1.01	1.00	393	8
	8238	63.49	35.90	1.00	0.96	664	37
	8268	65.50	740.39	0.79	0.75	3529	109
	9516	64.92	145.67	1.06	0.98	556	11
	10500	62.01	154.40	1.07	1.07	600	39
	29468	66.36	2252.33	0.65	0.47	12412	491
	2383.3	60.76	114.10	1.02	0.99	664	36
	6771.2	61.25	811.01	1.01	0.85	454	14
	6785.2	63.56	244.54	0.96	0.94	657	11

70-80	**1901**	75.91	357.20	1.12	1.08	1124	37
	8239	72.60	28.19	0.99	0.96	816	42
	8267	73.27	775.80	0.81	0.78	3864	113
	9508	71.42	488.59	1.09	0.98	526	17
	10480	78.59	206.81	1.05	1.02	581	26
	10494	77.77	347.27	1.08	1.03	874	44
	41375	72.66	255.34	1.12	1.08	222	23
	41399	71.17	220.05	1.10	1.09	1081	41
	22378	74.68	1141.51	1.01	0.92	1747	72
	22391	71.64	1644.69	0.89	0.95	2095	95
80-90	**1883**	86.78	319.44	1.11	1.07	844	29
	1899	86.90	368.39	1.11	1.07	1323	40
	8240	83.55	38.40	0.98	0.95	870	46
	8266	80.78	791.63	0.82	0.80	4113	115
	10482	86.93	236.17	1.05	1.02	830	35
	10492	85.62	341.73	1.08	1.03	924	44
	41377	85.31	397.61	1.13	1.09	964	53
	41395	89.46	403.55	1.12	1.09	1791	54
	22388	81.14	1054.86	0.91	0.92	2360	102
90-100	**1884**	93.33	359.02	1.11	1.07	936	34
	1895	92.42	386.99	1.11	1.07	1323	40
	8241	92.93	63.49	0.96	0.95	1380	55
	8265	90.34	973.78	0.83	0.81	4447	117
	10490	92.17	379.09	1.07	1.03	964	43
	41380	94.23	516.80	1.13	1.10	1451	54
	41392	96.45	455.96	1.12	1.09	1856	54
	22381	90.02	894.21	0.96	0.92	2006	94

Table B.4. Historical QPE events categorised by mean rainfall over Darlington (North) sewer catchment. $\boldsymbol{MR}$, $\boldsymbol{VAR}$, $\boldsymbol{I_1}$ and $\boldsymbol{I_2}$ are shown along with model simulated $\boldsymbol{V^a}$ and $\boldsymbol{V^b}$ values.

CATEGORY	***EVENT REF***	***MR (mm)***	***VAR***	I_1	I_2	$\boldsymbol{V^a}$ ***(m^3)***	$\boldsymbol{V^b}$
20-30	**365**	27.29	17.97	1.02	0.99	47	11
	1775	21.07	2.81	1.02	0.96	3	6
	1910	27.26	98.30	0.96	1.13	11	7
	4095	28.80	2.36	1.01	1.00	26	9
	8090	21.70	29.47	0.95	1.04	129	13
	11404	22.10	3.69	1.00	0.97	11	7
	18495	20.83	37.76	0.94	1.01	40	9
	27175	22.37	2.02	1.00	1.01	0	5
	30072	21.15	2.71	1.00	0.99	11	7
	33759	20.38	1.13	1.01	1.01	0	4
30-40	**1885**	39.45	209.01	0.91	1.02	896	26
	1923	32.16	105.06	0.94	1.11	83	11
	4112	32.18	2.82	1.00	1.00	70	11
	5390	31.84	394.37	0.90	0.99	3311	157
	9595	39.61	12.90	0.98	1.03	153	13
	16183	36.63	19.75	1.02	1.00	80	10
	20258	30.37	6.42	0.99	1.03	35	9
	28552	32.35	50.39	1.07	0.87	55	10
	34985	32.01	434.27	0.95	1.01	68	3
	35856	31.68	2.16	1.00	1.01	72	10
40-50	**5590**	42.88	8.90	0.99	0.99	185	11
	5940	44.16	14.20	1.02	0.96	695	28
	6190	42.47	32.50	0.99	0.95	343	21
	8240	47.57	74.51	1.05	0.95	139	12
	9573	40.50	3.58	1.00	0.98	99	10
	16232	47.27	89.92	1.02	0.98	183	14
	29447	45.41	8.80	1.00	1.00	211	14
	32618	41.58	83.75	0.99	0.96	777	20
	35000	46.75	435.06	1.00	1.00	445	21
	40970	45.88	22.56	1.01	0.99	154	15
50-60	**1858**	57.16	354.46	1.10	0.84	561	36
	1883	51.99	233.41	0.92	1.00	1486	31
	8263	55.44	42.27	1.03	1.01	437	18
	9512	53.67	9.70	1.02	0.99	261	13
	9529	52.90	12.80	1.02	0.98	393	16
	32604	58.25	38.62	1.00	0.97	683	26
	32616	53.03	74.33	1.01	0.95	995	24
	33777	50.89	9.45	0.99	1.04	234	12
	41369	59.78	31.92	0.98	0.98	131	11
	41394	52.16	226.29	1.05	0.89	1543	70

60-70	**1860**	69.83	306.97	1.07	0.87	1399	74
	8244	66.94	124.94	1.05	0.97	351	14
	32614	64.55	59.10	1.01	0.96	1324	26
	41370	67.05	32.39	0.99	0.97	750	33
	41849.2	66.89	353.95	1.00	1.10	884	26
	41867.2	63.11	248.27	0.99	1.07	1514	27
	25340.3	67.30	156.67	0.99	1.04	415	15
	25391.3	67.97	1268.80	0.89	1.05	1801	28
	27002.3	68.70	63.93	1.00	0.99	1316	29
	42095.3	64.70	2641.75	0.86	0.97	4041	66
70-80	**41850.2**	70.22	365.46	1.00	1.10	1122	28
	41865.2	70.39	303.27	0.99	1.08	1775	27
	25350.3	74.06	150.81	1.01	1.02	593	17
	25390.3	73.41	1260.01	0.89	1.08	2016	29
	26998.3	74.85	54.14	1.02	0.99	841	28
	42070.3	73.94	1876.64	1.10	0.79	476	19
	47942.3	70.91	1470.56	1.09	0.86	1009	27
	47962.3	74.61	3099.25	0.90	1.05	2962	63
	54283.3	72.12	2349.35	0.92	1.19	12062	365

Appendix C Cash flow and sewer floods per month

Table C.1. Monthly sewer floods for sample drainage area used to define frequency ratio of sewer floods per month for an annual period.

	Jan	Feb	Mar	Apr	May	Jun	Jul	Aug	Sep	Oct	Nov	Dec	TOTAL	RATIO
Internal	0	1	0	0	0	0	0	0	2	0	2	0	**5**	1
External	9	1	3	0	5	2	1	4	2	1	3	0	**31**	6.2
Highway/other	4	1	1	1	1	1	0	2	1	1	0	2	**15**	3
TOTAL	**13**	**3**	**4**	**1**	**6**	**3**	**1**	**6**	**5**	**2**	**5**	**2**		
AVG	**4**	**1**	**1**	**0**	**2**	**1**	**0**	**2**	**2**	**1**	**2**	**1**		

Cash flow (Per Month)				**MONTH 1**					
Sensitivity by number of drainage areas									
					1 DA	**2 DA**	**4 DA**	**8 DA**	**16 DA**
Crew cost single avg									
Internal	£242.50			**Cost saving (Internal flood)**					
External	£225.50			Crew numbers reduced	0	1	1	2	4
Highway/other	£190.00			Crew total	£72.75	£138.23	£262.63	£498.99	£948.09
				Cost saving (External flood)					
				Crew numbers reduced	9	17	32	62	117
				Crew total	£2,029.50	£3,856.05	£7,326.50	£13,920.34	£26,448.65
				Cost saving (Highway/other flood)					
				Crew numbers reduced	4	8	14	27	52
				Crew total	£760.00	£1,444.00	£2,743.60	£5,212.84	£9,904.40
				Net Savings	**£2,862.25**	**£5,438.28**	**£10,332.72**	**£19,632.17**	**£37,301.13**

Figure 0.1. Cash flow model used to calculate cash inflow for month 1.

Cash flow (Per Month)				MONTH 2					
Sensitivity by number of drainage areas									
					1 DA	2 DA	4 DA	8 DA	16 DA
Crew cost single avg									
Internal	£242.50			**Cost saving (Internal flood)**					
External	£225.50			Crew numbers reduced	1	2	4	7	13
Highway/other	£190.00			Crew total	£242.50	£460.75	£875.43	£1,663.31	£3,160.28
				Cost saving (External flood)					
				Crew numbers reduced	1	2	4	7	13
				Crew total	£225.50	£428.45	£814.06	£1,546.70	£2,938.74
				Cost saving (Highway/other flood)					
				Crew numbers reduced	1	2	4	7	13
				Crew total	£190.00	£361.00	£685.90	£1,303.21	£2,476.10
				Net Savings	**£658.00**	**£1,250.20**	**£2,375.38**	**£4,513.22**	**£8,575.12**

Figure 0.2. Cash flow model used to calculate cash inflow for month 2.

Cash flow (Per Month)				MONTH 3					
Sensitivity by number of drainage areas									
					1 DA	2 DA	4 DA	8 DA	16 DA
Crew cost single avg									
Internal	£242.50			**Cost saving (Internal flood)**					
External	£225.50			Crew numbers reduced	0	0	0	0	0
Highway/other	£190.00			Crew total	£0.00	£0.00	£0.00	£0.00	£0.00
				Cost saving (External flood)					
				Crew numbers reduced	3	6	11	21	39
				Crew total	£676.50	£1,285.35	£2,442.17	£4,640.11	£8,816.22
				Cost saving (Highway/other flood)					
				Crew numbers reduced	1	2	4	7	13
				Crew total	£190.00	£361.00	£685.90	£1,303.21	£2,476.10
				Net Savings	**£866.50**	**£1,646.35**	**£3,128.07**	**£5,943.32**	**£11,292.31**

Figure 0.3. Cash flow model used to calculate cash inflow for month 3.

Cash flow (Per Month)				MONTH 4					
Sensitivity by number of drainage areas									
					1 DA	2 DA	4 DA	8 DA	16 DA
Crew cost single avg									
Internal	£242.50			**Cost saving (Internal flood)**					
External	£225.50			Crew numbers reduced	0	0	0	0	0
Highway/other	£190.00			Crew total	£0.00	£0.00	£0.00	£0.00	£0.00
				Cost saving (External flood)					
				Crew numbers reduced	0	0	0	0	0
				Crew total	£0.00	£0.00	£0.00	£0.00	£0.00
				Cost saving (Highway/other flood)					
				Crew numbers reduced	1	2	4	7	13
				Crew total	£190.00	£361.00	£685.90	£1,303.21	£2,476.10
				Net Savings	**£190.00**	**£361.00**	**£685.90**	**£1,303.21**	**£2,476.10**

Figure 0.4. Cash flow model used to calculate cash inflow for month 4.

Cash flow (Per Month)				MONTH 5					
Sensitivity by number of drainage areas									
					1 DA	2 DA	4 DA	8 DA	16 DA
Crew cost single avg									
Internal	£242.50			**Cost saving (Internal flood)**					
External	£225.50			Crew numbers reduced	0	0	0	0	0
Highway/other	£190.00			Crew total	£0.00	£0.00	£0.00	£0.00	£0.00
				Cost saving (External flood)					
				Crew numbers reduced	0	0	0	0	0
				Crew total	£0.00	£0.00	£0.00	£0.00	£0.00
				Cost saving (Highway/other flood)					
				Crew numbers reduced	1	2	4	7	13
				Crew total	£190.00	£361.00	£685.90	£1,303.21	£2,476.10
				Net Savings	**£190.00**	**£361.00**	**£685.90**	**£1,303.21**	**£2,476.10**

Figure 0.5. Cash flow model used to calculate cash inflow for month 5.

Cash flow (Per Month)				MONTH 6					
Sensitivity by number of drainage areas									
					1 DA	2 DA	4 DA	8 DA	16 DA
Crew cost single avg									
Internal	£242.50			**Cost saving (Internal flood)**					
External	£225.50			Crew numbers reduced	0	0	0	0	0
Highway/other	£190.00			Crew total	£0.00	£0.00	£0.00	£0.00	£0.00
				Cost saving (External flood)					
				Crew numbers reduced	2	4	7	14	26
				Crew total	£451.00	£856.90	£1,628.11	£3,093.41	£5,877.48
				Cost saving (Highway/other flood)					
				Crew numbers reduced	1	2	4	7	13
				Crew total	£190.00	£361.00	£685.90	£1,303.21	£2,476.10
				Net Savings	**£641.00**	**£1,217.90**	**£2,314.01**	**£4,396.62**	**£8,353.58**

Figure 0.6. Cash flow model used to calculate cash inflow for month 6.

Cash flow (Per Month)				MONTH 7					
Sensitivity by number of drainage areas									
					1 DA	2 DA	4 DA	8 DA	16 DA
Crew cost single avg									
Internal	£242.50			**Cost saving (Internal flood)**					
External	£225.50			Crew numbers reduced	0	0	0	0	0
Highway/other	£190.00			Crew total	£0.00	£0.00	£0.00	£0.00	£0.00
				Cost saving (External flood)					
				Crew numbers reduced	1	2	4	7	13
				Crew total	£225.50	£428.45	£814.06	£1,546.70	£2,938.74
				Cost saving (Highway/other flood)					
				Crew numbers reduced	0	0	0	0	0
				Crew total	£0.00	£0.00	£0.00	£0.00	£0.00
				Net Savings	**£225.50**	**£428.45**	**£814.06**	**£1,546.70**	**£2,938.74**

Figure 0.7. Cash flow model used to calculate cash inflow for month 7.

Cash flow (Per Month)				MONTH 8					
Sensitivity by number of drainage areas									
					1 DA	2 DA	4 DA	8 DA	16 DA
Crew cost single avg									
Internal	£242.50			**Cost saving (Internal flood)**					
External	£225.50			Crew numbers reduced	0	0	0	0	0
Highway/other	£190.00			Crew total	£0.00	£0.00	£0.00	£0.00	£0.00
				Cost saving (External flood)					
				Crew numbers reduced	4	8	14	27	52
				Crew total	£902.00	£1,713.80	£3,256.22	£6,186.82	£11,754.95
				Cost saving (Highway/other flood)					
				Crew numbers reduced	2	4	7	14	26
				Crew total	£380.00	£722.00	£1,371.80	£2,606.42	£4,952.20
				Net Savings	**£1,282.00**	**£2,435.80**	**£4,628.02**	**£8,793.24**	**£16,707.15**

Figure 0.8. Cash flow model used to calculate cash inflow for month 8.

Cash flow (Per Month)				MONTH 9					
Sensitivity by number of drainage areas									
					1 DA	2 DA	4 DA	8 DA	16 DA
Crew cost single avg									
Internal	£242.50			**Cost saving (Internal flood)**					
External	£225.50			Crew numbers reduced	2	4	7	14	26
Highway/other	£190.00			Crew total	£485.00	£921.50	£1,750.85	£3,326.62	£6,320.57
				Cost saving (External flood)					
				Crew numbers reduced	2	4	7	14	26
				Crew total	£451.00	£856.90	£1,628.11	£3,093.41	£5,877.48
				Cost saving (Highway/other flood)					
				Crew numbers reduced	1	2	4	7	13
				Crew total	£190.00	£361.00	£685.90	£1,303.21	£2,476.10
				Net Savings	**£1,126.00**	**£2,139.40**	**£4,064.86**	**£7,723.23**	**£14,674.14**

Figure 0.9. Cash flow model used to calculate cash inflow for month 9.

Cash flow (Per Month)				MONTH 10					
Sensitivity by number of drainage areas									
					1 DA	2 DA	4 DA	8 DA	16 DA
Crew cost single avg									
Internal	£242.50			**Cost saving (Internal flood)**					
External	£225.50			Crew numbers reduced	0	0	0	0	0
Highway/other	£190.00			Crew total	£0.00	£0.00	£0.00	£0.00	£0.00
				Cost saving (External flood)					
				Crew numbers reduced	1	2	4	7	13
				Crew total	£225.50	£428.45	£814.06	£1,546.70	£2,938.74
				Cost saving (Highway/other flood)					
				Crew numbers reduced	1	2	4	7	13
				Crew total	£190.00	£361.00	£685.90	£1,303.21	£2,476.10
				Net Savings	**£415.50**	**£789.45**	**£1,499.96**	**£2,849.91**	**£5,414.84**

Figure 0.10. Cash flow model used to calculate cash inflow for month 10.

Cash flow (Per Month)				MONTH 11					
Sensitivity by number of drainage areas									
					1 DA	2 DA	4 DA	8 DA	16 DA
Crew cost single avg									
Internal	£242.50			**Cost saving (Internal flood)**					
External	£225.50			Crew numbers reduced	2	4	7	14	26
Highway/other	£190.00			Crew total	£485.00	£921.50	£1,750.85	£3,326.62	£6,320.57
				Cost saving (External flood)					
				Crew numbers reduced	3	6	11	21	39
				Crew total	£676.50	£1,285.35	£2,442.17	£4,640.11	£8,816.22
				Cost saving (Highway/other flood)					
				Crew numbers reduced	0	0	0	0	0
				Crew total	£0.00	£0.00	£0.00	£0.00	£0.00
				Net Savings	**£1,161.50**	**£2,206.85**	**£4,193.02**	**£7,966.73**	**£15,136.78**

Figure 0.11. Cash flow model used to calculate cash inflow for month 11.

Cash flow (Per Month)				MONTH 12					
Sensitivity by number of drainage areas									
					1 DA	2 DA	4 DA	8 DA	16 DA
Crew cost single avg									
Internal	£242.50			**Cost saving (Internal flood)**					
External	£225.50			Crew numbers reduced	0	0	0	0	0
Highway/other	£190.00			Crew total	£0.00	£0.00	£0.00	£0.00	£0.00
				Cost saving (External flood)					
				Crew numbers reduced	0	0	0	0	0
				Crew total	£0.00	£0.00	£0.00	£0.00	£0.00
				Cost saving (Highway/other flood)					
				Crew numbers reduced	2	4	7	14	26
				Crew total	£380.00	£722.00	£1,371.80	£2,606.42	£4,952.20
				Net Savings	**£380.00**	**£722.00**	**£1,371.80**	**£2,606.42**	**£4,952.20**

Figure 0.12. Cash flow model used to calculate cash inflow for month 12.

Appendix D Sensitivity analysis

Table D.1. NPV and IRR values for capital investment of £6,000

MONTH	CASH FLOW (NET SAVINGS)				
	1 DA	2 DA	4 DA	8 DA	16 DA
0	-£5,500.00	-£11,000.00	-£22,000.00	-£44,000.00	-£88,000.00
1	£2,789.50	£5,300.05	£10,070.10	£19,133.18	£36,353.04
2	£658.00	£1,250.20	£2,375.38	£4,513.22	£8,575.12
3	£866.50	£1,646.35	£3,128.07	£5,943.32	£11,292.31
4	£190.00	£361.00	£685.90	£1,303.21	£2,476.10
5	£1,317.50	£2,503.25	£4,756.18	£9,036.73	£17,169.79
6	£641.00	£1,217.90	£2,314.01	£4,396.62	£8,353.58
7	£225.50	£428.45	£814.06	£1,546.70	£2,938.74
8	£1,282.00	£2,435.80	£4,628.02	£8,793.24	£16,707.15
9	£1,126.00	£2,139.40	£4,064.86	£7,723.23	£14,674.14
10	£415.50	£789.45	£1,499.96	£2,849.91	£5,414.84
11	£1,161.50	£2,206.85	£4,193.02	£7,966.73	£15,136.78
12	£380.00	£722.00	£1,371.80	£2,606.42	£4,952.20
NPV	**£3,356.10**	**£5,826.58**	**£9,970.51**	**£16,743.97**	**£27,413.53**
IRR	**17%**	**15%**	**13%**	**12%**	**11%**
4.3%					

Table D.2. NPV and IRR values for capital investment of £7,000

MONTH	CASH FLOW (NET SAVINGS)				
	1 DA	2 DA	4 DA	8 DA	16 DA
0	-£6,000.00	-£12,000.00	-£24,000.00	-£48,000.00	-£96,000.00
1	£2,789.50	£5,300.05	£10,070.10	£19,133.18	£36,353.04
2	£658.00	£1,250.20	£2,375.38	£4,513.22	£8,575.12
3	£866.50	£1,646.35	£3,128.07	£5,943.32	£11,292.31
4	£190.00	£361.00	£685.90	£1,303.21	£2,476.10
5	£1,317.50	£2,503.25	£4,756.18	£9,036.73	£17,169.79
6	£641.00	£1,217.90	£2,314.01	£4,396.62	£8,353.58
7	£225.50	£428.45	£814.06	£1,546.70	£2,938.74
8	£1,282.00	£2,435.80	£4,628.02	£8,793.24	£16,707.15
9	£1,126.00	£2,139.40	£4,064.86	£7,723.23	£14,674.14
10	£415.50	£789.45	£1,499.96	£2,849.91	£5,414.84
11	£1,161.50	£2,206.85	£4,193.02	£7,966.73	£15,136.78
12	£380.00	£722.00	£1,371.80	£2,606.42	£4,952.20
NPV	**£2,856.10**	**£4,826.58**	**£7,970.51**	**£12,743.97**	**£19,413.53**
IRR	**14%**	**12%**	**11%**	**10%**	**8%**
4.3%					

Table D.3. NPV and IRR values for capital investment of £8,000

MONTH	CASH FLOW (NET SAVINGS)				
	1 DA	2 DA	4 DA	8 DA	16 DA
0	-£6,500.00	-£13,000.00	-£26,000.00	-£52,000.00	-£104,000.00
1	£2,789.50	£5,300.05	£10,070.10	£19,133.18	£36,353.04
2	£658.00	£1,250.20	£2,375.38	£4,513.22	£8,575.12
3	£866.50	£1,646.35	£3,128.07	£5,943.32	£11,292.31
4	£190.00	£361.00	£685.90	£1,303.21	£2,476.10
5	£1,317.50	£2,503.25	£4,756.18	£9,036.73	£17,169.79
6	£641.00	£1,217.90	£2,314.01	£4,396.62	£8,353.58
7	£225.50	£428.45	£814.06	£1,546.70	£2,938.74
8	£1,282.00	£2,435.80	£4,628.02	£8,793.24	£16,707.15
9	£1,126.00	£2,139.40	£4,064.86	£7,723.23	£14,674.14
10	£415.50	£789.45	£1,499.96	£2,849.91	£5,414.84
11	£1,161.50	£2,206.85	£4,193.02	£7,966.73	£15,136.78
12	£380.00	£722.00	£1,371.80	£2,606.42	£4,952.20
NPV	**£2,356.10**	**£3,826.58**	**£5,970.51**	**£8,743.97**	**£11,413.53**
IRR	**12%**	**10%**	**9%**	**8%**	**7%**
4.3%					

Table D.4. NPV and IRR values for capital investment of £9,000

MONTH	CASH FLOW (NET SAVINGS)				
	1 DA	2 DA	4 DA	8 DA	16 DA
0	-£7,000.00	-£14,000.00	-£28,000.00	-£56,000.00	-£112,000.00
1	£2,789.50	£5,300.05	£10,070.10	£19,133.18	£36,353.04
2	£658.00	£1,250.20	£2,375.38	£4,513.22	£8,575.12
3	£866.50	£1,646.35	£3,128.07	£5,943.32	£11,292.31
4	£190.00	£361.00	£685.90	£1,303.21	£2,476.10
5	£1,317.50	£2,503.25	£4,756.18	£9,036.73	£17,169.79
6	£641.00	£1,217.90	£2,314.01	£4,396.62	£8,353.58
7	£225.50	£428.45	£814.06	£1,546.70	£2,938.74
8	£1,282.00	£2,435.80	£4,628.02	£8,793.24	£16,707.15
9	£1,126.00	£2,139.40	£4,064.86	£7,723.23	£14,674.14
10	£415.50	£789.45	£1,499.96	£2,849.91	£5,414.84
11	£1,161.50	£2,206.85	£4,193.02	£7,966.73	£15,136.78
12	£380.00	£722.00	£1,371.80	£2,606.42	£4,952.20
NPV	**£1,856.10**	**£2,826.58**	**£3,970.51**	**£4,743.97**	**£3,413.53**
IRR	**10%**	**8%**	**7%**	**6%**	**5%**
4.3%					

Bibliography

Aboufirassi, M., and Mariño, M. A. (1983) Kriging of water levels in the Souss aquifer, Morocco. *Journal of the International Association for Mathematical Geology* (4): 537–551.

Achleitner, S., Fach, S., Einfalt, T., and Rauch, W. (2009) Nowcasting of rainfall and of combined sewage flow in urban drainage systems. *Water science and technology : a journal of the International Association on Water Pollution Research* 59(6): 1145–51.

Ahmadisharaf, E., Kalyanapu, A. J., and Chung, E. (2016) Spatial probabilistic multi-criteria decision making for assessment of flood management alternatives. *JOURNAL OF HYDROLOGY* 533: 365–378.

Albert, J. (2009) *Markov Chain Monte Carlo Methods*. doi:10.1007/978-0-387-92298-0.

Andalibi, M., Hoberock, L. L., and Mohamadipanah, H. (2015) Effects of texture addition on optical flow performance in images with poor texture ☆. *Imavis* 40: 1–15.

Anquetin, S., Braud, I., Vannier, O., Viallet, P., Boudevillain, B., Creutin, J. D., and Manus, C. (2010) Sensitivity of the hydrological response to the variability of rainfall fields and soils for the Gard 2002 flash-flood event. *Journal of Hydrology* 394(1–2): 134–147.

Barba-J, L., Moya-Albor, E., Escalante-Ram??rez, B., Brieva, J., and Vallejo Venegas, E. (2016) Segmentation and optical flow estimation in cardiac CT sequences based on a spatiotemporal PDM with a correction scheme and the Hermite transform. *Computers in Biology and Medicine* 69: 189–202.

Barillec, R., and Cornford, D. (2009) Data assimilation for precipitation nowcasting using Bayesian inference. *Advances in Water Resources* 32(7): 1050–1065.

Ben Bouallègue, Z. (2011) Upscaled and fuzzy probabilistic forecasts : verification results. (11): 124–132.

Berndt, C., Rabiei, E., and Haberlandt, U. (2014) Geostatistical merging of rain gauge and radar data for high temporal resolutions and various station density scenarios. *Journal of Hydrology* 508: 88–101.

Berne, A., Delrieu, G., Creutin, J. D., and Obled, C. (2004) Temporal and spatial resolution of rainfall measurements required for urban hydrology. *Journal of Hydrology* 299(3–4): 166–179.

Berrocal, V. J., Raftery, A. E., and Gneiting, T. (2008) Probabilistic Quantitative Precipitation Field Forecasting Using a Two-Stage Spatial Model. *The Annals of Statistics* 2(4): 1170–1193.

Beven, K., and Binley, A. (1992) The future of distributed models model calibration and uncertainty prediction. *Hydrological Processes*.

Beven, K., and Freer, J. (2001) A dynamic topmodel. *Hydrological Processes* 15(10): 1993–2011.

Biondi, D., and De Luca, D. L. (2012) A Bayesian approach for real-time flood forecasting. *Physics and Chemistry of the Earth, Parts A/B/C* 42–44: 91–97.

Bogner, K., and Pappenberger, F. (2011) Multiscale error analysis, correction, and predictive uncertainty estimation in a flood forecasting system. *Water Resources Research* 47(7).

Boldi, R. A., Wolfson, M. M., Dupree, W. J., Johnson, R. J., Theriault, K. E., Forman, B. E., and Wiilson, C. A. (2002) AN AUTOMATED, OPERATIONAL TWO HOUR CONVECTIVE WEATHER FORECAST FOR THE CORRIDOR INTEGRATED WEATHER. *MIT Lincoln Laboratory* 5.1: 4.

Boldina, I., and Beninger, P. G. (2016) Strengthening statistical usage in marine ecology: Linear regression. *Journal of Experimental Marine Biology and Ecology* 474: 81–91.

Borga, M., Boscolo, P., Zanon, F., and Sangati, M. (2007) Hydrometeorological Analysis of the 29 August 2003 Flash Flood in the Eastern Italian Alps. *Journal of Hydrometeorology* 8(5): 1049–1067.

Borga, M., Tonelli, F., Moore, R. J., and Andrieu, H. (2002) Long-term assessment of bias adjustment in radar rainfall estimation. *Water Resources Research* 38(11): 1–10.

Boucher, M. A., Tremblay, D., Delorme, L., Perreault, L., and Anctil, F. (2012) Hydro-economic assessment of hydrological forecasting systems. *Journal of Hydrology* 416–417: 133–144.

Bowler, N. E. H., Pierce, C. E., and Seed, A. (2004) Development of a precipitation nowcasting algorithm based upon optical flow techniques. *Journal of Hydrology* 288(1–2): 74–91.

Bowler, N. E. H., Pierce, C. E., and Seed, A. (2004) Development of a precipitation nowcasting algorithm based upon optical flow techniques. 288: 74–91.

Bowler, N. E., Pierce, C. E., and Seed, A. W. (2006) STEPS: A probabilistic precipitation forecasting scheme which merges an extrapolation nowcast with downscaled NWP. *Quarterly Journal of the Royal Meteorological Society* 132(620): 2127–2155.

Bowman, A. W., and Crujeiras, R. M. (2013) Inference for variograms. *Computational Statistics and Data Analysis* 66: 19–31.

Brezkova, L., Novak, P., Salek, M., Kyznarova, H., Jonov, M., Frolik, P., and Sokol, Z. (2012) Operational use of nowcasting methods for hydrological forecasting by the Czech Hydrometeorological Institute. *Weather Radar and Hydrology ((Proceedings of a symposium held in Exeter, UK, April 2011)* 351(April 2011): 2012.

Bringi, V. N., and Chandrasekar, V. (2001) *Polarimetric Doppler Weather Radar: Principles and Applications*. Cambridge: Cambridge University Press doi:10.1017/CBO9780511541094.

Brown, J. D., and Seo, D. J. (2013) Evaluation of a nonparametric post-processor for bias correction and uncertainty estimation of hydrologic predictions. *Hydrological Processes* 27(1): 83–105.

Brown, L. E., Mitchell, G., Holden, J., Folkard, a, Wright, N., Beharry-Borg, N., et al. (2010) Priority water research questions as determined by UK practitioners and policy makers. *The Science of the total environment* 409(2): 256–66.

Brox, T., Papenberg, N., and Weickert, J. (2004) High Accuracy Optical Flow

Estimation Based on a Theory for Warping. *Computer Vision - ECCV 2004* 4(May): 25–36.

Brus, D. J., and Heuvelink, G. B. M. (2007) Optimization of sample patterns for universal kriging of environmental variables. *Geoderma* 138(1–2): 86–95.

Buizza, R., Houtekamer, P. L., Pellerin, G., Toth, Z., Zhu, Y., and Wei, M. (2005) A Comparison of the ECMWF, MSC, and NCEP Global Ensemble Prediction Systems. *Monthly Weather Review* 133(5): 1076–1097.

Chandler, R., and Wheater, H. (2002) Analysis of rainfall variability using generalized linear models: A case study from the west of Ireland. *Water Resources Research* 38(10): 674–689.

Charbal, A., Dufour, J. E., Guery, A., Hild, F., Roux, S., Vincent, L., and Poncelet, M. (2016) Integrated Digital Image Correlation considering gray level and blur variations: Application to distortion measurements of IR camera. *Optics and Lasers in Engineering* 78: 75–85.

Chen, S. T., and Yu, P. S. (2007) Real-time probabilistic forecasting of flood stages. *Journal of Hydrology* 340: 63–77.

Cheng, T. (2013) Accelerating universal Kriging interpolation algorithm using CUDA-enabled GPU. *Computers and Geosciences* 54: 178–183.

Cheung, P., and Yeung, H. (2012) Application of optical-flow technique to significant convection nowcast for terminal areas in Hong Kong. *… WMO International Symposium on Nowcasting …* (August): 6–10.

Chib, S., and Greenberg, E. (1995) Understanding the Metropolis-Hastings Algorithm. *The American Statistician* : 9.

Clark, M., Gangopadhyay, S., Hay, L., Rajagopalan, B., and Wilby, R. (2004) The Schaake Shuffle: A Method for Reconstructing Space–Time Variability in Forecasted Precipitation and Temperature Fields. *Journal of Hydrometeorology* 5(1): 243–262.

Cloke, H. L., and Pappenberger, F. (2009) Ensemble flood forecasting : A review. *Journal of Hydrology* 375(3–4): 613–626.

Coccia, G., and Todini, E. (2011) Recent developments in predictive uncertainty

assessment based on the model conditional processor approach. *Hydrology and Earth System Sciences* 15(10): 3253–3274.

Cole, S. J., and Moore, R. J. (2008) Hydrological modelling using raingauge- and radar-based estimators of areal rainfall. *Journal of Hydrology* 358(3–4): 159–181.

Cole, S. J., and Moore, R. J. (2009) Distributed hydrological modelling using weather radar in gauged and ungauged basins. *Advances in Water Resources* 32(7): 1107–1120.

Collier, C. . (1989) *Applications of weather radar systems: a guide to uses of radar data in meteorology and hydrology*. Chichester: John Wiley and Sons Ltd.

Coppola, E. A., Szidarovszky, F., Davis, D., Spayd, S., Poulton, M. M., and Roman, E. (2007) Multiobjective analysis of a public wellfield using artificial neural networks. *Ground Water* 45(1): 53–61.

Coppola, E. a, Rana, A. J., Poulton, M. M., Szidarovszky, F., and Uhl, V. W. (2005) A neural network model for predicting aquifer water level elevations. *Ground water* 43(2): 231–241.

Coustau, M., Bouvier, C., Borrell-Estupina, V., and Jourde, H. (2012) Flood modelling with a distributed event-based parsimonious rainfall-runoff model: Case of the karstic Lez river catchment. *Natural Hazards and Earth System Science* 12(4): 1119–1133.

Cressie, N. A. C. (1993) *Statistics for Spatial Data*. New York: John Wiley & Sons.

Cressie, N. A. C. (2015) *Statistics for Spatial Data*. (Wiley Seri.). John Wiley & Sons.

Dai, Q. (2014) Radar Rainfall Uncertainty Analysis for Hydrological Applications By. (September).

Dale, M., Wicks, J., Mylne, K., Pappenberger, F., Laeger, S., and Taylor, S. (2014) Probabilistic flood forecasting and decision-making: An innovative risk-based approach. *Natural Hazards* 70(1): 159–172.

Darsono, S., and Labadie, J. W. (2007) Neural-optimal control algorithm for

real-time regulation of in-line storage in combined sewer systems. *Environmental Modelling & Software* 22(9): 1349–1361.

de Lima, J. L. M. P., and Singh, V. P. (2003) Laboratory experiments on the influence of storm movement on overland flow. *Physics and Chemistry of the Earth* 28(6–7): 277–282.

De Smith, M. J. (2013) *Statistical Analysis Handbook: A Comprehensive Handbook of Statistical Concepts, Techniques and Software Tools*. Winchelsea: The Winchelsea Press.

Delrieu, G., Nicol, J., Yates, E., Kirstetter, P.-E., Creutin, J.-D., Anquetin, S., et al. (2005) The Catastrophic Flash-Flood Event of 8–9 September 2002 in the Gard Region, France: A First Case Study for the Cévennes–Vivarais Mediterranean Hydrometeorological Observatory. *Journal of Hydrometeorology* 6(1): 34–52.

Demargne, J., Brown, J., Wu, L., Regonda, S., and He, M. (2013) Hydrologic Ensemble Forecast Service for Operational Short-to-Long Range Hydrometeorological and Hydrologic Ensembles in the U . S . National Weather Service. 15: 12702.

Dixon, M., Wiener, G., Dixon, M., and Wiener, G. (1993) TITAN: Thunderstorm Identification, Tracking, Analysis, and Nowcasting—A Radar-based Methodology. *Journal of Atmospheric and Oceanic Technology* 10(6): 785–797.

Dottori, F., Salamon, P., Kalas, M., Bianchi, A., Thielen, J., and Feyen, L. (2015) A NEAR REAL-TIME PROCEDURE FOR FLOOD HAZARD MAPPING AND RISK ASSESSMENT IN EUROPE. *E-proceedings of the 36th IAHR World Congress* (c): 1–8.

Douinot, A., Roux, H., Garambois, P., Larnier, K., Labat, D., and Dartus, D. (2016) Accounting for rainfall systematic spatial variability in flash flood forecasting. *Journal of Hydrology* 541: 359–370.

Duncan, A. P., Chen, A. S., Keedwell, E. C., Djordjevic, S., and Savic, D. (2012) MACHINE LEARNING-BASED EARLY WARNING SYSTEM FOR URBAN FLOOD MANAGEMENT Artificial Neural Networks for Urban Flood Modelling. *Weather Radar and Hydrology ((Proceedings of a symposium held in Exeter,*

UK, April 2011) 351(September).

Ebert, E. E. (2001) Ability of a Poor Man's Ensemble to Predict the Probability and Distribution of Precipitation. *Monthly Weather Review* 129(10): 2461–2480.

Eckel, F. A., and Walters, M. K. (1998) Calibrated probabilistic quantitative precipitation forecasts based on the MRF ensemble. *Weather and Forecasting* 13(4): 1132–1147.

Ehrhardt, J., Saring, D., and Handels, H. (2006) Optical flow based interpolation of temporal image sequences. *Proceedings of SPIE* 6144: 61442K–61442K–8.

Einfalt, T., Arnbjerg-Nielsen, K., Golz, C., Jensen, N.-E., Quirmbach, M., Vaes, G., and Vieux, B. (2004) Towards a roadmap for use of radar rainfall data in urban drainage. *Journal of Hydrology* 299(3–4): 186–202.

Emery, X. (2006) Ordinary multigaussian kriging for mapping conditional probabilities of soil properties. *Geoderma* 132(1–2): 75–88.

Emmanuel, I., Andrieu, H., Leblois, E., and Flahaut, B. (2012) Temporal and spatial variability of rainfall at the urban hydrological scale. *Journal of Hydrology* 430–431: 162–172.

Emmanuel, I., Andrieu, H., Leblois, E., Janey, N., and Payrastre, O. (2015) Influence of rainfall spatial variability on rainfall – runoff modelling : Benefit of a simulation approach ? 531: 337–348.

Eom, J., Park, M., Heo, T.-Y., and Huntsinger, L. (2006) Improving the Prediction of Annual Average Daily Traffic for Nonfreeway Facilities by Applying a Spatial Statistical Method. *Transportation Research Record: Journal of the Transportation Research Board* 1968: 20–29.

Esteves, L. S. (2013) Consequences to fl ood management of using different probability distributions to estimate extreme rainfall. *Journal of Environmental Management* 115: 98–105.

Even, S., Mouchel, J.-M., Servais, P., Flipo, N., Poulin, M., Blanc, S., Chabanel, M., and Paffoni, C. (2007) Modelling the impacts of Combined Sewer Overflows on the river Seine water quality. *The Science of the total environment* 375(1–3): 140–51.

Fabry, F., Bellon, A., Duncan, M. R., and Austin, G. L. (1994) High resolution rainfall measurements by radar for very small basins: the sampling problem reexamined. *Journal of Hydrology* 161(1–4): 415–428.

Fabry, F., and Seed, A. W. (2009) Quantifying and predicting the accuracy of radar-based quantitative precipitation forecasts. *Advances in Water Resources* 32(7): 1043–1049.

Faure, D., Auchet, P., and Payrastre, O. (2002) Management of a detention-settling basin using radar data and risk notion. *Water Science and Technology* 45(2): 19–26.

Favre, A.-C. (2004) Multivariate hydrological frequency analysis using copulas. *Water Resources Research* 40(July 2015): 1–12.

Flötteröd, G., and Bierlaire, M. (2013) Metropolis – Hastings sampling of paths. 48: 53–66.

Foudi, S., Oses-Eraso, N., and Tamayo, I. (2015) Integrated spatial flood risk assessment: The case of Zaragoza. *Land Use Policy* 42: 278–292.

Fournier, J. D. (/1999) REFLECTIVITY-RAINFALL RATE RELATIONSHIPS IN OPERATIONAL METEOROLOGY. Accessed: 4th September 2014 <http://www.srh.noaa.gov/tae/?n=research-zrpaper. >.

Franks, S. W., Gineste, P., Beven, K. J., and Merot, P. (1998) On constraining the predictions of a distributed model: the incorporation of fuzzy estimates of saturated areas into the calibration process. *Water Resources Research* 34(4): 787–797.

Freier, L., and von Lieres, E. (2015) Kriging based iterative parameter estimation procedure for biotechnology applications with nonlinear trend functions. *IFAC-PapersOnLine* 48(1): 574–579.

Fu, G., Butler, D., Khu, S.-T., and Sun, S. (2011) Imprecise probabilistic evaluation of sewer flooding in urban drainage systems using random set theory. *Water Resources Research* 47(2): n/a-n/a.

Fumo, N., and Rafe Biswas, M. A. (2015) Regression analysis for prediction of residential energy consumption. *Renewable and Sustainable Energy Reviews* 47: 332–343.

Gelman, A., B. Carlin, J., S. Stern, H., B. Dunson, D., Vehtari, A., and B. Rubin, D. (2013) *Bayesian Data Analysis*. (Third.). Chapman and Hall/CRC.

Georgakakos, K. P., and Smith, G. F. (1990) On improved hydrologic forecasting - results from a WMO real-time forecasting experiment. *Journal of Hydrology* 114.

Germann, U., Berenguer, M., Sempere-Torres, D., and Zappa, M. (2009) REAL – Ensemble radar precipitation estimation for hydrology in a mountainous region. *Quarterly Journal of the Royal …* 135(October): 445–456.

Ghimire, B., Chen, A. S., Guidolin, M., Keedwell, E. C., Djordjević, S., and Savić, D. a. (2013) Formulation of a fast 2D urban pluvial flood model using a cellular automata approach. *Journal of Hydroinformatics* 15(3): 676.

Gjertsen, U., Salek, M., and Michelson, D. B. (2003) Gauge-adjustment of radar-based precipitation estimates – a review.

Golding, B. . (2000) Quantitative precipitation forecasting in the UK. *Journal of Hydrology* 239(1–4): 286–305.

Golding, B. W., Office, M., Road, L., and Rg, B. (1998) Nimrod : A system for generating automated very short range forecasts. 16: 1–16.

Gotway, C. A., Ferguson, R. B., Hergert, G. W., and Peterson, T. A. (1996) Comparison of Kriging and Inverse-Distance Methods for Mapping Soil Parameters. *Soil Science Society of America Journal* 60(4): 1237–1247.

Goudenhoofdt, E., and Delobbe, L. (2009a) Evaluation of radar-gauge merging methods for quantitative precipitation estimates. *Hydrology and Earth System Sciences* 13(2): 195–203.

Goudenhoofdt, E., and Delobbe, L. (2009b) Evaluation of radar-gauge merging methods for quantitative precipitation estimates. *Hydrology and Earth System Sciences* 13(2): 195–203.

Guntaka, R., Myler, H. R., and Drayer, P. M. (2014) ScienceDirect Regression and kriging analysis for grid power factor estimation. *Journal of Electrical Systems and Information Technology* 1(3): 223–233.

Habib, E., Qin, L., and Seo, D.-J. (2012) Comparison of different radar-gauge

merging techniques in the NWS multi-sensor precipitation estimator algorithm. *Weather Radar and Hydrology ((Proceedings of a symposium held in Exeter, UK, April 2011)* (April 2011): 2012.

Hamill, T. M., Whitaker, J. S., Hagedorn, R., Whitaker, J. S., Hamill, T. M., and Whitaker, J. S. (2008) Probabilistic Forecast Calibration Using ECMWF and GFS Ensemble Reforecasts. Part II: Precipitation. *Monthly Weather Review* 136(7): 2608–2619.

Han, S., Wong, R. K. W., Lee, T. C. M., and Shen, L. (2014) A Full Bayesian Approach for Boolean Genetic Network Inference. : 1–13. doi:10.1371/journal.pone.0115806.

Hantush, M. M., and Kalin, L. (2008) Stochastic Residual-Error Analysis for Estimating Hydrologic Model Predictive Uncertainty. *Journal of Hydrologic Engineering* 13(7): 585–596.

Hardy, J., Gourley, J. J., Kirstetter, P., Hong, Y., Kong, F., and Flamig, Z. L. (2016) A method for probabilistic flash flood forecasting. *Journal of Hydrology* 541: 480–494.

Hartnack, H. J., Engrob, G. H., and Rungo, M. (2009) 2D overland modelling using fine scale DEM with manageable runtimes. *Flood Risk Management: Research and Practice* : 119–124.

Hasan, M. M., Sharma, A., Johnson, F., Mariethoz, G., and Seed, A. (2014) Correcting bias in radar Z–R relationships due to uncertainty in point rain gauge networks. *Journal of Hydrology* 519: 1668–1676.

Haykin, S. (1994) *Neural Networks: A Comprehensive Foundation*. Prentice Hall.

He, X., Sonnenborg, T. O., Refsgaard, J. C., Vejen, F., and Jensen, K. H. (2013) Evaluation of the value of radar QPE data and rain gauge data for hydrological modeling. *Water Resources Research* 49(9): 5989–6005.

Hénonin, J., Russo, B., Roqueta, D. S., Sanchez-, R., Donna, N., Domingo, S., Thomsen, F., and Mark, O. (2013) Urban flood real-time forecasting and modelling: a state-of-the-art review. (September 2010): 6–8.

Herbst, E., Seitz, S., and Baker, S. (2009) Occlusion reasoning for temporal

interpolation using optical flow. *Tech. Rep. UW-CSE-09-08-01* : 1–41.

Hongwei, W., Zhan, H., Jian, G., and Hongliang, X. (2015) The Optical Flow Method Research of Particle Image Velocimetry. *Procedia Engineering* 99: 918–924.

Hossain, F., and Anagnostou, E. N. (2005) Using a multi-dimensional satellite rainfall error model to characterize uncertainty in soil moisture fields simulated by an offline land surface model. *Geophysical Research Letters* 32(15): 1–4.

Hunter, N. M., Bates, P. D., Horritt, M. S., De Roo, a. P. J., and Werner, M. G. F. (2005) Utility of different data types for calibrating flood inundation models within a GLUE framework. *Hydrology and Earth System Sciences* 9(4): 412–430.

Hussain, I., Spöck, G., Pilz, J., Faisal, M., and Yu, H. L. (2012) Spatio-temporal interpolation of precipitation including covariates: During monsoon periods in Pakistan. *Pakistan Journal of Statistics* 28(3): 351–365.

Iqbal, A., Xuan, Y., Butler, D., and Fu, G. (2017) Improving the accuracy of temporally and spatially interpolated radar Quantitative Precipitation Forecasts. *Journal of Hydrology*.

Jongh, I. De, Quintelier, E., and Cauwenberghs, K. (2012) Using combined raingauge and high-resolution radar data in an operational flood forecast system in Flanders. *Weather Radar and Hydrology ((Proceedings of a symposium held in Exeter, UK, April 2011)* (April 2011): 2012.

Journel, A. G., and Huijbregts, C. J. (1978) *Mining geostatistics*. New York.

Kasiviswanathan, K. S., and Sudheer, K. P. (2016) Methods used for quantifying the prediction uncertainty of artificial neural network based hydrologic models. *Stochastic Environmental Research and Risk Assessment* 2(1): 1–12.

Katz, R. W., Parlange, M. B., and Naveau, P. (2002) Statistics of extremes in hydrology. 25: 1287–1304.

Kelly, K. S., and Krzysztofowicz, R. (2000) Precipitation uncertainty processor for probabilistic river stage forecasting. *Water Resources Research* 36(11): 3265.

Khajehei, S., and Moradkhani, H. (2017) Towards an improved ensemble precipitation forecast : A probabilistic post-processing approach. *Journal of Hydrology* 546: 476–489.

Khan, U., and Valeo, C. (2015) Comparing a Bayesian and fuzzy number approach to uncertainty quantification in short–term dissolved oxygen prediction. *Journal of Environmental Informatics* 53(9): 1689–1699.

Kimura, M., Kido, Y., and Nakakita, E. (2010) Development of real-time flood forecasting method in urban drainage areas. *Proceedings of 9th International Conference on Hydroinformatics* 3: 1802–1810.

Kimura, M., Kido, Y., and Nakakita, E. (2012) Study on a real-time flood forecasting method for locally heavy rainfall with high-resolution x-band polarimetric radar information. *Weather Radar and Hydrology ((Proceedings of a symposium held in Exeter, UK, April 2011)* 351(April 2011): 454–459.

KIMURA, M., KIDO, Y., and NAKAKITA, E. (2011) FUNDAMENTAL STUDY ON REAL-TIME FLOOD FORECASTING METHOD FOR LOCALLY HEAVY RAINFALL IN URBAN DRAINAGE AREAS. : 931–936.

Kitanidis, P. K., and Bras, R. L. (1980) Real-time forecasting with a conceptual hydrologic model: 2. Applications and results. *Water Resources Research* 16(6): 1034–1044.

Kleiber, W., Raftery, A. E., and Gneiting, T. (2010) Geostatistical Model Averaging for Locally Calibrated Probabilistic Quantitative Precipitation Forecasting. (May 2012): 37–41. doi:10.1198/jasa.2011.ap10433.

Koizumi, K. (1999) An Objective Method to Modify Numerical Model Forecasts with Newly Given Weather Data Using an Artificial Neural Network. *Wea. Forecasting* 14(1): 109–118.

König, A., Sveinung, S., and Schilling, W. (2002) Damage Assessment for Urban Flooding.

Koriche, S. A., and Rientjes, T. H. M. (2016) Application of satellite products and hydrological modelling for fl ood early warning. *Physics and Chemistry of the Earth* 93: 12–23.

Krajewski, W. F., and Smith, J. a. (2002) Radar hydrology: Rainfall estimation. *Advances in Water Resources* 25: 1387–1394.

Krige, D. . (1951) A Statistical Approaches to Some Basic Mine Valuation Problems on the Witwatersrand. *Journal of the Chemical, Metallurgical and Mining Society of South Africa* (52): 119–139.

Krzy (1999) Calibration of Probabilistic Quantitative Precipitation Forecasts. : 427–442.

Krzysztofowicz, R. (1999) Bayesian forecasting via deterministic model. *Risk Analysis* 19(4): 739–749.

Krzysztofowicz, R. (2001) Bayesian theory of probabilistic forecasting via deterministic hydrologic model. *Water Resources Research* 37(2): 441.

Krzysztofowicz, R., and Herr, H. D. (2001) Hydrologic uncertainty processor for probabilistic river stage forecasting : precipitation-dependent model. 249: 46–68.

Krzysztofowicz, R., and Kelly, K. S. (2000) Hydrologic uncertainty processor for probabilistic river stage forecasting. *Water Resources Research* 36(11): 3265–3277.

Kuczera, G., and E Parent (1998) Monte Carlo assessment of parameter uncertainty in conceptual catchment models: the Metropolis algorithm. *Journal of Hydrology*.

Kumar, V., and Remadevi (2006) Kriging of Groundwater Levels – A Case Study. *Journal of Spatial Hydrology* 6(1): 12.

Lallahem, S., Mania, J., Hani, A., and Najjar, Y. (2005) On the use of neural networks to evaluate groundwater levels in fractured media. *Journal of Hydrology* 307(1–4): 92–111.

Lan, J., Li, J., Hu, G., and Zeng, Y. (2013) Distance estimation using a panoramic sensor based on a novel spherical optical flow algorithm. *Optics and Laser Technology* 45(1): 168–176.

Laroche, S., and Zawadzki, I. (1994) A Variational Analysis Method for Retrieval of 3-Dimensional Wind-Field from Single Doppler Radar Data. *Journal of the*

Atmospheric Sciences.

Laroche, S., and Zawadzki, I. (1995) Retrievals of Horizontal Winds from Single-Doppler Clear-Air Data by Methods of Cross Correlation and Variational Analysis. *Journal of Atmospheric and Oceanic Technology*.

Lay, M. Le, and Saulnier, G. M. (2007) Exploring the signature of climate and landscape spatial variabilities in flash flood events : Case of the 8 – 9 September 2002 Ce catastrophic event. *Geophysical Research Letters* 34(September 2002): 1–5.

Lebel, T., and Bastin, G. (1985) Variogram identification by the mean-squared interpolation error method with application to hydrologic fields. *Journal of Hydrology* 77(1–4): 31–56.

Lee, C.-S., Ho, H.-Y., Lee, K. T., Wang, Y.-C., Guo, W.-D., Chen, D. Y.-C., Hsiao, L.-F., Chen, C.-H., Chiang, C.-C., Yang, M.-J., and Kuo, H.-C. (2013) Assessment of sewer flooding model based on ensemble quantitative precipitation forecast. *Journal of Hydrology* 506: 101–113.

Li, J., and Heap, A. D. (2008) A Review of Spatial Interpolation Methods for Environmental Scientists. *Australian Geological Survey Organisation* GeoCat# 68(2008/23): 154.

Li, L., Romary, T., and Caers, J. (2015) Universal kriging with training images. *Spatial Statistics* 14: 240–268.

Li, L., and Schmid, W. (1994) Nowcasting of Motion and Growth of Precipitation with Radar over a Complex Orography. *Journal of Applied Meteorology* 34.

Liechti, K., Zappa, M., Fundel, F., and Germann, U. (2013) Probabilistic evaluation of ensemble discharge nowcasts in two nested Alpine basins prone to flash floods. *Hydrological Processes* 27(1): 5–17.

Liguori, S., and Rico-Ramirez, M. A. (2012) Quantitative assessment of short-term rainfall forecasts from radar nowcasts and MM5 forecasts. *Hydrological Processes* 26(25): 3842–3857.

Liguori, S., Rico-Ramirez, M. a., Schellart, a. N. a., and Saul, a. J. (2012) Using probabilistic radar rainfall nowcasts and NWP forecasts for flow prediction in urban catchments. *Atmospheric Research* 103: 80–95.

Lin, C.-Y., and Lee, T. H. (2011) Combination of radar and raingauge observations using a co-kriging method. 351: 237–242.

Lobligeois, F., Andréassian, V., Perrin, C., Tabary, P., and Loumagne, C. (2014) When does higher spatial resolution rainfall information improve streamflow simulation? An evaluation using 3620 flood events. *Hydrology and Earth System Sciences* 18(2): 575–594.

Loewe, R., Thomdahl, S., Mikkelsen, P. S., Rasmussen, M. R., and Madsen, H. (2014) Probabilistic online runoff forecasting for urban catchments using inputs from rain gauges as well as statically and dynamically adjusted weather radar. *Journal of Hydrology* 512: 397–407.

Looper, J. P., and Vieux, B. E. (2012) An assessment of distributed flash flood forecasting accuracy using radar and rain gauge input for a physics-based distributed hydrologic model. *Journal of Hydrology* 412–413: 114–132.

Luk, K. C., Ball, J. E., and Sharma, A. (2000) A study of optimal model lag and spatial inputs to artificial neural network for rainfall forecasting. *Journal of Hydrology* 227(1–4): 56–65.

Madadgar, S., Moradkhani, H., and Garen, D. (2014) Towards improved post-processing of hydrologic forecast ensembles. *Hydrological Processes* 28(1): 104–122.

Maier, H. R., Jain, A., Dandy, G. C., and Sudheer, K. P. (2010) Methods used for the development of neural networks for the prediction of water resource variables in river systems: Current status and future directions. *Environmental Modelling and Software* 25(8): 891–909.

Mantovan, P., and Todini, E. (2006) Hydrological forecasting uncertainty assessment: Incoherence of the GLUE methodology. *Journal of Hydrology* 330(1–2): 368–381.

Matheron, G. (1971) The theory of regionalized variables and its applications. *Les Cahiers Du Centre de Morphlogie Mathematique*.

McCollor, D., and Stull, R. (2008) Hydrometeorological Short-Range Ensemble Forecasts in Complex Terrain. Part I: Meteorological Evaluation. *Weather and Forecasting* 23(4): 533.

Mecklenburg, S., Joss, J., and Schmid, W. (2000) Improving the nowcasting of precipitation in an Alpine region with an enhanced radar echo tracking algorithm. *Journal of Hydrology* 239(1–4): 46–68.

Mei, Y., Anagnostou, E. N., Stampoulis, D., Nikolopoulos, E. I., Borga, M., and Vegara, H. J. (2014) Rainfall organization control on the flood response of mild-slope basins. *JOURNAL OF HYDROLOGY* 510: 565–577.

Met Office (2013) National Meteorological Library and Archive Fact sheet 15 — Weather radar. : 22.

Michaud, J., and Sorooshian, S. (1994) Comparison of simple versus complex distributed runoff models on a midsized semiarid watershed. *Water Resources Research* 30(3): 593–605.

Mizukami, N., and Smith, M. B. (2012) Analysis of inconsistencies in multi-year gridded quantitative precipitation estimate over complex terrain and its impact on hydrologic modeling. doi:10.1016/j.jhydrol.2012.01.030.

Mogil, H. M., Monro, J. C., and Groper, H. S. (1978) NWS's Flash Flood Warning and Disaster Preparedness Programs. *Bulletin of the American Meteorological Society*.

Montanari, A. (2005) Large sample behaviors of the generalized likelihood uncertainty estimation (GLUE) in assessing the uncertainty of rainfall-runoff simulations. *Water Resources Research* 41(8): 1–13.

Montanari, A., and Brath, A. (2004) A stochastic approach for assessing the uncertainty of rainfall-runoff simulations. 40: 1–11.

Montanari, A., and Grossi, G. (2008) Estimating the uncertainty of hydrological forecasts: A statistical approach. *Water Resources Research* 44(12): 1–9.

Moore, R. J. (2007) The PDM rainfall-runoff model. *Hydrology and Earth System Sciences* 11(1): 483–499.

Moore, R. J., Bell, V. A., Cole, S. J., and Jones, D. A. (2006) Spatio-temporal rainfall datasets and their use in evaluating the extreme event performance of hydrological models. *Extremes*.

Moore, R. J., Cole, S. J., and Illingworth, A. J. (2012) *Weather Radar and*

Hydrology. Wallingford: IAHS Publication.

Moore, R. J., Jones, A. E., Jones, D. A., Black, K. B., and Bell, V. A. (2004) Weather Radar for Flood Forecasting : Some Uk Experiences. *Sixth International Symposium on Hydrological Applications of Weather Radar* (February): 11.

Morin, E., Goodrich, D. C., Maddox, R. A., Gao, X., Gupta, H. V., and Sorooshian, S. (2006) Spatial patterns in thunderstorm rainfall events and their coupling with watershed hydrological response. *Advances in Water Resources* 29(6): 843–860.

Morin, E., and Yakir, H. (2014) Hydrological impact and potential flooding of convective rain cells in a semi-arid environment semi-arid environment. *Hydrological Sciences Journal – Journal des Sciences Hydrologiques* 59(7): 1353–1362.

Moustafa, M. M., and Yomota, A. (1998) Use of a covariance variogram to investigate influence of subsurface drainage on spatial variability of soil-water properties. *Agricultural Water Management* 37(1): 1–19.

Mueller, C., Saxen, T., Roberts, R., Wilson, J., Betancourt, T., Dettling, S., Oien, N., and Yee, J. (2003) NCAR Auto-Nowcast System. *Weather and Forecasting* 18: 17.

Nayak, P. C., Satyaji Rao, Y. R., and Sudheer, K. P. (2006) Groundwater level forecasting in a shallow aquifer using artificial neural network approach. *Water Resources Management* 20(1): 77–90.

Néelz, S., and Pender, G. (2013) *Benchmarking the latest generation of 2D hydraulic modelling packages*. Bristol: Environment Agency.

Nielsen, J. E., Thorndahl, S., and Rasmussen, M. R. (2014) A numerical method to generate high temporal resolution precipitation time series by combining weather radar measurements with a nowcast model. *Atmospheric Research* 138: 1–12.

Nogueira, M., and Barros, A. P. (2015) Transient stochastic downscaling of quantitative precipitation estimates for hydrological applications. *Journal of Hydrology* 529: 1407–1421.

Novikov, A., Melchers, R. E., Shinjikashvili, E., and Kordzakhia, N. (2005) First passage time of filtered Poisson process with exponential shape function. *Probabilistic Engineering Mechanics* 20: 57–65.

Ofwat (2004) *Customer Research 2004 : Survey of customers affected by sewer flooding*. Birmingham.

Ofwat (2011) *Future Impacts on Sewer Systems in England and Wales*. Cambridge.

Olsson, J., Simonsson, L., and Ridal, M. (2013) Rainfall nowcasting: predictability of short-term extremes in Sweden. *Urban Water Journal* (January): 1–11. doi:10.1080/1573062X.2013.847465.

Onyutha, C., and Willems, P. (2017) Influence of spatial and temporal scales on statistical analyses of rainfall variability in the River Nile basin. *Dynamics of Atmospheres and Oceans* 77: 26–42.

Pappenberger, F., Beven, K. J., Hunter, N. M., Bates, P. D., Gouweleeuw, B. T., Thielen, J., and Roo, A. P. J. De (2005) Cascading model uncertainty from medium range weather forecasts (10 days) through a rainfall-runoff model to flood inundation predictions within the European Flood Forecasting System (EFFS). *Hydrology and Earth System Sciences Discussions* 9(4): 381–393.

Parker, D. J., Priest, S. J., and McCarthy, S. S. (2011) Surface water flood warnings requirements and potential in England and Wales. *Applied Geography* 31(3): 891–900.

Piccolo, F., and Chirico, G. B. (2005) Sampling errors in rainfall measurements by weather radar. *Advances in Geosciences* 2: 151–155.

Pierce, C. E., Ebert, E., Seed, a. W., Sleigh, M., Collier, C. G., Fox, N. I., Donaldson, N., Wilson, J. W., Roberts, R., and Mueller, C. K. (2004) The Nowcasting of Precipitation during Sydney 2000: An Appraisal of the QPF Algorithms. *Weather and Forecasting* 19(1): 7–21.

Priest, S. J., Parker, D. J., Hurford, a P., Walker, J., and Evans, K. (2011) Assessing options for the development of surface water flood warning in England and Wales. *Journal of environmental management* 92(12): 3038–48.

Rafieeinasab, A., Norouzi, A., Seo, D. J., and Nelson, B. (2015) Improving high-

resolution quantitative precipitation estimation via fusion of multiple radar-based precipitation products. *Journal of Hydrology* 531: 320–336.

Ramos, M. H., Van Andel, S. J., and Pappenberger, F. (2013) Do probabilistic forecasts lead to better decisions? *Hydrology and Earth System Sciences* 17(6): 2219–2232.

Reggiani, P., and Weerts, A. H. (2007) Probabilistic Quantitative Precipitation Forecast for Flood Prediction : An Application. *Journal of Hydrometeorology* (Krzysztofowicz 1999): 76–95. doi:10.1175/2007JHM858.1.

Regonda, S. K., Seo, D.-J., Lawrence, B., Brown, J. D., and Demargne, J. (2013) Short-term ensemble streamflow forecasting using operationally-produced single-valued streamflow forecasts – A Hydrologic Model Output Statistics (HMOS) approach. *Journal of Hydrology* 497(0): 80–96.

Rene, J.-R. (2014) Probabilistic Real-Time Urban Flood Forecasting Based on Data of Varying Degree of Quality and Quantity.

Renshaw, E. (2004) Metropolis – Hastings from a stochastic population dynamics perspective. 45: 765–786.

Rezacova, D., Sokol, Z., and Pesice, P. (2007) A radar-based verification of precipitation forecast for local convective storms. *Atmospheric Research* 83(2–4): 211–224.

Rico-Ramirez, M. a., Liguori, S., and Schellart, a. N. a. (2015) Quantifying radar-rainfall uncertainties in urban drainage flow modelling. *Journal of Hydrology* 528: 17–28.

Rinehart, R. E., and Garvey, E. T. (1978) Three-dimensional storm motion detection by conventional weather radar. *Nature* 273: 287–289.

Robertson, D. E., Shrestha, D. L., Wang, Q. J., Land, C., and Box, P. O. (2013) Post-processing rainfall forecasts from numerical weather prediction models for short-term streamflow forecasting. : 3587–3603. doi:10.5194/hess-17-3587-2013.

Rossa, A., Liechti, K., Zappa, M., Bruen, M., Germann, U., Haase, G., Keil, C., and Krahe, P. (2011) The COST 731 Action: A review on uncertainty propagation in advanced hydro-meteorological forecast systems. *Atmospheric*

Research 100(2–3): 150–167.

Rozalis, S., Morin, E., Yair, Y., and Price, C. (2010) Flash flood prediction using an uncalibrated hydrological model and radar rainfall data in a Mediterranean watershed under changing hydrological conditions. *Journal of Hydrology* 394(1–2): 245–255.

Ruzanski, E., Chandrasekar, V., and Wang, Y. (2011) The CASA Nowcasting System. *Journal of Atmospheric and Oceanic Technology* 28(5): 640–655.

Sadek, R., Ballester, C., Garrido, L., Meinhardt, E., and Caselles, V. (2012) Frame Interpolation With Occlusion Detection Using a Time Coherent Segmentation. *Proceedings of the International Conference on Computer Vision Theory and Applications* : 367–372. doi:10.5220/0003830803670372.

Šálek, M., Novák, P., and Seo, D. (2004) Operational application of combined radar and raingauges precipitation estimation at the …. *Proceedings of ERAD* 2000: 16–20.

Samani, N., Gohari-Moghadam, M., and Safavi, A. A. (2007) A simple neural network model for the determination of aquifer parameters. *Journal of Hydrology* 340(1–2): 1–11.

Sangati, M., Borga, M., Rabuffetti, D., and Bechini, R. (2009) Advances in Water Resources Influence of rainfall and soil properties spatial aggregation on extreme flash flood response modelling : An evaluation based on the Sesia river basin , North Western Italy. *Advances in Water Resources* 32(7): 1090–1106.

Sapriza-Azuri, G., J??dar, J., Navarro, V., Slooten, L. J., Carrera, J., and Gupta, H. V. (2015) Impacts of rainfall spatial variability on hydrogeological response. *Water Resources Research* 51(2): 1300–1314.

Schaake, J., Demargne, J., Hartman, R., Mullusky, M., Welles, E., Wu, L., Herr, H., Fan, X., and Seo, D. J. (2007) Precipitation and temperature ensemble forecasts from single-value forecasts. *Hydrology and Earth System Sciences Discussions* 4: 655–717.

Schellart, A. N. ., Rico-Ramirez, M. ., Liguori, S., and Saul, a J. (2009) Quantitative Precipitation Forecasting for a Small Urban Area : Use of Radar Nowcasting. *Change* : 22–26.

Schellart, A., Ochoa, S., Simões, N., Wang, L., Rico-ramirez, M., Duncan, A., Chen, A. S., Keedwell, E., Djordjević, S., Savić, D. a, Saul, A., and Maksimović, Č. (2011) Urban pluvial flood modelling with real time rainfall information – UK case studies. *12th International Conference on Urban Drainage* 2(September): 10–15.

Schellart, a. N. a., Shepherd, W. J., and Saul, a. J. (2012) Influence of rainfall estimation error and spatial variability on sewer flow prediction at a small urban scale. *Advances in Water Resources* 45: 65–75.

Scheuerer, M. (2014) Probabilistic quantitative precipitation forecasting using Ensemble Model Output Statistics. (April): 1086–1096. doi:10.1002/qj.2183.

Schilling, W. (1991) Rainfall data for urban hydrology: what do we need? *Atmospheric Research* 27(1–3): 5–21.

Schlather, M., and Gneiting, T. (2006) Local approximation of variograms by covariance functions. *Statistics and Probability Letters* 76(12): 1303–1304.

Schloeder, C. A., Zimmerman, N. E., and Jacobs, M. J. (2001) Comparison of Methods for Interpolating Soil Properties Using Limited Data. *Soil Science Society of America Journal* 65(August): 470–479.

Schmid, W., Mathis, A., Keller, U., and Sprengi, W. (2002) NOWCASTING THE RISK OF SNOWFALL AND FREEZING RAIN WITH RADAR AND GROUND DATA.

Segond, M. L., Wheater, H. S., and Onof, C. (2007) The significance of spatial rainfall representation for flood runoff estimation: A numerical evaluation based on the Lee catchment, UK. *Journal of Hydrology* 347(1–2): 116–131.

Selby, B., and Kockelman, K. M. (2013) Spatial prediction of traffic levels in unmeasured locations: Applications of universal kriging and geographically weighted regression. *Journal of Transport Geography* 29: 24–32.

Sempere-Torres, D., Berenguer, M., Pattazzi, A., and Salsón, S. (2012) Towards wind farms and meteorological radar coexistence: guidelines for mitigating impacts and examples of operational corrections. *ERAD 2012 -THE SEVENTH EUROPEAN CONFERENCE ON RADAR IN METEOROLOGY AND HYDROLOGY* 23: 1157–1180.

Seo, B.-C., and Krajewski, W. F. (2015) Correcting temporal sampling error in radar-rainfall: Effect of advection parameters and rain storm characteristics on the correction accuracy. *Journal of Hydrology* 1: 1–12.

Seo, D.-J., Herr, H. D., and Schaake, J. C. (2006) A statistical post-processor for accounting of hydrologic uncertainty in short-range ensemble streamflow prediction. *Hydrology and Earth System Sciences Discussions* 3(4): 1987–2035.

Seo, D.-J., Seed, A., and Delrieu, G. (2010) Radar and Multisensor Rainfall Estimation for Hydrologic Applications. *Rainfall: State of the Science* 191(American Geophysical Union): 288.

Seo, D., Perica, S., Welles, E., and Schaake, J. C. (2000) Simulation of precipitation fields from probabilistic quantitative precipitation forecast. 239: 203–229.

Seo, Y., Schmidt, A. R., and Sivapalan, M. (2012) Effect of storm movement on flood peaks: Analysis framework based on characteristic timescales. *Water Resources Research* 48(5): 1–12.

Sepúlveda, F., Rosenberg, M. D., Rowland, J. V., and Simmons, S. F. (2012) Kriging predictions of drill-hole stratigraphy and temperature data from the Wairakei geothermal field, New Zealand: Implications for conceptual modeling. *Geothermics* 42: 13–31.

Sharif, H. O., Yates, D., Roberts, R., and Mueller, C. (2005) The Use of an Automated Nowcasting System to Forecast Flash Floods in an Urban Watershed. : 190–202.

Shucksmith, P. E., Sutherland-Stacey, L., and Austin, G. L. (2011) The spatial and temporal sampling errors inherent in low resolution radar estimates of rainfall. *Meteorological Applications* 18(3): 354–360.

Silvestro, F., and Rebora, N. (2014) Impact of precipitation forecast uncertainties and initial soil moisture conditions on a probabilistic flood forecasting chain. *JOURNAL OF HYDROLOGY* 519: 1052–1067.

Simoncelli, E. P., and Adelson, E. H. (1991) Computing Optical Flow Distributions Using Spatio-temporal Filters. *Cognitive Science*.

Siswantoro, J., Satria, A., Abdullah, A., and Idrus, B. (2016) A linear model based on Kalman filter for improving neural network classification performance. 49: 112–122.

Sloughter, J. M. L., Raftery, A. E., Gneiting, T., and Fraley, C. (2007) Probabilistic Quantitative Precipitation Forecasting Using Bayesian Model Averaging. *Monthly Weather Review* 135(2005): 3209–3220.

Smith, J. a., Baeck, M. L., Meierdiercks, K. L., Miller, A. J., and Krajewski, W. F. (2007) Radar rainfall estimation for flash flood forecasting in small urban watersheds. *Advances in Water Resources* 30: 2087–2097.

Smith, M. B., Koren, V. I., Zhang, Z., Reed, S. M., Pan, J. J., and Moreda, F. (2004) Runoff response to spatial variability in precipitation: An analysis of observed data. *Journal of Hydrology* 298(1–4): 267–286.

Smith, P. J., Beven, K. J., Weerts, A. H., and Leedal, D. (2012) Adaptive correction of deterministic models to produce probabilistic forecasts. *Hydrology and Earth System Sciences* 16(8): 2783–2799.

Ta'any, R. A., Tahboub, A. B., and Saffarini, G. A. (2009) Geostatistical analysis of spatiotemporal variability of groundwater level fluctuations in Amman-Zarqa basin, Jordan: a case study. *Environmental Geology* 57(3): 525–535.

Tapoglou, E., Karatzas, G. P., Trichakis, I. C., and Varouchakis, E. A. (2014) A spatio-temporal hybrid neural network-Kriging model for groundwater level simulation. *Journal of Hydrology* 519(PD): 3193–3203.

Thiemann, M., Trosset, M., Gupta, H., and Sorooshian, S. (2001) Bayesian recursive parameter estimation for hydrologic models Water Resources Research Volume 37, Issue 10. *Water Resources Research* 37(10): 2521–2535.

Thompson, C. M., and Frazier, T. G. (2014) Deterministic and probabilistic flood modeling for contemporary and future coastal and inland precipitation inundation. *Applied Geography* 50: 1–14.

Tramblay, Y., Bouvier, C., Martin, C., Didon-lescot, J., Todorovik, D., and Domergue, J. (2010) Assessment of initial soil moisture conditions for event-based rainfall – runoff modelling. *Journal of Hydrology* 387(3–4): 176–187.

Trichakis, I. C., Nikolos, I. K., and Karatzas, G. P. (2009) Optimal selection of artificial neural network parameters for the prediction of a karstic aquifer's response. *Hydrological Processes* 2274(November 2008): 2956–2969.

Trichakis, I., Nikolos, I., and Karatzas, G. P. (2011) Comparison of bootstrap confidence intervals for an ANN model of a karstic aquifer response. *Hydrological Processes* 25(18): 2827–2836.

Tu, J. V (1996) Advantages and Disadvantages of Using Artificial Neural Networks versus Logistic Regression for Predicting Medical Outcomes. 49(11): 1225–1231.

van Werkohoven, K., Wagener, T., Reed, P., and Tang, Y. (2008) Rainfall characteristics define the value of streamflow observations for distributed watershed model identification. *Geophysical Research Letters* 35(11): 1–6.

Verkade, J. S., and Werner, M. G. F. (2011) Estimating the benefits of single value and probability forecasting for flood warning. *Hydrology and Earth System Sciences* 15(12): 3751–3765.

Versini, P.-A. (2012) Use of radar rainfall estimates and forecasts to prevent flash flood in real time by using a road inundation warning system. *Journal of Hydrology* 416–417: 157–170.

Vieira, S. R., Hatfield, J. L., Nielsen, D. R., and Biggar, J. W. (1983) Geostatistical theory and application to variability of some agronomical properties. *Hilgardia* 51(3)(3): 1–75.

Vieux, B. E., Park, J.-H., and Kang, B. (2009) Distributed Hydrologic Prediction: Sensitivity to Accuracy of Initial Soil Moisture Conditions and Radar Rainfall Input. *Journal of Hydrologic Engineering* 14(7): 671–689.

Vieux, B. E., and Vieux, J. E. (2005) Statistical evaluation of a radar rainfall system for sewer system management. *Atmospheric Research* 77(1–4): 322–336.

Viglione, A., Chirico, G. B., Woods, R., and Blöschl, G. (2010) Generalised synthesis of space-time variability in flood response: An analytical framework. *Journal of Hydrology* 394(1–2): 198–212.

Villarini, G., Krajewski, W. F., Ntelekos, A. a., Georgakakos, K. P., and Smith, J.

a. (2010) Towards probabilistic forecasting of flash floods: The combined effects of uncertainty in radar-rainfall and flash flood guidance. *Journal of Hydrology* 394(1–2): 275–284.

Vivoni, E. R., Entekhabi, D., and Hoffman, R. N. (2007) Error propagation of radar rainfall nowcasting fields through a fully distributed flood forecasting model. *Journal of Applied Meteorology and Climatology* 46(6): 932–940.

Wang, D., Diazdelao, F. A., Wang, W., Lin, X., Patterson, E. A., and Mottershead, J. E. (2016) Uncertainty quantification in DIC with Kriging regression. *Optics and Lasers in Engineering* 78: 182–195.

Wang, L.-P., Ochoa-Rodríguez, S., Onof, C., and Willems, P. (2015) Singularity-sensitive gauge-based radar rainfall adjustment methods for urban hydrological applications. *Hydrology and Earth System Sciences* 19(9): 4001–4021.

Wang, L.-P., Ochoa-Rodríguez, S., Simões, N. E., Onof, C., and Maksimović, C. (2013) Radar-raingauge data combination techniques: a revision and analysis of their suitability for urban hydrology. *Water science and technology : a journal of the International Association on Water Pollution Research* 68(4): 737–47.

Wang, L.-P., Ochoa-Rodríguez, S., Van Assel, J., Pina, R. D., Pessemier, M., Kroll, S., Willems, P., and Onof, C. (2015) Enhancement of radar rainfall estimates for urban hydrology through optical flow temporal interpolation and Bayesian gauge-based adjustment. *Journal of Hydrology*. doi:10.1016/j.jhydrol.2015.05.049.

Wang, Q. J., and Robertson, D. E. (2011) Multisite probabilistic forecasting of seasonal flows for streams with zero value occurrences. *Water Resources Research* 47(2): 1–19.

Wang, Q. J., Robertson, D. E., and Chiew, F. H. S. (2009) A Bayesian joint probability modeling approach for seasonal forecasting of streamflows at multiple sites. *Water Resources Research* 45(5): 1–18.

WaPug (2004) Report By the Foundation for Ater Research Wastewater Research & Industry Support Forum.

Wasson, R. J. (2016) Uncertainty , ambiguity and adaptive flood forecasting. *Policy and Society* 35(2): 125–136.

Weerts, A. H., Winsemius, H. C., and Verkade, J. S. (2011) Estimation of predictive hydrological uncertainty using quantile regression: Examples from the National Flood Forecasting System (England and Wales). *Hydrology and Earth System Sciences* 15(1): 255–265.

Wen, Y., Hou, L., He, L., Peterson, B. S., and Xu, D. (2015) A highly accurate symmetric optical flow based high-dimensional nonlinear spatial normalization of brain images. *Magnetic Resonance Imaging* 33(4): 465–473.

Werner, M., Reggiani, P., Roo, A. De, Bates, P., and Sprokkereef, E. (2005) Flood Forecasting and Warning at the River Basin and at the European Scale. *Natural Hazards* 36(1–2): 25–42.

Wilks, D. (2011) *Statistical Methods in the Atmospheric Sciences*.

Wood, A., and Schaake, J. (2007) Correcting Errors in Streamflow Forecast Ensemble Mean and Spread. : 132–148. doi:10.1175/2007JHM862.1.

Wood, E. F., Sivapalan, M., Beven, K., and Band, L. (1988) Effects of spatial variability and scale with implications to hydrologic modeling. *Journal of Hydrology* 102(1–4): 29–47.

Wu, J., Norvell, W. A., and Welch, R. M. (2006) Kriging on highly skewed data for DTPA-extractable soil Zn with auxiliary information for pH and organic carbon. *Geoderma* 134(1–2): 187–199.

Wu, L., Seo, D. J., Demargne, J., Brown, J. D., Cong, S., and Schaake, J. (2011) Generation of ensemble precipitation forecast from single-valued quantitative precipitation forecast for hydrologic ensemble prediction. *Journal of Hydrology* 399(3–4): 281–298.

Wu, M. C., and Lin, G. F. (2017) The very short-term rainfall forecasting for a mountainous watershed by means of an ensemble numerical weather prediction system in Taiwan. *Journal of Hydrology* 546: 60–70.

Xianzhao, L. I. U., and Jiazhu, L. I. (2008) Application of SCS Model in Estimation of Runoff from Small Watershed in Loess Plateau of China. 18(40101005): 235–241.

Yan, F., Cao, S., Liu, X., and Yang, K. (2008) Design of groundwater level monitoring network with ordinary kriging. *Journal of Hydrodynamics, Ser. B* 20(3): 339–346.

Yang, C., Yan, Z., and Shao, Y. (2012) Probabilistic Precipitation Forecasting Based on Ensemble Output Using Generalized Additive Models and Bayesian Model Averaging. (973): 1–12. doi:10.1007/s13351-012-0101-8.1.

Yasrebi, J., Saffari, M., Fathi, H., Karimian, N., Moazallahi, M., and Gazni, R. (2009) Evaluation and Comparison of Ordinary Kriging and Inverse Distance Weighting Methods for Prediction of Spatial Variability of Some Soil Chemical Parameters. *Research Journal of Biological Sciences* 4(1): 93–102.

Yeung, H. Y., Man, C., Chan, S. T., Seed, A., Man, C., Chan, S. T., and Development, A. S. (2017) Development of an operational rainfall data quality-control scheme based on radar-raingauge co-kriging analysis based on radar-raingauge co-kriging analysis. *Hydrological Sciences Journal – Journal des Sciences Hydrologiques* 59(7): 1293–1307.

Young, P. C. (2002) Advances in real–time flood forecasting. *The Royal Society*.

Younger, P. M., Freer, J. E., and Beven, K. J. (2009) Detecting the effects of spatial variability of rainfall on hydrological modelling within an uncertainty analysis framework. *Hydrological Processes* 23(November 2008): 1988–2003.

Yu, C., Shao, T., and Li, D. (2016) Distribution of standard deviation of an observable among superposed states. *Annals of Physics* 373: 43–51.

Yu, W., Nakakita, E., Kim, S., and Yamaguchi, K. (2016) Impact Assessment of Uncertainty Propagation of Ensemble NWP Rainfall to Flood Forecasting with Catchment Scale. 2016.

Yussouf, N., and Stensrud, D. J. (2007) Bias-Corrected Short-Range Ensemble Forecasts of Near-Surface Variables during the 2005/06 Cool Season. *Weather and Forecasting* 22(6): 1274–1286.

Zappa, M., Rotach, M. W., Arpagaus, M., Dorninger, M., Hegg, C., Montani, A., Ranzi, R., Ament, F., Germann, U., Grossi, G., Jaun, S., Rossa, A., Vogt, S., Walser, A., Wehrhan, J., and Wunram, C. (2008) MAP D-PHASE: real-time

demonstration of hydrological ensemble prediction systems. *Atmospheric Science Letters* 9(October): 80–87.

Zare-mehrjardi, M., Taghizadeh-, R., and Ali, A. (2010) Evaluation of Geostatistical Techniques for Mapping Spatial Distribution of Soil PH , Salinity and Plant Cover Affected by Environmental Factors in Southern Iran. *Notulae Scientia Biologicae* 2(4): 92–103.

Zhang, Q., and Wu, J. (2015) Image super-resolution using windowed ordinary Kriging interpolation. *Optics Communications* 336: 140–145.

Zhao, L., Duan, Q., Schaake, J., Ye, A., and Xia, J. (2011) A hydrologic post-processor for ensemble streamflow predictions. *Advances in Geosciences* 29(1999): 51–59.

Zhao, T., Wang, Q. J., Bennett, J. C., Robertson, D. E., Shao, Q., and Zhao, J. (2015) Quantifying predictive uncertainty of streamflow forecasts based on a Bayesian joint probability model. *Journal of Hydrology* 528: 329–340.

Zhou, H., Deng, Z., Xia, Y., and Fu, M. (2016) Neurocomputing A new sampling method in particle fi lter based on Pearson correlation coef fi cient. 216: 208–215.

Zoccatelli, D., Borga, M., Viglione, A., Chirico, G. B., Bl, G., and Federico, N. (2011) Spatial moments of catchment rainfall : rainfall spatial organisation , basin morphology , and flood response. *Hydrology and Earth System Sciences* : 3767–3783. doi:10.5194/hess-15-3767-2011.

Zoccatelli, D., Borga, M., Zanon, F., Antonescu, B., and Stancalie, G. (2010) Which rainfall spatial information for flash flood response modelling ? A numerical investigation based on data from the Carpathian range , Romania. *Journal of Hydrology* 394(1–2): 148–161.